Detectors for Functional Medical Imaging

Dissertation
zur Erlangung des Doktorgrades
an der Fakultät für Mathematik, Informatik und Naturwissenschaften
Fachbereich Physik
der Universität Hamburg

vorgelegt von

Ole Brandt

Hamburg
2019

Gutachter/innen der Dissertation	:	Prof. Dr. Erika Garutti Dr. Ties Behnke
Zusammensetzung der Prüfungskommission	:	Prof. Dr. Erika Garutti Dr. Ties Behnke Prof. Dr. Robin Santra Prof. Dr. Florian Grüner Dr. Etiennette Auffray Hillemanns
Vorsitzender der Prüfungskommission:	:	Prof. Dr. Robin Santra
Datum der Disputation	:	13.12.2019
Vorsitzender des Fach-Promotionsausschusses Physik	:	Prof. Dr. Günter Hans Walter Sigl
Leiter des Fachbereichs Physik	:	Prof. Dr. Wolfgang Hansen
Dekan der Fakultät MIN	:	Prof. Dr. Heinrich Graener

Nothing in life is to be feared, it is only to be understood.
Now is the time to understand more, so that we may fear less.

- Marie Curie

For Anika,
and the adventures yet to come.

Abstract

The work in this thesis deals with two functional medical imaging methods, i.e. positron emission tomography (PET) and X-ray fluorescence imaging (XFI). More specifically, this thesis comprises the commissioning, optimization and simulation of an asymmetric time-of-flight positron emission tomography (TOFPET) prototype within the EndoTOFPET-US (Endoscopic Time-of-Flight Positron Emission Tomography Ultrasound) project as well as the proposition and simulation of several reconstruction methods for X-ray fluorescence imaging.

The EndoTOFPET-US project aims to develop a multimodal endoscopic imaging device combining ultrasound (US) and positron emission tomography (PET). Application areas of the EndoTOFPET-US detector are within image-guided surgery and biopsy, diagnostics as well as development of new biomarkers for pancreas and prostate carcinoma. It consists of an external plate that is positioned in close proximity to the patient and an endoscopic probe comprised of a miniaturized PET detector mounted on an US endoscope. The external plate includes a total of 4096 single channels, each made up of a LYSO (lutetium-yttrium oxyorthosilicate) scintillator crystal optically coupled to a silicon photomultiplier (SiPM). The commissioning of the external plate is performed in terms of maintenance, calibration, slow control implementation and coincidence time resolution (CTR) optimization. Several automated procedures for the calibration of the external plate are developed and the cooling of the external plate is improved via mechanical repositioning and rerouting of some electronic components. An automated online CTR optimization is set up for optimizing the CTR of each channel individually in the external plate in coincidence with a spare module of the external plate. This is necessary to achieve the best possible results in terms of image quality with the EndoTOFPET-US detector. Furthermore, an endoscopic PET detector prototype consisting of 64 channels with size close to the original design is constructed and its time resolution is optimized. An overall system CTR of 255 ps is achieved. After the commissioning and optimization of the setup, first data acquisition with a fully functional and optimized EndoTOFPET-US prototype is performed. A point-like sodium-22 (^{22}Na) source is used in the data acquisition. The spatial resolution achieved with a point-like source is ∼1.4 mm parallel to the detector surfaces and ∼7.0-9.0 mm orthogonal to the detector surfaces, depending on the detector distance and the distance of the source to the endoscopic PET detector.

In order to perform more complex measurements in a controlled environment, a simulation of the EndoTOFPET-US prototype is developed with GAMOS (Geant4-based Architecture for Medicine-Oriented Simulations). It is verified that the simulation fully represents the prototype by replicating the measurements performed and comparing the spatial resolution results. After this verification, application-specific simulations using the NEMA IEC Body Phantom Set^{TM} are developed and implemented. The simulation design intends to determine the quantitative and qualitative image quality of the EndoTOFPET-US prototype and to be easily reproduced in a lab at a later stage. It is shown that a hot volume can be

identified inside a warm background down to a signal-to-background ratio of 3:1. The image quality as a function of detector CTR is studied and co-registration to an existing PET image acquired with two conventional PET detectors is demonstrated. A detailed sensitivity study of the detector is performed.

X-ray fluorescence imaging (XFI) is newly emerging in the field of functional medical imaging and can potentially be used to reconstruct the 3D concentration of metallic compounds (e.g. platinum containing anti-cancer drugs) in-vivo. Four possible imaging and reconstruction methods are proposed for XFI in this thesis: collimated detector reconstruction, fluorescence photon flux reconstruction, timing based rconstruction and X-ray fluorescence tomography (XFT). Each of the proposed imaging methods utilizes an X-ray pencil beam with small energy bandwidth. The timing based imaging approach and XFT are tested in terms of feasibility by means of simulations that are performed with GAMOS. The X-ray source is in approximation modeled after a possible laser-driven Thomson source. Only gold is used as active imaging component. Although the timing based imaging approach works, it requires outstanding detector properties to achieve acceptable results (i.e. time resolution $\leq$ 30 ps at 70 keV photon energies). XFT shows promising results. It is shown that a millimeter sized object with a gold concentration of 500 µg/mL can be visualized with high precision inside a water phantom similar in size to a small rodent.

Zusammenfassung

Die vorliegende Arbeit beschäftigt sich mit zwei medizinischen Bildgebungmethoden, i.e. Positronen-Emissions-Tomographie (PET) und Röntgenfluoreszenz-Bildgebung (XFI). Genauer, beinhaltet die vorliegende Arbeit die Inbetriebnahme, Optimierung und Simulation eines neuartigen multimodalen Bildgebungssystems mit Ultraschall-Endoskopie (US) und Positronen-Emissions-Tomographie (PET) im Rahmen des EndoTOFPET-US (Endoscopic Time-of-Flight Positron Emission Tomography Ultrasound) Projekts sowie Ideen zu und Simulation von verschiedenen Rekonstruktionsmethoden für die Röntgenfluoreszenz-Bildgebung.

Das Detektorsystem im Rahmen des EndoTOFPET-US Projekts soll für bildgestützte Operationen und Biopsien, Diagnostik sowie Entwicklung neuer Biomarker für Prostata- und Bauchspeicheldrüsenkrebs in der Onkologie eingesetzt werden. Es besteht aus einer externen Detektorplatte und einer kleinen endoskopischen Detektorprobe. Während der Anwendung wird die externe Platte in unmittelbarer Nähe des Patienten platziert, während die Probe auf einem Ultraschallendoskop befestigt sein wird. Die externe Platte beinhaltet 4096 Kanäle, von denen jeder aus einem LYSO (lutetium-yttrium-oxyorthosilicat) Szintillator besteht, der optisch an einen Silizium Photomultiplier (SiPM) gekoppelt ist.

Die Inbetriebnahme der externen Platte beinhaltet die Wartung, Kalibrierung, Implementierung von langsam ablaufenden Regelprozessen (z.B. Kühlung) und die Optimierung der Koinzidenz-Zeitauflösung (CTR) jedes einzelnen Kanals. Die Kalibrierung ist automatisiert worden. Die Betriebstemperatur in der externen Platte ist reduziert worden, indem einige der elektronischen Bauteile neu positioniert und Verbindungen umgeleitet worden sind. Es ist eine automatische online Optimierung entwickelt worden, welche eine individuelle Optimierung der CTR für jeden Kanal durchführt. Eine individuelle Optimierung ist notwendig, um die bestmögliche durchschnittliche CTR in der externen Platte zu erreichen. Ein Prototyp für die endoskopische Detektorprobe ist konstruiert und in Bezug auf die CTR optimiert worden, was zu einer CTR von 255 ps geführt hat. Nach der Inbetriebnahme und Optimierung des EndoTOFPET-US Prototyps sind erste Messungen mit einer punktförmigen radioaktiven Quelle (Natrium-22, ^{22}Na) Quelle vorgenommen worden und dabei Ortsauflösung des Prototyps bestimmt worden. Die Ortsauflösung beträgt $\sim$1.4 mm in der Ebene parallel zu den Detektoroberflächen und $\sim$7.0-9.0 mm orthogonal zu den Detektoroberflächen. Die Ortsauflösung orthogonal zu den Detektoroberflächen hängt von der Entfernung der Detekoren zueinander und der Entfernung der radioaktiven Quelle zur endoskopischen Detektorprobe ab.

Eine Simulation des EndoTOFPET-US Prototyps ist entwickelt worden in GAMOS, einem Geant4-basierten Simulationsprogramm, um komplexere Messungen in einer kontrollierten Umgebung durchführen zu können. Zunächst ist sichergestellt worden, dass die Simulation den Prototyp korrekt repräsentiert. Dafür sind die bereits durchgeführten Messungen in der Simulation wiederholt und beide Ergebnisse miteinander verglichen worden. Die Simulation und Messung des EndoTOFPET-US Prototyps stimmen

vollständig überein, weshalb nachfolgend anwendungsbezogene Simulationsszenarien mit dem NEMA IEC Body Phantom Set^{TM} entwickelt worden sind. Die Simulationsszenarien sind so konstruiert worden, dass sie ohne großen Aufwand in einem Labor wiederholt werden können. Die Simulationen zeigen, dass ein heißes Objekt in einem warmen Hintergrund bis zu einem Signal-Hintergrund-Verhältnis von 3:1 identifiziert werden kann. Darüber hinaus ist die qualitative und quantitative Bildqualität in Abhängigkeit von der CTR untersucht und die Co-Registrierung eines EndoTOFPET-US Bildes mit einen von zwei konventionellen PET Detektoren aufgenommenem Bild demonstriert worden. Zusätzlich ist die Sensitivität des EndoTOFPET-US Detektors detailliert untersucht worden.

Röntgenfluoreszenz-Bildgebung (XFI) ist ein Bildgebungsverfahren, welches nach und nach mehr Aufmerksamkeit im Bereich der funktionalen medizinischen Bildgebung erhält. Es kann genutzt werden, um metallische Verbindungen (z.B. Platin beinhaltende Krebsmedikamente) in-vivo 3D zu rekonstruieren. Es werden vier unterschiedliche Bildgebungs- und Rekonstruktionsverfahren für XFI vorgeschlagen: kollimierte Detektorenmethode, Fluoreszenz-Photonen-Fluss-Methode, zeitbasierte Methode und Röntgenfluoreszenz-Tomographie (XFT). Jede dieser Bildgebungsmethoden verwendet einen gebündelten Röntgenstrahl mit einer geringen Energiebandbreite. Die zeitbasierte Methode und XFT werden mit Hilfe einer Simulation in GAMOS auf Durchführbarkeit getestet. Die Röntgenquelle ist dabei dem Röntgenstrahl einer Laser angetriebenen Thomson-Quelle (in Näherung) nachempfunden. Gold ist dabei ausschließlich als aktive Bildgebungskomponente verwendet worden. Die zeitbasierte Bildgebung ist möglich, benötigt jedoch für akzeptable Ergebnisse außergewöhlich gute Detekoreigenschaften (d.h. Zeitauflösung $\leq$ 30 ps bei einer Photonenenergie von 70 keV). XFT weist vielversprechende Ergebnisse auf. Es wird gezeigt, dass ein Objekt, das wenige Millimeter groß ist und eine 500 µg/mL Goldkonzentration beinhaltet, mit großer Präzision innerhalb eines Wasserphantoms in der Größe eines kleinen Nagetieres visualisiert werden kann.

Contents

Chapter 1

Introduction

Functional imaging deals with visualizing metabolic activity and/or distribution of biological active molecules. One of the most prominent examples of functional imaging is nuclear imaging.

Nuclear imaging, such as single photon emission computed tomography (SPECT) and positron emission tomography (PET), is based on the localization of a radioactive compound. It can be used to measure in-vivo the 2D or 3D distribution of a functionalized radioactive tracer molecule (radiotracer). The idea to utilize radiotracers to investigate human physilogy was already conceived in 1923 [1]. Detection in nuclear imaging is mainly based on scintillation and subsequent photodetection. The first scintillator was already built in 1903 by Sir William Crookes. It was a zinc sulfide screen that produced light upon interaction with sufficiently energetic particles. Photomultiplier tubes (PMT) that allow to count the number of photons that are produced in the scintillator were invented in 1930s. Having an electronic device that measures the photons created in the scintillator makes it possible to build large detectors that measure the radioactivity within a large sample. PET utilizes this detection method to this day: (1) converting of a high energetic photon to visible light (scintillation) and (2) counting the number of visible photons created. The radiotracer in PET is labeled with a positron emitting radioisotope. After emission, the positron undergoes electron-positron-annihilation and emits two back-to-back 511 keV photons. The two high energy photons are measured in the PET scanner and the radiotracer distribution in the body can be reconstructed. The main application of PET is in oncology, where it is used to diagnose and localize cancer. In addition to diagnostics, it can be used in radiation therapy to perform treatment verification.

Until a few years ago most PET scanners were mainly equipped with PMTs, wheres new state of the art scanners often utilize silicon photomultipliers (SiPM) or digital silicon photomultipliers (d-SiPM). SiPMs have several advantages compared to PMTs: (1) they are very compact, allowing to build endoscopic devices, (2) they are insensitive to magnetic fields, allowing for combined PET/MRI (magnetic resonance imaging) imaging and (3) d-SiPMs allow to digitize data on the SiPM and to use several time thresholds leading to excellent time resolution.

Time-of-flight PET (TOFPET) was made possible by the advances in detector and readout electronics technology. In TOFPET the arrival time of the two 511 keV photons is measured with a high precision leading to enhanced background rejection and possibly improved localization of the annihilation position. Utilizing the TOF information of the two photons leads to an increased SNR and effectively increases the sensitivity of the detector. This implies that the acquisition time and/or radiation exposure to the patient can potentially be reduced and at the same time image quality can be improved in condition of sufficiently good time resolution. Furthermore, TOFPET can be used to gain artifact free images in

imaging systems that have a limited field of view and/or limited angular coverage.

Intraoperative guidance via nuclear imaging has already been proposed in 1949 [2]. It is a strong tool to guide cancer removal or biopsy. Miniaturized detectors that measure the positron directly have been proposed in the 1990s [3, 4]. However, direct contact of the detector with the tumor is necessary because of the small range of the positron inside the human body (∼1 mm). Even if contact to the cancer is made, only positrons from the cancer surface can be effectively measured. Miniaturized PET probes that either are used in coincidence with a conventional PET scanner improving sensitivity and resolution for a specific organ or are used as handheld devices were proposed ever since.

The EndoTOFPET-US (Endoscopic Time-of-Flight Positron Emission Tomography Ultrasound) project [5] aims to develop an endoscopic multimodal imaging device for simultaneous ultrasound (US) and TOF-PET imaging. The main areas of application of the device are within image-guided surgery and biopsy, diagnostics as well as development of new biomarkers for pancreas and prostate carcinoma [6–9]. Pancreas and prostate cancer are chosen as main focus due to their high frequency and difficult diagnosis/bad prognosis if not detected and treated at an early stage, respectively. The detector consists of two parts: (1) an external PET plate that is located close to the patient and (2) a miniaturized PET detector mounted on an US endoscope. The detectors are build out of scintillator crystals that are read out by silicon photomultipliers (SiPM). A first prototype of the system was developed for prostate imaging. The proposed detector design for prostate imaging is presented in figure 1.1. The small size of the endoscopic

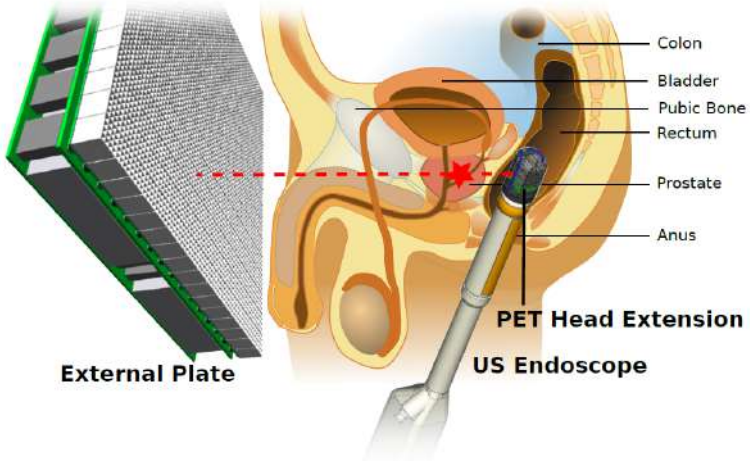

Figure 1.1: Sketch of the EndoTOFPET-US detectors application in the prostate case.

PET detector allows to use a high granularity that would not be feasible in conventional PET detectors due to cost. Because of the high granularity and the close proximity of the probe to the organ under study, a spatial resolution far better than that obtained with conventional PET scanners can be achieved. The EndoTOFPET-US project aims to achieve a spatial resolution of 1 mm and a coincidence time resolution of 200 ps. A wide range of challenge emerge from the detector concept and goals: (1) fast and efficient conversion of the 511 keV photon to optical photons, (2) excellent coupling to the photodetector, (3) compact low noise low power consumption electronics, (3) integration miniaturized cooling in the probe, (4) precise tracking and (5) real-time image reconstruction.

A newly emerging functional imaging method is X-ray fluorescence imaging (XFI). It is based on the in-vivo localization of metallic compounds. XFI utilizes X-rays to excite metal atoms that are attached to biological active molecules. The excited metal atoms can subsequently emit fluorescence photons. By

detecting these photons the location of the metallic compound can be reconstructed. With new brilliant high energy X-ray sources on the horizon (i.e. laser plasma based x-ray sources), XFI is gaining in interest. The applications are within diagnostics, treatment verification and drug development. For example the localization of administered platinum containing anti-cancer drugs can be studied. Furthermore, using functionalized gold nanoparticles as early stage tumor diagnostics has been proposed [10]. However, the best imaging and reconstruction methods for XFI are still subject to research. The small amount of fluorescence photons that are created and homogeneity of them pose big challenge to the detector and the reconstruction both.

The scope of this thesis is as follows:

- **Chapter 2** introduces the physics principals of PET such as radioactivity, electron-positron annihilation, light matter interactions and detection of 511 keV photons. Furthermore, a detailed explanation of the time resolution of a PET detector, the medical application of PET and an introduction to tomographic image reconstruction are presented.
- **Chapter 3** is dedicated to the EndoTOFPET-US project. The initial project goals, the detector design and the image reconstruction software are presented.
- **Chapter 4** introduces X-ray fluorescence imaging.
- **Chapter 5** outlines the simulation tools that were used throughout the thesis.
- **Chapter 6** describes the commissioning of an EndoTOFPET-US prototype. This includes a maintenance phase during which broken electronics were replaced or fixed, slow control was implemented, automatic calibration procedures for the detector were developed and cooling issues in the external plate were fixed. Afterwards, the developed online coincidence time resolution optimization is explained and the results achieved with it are presented. Additionally, the first endoscopic PET detector with a voxel size close to the intended design was put into operation.
- **Chapter 7** presents the first data acquisition with a fully functional and optimized EndoTOFPET-US prototype and the results in terms of point resolution achieved with it.
- **Chapter 8** describes the extensive simulation studies performed in this thesis. The studies include a replication of the data acquisition described in chapter 6, an application specific imaging scenario utilizing the NEMA IEC Body Phantom Set^{TM}, qualitative and quantitative image analysis as a function of signal to background ratio and coincidence time resolution, a co-registration of the EndoTOFPET-US image to conventional PET scanner images and a sensitivity study of the EndoTOFPET-US prototype.
- **Chapter 9** describes possible imaging and reconstruction methods for X-ray fluorescence imaging. Furthermore, a feasibility study of two of the proposed imaging methods is performed by means of a simulation.
- **Chapter 10** comprises the conclusion.

Chapter 2

Positron Emission Tomography

In the following chapter, the physics principles as well as detection and reconstruction principles of positron emission tomography (PET) are covered. PET is a metabolic imaging method that yields only limited information about the anatomy of the patient. It is utilized in clinical diagnostics of diseases and in radiotherapy for treatment verification. PET is based on the localization of a functionalized, biologically active molecule that is called radiotracer. The radiotracer undergoes radioactive β^+ decay and the subsequent positron electron annihilation yields two back-to-back gamma photons. These photons are measured in detecting elements usually organized in a cylindrical shape surrounding the patient.

2.1 Radioactivity

Radioactivity is the process of an unstable nucleus spontaneously decaying to an energetically more stable configuration while emitting either alpha (α), beta (β) or gamma (γ) radiation. The type and energy of radiation depends on the type of nucleus. The stability of a nucleus, in turn, depends on the number of its neutrons and protons. Figure 2.1 shows the stable configurations of nuclei and the type of decay unstable configurations undergo. Stable nuclei form the so called stability line (black indicated nuclei in figure 2.1). Smaller nuclei including up to 20 protons are stable if the number of neutrons equals the number of protons. Beyond that a larger number of neutrons is necessary to establish a stable nucleus and thus prevent a nucleus from undergoing radioactive decay. If a nucleus has an excess of neutrons or protons compared to the stability line, it will undergo radioactive decay. In addition, any nucleus exceeding either 126 neutrons or 82 protons is unstable. Lighter nuclei with excess of either neutrons or protons decay mainly via β^+ or β (sometimes called β^-) decay, while heavier nuclei with an excess of protons tend to undergo α decay. For lighter nuclei having a big mismatch between neutron and proton number, neutron and proton emission can occur. If nuclei end their decay in an excited state, an additional γ can be produced.
The radioactive decay of a nucleus is a random process that is why it is not possible to predict when the decay takes place. But statistical statements about a large sample of radioactive nuclei can be made. A decay constant can be defined for each radioactive nucleus. It defines the number of decays after a certain time interval in a large sample of nuclei. The differential equation 2.1 links the number of decays dN/dt in a time interval to the number of radioactive nuclei N and the decay constant λ.

$$-dN = N\lambda dt \tag{2.1}$$

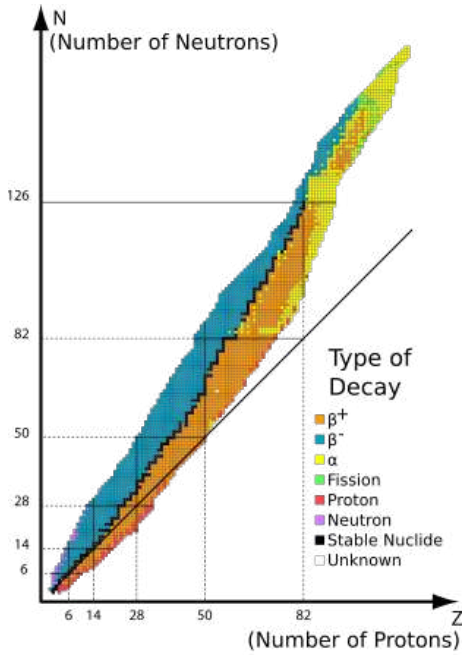

Figure 2.1: Table of nuclides. Black colored nuclides are stable, whereas orange and blue colored nuclides undergo β^+ and β^- decay, respectively. Yellow nuclides undergo α decay. Proton numbers equal neutron numbers on the solid black line.

It is noteworthy that this formula assumes that the decay probability of a nucleus is not influenced by its prior history. This implies that the number of decays in a time interval does not depend on the number of decays in a previous time interval. In statistics, this is the key definition for a Poisson process. Hence, the radioactive decay follows Poisson statistics. The solution of the differential equation 2.1 is shown in equation 2.2.

$$N(t) = N_0 e^{-\lambda t} \tag{2.2}$$

It is an exponential decay law where N_0 is the number of nuclei at time $t = 0$. The so called half-life of a radioactive isotope is defined as the time needed to halve the number of radioactive nuclei in a sample and is calculated by

$$T_{1/2} = \frac{ln(2)}{\lambda} \tag{2.3}$$

The activity of a radioactive probe is the number of decays per time. It is defined as

$$A = -\frac{dN}{dt} = \lambda N_0 E^{-\lambda t} \tag{2.4}$$

and is given in Becquerel, where 1 Bq = 1 s^{-1}.

2.1.1 β Decay

The β decay was first observed by Ernest Rutherford (1899) and later explained by Henri Becquerel (1900). He suggested that the particle ejected from the nuclei is the electron. It was speculated from observations that the β decay was a two body process including the electron and recoiling nucleus. James Chadwick (1914), however, observed that the energy spectrum of the emitted electron is continuous.

Consequently, energy conservation does not hold if no other particle is involved in the decay. Wolfgang Pauli (1930) solved this problem by postulating a new particle called the neutrino. He suggested that the neutrino is a very light uncharged particle carrying part of the energy and, in turn, leading to the continuous spectrum of the electron energy [11]. Enrico Fermi (1934) postulated that a neutron decays directly into an electron and electron antineutrino during the β decay [12]. After the theory of the weak interaction was developed, a virtual W^- boson was added to the decay process. The Feynman diagram of the complete decay process, as known today, is shown in figure 2.2. The β decay leads to a daughter

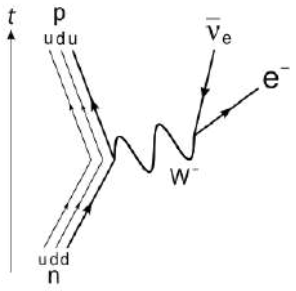

Figure 2.2: Feynman diagram of the β decay. A down quark (d) insight a neutron (n) emits a virtual W^- boson while converting to an up quark (u). The W^- boson decays leptonically into an electron (e^-) and an electron antineutrino ($\bar{\nu}_e$).

nucleus with one more proton than and the same mass number as the parent nucleus.

The discovery of the positron in 1932 by Carl David Anderson [13] paved the way for the discovery of the β^+ decay in 1934 by Frédéric and Irène Joliot-Curie.

2.1.2 β^+ Decay

During β^+ decay, the weak interaction converts a proton to a neutron by either absorption of a virtual W^- boson or emission of a virtual W^+ boson further decaying to a positron and an electron neutrino. The Feynman diagram of the β^+ decay is shown in figure 2.3 β^+ decay mainly occurs in proton rich

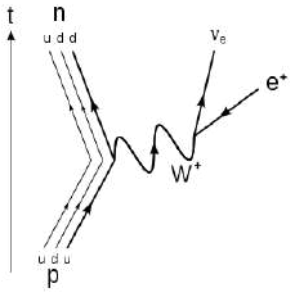

Figure 2.3: Feynman diagram of the β^+ decay. An up quark (u) insight a proton (p) emits a W^+ boson while converting to a down quark (d). The W^+ boson subsequently decays into a positron (e^+) and an electron neutrino (ν_e).

nuclei. The generic β^+ decay equation is

$$ {}^{A}_{Z}X \rightarrow {}^{A}_{Z-1}X' + e^+ + \nu_e \tag{2.5} $$

$$p \rightarrow n + e^{+} + \nu_e \tag{2.6}$$

In contrast to β decay, β^+ decay cannot occur on an isolated proton due to the neutron having a higher mass than the proton ($m_n = 939.6\ MeV$, $m_p = 938.3\ MeV$). Consequently, the β^+ decay can only occur within a nucleus if the binding energy of the daughter nucleus exceeds the binding energy of the mother nucleus. The amount of energy being released during the β^+ decay is often denoted as Q and is given by

$$Q = m_N({}^{A}_{Z}X) - m_N({}^{A}_{Z-1}X') - m_e - m_{\nu_e} \tag{2.7}$$

where $m_N({}^{A}_{Z}X)$ and $m_N({}^{A}_{Z-1}X)$ are the masses of the mother and daughter nuclei, respectively, m_e and m_{ν_e} are the masses of the positron and the neutrino, respectively. The masses m_N of the nuclei are defined as

$$m_N({}^{A}_{Z}X) = -m_N({}^{A}_{Z}X) + Z_{m_e} - \sum_{i=1}^{Z} B_i \tag{2.8}$$

where B_i is the binding energy. By combining equation 2.7 and 2.8, the energy Q is

$$Q = m({}^{A}_{Z}X) - m({}^{A}_{Z-1}X') - 2m_e \tag{2.9}$$

The equation shows that the β^+ decay can only take place if the difference in mass between daughter and primary nucleus is bigger than twice the mass of the electron 1.022 MeV.

2.1.3 Electron Capture

Electron capture, a competing process to β^+ decay, was first observed by Alvarez [14]. Whenever β^+ decay can occur, electron capture can also occur. During electron capture a proton captures one of the atom's electrons, usually an inner electron from the K shell, converts to a neutron and emits a neutrino. The energy of the neutrino is specific for each nucleus and depends on the electron binding energy.

$${}^{A}_{Z}X + e^{-} \rightarrow {}^{A}_{Z-1}X' + \nu_e \tag{2.10}$$

The resulting vacancy is either filled by an outer electron resulting in photon emission with an energy specific to the nucleus or by an inner electron while dissipating the excess (binding) energy by ejecting a valence electron, which is called Auger effect [15]. Whether electron capture or β^+ decay is the dominant decay mode depends on the mass difference between mother and daughter nuclei. The greater the mass difference between mother and daughter nucleus over the required 1.022 MeV, the more likely positron decay will occur. Fluorine-18 (^{18}F, an often used isotope in PET), for example, has a mass difference of 1.66 MeV resulting in 96.86% of decays being via β^+ decay and 3.14% of decays being via electron capture.

2.2 Electron-Positron Annihilation

After emission the positron moves through the surrounding tissue and looses its kinetic energy via inelastic scattering with the surrounding electrons. In most cases, the annihilation with an electron takes place after reaching thermal energy. This is due to the fact that cross section for inelastic scattering is significantly higher than the one for annihilation if the positron has a kinetic energy higher than thermal

energy. Thermal energy can be derived from the Boltzmann distribution and is $3/2k_BT \approx 0.04$ eV, with k_B the Boltzmann constant at $T = 300$ K. The annihilation can take two different forms: (1) the slow (compared to the bound electron with binding energies in the range of tens of electronvolt) positron annihilates directly with a bound electron or (2) the positron and electron form a metastable hydrogen-like state called positronium before annihilating. In the first case, the outcome is two photons which are exactly back to back and have an energy of 511 keV each in the center-of-mass frame. In the second case, the positron and electron can form either para-positronium (pPs) having anti-parallel spin or ortho-positronium (oPs) having parallel spin [16].
Simple statistical assumptions about oPs being a singlet and pPs being a triplet state lead to a formation ratio of 1:3 [17]. pPs has a lifetime of about 0.125 ns and decays to an even number of photons with two being the most probable. The branching ratio of pPs for the decay to four photons is $1.439 * 10^{-6}$. oPs has a significantly longer lifetime of approximately 142 ns and decays mainly to three photons. Other modes of decay such as five photon decay are negligible. The branching ratio of oPs for the decay to five photons, for example, is approximately 10^{-6}. The energies of the three/five photons are distributed between 0 and 511 keV.

The amount of 4 MeV positrons forming positronium is 38% in water and 70% in organic material. It can be assumed that it is higher for lower positron energies. All decays but the two photon decays decrease sensitivity of PET imaging and increase the low energy background.

oPs can also decay to two photons by a process called pick-off. In this process the positron in the oPs annihilates with an electron of opposite spin from the surrounding tissue (lifetime 0.6-20 ns) [17]. oPs lifetime is highly reduced if it is placed in water (1800 ps). Thus, it can be concluded that oPs decays mainly via the pick-off process if surrounded by in water. Therefore, the ratio of three photon to two photon decays is not 3:1.

The ratio of two photon decays to decays with a higher number of photons in the final state is a limiting factor for the sensitivity of PET detectors. In the following chapters, two inherently limiting factors for the spatial resolution of PET scanners are discussed.

2.2.1 Positron Range

The positron usually looses its kinetic energy before annihilating with an electron. The distance the positron travels within the patient is a significant and limiting factor for PET image resolution and, thus, needs to be well understood. [18] shows the influence of positron range for three different radionuclides on spatial resolution and activity concentration quantification. The positron emission energies of three frequently used radionuclides (^{18}F, gallium-68 (^{68}Ga) and nitrogen-13 (^{13}N)) are shown in figure 2.4 In the study of [18], cylindrical phantoms with an inner diameter of 0.69 mm are used in a microPET Focus 120 (Siemens Preclinical Solutions, Knoxville, TN, USA, previously Concorde Microsystems). The reconstructed activity of three frequently used radionuclides in two different materials (lung inhale and cortical bone) is presented in figure 2.5. The spatial resolution of these images is determined as the full width half maximum (FWHM) of the reconstructed activity, which is also shown in figure 2.5. It can be seen that the FWHM is largest for the ^{68}Ga, which has the highest mean positron emission energy and, thus, the highest positron range. The positron range depends on the positron energy and the rate at which it looses energy. This rate, in turn, depends on the type of tissue it is moving through, most noticeably on the electron density of the tissue. Since the tissue is fixed within a given PET examination, it is preferable to find a radioactive nuclide that ejects the positron with the smallest possible energy. In addition, [18] shows that quantification of the activity becomes difficult when dealing with changing

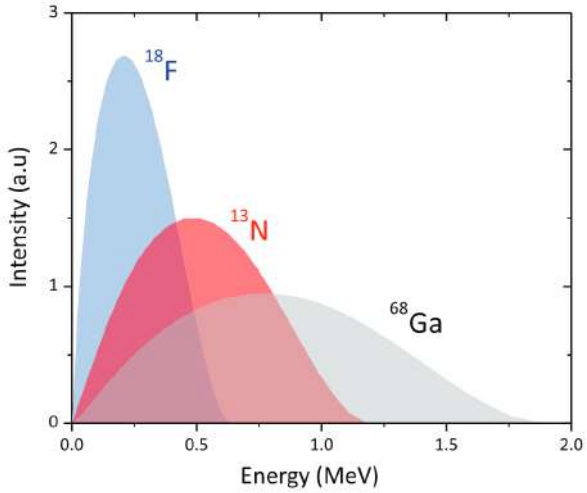

Figure 2.4: Positron emission energy spectra for the decay of fluorine-18 (^{18}F), gallium-68 (^{68}Ga) and nitrogen-13 (^{13}N). Taken from [18].

tissue densities within one image. This is due to the density dependent change in positron range: when the positron range changes, density of positron electron annihilation changes around the emitter. Figure 2.6 shows the reconstructed image of a cylindrical capillary source filled with ^{68}Ga and enclosed by three different materials (water, air, cortical bone). All data are acquired in a single measurement in which the source has been embedded in the three materials at different positions. The qualitative difference between the three materials is clearly visible. The quantitative difference becomes evident when comparing the reconstructed intensity within the three materials as a function of radial distance, which is also shown in figure 2.6. The maximum intensity is 1.24 in cortical bone and 0.55 in air providing that the intensity is normalized to the maximum value of water.

2.2.2 Non-Collinearity of the Back-to-Back Photons

Another effect that reduces image quality in PET scanners is the non-collinearity of the two photons arising from the electron positron annihilation [19]. While the photons in the rest frame of the electron positron annihilation are exactly back to back (have an angle of 180° between them), they are not in the detector frame. This is because the electron and positron have a non-zero kinetic energy when annihilating. The kinetic energy arises from the electron being in a bound state orbiting the nucleus or from the formation of positronium. The study undertaken by [20] shows that the angular deviation from 180°, defined as $180° - \Theta$, has two components: a broad component which is due to the kinetic energy of the bound electrons and a narrow component which is due to the annihilation after forming positronium. The FWHM of these angular distributions are $0.619 \pm 0.012°$ and $0.301 \pm 0.017°$, respectively. This angular deviation from 180° leads to a wrong determination of the line of response (LOR) as shown in figure 2.7. LOR is the line between the two detection points of the photons. In conventional PET, the influence of non-collinearity on image quality depends on the ring diameter. The distance d between the LOR and the true annihilation point is $d = (0.00243 \pm 0.00014) \cdot D$, where D is the ring diameter.

In case of the EndoTOFPET-US detector, the equation has to be modified since the detector is not cylindric. Three assumptions are made for the calculation: (1) an angular deviation of $0.619/2°$ from 180° is assumed for each of the two photons, (2) the maximum distance of the external plate from the

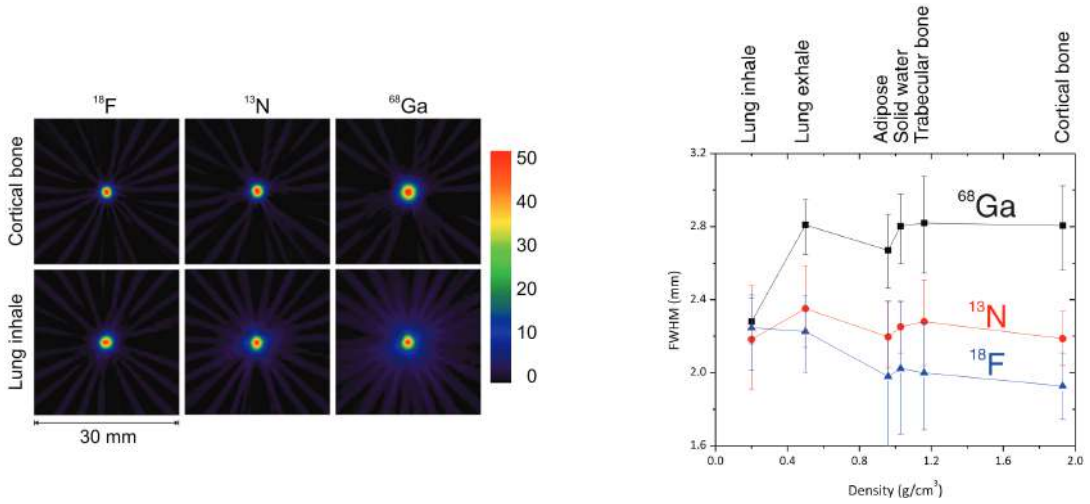

Figure 2.5: (left) Reconstructed activity of fluorine-18 (^{18}F), gallium-68 (^{68}Ga) and nitrogen-13 (^{13}N) in lung tissue and cortical bone. (right) Full width half maximum (FWHM) of the reconstructed activity for the three radionuclides in six different materials. The real diameter of the radioactive source is 0.69 mm. Taken from [18].

radioactive source is 30 cm and (3) the maximum distance of the endoscopic head is to the radioactive source is 7 cm. The resulting deviation from the original LOR in the two detectors is $d_{ext}^{max} = 0.16$ cm and $d_{endo} = 0.038$ cm, which is in both cases considerably smaller than the pixel size of the two detectors. The pixel sizes of the external plate and endoscopic head are 3.5 x 3.5 mm^2 and 0.7 x 0.7 mm^2, respectively. Hence, the hits can maximally be displaced by one pixel in the two detectors due to the non-collinearity. The equation for the distance d between original LOR and displaced LOR for the EndoTOFPET-US detector is

$$d = 0.07 + sin\left(arctan\left(\frac{0.28}{D_{det}}\right)\right) * \frac{D_s}{cos\left(arctan\left(\frac{0.28}{D_{det}}\right)\right)} \tag{2.11}$$

with D_{det} the distance between the two detectors and D_s the distance between the radioactive source and the endoscopic head. The maximum LOR shift is $d = 0.17$ cm in case that the distance between the detectors is 20 cm and the source distance to the endoscopic head is 7 cm. The minimum LOR shift is $d = 0.08$ cm in case that the distance between the detectors is 30 cm and the source distance to the endoscopic head is 1 cm.

2.3 Light Matter Interactions

This chapter is based on [21–24]. The 511 keV photons can undergo several interactions while traveling through the body and the detector. Photon interactions inside the patient's body always lead to a deterioration of the resulting image. However, interactions with the biggest possible energy deposition inside the detector are mandatory for detection. In contrast to electromagnetically charged particles, photons only interact in singular events with the surrounding matter and not in between two single events. The main interactions of photons with matter are Compton scattering, photoelectric effect, Rayleigh scattering and pair production. Compton scattering and photoelectric effect will be discussed in the next two chapters. Pair production will not be further discussed. It is of no relevance for PET as its minimum required energy, which is twice the electrons' rest mass (1.022 MeV), is far above the

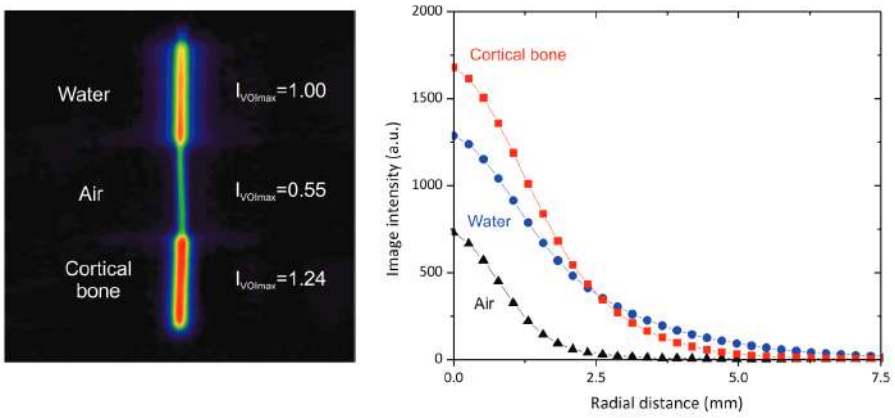

Figure 2.6: (left) Reconstructed image of a cylindrical capillary source (diameter of 0.69 mm) filled with gallium-68 (^{68}Ga) and enclosed by water, air and cortical bone. (right) The image intensity in arbitrary units within the three different material regions as a function of radial distance. Taken from [18].

511 keV of the two created photons in PET.
Compton scattering and photoelectric effect inside the patient lead to a decrease in photon count or photon energy. The intensity of a photon beam traversing matter can be described using the Beer-Lambert law

$$I = I_0 e^{-\mu x} \tag{2.12}$$

where μ is the matter specific mass attenuation coefficient, x the traversed path length and I_0 the intensity at $x = 0$. The mass attenuation coefficients as a function of photon energy for water and lead are shown in figure 2.8. The total and process specific attenuation coefficients are indicated. It can be seen that the mass attenuation coefficients highly depend on the material, i.e. energies and abundance of bound electrons in the material. It can also be seen that the process photons most likely undergo is reliant on photon energy. The photoelectric effect, for example, can not occur on free electrons due to energy conservation laws. The electrons seem like free electrons on condition that the photon energy is very high compared to the electron bound state energy. Consequently, photoelectric effect mainly occurs at lower photon energies. Photoelectric effect is the desired interaction for photon detection in PET application. In order to increase the photoelectric effect probability at a specific photon energy, however, a heavier detector material with higher bound state energies can be chosen.

2.3.1 Compton Scattering

Compton scattering is the process of a photon undergoing inelastic scattering with an atomically bound electron. The electron is potentially ejected from the atom and the photon is scattered by the angle Θ during this interaction. A schematic of the process is shown in figure 2.9.
The photon energy after the scattering process can be calculated as

$$E_{\gamma'} = \frac{E_\gamma}{1 + \frac{E_\gamma}{m_e c^2} * (1 - cos(\Theta))} \tag{2.13}$$

where E_γ is the photon energy before the scattering process, m_e the electron rest mass and c the speed of light. It can be seen that the biggest energy carry over occurs at a scattering angle of 180°. In the case of

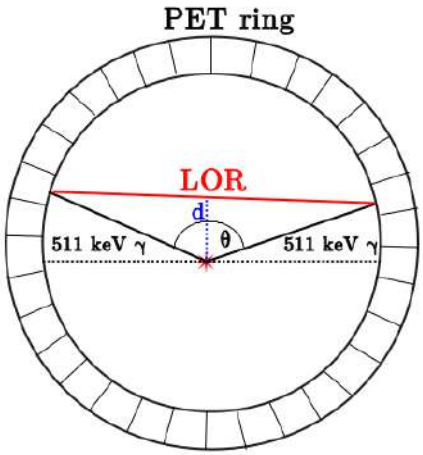

Figure 2.7: Schematic of the non-collinearity of the two annihilation photons. Θ is the angle between the two photons.

a 511 keV photon, the biggest energy carry-over is exactly one third of the photon energy ($\sim$ 170.33 keV). The directionality of the process can be calculated using the Klein-Nishina formula [26]. It calculates the differential cross sections of photons scattered of a single free electron which is given by

$$\frac{d\sigma}{d\Omega} = \alpha^2 r_c^2 P(E_\gamma, \Theta)^2 \left[P(E_\gamma, \Theta) + P(E_\gamma, \Theta)^{-1} - sin^2(\phi)\right]/2 \tag{2.14}$$

with α being the fine structure constant, Θ the scattering angle, r_c the reduced Compton wavelength of the electron and $P(E, \gamma) = \frac{1}{1+(E_\gamma/m_e c^2)(1-cos(\Theta)}$. The the differential Compton cross section for a 511 keV photon is shown in figure 2.10. It can be seen that at a photon energy of 511 keV Compton scattering is highly forward boosted. Nevertheless, Compton scattering inside the patient's body or the detector has a negative effect on image quality of PET scanners. A change in direction of the photon can lead, as explained in chapter 2.2.2, to misinterpretation of the LOR and, thus, to blurring of the reconstructed image.

2.3.2 Photoelectric Effect

Photoelectric effect is the process of a photon being absorbed by an atomically bound electron. The photon transfers its full energy to the electron during this interaction. The electron is ejected from the atom if the photon energy exceeds its binding energy. The occurring gap is either filled by an electron from a higher shell emitting a photon with a specific energy (fluorescence) or by an inner electron while dissipating the excess (binding) energy through ejection of a valence electron (Auger effect). Photoelectric effect cannot occur on a free electron, but only in the vicinity of an atom absorbing the recoil of the electron due to energy conservation. If the photon energy exceeds the electron binding energy by a huge margin, the electron can be considered a free electron. Consequently, the probability for photoelectric effect is bigger for inner (stronger bound) electrons than for outer (weaker bound) electrons. The photoelectric effect cross section is proportional to the atomic number to the fourth or fifth power (Z^4 orZ^5). The non-relativistic approximation for the K shell, which is the innermost electron shell in an atom, is given

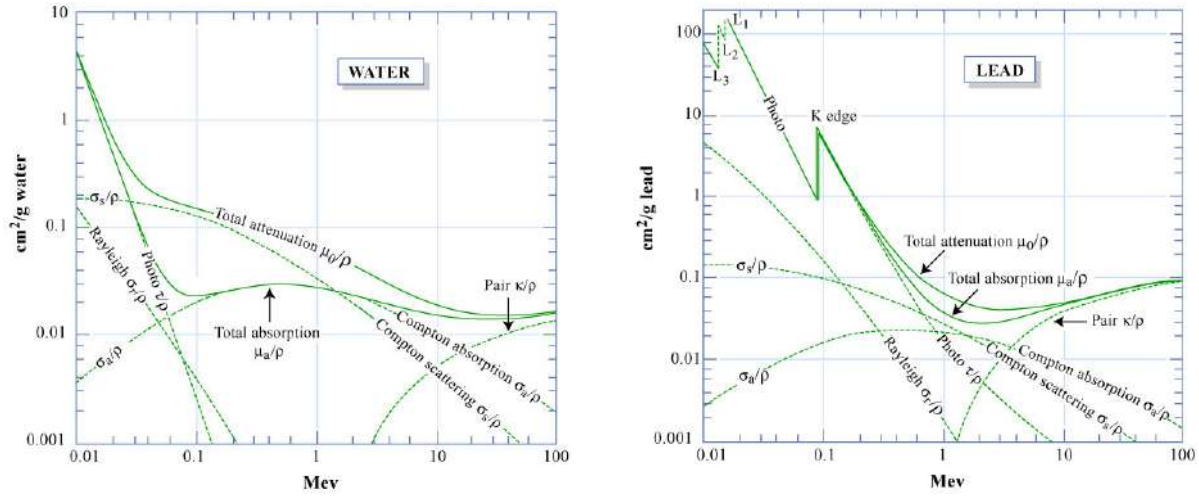

Figure 2.8: The mass attenuation coefficient (left) for water and (right) for lead. Taken from MIT OpenCourseWear (Applied Nuclear Physics); adapted from [25].

by [22]

$$\sigma_{p.e.}^{K} = \left(\frac{32}{\epsilon^7}\right)^{1/2} \alpha^4 Z^5 \sigma_{Th}^{e} \tag{2.15}$$

with ϵ being the reduced photon energy $\epsilon = E_\gamma / m_e c^2$, α the fine structure constant, Z the atomic number and σ_{Th}^{e} the Thomson cross section. Furthermore, the photoelectric effect cross section is sharply increased provided that the photon energy coincides with a shell's binding energy. This can be seen in figure 2.8 for lead and its K shell energy at ∼88 keV.

A high photoeffect cross section is preferable for PET in order to ensure that the whole photon energy is absorbed inside a small detector volume. Hence, a high Z material should be utilized as detector material.

2.4 Detection of 511 keV Photons

In the case of PET, two 511 keV photons need to be detected in coincidence while conserving information about the photon energy. The whole photon energy needs to be deposited and the detection time needs to be measured accurately in the detector. As a result, a high stopping power (high Z) and a fast signal response are required. In contrast to the necessary high stopping power and fast signal response, the requirements on the energy resolution are lower since only the Compton background needs to be suppressed. An energy resolution of 10% to 15% usually is sufficient. These constraints leave only few options for detector material. The most used detector type for PET are inorganic scintillators in combination with a photodetector, either photomultiplier tubes (PMT) or silicon photomultiplier (SiPM). The scintillator converts the high energy photon to visible light which is converted to an electrical measurable signal by the photodetector.
For the EndoTOFPET-US project, inorganic scintillators and SiPMs are employed. The working principles of these two detector types are described in the following sections.

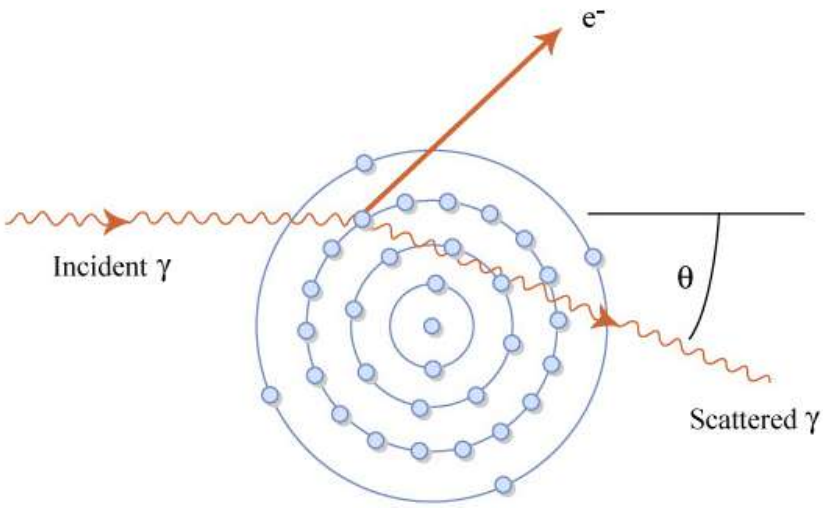

Figure 2.9: Schematic of Compton scattering. Taken from MIT OpenCourseWear (Compton Scattering).

2.4.1 Scintillators

Scintillation is the emission of photons through the deexcitation of atoms or molecules that previously have been excited by radiation. Scintillators are generally divided into organic and inorganic scintillators. Scintillation process in organic scintillators stems from molecular transitions in the material, while scintillation process in inorganic scintillators stems from electronic transitions between the valence and conduction band. Organic scintillators are made up of carbon based molecules and, thus, are often called plastic scintillators. They are cheap and easily molded into any shape needed, but are not suitable for efficient high energy photon detection, such as the 511 keV photons used in PET, due to their low density and low Z. Inorganic scintillators are crystals that are usually made of high Z materials and, thus, have a high stopping probability for high energy photons. These kind of scintillators are mainly grown in high temperature furnaces which limits their form and size. In medicine, scintillators like lutetium-yttrium oxyorthosilicate (LYSO) and bismuth germanate (BGO) are typically used since they have a high stopping power and are not hygroscopic. Hygroscopic means that material attracts water and, thus, needs to be housed in an airtight housing in order to protect them from moisture.

2.4.1.1 Scintillation Process in Inorganic Scintillators

This chapter is partly based on [28]. The scintillation process in inorganic scintillators is possible due to the band structure of the crystals and the energy states in the band gap that are introduced by impurities. The whole process is schematically shown in figure 2.11 and involves three subsequent processes leading to the emission of scintillation light, namely conversion and multiplication, charge carrier migration and luminescence. Conversion and multiplication includes the absorption of the photon which excites an electron from the inner shell of an atom to the conduction band. Simultaneously, a hole in the valence band is created. The electron can move freely in the conduction band and ionize more atoms by scattering on them. Further electrons can be elevated to the conduction band via the Auger effect or the emission and subsequent absorption of secondary x-rays. After the free electrons have reached an energy lower than the ionization energy of the material, electrons thermalize at the bottom of the conduction band

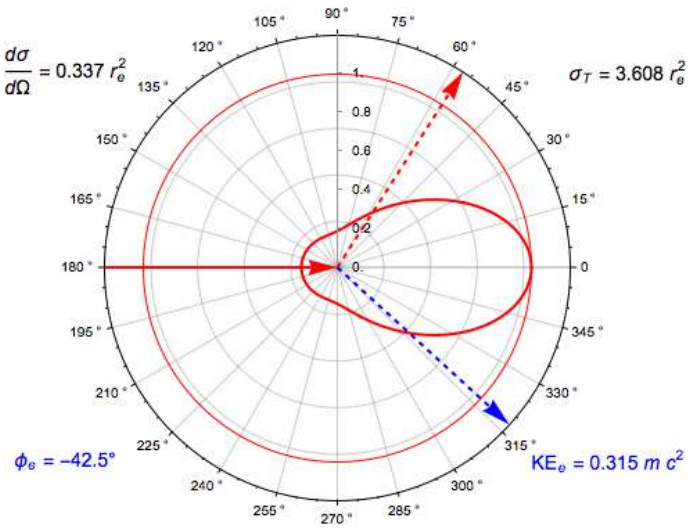

Figure 2.10: Polar plot of the differential Compton scattering cross section as a function of scattering angle for a 511 keV photon. The incident photon comes from the left as indicated by the red arrow. The maximum differential cross section in units of r_e^2 is $\frac{d\sigma}{d\Omega} = 1$. The thin red circle outlines the whole parameter space. The thick red line indicates the differential cross section for a 511 keV photon as a function of scattering angle ϕ. The cross section is clearly increased in forward direction. The dotted red and blue arrow indicate the photon and electron path, respectively, in case of a photon scattering angle $\phi = 57°$. The electron angle ϕ_e, electron energy KE_ϕ, differential cross section and total cross section are given for this specific case. Modified from [27].

and holes thermalize at the top of the valence band. During migration, the electrons and holes migrate towards the luminescence centers inside the crystal and excite them. These luminescence centers are formed by impurities, which are introduced during the growing process of the crystals, and lead to energy states that are within the bandgap of the crystal. The excited luminescence center can decay either by emitting a photon or via a non-radiative process (e.g. phonon interactions). The impurity states are usually chosen to have an allowed decay in order to speed up the process. They are also chosen for the photon created to be in the optical range since well suited and highly efficient photodetectors exist in the optical range. The scintillation rise and decay times depend on the excitation process, the charge carrier migration speed and the lifetime of the luminescence centers. The rise time is usually very quick, i.e. in the range of picoseconds. An upper limit on the rise time in LSO:Ce:Ca, for example, is stated as 10 ps by [29]. The decay times of scintillators used in PET are in the range of several up to tens of nanoseconds. Scintillators often have a slow and quick decay component [29]. A schematic of the scintillation signal shape is shown in figure 2.12.

Phosphorescence is a competing process to the scintillation process. During phosphorescence an electron is trapped within traps which are introduced by unwanted impurities in the crystal. These traps often do not have allowed decays to the valence band. Therefore, the electron needs to escape the trap by excitation (e.g. via thermal excitation) and decays through the before mentioned process. This type of delayed light emission is also called afterglow and can have a decay time of up to hours.

2.4.1.2 Light Yield of Inorganic Scintillators

Besides timing of the light emission and the stopping power, the light yield (LY) of the scintillator is a very important property. The energy resolution is proportional to $(\mathrm{LY})^{-0.5}$ while the time resolution is

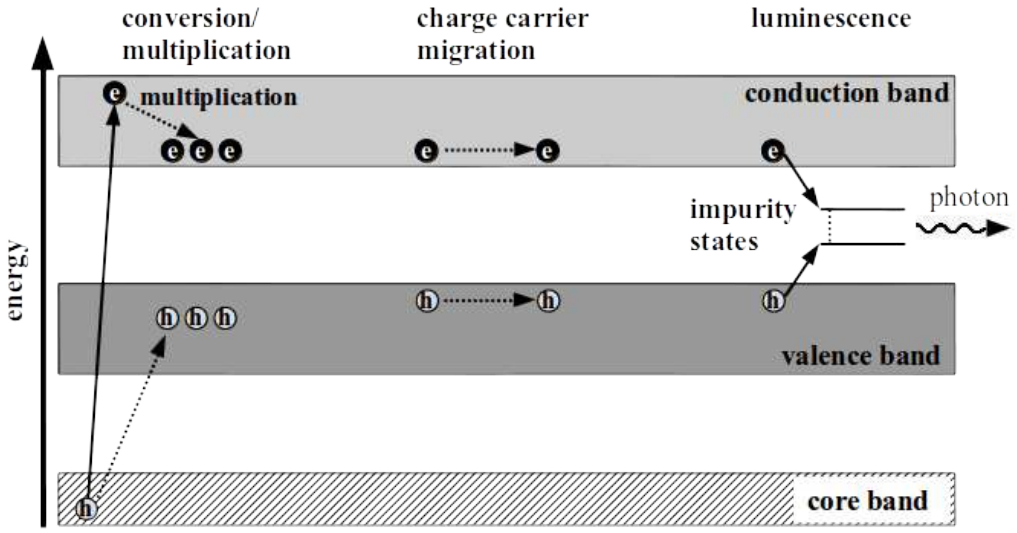

Figure 2.11: Schematic of the scintillation process. First, photon absorption creates a high energetic free electron (e) in the conduction band. The electron ionizes more atoms in the material leading to a high number of free electrons in the conduction band and holes (h) in the valence band, respectively. After thermalization, the electrons migrate towards luminescence centers that are introduced by impurities in the crystal. An excited luminescence center can decay optically creating a visible photon.

proportional to $(\tau_d/\mathrm{LY})^{0.5}$ with τ_d being the scintillation decay time. The LY depends on several effects whereby the number of electron hole pairs created by the incident particle is the most dominant effect setting the upper limit on it. The number of electron hole pairs mainly depends on the ionization energy. The number of photons created is

$$n_{eh} = \frac{E_\gamma}{\beta \cdot E_{gap}} \cdot \eta_{CAP} \cdot \eta_{PH} \tag{2.16}$$

with E_γ being the energy of the incident particle, $\beta \cdot E_{gap}$ the mean energy necessary to create an electron hole pair in a scintillator with a band gap of E_{gap} [30]. Consequently, $\frac{E_\gamma}{\beta \cdot E_{gap}}$ denotes the number of created electron hole pairs. η_{CAP} is the efficiency of capturing a free charge carrier in a luminescent center and η_{PH} is the quantum efficiency of the luminescent center itself. β depends on the material, is usually close to 2.3 for ionic crystals and accounts for energy loss due to phonon coupling to the lattice [31]. The LY for several scintillators as a function of their E_{gap} is shown in figure 2.13. It can be seen that a smaller band gap leads to a higher LY and, thus, is preferred.

2.4.1.3 Energy Resolution of Inorganic Scintillators

The energy resolution achievable with scintillators always depends on the detector as a whole. This includes the wrapping of the scintillator, the light transfer efficiency to the photodetector, quantum efficiency of the photodetector and the intrinsic resolution of the crystal. Three parameters of the scintillator directly influence the energy resolution of the detector.

The first property influencing the energy resolution is the LY. Since a photodectector is always involved in converting the photons to an electrical signal, the energy resolution always depends on the statistics of photons being converted to photoelectrons in the photodetector. This leads to the energy resolution being inversely proportional to the square root of the number of photons $[(\mathrm{n}_{ph})^{-0.5}]$ extracted from the

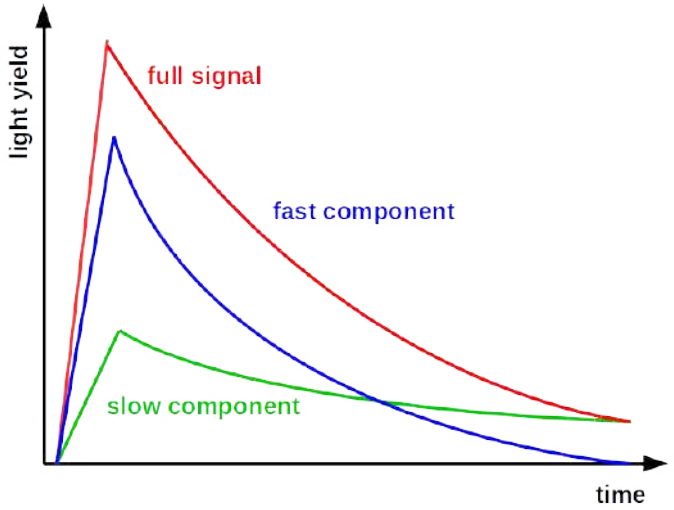

Figure 2.12: Schematic of the scintillation signal. It consists of a slow (green) and a fast (blue) component. The signal usually has a fast rise time and a slower exponential decay.

scintillator which, in turn, is directly proportional to the number photons created in the scintillator.

The second property is the intrinsic non-linearity of scintillators at low energies. The amount of energy deposited from a charged particle (i.e the electron generated by the photoelectric effect in the case discussed here) alters as the energy of a particle changes. If a particle has low kinetic energy, it deposits a lot of energy per area resulting in high density of free charge carriers, excitons and excited ions. The high density, in turn, leads to increased interaction probabilities between them and thus can lead to non-radiative relaxations [32]. The so called Landau fluctuations lead to further degradation of the energy resolution [33]. Landau fluctuations are statistical variations in the deposited energy per covered distance (dE/dx) that occur while the primary electron slows down. Moreover, the creation and absorption of secondary x-rays and electrons (δ-rays) are often seen as a cause for the non-linear response of scintillators. It has been shown that these have a similar contribution on energy resolution as the Landau fluctuations [34]. The non-linearity of the scintillator response to an absorbed energetic particle is a fundamental limitation of the energy resolution of scintillators, which might be reducible by codoping the crystals [35].

The third property influencing the energy resolution is afterglow and other complex processes delaying the light emission. This has been displayed by showing the influence of the shaping time on the energy resolution of scintillators. The energy resolution decreases provided that the afterglow increases. This clearly demonstrates that not all photons are integrated by the electronics when utilizing a small shaping time [36].

2.4.1.4 Time resolution of inorganic scintillators

The time resolution achievable with a scintillation detector highly depends on the scintillators properties: LY, scintillator size, scintillation rise and decay time. The rise time determines the time delay and the time jitter of photon creation after the absorption of the incident particle, while the decay time and the LY determine the initial photon density [31]. Photon travel time also has an influence on the time resolution of the scintillator. Photons do not necessarily travel straight to the photodetector, but in most

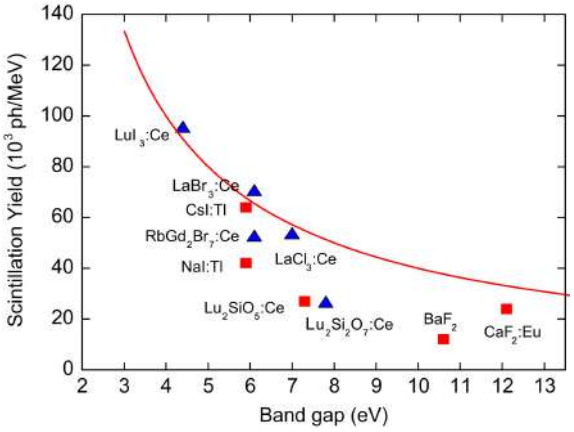

Figure 2.13: Scintillation light yield (LY) of several scintillators as a function of the band gap E_{gap}. Taken from [31].

cases undergo internal reflection on their way to detection. Crystal size has an influence on the mean number of reflections that take place before a photon reaches the photodetector. Hence, crystal size adds to the time jitter of the photons reaching the photodetector.
The overall time resolution of a PET detector will be described in more detail in section 2.5 due to the high number of detector parts having an influence on the time resolution of the system (e.g. scintillator, wrapping, light guidance, photodetector and electronics).

2.4.2 Silicon Photodetectors

Silicon photomultipliers (SiPMs) are silicon based photodetectors specialized on the detection of visible (in most cases blue) light. They start to be utilized more and more in PET detectors and open up new possibilities for either endoscopic PET detectors, because of their small size, or new PET/MRI detectors, because they are not influenced by high magnetic fields. The functionality and main parameters of SiPMs are presented in the following sections.

2.4.2.1 PIN Diode

The simplest approach to a silicon-based photodetector is the PIN diode. It is a silicon structure consisting of a low p-/n-doped bulk material that is sandwiched by two highly n-/p-doped silicon layers which form the ohmic contacts of the device. Around the contact surface of the low doped and the highly doped zones, a so called depletion area develops that is free of free charge carriers. The width of the depletion zone is increased by applying a reverse bias voltage to the diode. If the width of the depletion zone spans over the whole detector depth, full depletion is reached. The PIN diode has an intrinsic low doped layer that increases the depletion depth and, thus, leads to higher probability of photon detection. If, for example, a photon with an energy exceeding the band gap of silicon ($\sim$1.12 eV) impinges the diode and is absorbed, it can create an electron hole pair. The electrons start drifting towards the n-doped side of the diode while the holes drift towards the p-doped side due to the electric field in the device. The movement of charge carriers produce a current signal at the electrodes. In the case of a PIN diode, the signal produced is proportional to the number of photons being absorbed. The signal of a single photon being absorbed, however, is not possible to resolve.

2.4.2.2 Avalanche Photo Diode

An avalanche photo diode (APD) is a PIN diode operated at sufficiently high voltages so that primary electrons and holes gain enough energy to ionize the material by impact ionization. Thus, the primary photo-electron can produce an amplified current signal. The amplification of the signal is also called gain (G). The gain of an APD is subject to statistical fluctuations due to the statistical nature of the charge carrier multiplication. The so called excess noise factor (ENF) is a measure for those fluctuations and is defined as

$$\text{ENF} = k \cdot G + (1 - k) \cdot (2 - \frac{1}{G}) \tag{2.17}$$

with the gain G and $k = \alpha(x)_h/\alpha x_e$ the ratio between hole ($\alpha(x)_h$) and electron ($\alpha(x)_e$) ionization probabilities. In proportional mode (voltage below breakdown), the gain of an APD is usually between ten to a few hundred and the ionization probability of holes is close to zero. At sufficiently low k and large G equation 2.17 can be approximated as

$$\text{ENF} \approx 2 + k \cdot G \tag{2.18}$$

so that the minimum ENF is equal to 2. It is not possible to differentiate a single photon signal from the noise level due to the high excess noise factor of > 2 and the limited gain in proportional mode [37].

Another operation mode of an APD is the Geiger mode. Geiger mode is attained when the applied voltage surpasses the breakdown voltage of the device. Above the breakdown voltage, the amplification of the signal resulting from impact ionization is higher than the charge extraction rate and, thus, the charge increases exponentially (theoretically forever). This is due to the fact that electrons, holes, as well as secondary electrons and holes contribute to the charge multiplication. Such a signal formation is called avalanche breakdown. APDs operated in Geiger mode are also called G-APD or single photon avalanche diodes (SPAD). The avalanche breakdown needs to be stopped externally, which can be achieved by connecting a high ohmic resistor in series to the SPAD. The current flowing through the resistor leads to a voltage drop at the SPAD below the breakdown voltage and, thus, stops the avalanche. The charge of the avalanche does not depend on the number of photons that triggered it. Therefore, SPADs are binary devices and have no quantitative information about the light shining on them. The signal of a SPAD in Geiger mode is characterized by a quick rise time of the signal in the range of $\sim$1 ns [38] and a exponential decay in the range 10 ns.

2.4.2.3 Silicon Photomultiplier

Silicon photomultipliers (SiPM) are composed of an array of SPADs that are connected in parallel and have a common output. Each SPAD is operated above breakdown voltage and is connected in series to its own quenching resistor which terminates the avalanche process passively. Alternatively, there are active approaches to terminate the avalanche. Each single SPAD along with its quenching component can be viewed as a single pixel of the SiPM. A schematic of the doping profile of such a pixel is shown in figure 2.14. The photon conversion takes place in the n substrate. In the n substrate the fields are not strong enough to cause impact ionization. The multiplication region is situated between the p^+ and the n^+ region, where the electric field is strongest. The guard ring is used to increase field uniformity at the edge of the pixel. SiPMs vary in size from 1x1 mm^2 up to 6x6 mm^2 and pixel sizes vary between 10x10 µm^2 and 100 µm^2. This leads to a pixel density of 100-10000 pixel/mm^2.

The main properties defining a SiPM are the breakdown voltage, photon detection efficiency (PDE),

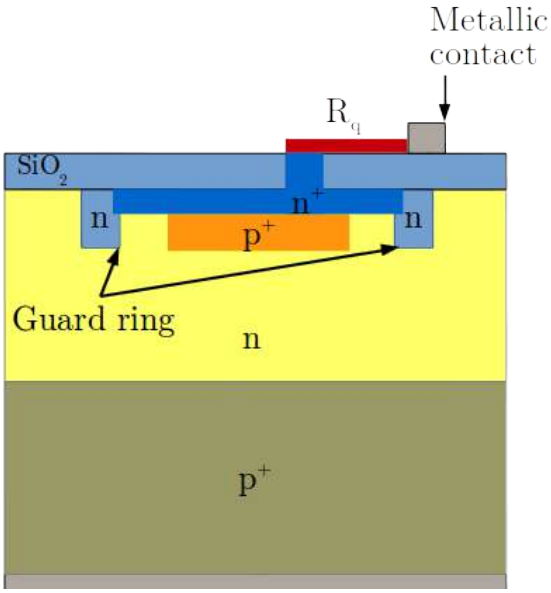

Figure 2.14: Schematic doping profile of a single pixel of a Hamamatsu SiPM. Adapted from [39].

gain, noise, single photon time resolution and dynamic range. Breakdown voltage typically ranges from 30 V to 60 V. PDE highly depends on pixel size and photon wavelength. The maximum PDE is usually achieved around 400-500 nm and is in the range of 15% (for small pixels) to 50% (for larger pixels). Noise has to be distinguished between dark count rate (number of avalanches per second that occur in the absence of light) and correlated noise (avalanches occurring depending on previous avalanches). The dark count rate is usually in the range of several tens of kilohertz per square millimeter, while the correlated noise is on the order of several percent. A more detailed explanation of these parameters is given in the next section.

2.4.3 Main Properties of SiPMs

2.4.3.1 Breakdown voltage

The breakdown voltage (V_{bd}) is the voltage at which the charge multiplication is high enough to form a plasma channel [40] leading to a self-sustained avalanche. V_{bd} can be determined by measuring the current-voltage characteristics of the SiPM. The SiPM current, when shown upon by light, as a function of voltage is at first constant and then starts rising due to impact ionization. The plasma channel formation leads to an abrupt increase of the current at $V = V_{bd}$. One way to extract V_{bd} from the current-voltage curve is to find the minimum of the inverse logarithmic derivative.

The breakdown voltage usually exhibits a small temperature dependency as presented in [41]. This is because the number of charge carrier phonon interactions increases with rising temperature and, consequently, reduces the efficiency of the impact ionization. Therefore, more energetic charge carriers are needed to create an avalanche breakdown, which results in a higher breakdown voltage [42].

2.4.3.2 Gain

The gain (G) of a SiPM is the average amount of charge created for each detected photon (and each free charge carrier, respectively) and is a function of applied voltage and pixel size. It is usually in the range

of 10^5 to 10^7 [43]. It depends on the pixel capacity C_{pix}, the parasitic capacity of the quenching resistor C_q and the applied voltage V.

$$G(V) = (C_{pix} + C_q) \cdot (V - V_{off})/e \tag{2.19}$$

with V_{off} being the so called turn-off voltage and e the electron charge. Usually $C_q << C_{Pix}$, so the gain mainly depends on the pixel capacity.The turn-off voltage is the voltage at which an existing avalanche stops being self-sustained. It can also be defined as the voltage at which the gain is equal to one $V(G = 1)$. The gain exhibits no direct temperature dependence. However, V_{off} depends linearly on the temperature. If the gain is defined in dependence of overvoltage [$G = G(V_{OV})$, with $V_{OV} = V - V_{off}$], it is temperature independent.

2.4.3.3 Photon Detection Efficiency

The photon detection efficiency (PDE) is a measure of the sensitivity of a SiPM and is a strong function of the incident photons wavelength and the applied voltage. In the limit of low intensity light detection, it is mainly defined by the quantum efficiency (QE), the fill factor (FF) and the avalanche initiation probability (P_A).

$$\mathrm{PDE}(\lambda, V) = \mathrm{QE}(\lambda) \cdot \mathrm{FF} \cdot P_A(V) \tag{2.20}$$

The fill factor is defined as the active (photo-sensitive) area of the sensor divided by the area of the whole SiPM. It is limited by the quenching resistors, the separation between single pixels and bias lines running along the top side of the SiPM and is proportional to pixel size. The quantum efficiency is the probability of the incident photon to create an electron hole pair in the sensitive volume of the SiPM and is a strong function of the wavelength [44]. The avalanche initiation probability denotes the probability that an electron hole pair triggers an avalanche. It highly depends on the electric field strength, i.e. the bias voltage, and the location of the initial electron hole pair creation/photon absorption. The location of the electron hole pair creation determines whether the electron or the hole traverses the high field region at the p-n-junction. Electrons have a higher ionization coefficient and, therefore, a higher probability to trigger an avalanche. Further losses might occur at the entrance window to the SiPM due to reflections of photons.

The recovery time of the single pixels has an influence on the PDE in condition of high intensity light detection. If the number of photons shown upon the SiPM approaches the number of pixels in it, there is a non-zero probability that a photon hits a recovering pixel. A recovering pixel does not trigger a new avalanche effectively reducing the PDE.

2.4.3.4 Dynamic Range

The dynamic range can be defined as the signal intensity range over which the SiPM provides an output that is proportional to the input. For applications such as PET, where a large number of photons shall be detected by a single SiPM, a high dynamic range and linearity of signal output is required. The output of a SiPM is a current that is proportional to the number of fired pixels. This output can only be linear provided that the number of photons hitting the SiPM per pixel is smaller or equal to one. If the number of photons hitting the SiPM within a time interval smaller than the recovery time of the pixels approaches or even exceeds the number of pixels in the SiPM, the signal response becomes non-linear due to saturation. The reason is that several photons hitting a single pixel only trigger a single avalanche. In

the case of PET, this means that the amount of light detected in the SiPM does not necessarily increase linearly with the amount of light created in the scintillator, i.e. the amount of energy deposited in the scintillator. The number of fired pixels can be calculated by

$$N_{fired} = N_{pix}\left(1 - e^{-PDE\frac{N_{ph}}{N_{pix}}}\right) \tag{2.21}$$

with N_{fired} being the number of pixels that fired and N_{ph} the number of incident photons. This equation, however, is simplified and does not take into account crosstalk and afterpulsing. These can be introduced into equation 2.21 in the following way [45]

$$N_{fired} = N_{pix}\left(1 - e^{-PDE(1-P_{CT})\frac{N_{ph}}{N_{pix}}}\right) + N_{ph} \cdot PDE \cdot (1 - P_{CT}) \cdot P_{AP} \tag{2.22}$$

with P_{CT} being the crosstalk probability and P_{AP} the afterpulse probability. It can be seen that a high crosstalk probability decreases the dynamic range of a SiPM. But equation 2.22 still only holds for a uniform light distribution over the SiPM and for light pulses which are shorter than the recovery time of the single pixels. Pixels have the chance to recover after firing and to detect a second or even third photon within one light pulse if a slow light pulse, created from scintillation with a slow decay time of several 10's of nanoseconds, hits the SiPM as in PET. Hence, the dynamic range of a SiPM is increased for long light pulses. The dynamic range can also be increased by increasing the number of pixels in the SiPM which consequently reduces the PDE of the device. So a tradeoff between dynamic range and PDE has always to be made while choosing a SiPM. The consequence of a small dynamic range in PET is a low energy resolution and, thereby, a low Compton rejection ability, which can deteriorate the image quality of the scanner. Furthermore, a low dynamic range can lead to small rejection capability of pile up causing false determination of the line of response. Pile up occurs when two photons hit a single crystal in a small time interval.

2.4.3.5 Dark Count Rate

The dark count rate (DCR) is the amount of avalanches that occur in a SiPM in the absence of light. DCR events cannot be distinguished from events that were produced by the absorption of a photon. There are two contributions to the DCR: (1) thermal excitation of electrons to the valence band and (2) tunneling. Tunneling is a rather rare process and depends on the electric field strength, i.e. the applied bias voltage, inside the SiPM. In contrast, thermal excitation is the main source of dark counts at room temperature. Impurities in the crystal which introduce trap centers inside the band gap of silicon increase the amount of dark counts by thermal excitation. This is because the energy needed to excite an electron into a trap center and subsequently to the valence band is smaller than the energy needed to directly excite an electron to the conduction band (band gap of 1.12 eV). Additionally the indirect nature of silicons band gap suppresses direct excitation to the conduction band. The thermally generated current of a SiPM can be described by the Shockley-Read-Hall model

$$I = e \cdot |U| \cdot W \cdot A \tag{2.23}$$

with e being the elementary charge, A the depletion area, W the depletion depth and U the carrier recombination-generation rate in the silicon [46]. Under the assumption that the capture cross sections

for holes and electrons are equal the carrier recombination-generation rate can be written as

$$U = -\frac{\sigma_{th} N_t n_i}{2cosh\left(\frac{E_i - E_t}{k_b T}\right)} \tag{2.24}$$

where N_t is the concentration of recombination centers, E_i the intrinsic Fermi level, E_t the energy level of the recombination centers, v_{th} the thermal velocity ($v_{th} \propto T^{0.5}$) and k_B the Boltzman constant. n_i is the intrinsic carrier concentration and is proportional to

$$n_i(T) \propto T^{3/2} \cdot e^{-(\frac{E_G}{2k_B T})} \tag{2.25}$$

with T being the temperature and E_G the band gap of silicon (1.12 eV). The generation current is proportional to

$$I(T) \propto \frac{T^2 e^{-\frac{E_G}{(2k_B T)}}}{cosh\left(\frac{\frac{E_G}{2} + |E_i - E_t|}{k_B T}\right)}. \tag{2.26}$$

This is strictly speaking only valid below breakdown since it does not include the avalanche process, however, the generation current is proportional to the DCR observed in a SiPM. The DCR has a strong temperature dependency. It was shown that decreasing the temperature of a specific SiPM from room temperature to the temperature of liquid nitrogen leads to a decrease of DCR from ∼10 MHz to ∼10 Hz [41]. Otherwise, the DCR depends on the applied voltage and can be artificially reduced in the system by increasing the trigger threshold. This can be seen in figure 2.15, where DCR is shown as a function of trigger threshold for two different bias voltages. The DCR at a fixed bias voltage as a function of

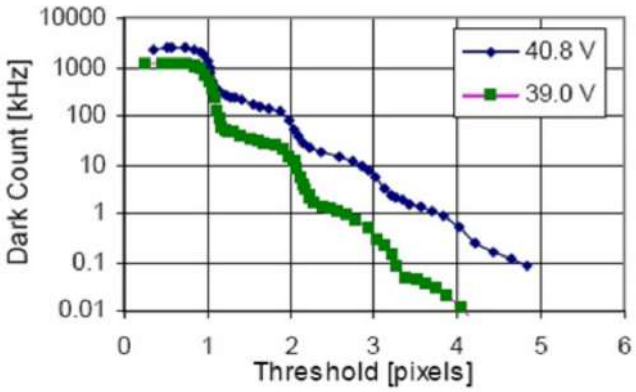

Figure 2.15: Dark count rate for two different bias voltages as a function of the threshold level. Taken from [37].

threshold level takes on a staircase-like shape. The first plateau represents the number of events with a single pixel of the SiPM firing. The drop to the second plateau occurs when the threshold exceeds the maximum current created in a single avalanche. The second plateau represents the number of events with two pixels firing at the same time. The probability of two dark counts occurring at the same time is negligible. Hence, events in the second and subsequent plateaus arise almost exclusively from correlated noise (CN). CN is the effect of an avalanche being triggered by an avalanche occurring in another (or the same) pixel. The two main sources: optical crosstalk and afterpulsing are described in the following

sections.

2.4.3.6 Optical Crosstalk

Optical crosstalk is an additional part of SiPM noise. During the avalanche breakdown photons can be created. The number of photons created with an energy above 1.14 eV was determined to be about $3 \cdot 10^{-5}$ photons per charge carrier crossing the junction [47]. These photons can travel through the SiPM, be absorbed in a neighboring pixel and trigger an avalanche in this pixel. The time delay between the original and secondary avalanche is defined by the photon travel time, which is negligible. Thus, the two avalanches occur seemingly at the same time. Optical crosstalk increases the amount of apparently detected photons in an event and, thus, has an effect on energy and time resolution of a detector system.

The amount of optical crosstalk can be decreased by several options. One option is to lower the applied bias voltage. This leads to a lower gain and therefore less secondary photons, but also decreases the PDE. Also during the manufacturing of the SiPMs the pitch between the single pixels can be increased or trenches can be etched between pixels and filled with an opaque medium. Both of theses options decrease the FF of the SiPM.

2.4.3.7 Afterpulse

Another cause for SiPM noise are the so called afterpulses. During the avalanches charge carriers can be trapped in trapping centers that are introduced by impurities. After being released, the charge carriers can trigger another avalanche in the same pixel. Afterpulses have, as optical crosstalk, implications on the timing performance and energy resolution of a detector system. The afterpulse probability can be somewhere between 0.3% and 10% [48] [49]. The afterpulse probability can only be reduced by decreasing the amount of impurities introduced to the silicon crystals during the growing process.

2.4.3.8 Timing Properties

The time resolution of a SiPM depend on the signal formation, e.g. the signal rise and decay time. Figure 2.16 depicts a single pixel discharge of a SiPM. The time constant of the exponential discharge is

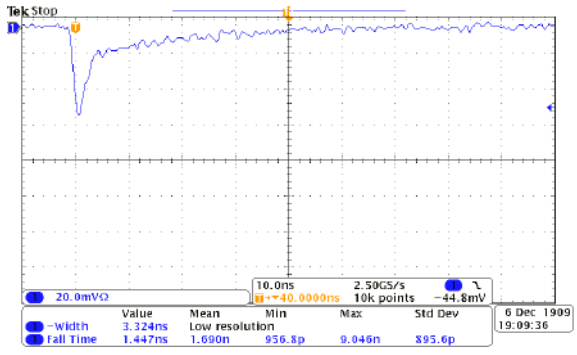

Figure 2.16: A single pulse of a SiPM, taken with an oscilloscope.

on the order of 100 ps, depending on pixel capacitance and resistance of the plasma channel. The decay time depends on the quenching circuit and in the case of passive quenching is on the order of 10's of nanoseconds. Signal rise and decay time increase with the total SiPM capacity, which increases with the area of the device. Hence, overall smaller SiPMs have a better timing resolution. The time resolution

of a SiPM is defined as the statistical variations in the response time to a detected photon, which arise due to fluctuations in the formation of the signal. Since the avalanche formation is a statistical process it varies slightly every time. Additionally, the process can vary with the position inside the pixel and due to fabrication fluctuations from pixel to pixel. A single photon time resolution of 65 ps and 80 ps sigma has been measured for a 1 x 1 mm^2 and a 3 x 3 mm^2 respectively [50] [49]. For higher photon fluxes time resolutions down to 10 ps sigma have been measured [50].

2.5 Coincidence Time Resolution of a PET detector

There are several properties that influence the time resolution of a PET detector. The following properties will be discussed in the ensuing sections:

- Scintillator properties
  - Rise and decay time of the scintillation process
  - Light yield
  - Photon transport
  - Prompt photons
- Photodetector
  - Single photon time resolution
  - PDE
- Electronics
  - TDC resolution
  - Trigger level
  - Electronic noise

2.5.1 Scintillator Properties

The scintillator has a big influence on the achievable timing of a PET detector.

2.5.1.1 Rise and Decay Time of the Scintillation Process

As stated above, free charge carriers, created by the absorption of a 511 keV photon, first thermalize before being captured by luminescent centers. This process makes up the main part of the scintillators rise time. The presence of traps can increases the rise time due to delayed charge transfer to the luminescent centers. Scintillation decay time depends mainly on the time of optical transitions in the luminescent centers. Both, rise and decay time of the scintillation process, have strong implications on the time resolution. The coincidence time resolution (CTR) of a PET detector is proportional to the square root of the rise and decay time multiplied [29].

$$\mathrm{CTR} \propto \sqrt{\tau_r \cdot \tau_d} \tag{2.27}$$

with τ_r and τ_d being the rise and decay time of the scintillation process, respectively. However, the equation is only strictly valid if $\tau_d << tau_r * N_{det}$, with N_{det} being the number of photons detected in the photodetector.

2.5.1.2 Light Yield

The light yield (LY) determines the photon density (also influenced by the decay time) and the number of photons that can be extracted from the scintillator and guided to the photodetector. The time fluctuation

t_n of the nth photo electron producing a total of N photons and possessing a decay time τ_d is [51]

$$t_n = \tau_d \cdot ln\left(0.5\left(n - N + \sqrt{(n-N)^2 + 4N}\right)\right) \tag{2.28}$$

The time resolution achievable with the n^{th} photon can be calculated with this equation. It is the probability that the $(n-1)^{th}$ photon is detected at the time t and the n^{th} photon is detected at the time $t + dt$, integrated over all photons until the n^{th}.

The number of photons can be added to equation such that

$$\text{CTR} \propto \sqrt{\frac{\tau_r \cdot \tau_d}{N}} \tag{2.29}$$

with N being the number of photons created in the scintillator.

2.5.1.3 Photon Transport

The photons created in the scintillator need to reach the photodetector. To achieve good time resolution, the time delay between photon creation and conversion in the photodetector needs to be as small as possible.

Scintillation light is emitted isotropically in the crystal and therefore needs to be redirected towards the photodetector which is (in most cases) located on one side of the scintillator. Photons not moving directly towards the photodetector undergo reflection at the crystal surface. Some of these photons can escape the crystal since total internal reflection only occurs for angles below the critical angle given by $\Theta_c = arcsin(n_s/n_{cr})$, where n_s is the reflective index of the surrounding and n_{cr} is the reflective index of the crystal. Scintillators are often wrapped in some kind of reflector foil to reflect photons back into the crystal and, thereby, to minimize the loss of photons. Hence, wrapping increases the effective number of photons in equation 2.29. The influence of wrapping on the time resolution of scintillation detectors has been demonstrated by [52]. An improvement of CTR from 309 ps to 206 ps was achieved by changing the wrapping of the scintillator. While total internal reflection is desirable on most crystal surfaces, it is not desired on the surface facing the photodetector. Therefore, the amount of total reflection between scintillator and photodetector is minimized by using a proper optical coupling medium between them.

Crystal size also influences photon transport. It has an influence on the number of photons reaching the photodetector as well as the time jitter of the photon arrival time. For smaller crystals, the path a photon has to travel to get to the photodetector is shorter and, thereby, the time jitter on the photon arrival time is reduced. The CTR can be improved by using shorter crystals, as demonstrated by Gundacker et. al [53]. Moving from a crystal with size 2 x 2 x 20 mm^2 to a crystal with size 2 x 2 x 3 mm^2 improved the CTR from 176 ps to 108 ps. However, this only applies universally to making the crystals shorter. Reducing the scintillator cross section can lead to decreased light output of the scintillators [53]. This loss is due to the increased amount of reflections on the crystal surface. Photon transport overall changes the number and the time jitter of photons reaching the photodetector.

2.5.1.4 Prompt Photons

Lately, several research groups try to improve the time resolution of scintillators by taking advantage of other light emitting processes occurring in the scintillator. Some of these processes have an emission time much shorter than the scintillation process and could, therefore, improve the time resolution of the system.

Lecoq et. al [54] make a case for hot intra-band luminescence, which occurs very quickly after the absorption of the incident 511 keV photon. In existing scintillators, however, the amount of photons created by hot intra-band luminescence that are within the energy range suitable for detection with SiPMs is very low (∼10 photons). Nonetheless, it might be possible to tweak the density of states in the conduction band such that the amount of photons created will be increased.

Colloidal nano-structure based scintillators, which have excellent timing properties, are another option to increase the amount of prompt photons. The idea is to embed the nano structures into inorganic scintillators in order to utilize their high stopping power and the fast timing of the nano crystals [55]. A sandwich structure could be chosen, where the distance between neighboring nano-structure based slices is smaller than the typical mean free path of the first photoelectron in the inorganic scintillator. Another option is to exploit Cherenkov light that is produced by the initial photoelectron in the scintillator [31]. Cherenkov light is a prompt emission of light that occurs provided that a charged particle exceeds the speed of light in the medium it traverses. This is the case for the initial photoelectron, created by the absorption of a 511 keV photon, in most inorganic scintillators. The Cherenkov threshold in LYSO is ∼100 keV. The Cherenkov light yield is rather small (tens of photons from a 511 keV photon) and they are mainly emitted in the ultraviolet (UV) range. SiPMs usually have a low quantum efficiency in the UV range. Nevertheless, Cherenkov photons can potentially be used for time tagging of the incident 511 keV photon.

There are designs for PET detectors solely utilizing Cherenkov light and no scintillation, as proposed by [56]. The detector is built out of non-scintillating lead fluoride (PbF_2) crystals with high stopping power and high refractive index coupled to a micro-channel-plate photo-multiplier tube. First detector modules achieved a CTR of 71-95 ps (depending on crystal size). However, so far the proposed design has low sensitivity.

2.5.2 Photodetector Properties

The photodetector adds to the overall time resolution of the system.

2.5.2.1 Single Photon Time Resolution

The single photon time resolution of the photodetector adds to the photon time jitter already introduced by the scintillator (equation 2.28). As mentioned SPTRs of 65-80 ps sigma were measured with SiPMs and ∼10 ps sigma at saturation photon fluxes [50].

2.5.2.2 Photon Detection Efficiency and Noise

The PDE of the photodetector has a direct influence on the number of detected photons. It adds to equation 2.29 as follows

$$\mathrm{CTR} \propto \sqrt{\frac{\tau_r \cdot \tau_d}{N' * PDE}} \tag{2.30}$$

where N' is the number of photons reaching the photodetector. This equation shows that a maximum PDE is desirable to achieve maximum CTR. The PDE of a SiPM is a function of the pixel size and the bias voltage. Hence, large pixels are preferred in condition of reaching a goal of maximum CTR. A large bias voltage, however, also leads to increased noise of the device, which in turn increases the time jitter on the n^{th} photon. In terms of bias voltage, a tradeoff between PDE and noise level must be found to achieve optimal CTR.

2.5.3 Electronics

Electronics are the last part in the detector chain that influence the time resolution by means of: (1) the electronic noise, (2) the capability to vary trigger levels and (3) the time resolution of the employed TDC. The electronic noise might restrict the ability to trigger on the first photons reaching the SiPM and thereby deteriorate the overall timing performance of the detector. The same applies to the ability to vary trigger levels. A large threshold step size may lead to an incapability to trigger on the photon that yields the best time resolution. The time resolution of the TDC adds to the overall time resolution of the system.

2.5.4 Coincidence Time Resolution Lower Bound Estimation

An estimation on the lower bound of time resolution, excluding electronics and assuming a fixed amount of measured photons in the SiPM, were performed by [57]. For a detector system composed of scintillators and SiPMs, the lower bound on the time resolution can be calculated by using photon counting statistics. Photon counting statistics are a limiting factor for time resolution of scintillator based detector systems. The time resolution of a given system depends mainly on the variance of the registration times of scintillation photons in the SiPM. The result of this study for a LYSO:Ce scintillator and a SiPM of type MPPC-S10362-33-50C are shown in figure 2.17. The intrinsic limit on time resolution for this detector combination is shown to be ∼37 ps sigma. As presented it cannot be achieved by utilizing the time stamp of a single photon, but by utilizing the timestamps of the first ∼25 photons. In this study, however, the number of photons being detected by the SiPM were fixed and statistical fluctuations as well as electronics were not included in the calculations. Only the scintillation process itself is considered as source of photons hitting the photodetector, while other instant sources of light are neglected.

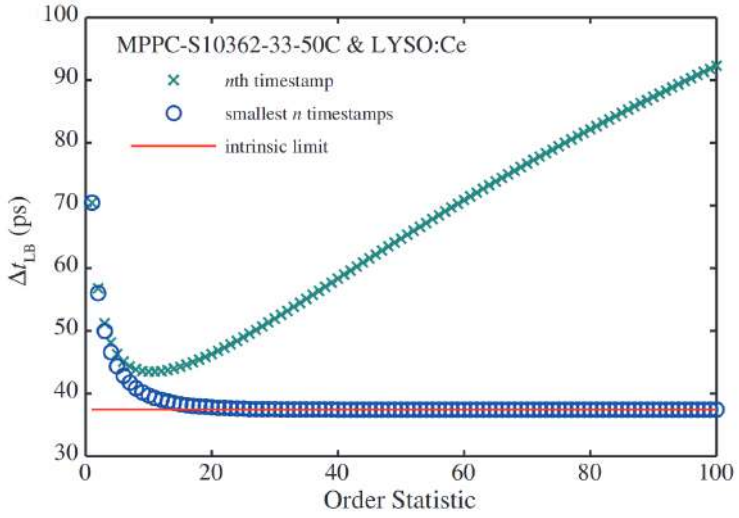

Figure 2.17: Lower bound on the timing resolution (sigma) based on single timestamp (crosses) and on the first n timestamps (circles) as a function of the order statistic. The solid line indicates the intrinsic limit on the time resolution that could be achieved utilizing all timestamps. These numbers are calculated for the combination of a Hamamatsu SiPM (MPPC-S10362-33-50C) and LYSO:Ce scintillator. Taken from [57].

So far a CTR FWHM of 58±2 ps is achieved using current photodetectors, high frequency readout

electronics and small (2 x 2 x 3mm^3) LSO:Ce:Ca crystals. Using bigger crystals (2 x 2 x 20 mm^3) a CTR FWHM of 98±3 ps is achieved [58].

2.6 Medical Application

The main application of PET is in the field of medical research and medical imaging, with a focus on cancer diagnosis. It measures the distribution of radioactive compounds in-vivo to create metabolic/functional images of the body. The compound can be a metabolic agent or a molecule only binding to specific receptors, which leads to an uptake that either depends on tissue metabolic rate or on the number of receptors in the tissue. Hence, PET imaging can exhibit contrast that is highly specific to the application. However, PET does yield limited anatomical information because only the tissues that take up the radioactive compound can be visualized. This is in contrast to anatomical imaging. The most widely used anatomical tomographic imaging methods are computed tomography (CT) and magnetic resonance imaging (MRI). CT measures the attenuation of x-rays in the patient's body. The image produced by a CT is a map of attenuation coefficients. However, the difference in attenuation coefficients between healthy tissue and, for example, cancerous tissue can be very small, which leads to a low contrast. MRI measures radio waves that are emitted by excited hydrogen atoms in a strong external magnetic field. Tissues are differentiated in MRI by hydrogen density and signal decay time, which depends on the composition of the tissue. Cancerous tissue can have similar hydrogen density and composition as healthy tissue. This can lead to low contrast, just as in CT. PET with its high specificity and consequent high contrast between healthy tissue and cancerous tissue can increase the capability to identify lesions. A PET image is usually accompanied by either a CT or MRI allowing to exploit the high contrast of PET and the anatomical information of CT or MRI.

2.6.1 Cancer and its Radiotracers

Cancer is a subcategory of neoplasms. Neoplasms are unregulated and uncoordinated growths of cells which do not stop even in the absence of the original trigger. These growths usually form some kind of mass which is called tumor. A tumor can be benign or malignant. Benign tumors do not invade surrounding tissue and typically do not grow back after removal. Malignant tumors are characterized by the ability to invade and destroy surrounding tissue and to spread to more distant parts of the body (forming new/secondary growths). They are also called cancer. Secondary growths of a cancer are called metastases. Further characteristics of cancer are: (1) cell growth and division in absence of the proper signals, (2) avoidance of programmed cell death, (3) limitless number of cell divisions and (4) promotion of blood vessel construction. One of the most prominent forms of cancer are carcinoma that develop from epithelial cells. Epithelial cells are found on the outer surface of organs and blood vessels, as well as inner surfaces of cavities in many organs. An example for epithelial cells is the epidermis. The causes for cancer are manifold and include: (1) over or under production of hormones, (2) autoimmune diseases, (3) radiation, (4) diet and exercise, and (5) several chemicals interacting with the cells. Symptoms of cancer can be very unspecific and make diagnosis difficult, especially during the early stages of the cancer.

There are several options for the detection of cancer: (1) metabolic imaging, (2) tomographic anatomical imaging, (3) palpation and (4) blood tests. The exact type of cancer can only be identified via biopsy and subsequent tissue analysis. Nuclear metabolic imaging uses radioactively tagged biological active molecules, also called radiotracers. These radiotracers are designed in a way that they have a higher up-

take in cancerous tissue than in normal tissue. This can be achieved by either using a molecule of which receptors are overexpressed in the cancer or by utilizing the fast metabolism of cancer. Radiotracers can be highly specific to one type of cancer. Prostatic and pancreatic cancer, which are the main application areas of the EndoTOFPET-US detector, as well as the radiotracers used to visualize them are described in the following sections.

2.6.1.1 Prostatic Cancer

Prostatic cancer is the most frequently diagnosed form of cancer and the third most common cancer cause of death in men. The risk of a 75 year old male to get prostate cancer within the next ten years of his life is about 6%, while it is below 0.1% for a 35 year old male. Prostate cancer also has a high survival rate if diagnosed at an early stage. The five year survival rate of prostate cancer is ∼93% [59]. There are two mainly utilized options for the treatment of prostate carcinoma. The first therapy option is the radical prostaectomy during which the prostate and the surrounding lymph nodes are surgically removed. The second therapy option is radiation therapy. It can be either applied externally by an external radiation source or internally via brachytherapy. So called radioactive seeds are inserted into the prostate during brachytherapy. In general, brachytherapy is seen as the superior of the two. One problem of external radiation treatment is the planning of the radiation administration. This has two reasons: (1) the prostate is closely positioned to the rectum, which is very vulnerable to radiation, and (2) the prostate's position changes daily.

There are several options for diagnosing prostate cancer: (1) the physical examination of the prostate, also called palputation, (2) transrectal sonography with ultrasound (US), (3) MRI and (4) PET/CT [60]. True evidence for the existence of a carcinoma, however, can only be given by bioptically extracted tissue samples. The guidance during the sample extraction is usually done by transrectal US. One of the problems with prostate cancer is that it is often multifocal, meaning that there are several carcinoma within the prostate that occur at the same time. This means that a standard biopsy misses around 38% of the carcinoma within the prostate [61]. Therefore, more accurate diagnosis methods are needed. The purpose of a functioning diagnose is manifold: (1) detection of the tumor, (2) local staging, (3) detection of metastases and (4) post treatment evaluation of the cancer. Especially incorrect staging of the cancer can have severe consequences for the therapy of the patient.

As mentioned, so called radiotracers are used in nuclear metabolic imaging. The most common radiotracer used in PET/CT is fludeoxyglucose (FDG) labeled with ^{18}F. It is, however, not very effective for prostate cancer detection because of the small ratio of uptake between the tumor and the prostate. FDG also has a high uptake in the urinary bladder which can have effects on the prostate and prostate lesion visibility in the image [62]. A lot of effort goes into the research for new tracers. One promising tracer for prostate cancer are ligands of the prostate-specific membrane antigen (PSMA). PSMA is a cell surface protein which is overexpressed in prostate carcinoma cells [63, 64]. It can be labeled with ^{68}Ga, technetium-99m (^{99m}Tc) and different iodine isotopes.

2.6.1.2 Pancreatic Cancer

Pancreatic cancer is often free of symptoms or shows unspecific symptoms in the early stages making it difficult to diagnose. When diagnosed, it usually already formed metastases resulting in a low five year survival rate of 8% [59]. The risk of having pancreatic cancer compared to prostatic cancer is small. The risk of a 75 year old person to get pancreatic cancer within the next ten years is about 0.7%, while

it is below 0.1% for a 35 year old person. The therapy of pancreatic cancer depends on the type and stage of the cancer as well as the health and age of the patient. Therapy options include: (1) surgical removal of the cancerous tissue and the lymph nodes, (2) chemotherapy (often accompanies surgery), (3) radiation therapy (can accompany chemotherapy). There are non-invasive diagnosis methods: (1) abdominal US, (2) CT, (3) MRI and (4) endoscopic retrograde cholangiopancreatography. Diagnosis of pancreatic cancer is difficult because of its often unspecific symptoms and the challenging distinction between cancer and inflamed tissue. Furthermore, inflamed tissue or fibrosis surrounding the cancer can lead to a non-accurate sampling during biopsy. Pancreatic adenocarcinoma (tumors arising from epithelial cells of the gland) show a high uptake of FDG due to an overexpression of Glut-1 (a uniporter protein) in the tumor. The application area of FDG in PET is vast: (1) to perform pre-surgery diagnosis, (2) to differentiate between benign and malignant tumor, (3) to perform cancer staging, (4) to detect metastatic diseases and (5) to monitor the response of the therapy. The sensitivity and specificity of FDG have been shown to be 85-100% and 67-99% respectively [65]. False negatives can, however, occur if the lesion is small and the patient exhibits a high blood sugar. False positives can occur if the patient has chronic or acute pancreatitis [65]. New labeled molecules such as sigma-receptor ligands and ^{18}F-3-fluoro-deoxy-I-thimidine (FLT) are developed. Their purpose is to increase the distinction capability of recurrent tumors from postoperative fibrosis and inflammation and to guide the biopsy [66]. PSMA, in particular ^{68}Ga-HBED-CC, has been shown to have a uptake in pancreatic cancer [67].

2.6.2 Fundamental Functionality of PET

As mentioned above, PET is a nuclear metabolic medical imaging method. It utilizes β^+ emitting nuclides attached to a tracer molecule. The two 511 keV photons originating from the positron electron annihilation are measured by the PET detector. If two photons are measured in coincidence, i.e. are measured within a predefined time window, they are expected to originate from the same annihilation. The coincidence time window is usually in the range of several nanoseconds and is constrained by the detector's geometry and the patient's physiology. The line defining the two detection points of the photons is called line of response (LOR). The geometry of the detector needs to be chosen in such a way that both back-to-back photons can be detected. Most PET scanners consist of a cylindric detector in which the patient is inserted. Such a geometry leads to a high angular coverage and a big field of view.

An image reconstruction software converts all detected LORs to a 3D image of the radioactivity distribution. The radioactivity distribution depends on the uptake of the radiotracer in different tissues. This leads to the reconstructed image representing metabolic information rather than physiological information. PET imaging is mainly used to identify, locate and stage cancer [68], but can also be used to identify degenerative brain diseases. To gain comprehensive anatomical information complementing the metabolic information, either CT or MRI is used. Full body PET/CT scanners are widely available and are often comprised of two separate PET and CT scanners with a common gantry. The development of PET/MRI scanners have gotten a huge boost due to the development and wide availability of SiPMs. This is because the widely used photomultiplier tubes are affected by magnetic fields in contrast to SiPMs [69] [70]. The magnetic fields inside MRI scanner are in the range of 0.5 up to 7 tesla. PET/MRI has some advantages over PET/CT: (1) smaller radiation dose for the patient and (2) enhanced image quality due to organ specific imaging sequences [71]. Both of the multimodal imaging techniques mentioned above need co-registration. Co-registration is the matching of the two images leading to a single image including the 3D physiological as well as metabolic information. The high resolution of the CT/MRI images adds a lot of information to the PET image and, thus, helps in identifying diseases.

PET resolution is intrinsically limited by the range of the positron after emission and the non-collinearity of the two back-to-back photons. Additionally, scattering and false/random coincidences further limit PET resolution. Scattering can deviate a photon from its original path and lead to the formation of a wrong LOR. False coincidences occur if two photons coming from two different annihilations are measured within the coincidence time window and are paired as a single event, also leading to an incorrect LOR. Figure 2.18 shows examples of a true and false LORs that can occur within a PET

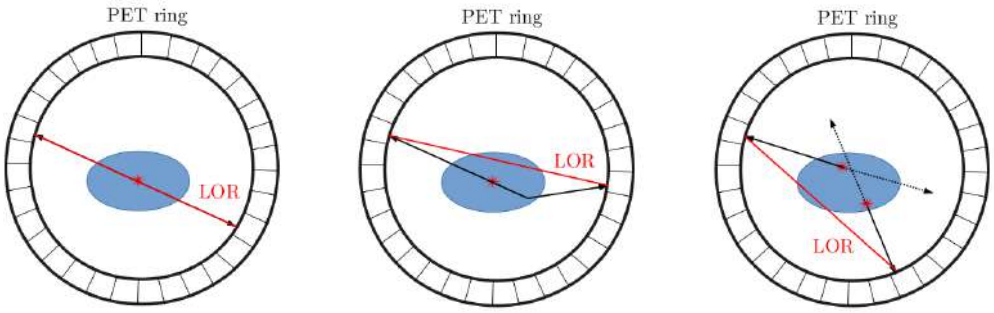

Figure 2.18: An example of (left) true line of response (LOR) inside a cylindric PET scanner, (center) LOR originating from a scattered event, (right) LOR originating from a random coincidence of two annihilations occurring at a similar time.

scanner.

2.6.3 Fundamental Functionality of Time-of-Flight PET

Time-of-flight PET (TOFPET) aims to increase the image quality of PET images and to push towards the intrinsic limits of the modality. In conventional PET, the time stamps of the two photons are measured with nanosecond precision and are solely used to determine whether two photons are detected within the coincidence time window. After that the time information is not used anymore. The annihilation probability along the LOR is expected to be uniform. In TOFPET, the time of arrival of the two photons forming the LOR is measured as precisely as possible. The time information is used to determine the annihilation point along the LOR via the following equation:

$$\delta t = t_1 - t_2 = \frac{d_c + d_a}{c} - \frac{d_c - d_a}{c} = \frac{2d_a}{c} \tag{2.31}$$

where t_1 and t_2 are the times of arrival of the first and second photon, respectively, d half the length of the LOR, and d_a the distance between the center of the LOR to the annihilation point. This concept is illustrated in figure 2.19. The annihilation probability along the LOR is constant for conventional PET. This can lead to smearing of a small source along the LOR or to noise provided that several sources are located along the same LOR. In contrast to conventional PET, the annihilation probability is adjusted according to the two photon hit times in TOFPET. It is approximated with a Gaussian of mean at $d + d_a$ and a FWHM/sigma according to the time resolution of the detector. A good time resolution leads to a precise determination of the annihilation point and, thus, results in reduced cross dependencies of voxels. This is because the forward and backward projections are only performed over a limited number of voxels, defined by the annihilation probability function. Including TOF increases the signal to noise ratio (SNR) and accelerates convergence of iterative reconstruction algorithms [72]. The time resolution of a PET

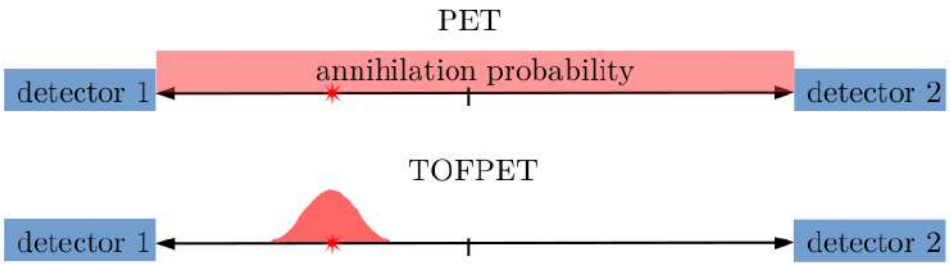

Figure 2.19: The annihilation probability along the LOR in case of (top) PET and (bottom) TOFPET.

detector depends on several factors and is explained in detail in chapter 2.5. The ability to localize the annihilation point depends on the time resolution. The uncertainty in terms of full width half maximum (FWHM) on the annihilation position can be expressed by

$$\mathrm{FWHM}_x = \frac{c}{2}\mathrm{FWHM}_t \tag{2.32}$$

with FWHM_t being the CTR of the detector and c the speed of light. A CTR of 10 ps FWHM would allow to determine annihilation position with an uncertainty of 1 mm, which is the intrinsic resolution of PET. Such a CTR would make sophisticated iterative reconstruction algorithms obsolete. More recently, a commercial scanner with a time resolution of up to ∼215 ps was build [73]. The SNR of a cylindric TOFPET scanner can be expressed as [74]

$$\mathrm{SNR}_{\mathrm{TOF}} = \sqrt{\frac{D}{\sigma_x}}\mathrm{SNR}_{\mathrm{non-TOF}} \tag{2.33}$$

with D being the detector diameter. The SNR is proportional to the square root of the noise equivalent count rate. That means that the SNR increases with the number of counts detected during a scan. As a simplified model, the SNR of a TOFPET scan is comparable to the SNR reached in a longer conventional PET scan. This does not necessarily hold for iterative reconstruction algorithms. The SNR is still improved when using iterative reconstruction. In contrast to a conventional PET, TOFPET results in: (1) a reduced dose for the patient or (2) a reduced acquisition time or (3) an improved image quality. TOFPET also leads to a quicker convergence of the iterative reconstruction towards a specific contrast [72]. Another benefit of TOFPET is the potential compensation for missing information (e.g. in case of a small angular coverage). The necessity of TOF for the EndoTOFPET-US detector will be presented in chapter 8.

2.7 Tomographic Image Reconstruction

The goal of medical imaging is to provide 2D planar or cross-sectional images of the patient for diagnostic purposes. In the case of cross-sectional images, they can be merged to a 3D representation of the patient. Tomographic image reconstruction is necessary to achieve precise cross-sectional images from PET data (except if CTR=10 ps). There are two different methods of tomographic imaging: (1) transmission tomography (TT) and (2) emission tomography (ET). In the case of transmission tomography (e.g. CT),

the radioactive source (x-ray tube) is rotating around the patient and the measured quantity is the beam intensity behind the patient. The linear attenuation coefficient of the patient's body can be calculated from a single measurement. Combining measurements at several angles allows to calculate the attenuation coefficients at each point inside the patient. In the case of emission tomography, the radiation source is located inside the patient in form of a radioactive isotope, that is connected to a tracer molecule and that either undergoes γ decay (in single photon emission computed tomography, SPECT) or β^+ decay (in PET). The reconstructed quantity is the tracer activity concentration in the patient. For both tomography types, the reconstruction of the sought-after quantity is an inverse problem, the measured data are known and the process leading to this measurement needs to be determined. An overview of analytical image reconstruction (used in CT imaging) and iterative image reconstruction (used in PET imaging) is provided in the following sections.

2.7.1 Analytical Image Reconstruction

In TT and ET, the 2D projection of an object onto the detector is measured. The measurement in each single detector cell corresponds to a line integral of the attenuation coefficients (TT) or the activity (ET) along the line between radiation source and the detector cell. The projection principle can be illustrated in the case of a pointsource (point of emission for ET and high attenuation for TT, respectively) in the $x-y$ plane and a detector in the $s-\phi$ plane with an angle ϕ (with $\vec{e}_\phi \cdot \vec{e}_s = 0$). The position of the signal on the 1D detector is $s + rsin(\phi)$, with $r = \sqrt{x^2 + y^2}$. The projection of a single point onto the detector is a sine function when scanning ϕ, resulting in the name sinogram. Such a scenario is visualized in figure 2.20. Hence, the Radon transform $p(s, \phi)$ of the original image $f(x, y)$ is measured. An estimate of the

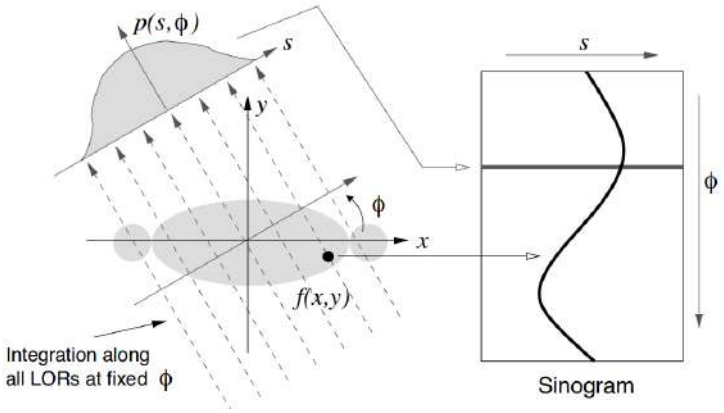

Figure 2.20: The projection $p(s, \phi)$ onto the detector of a parallel beam measurement. Each single projection fills a single row of ϕ in the sinogram. A single point in $f(x, y)$ follows a sine function in the sinogram. Taken from [75].

original image can be gained by performing a backprojection:

$$b(x, y) = \int_0^\pi p(s, \phi)|_{s=xcos\phi+ysin\phi} \tag{2.34}$$

The backprojection smears the measured activity at each detector angle over the field of view of the detector (FOV), as demonstrated in figure 2.21. But a simple backprojection leads to blurring and oversampling in the center of the fourier space, because it asserts the same activity everywhere along the

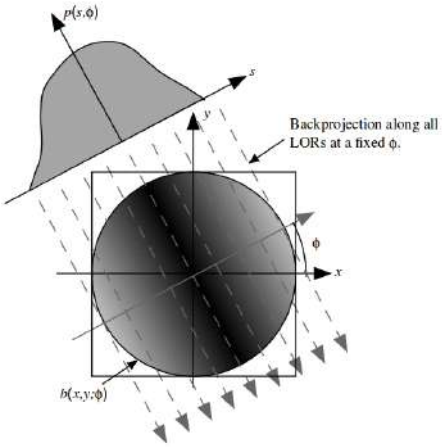

Figure 2.21: Visualization of a simple backprojection at a specific angle ϕ. Taken from [75].

line. Oversampling can be reduced by utilizing the central slice theorem (CST) and adding a frequency filter to the Fourier transform of the projection. Additionally, such an approach keeps the reconstruction matrix small and thereby the reconstruction efficient. The CST states that the one dimensional Fourier transform $\mathcal{F}_1$ of a projection $p(s, \phi)$ is equal to the two dimensional Fourier transform of the image at the corresponding angle ϕ.

$$\mathcal{F}_1\{p(s, \phi')\} = \mathcal{F}_2\{f(x, y)\}_{|\phi=\phi'} \tag{2.35}$$

This means that a slice through the center of the two dimensional Fourier transform of an image $f(x, y)$ at angle ϕ is equivalent to the one dimensional Fourier transform of a one dimensional projection of the image $f(x, y)$ with projection angle ϕ. This correlation is visually presented in figure 2.22. The following

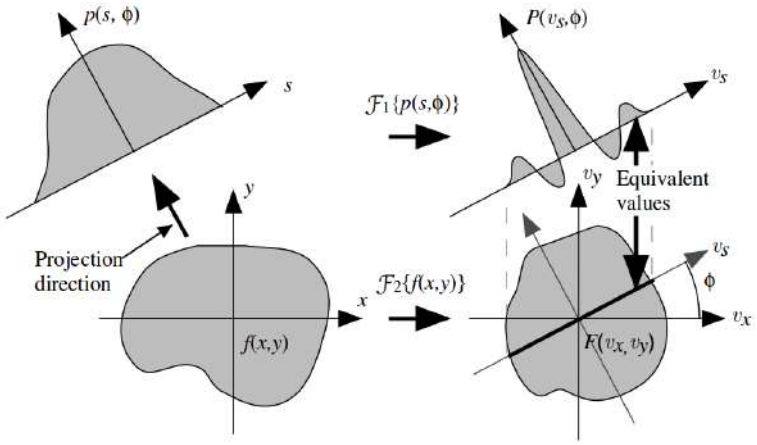

Figure 2.22: Visualization of the central slice theorem. $p(s\phi)$ is the measured projection (top left) of the real activity distribution $f(x, y)$ (bottom left). P and F are the corresponding fourier transformations. Taken from [75].

equation can be used to calculate the original image from the measured projections:

$$f(x, y) = \int_0^{\pi} \left[\int_{-\infty}^{+\infty} d\omega |\omega| P(\omega) e^{2\pi i \omega s} \right] = \int_0^{\pi} p'(s, \phi) \tag{2.36}$$

with

$$\int_{-\infty}^{+\infty} d\omega |\omega| P(\omega) e^{2\pi i \omega s} = \mathcal{F}^{-1}\{|\omega| P(\omega)\} \equiv p'(s, \phi). \tag{2.37}$$

This equation is similar to equation 2.34 with the addition of a frequency filter $|\omega|$ being applied in the Fourier space.

The overall reconstruction process includes: (1) performing Fourier transformation on the projection, (2) multiplying the Fourier transform with the frequency filter, (3) inversing transform to real space, (4) performing backprojection of filtered projection, (5) summing over all filtered backprojections. A reconstruction with a complete, continuous set of projections would yield no loss of information. Filtered backprojection is a simple and fast reconstruction method which, if stochastic noise is low, can yield great results. Therefore, it is still used in CT to this day.

2.7.2 Iterative Image Reconstruction

The assumption of a line integral in the analytical reconstruction is only an estimate and does break down in condition of a more significant noise. Several effects lead to the invalidity of the line integral assumption and, thereby, impair the results obtained with analytical reconstruction methods in PET. On the one hand, the underlying physics of PET imaging need to be taken into account for an accurate reconstruction: (1) positron range, (2) acollinearity, (3) false coincidences, (4) scattering and absorption of the photons, (5) the Poissonian nature of the radioactive decay and the subsequent Poissonian noise, and (6) low statistics . On the other hand, detector effects need to be included: (1) detector cell size, (2) gaps in the detector, (3) limited FOV, (4) non-uniform resolution. In iterative image reconstruction, all the above mentioned effects can be modeled and included in the reconstruction. It has been found that it is especially important to include a realistic model of the Poissonian noise occurring in PET imaging. A mathematical expression for the imaging process can be formulated as

$$\boldsymbol{p} = \boldsymbol{H}(\boldsymbol{f}) + n \tag{2.38}$$

where $\boldsymbol{p}$ is the measured data, $\boldsymbol{H}$ the system model, $\boldsymbol{f}$ the unknown image producing the data and n a noise term. The system model is in general a non-linear continuous transform that maps the image to the acquired data. It can be simplified to a matrix of probabilities $\boldsymbol{S}$, called the system matrix. Each matrix element S_{ij} of the system matrix represents the probability that an emission in voxel x_i leads to a detection in the detector pair j.

$$\boldsymbol{y} = \boldsymbol{S}\boldsymbol{x} \qquad or \qquad y_i = \sum_i S_{ij} x_i. \tag{2.39}$$

A voxelization of the image is necessary to utilize such an approach. A visual representation of the matrix elements is presented in figure 2.23. The goal of the reconstruction is an inverse problem of finding the image $\boldsymbol{x}$ from a set of measurements $\boldsymbol{y}$, that can be accomplished by inverting the system matrix. However, it is often not possible to invert the system matrix analytically and, thus, is performed iteratively. This is commonly done by defining an objective function that checks the probability that the measured data arises from the reconstructed image.

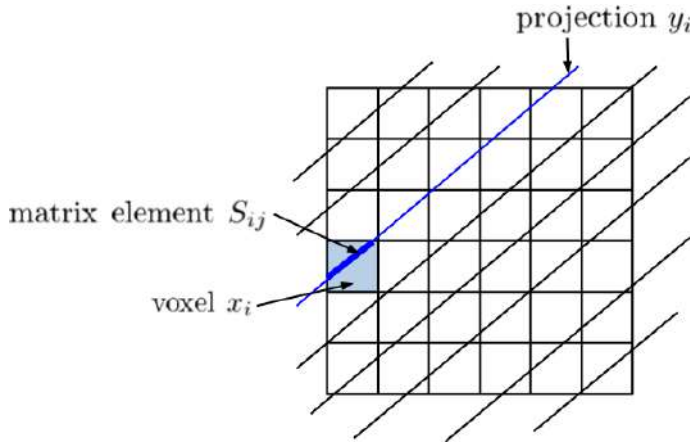

Figure 2.23: Voxelization of the image and schematic interpretation of a single system matrix element S_{ij}. The matrix element S_{ij} gives the probability that an emission in voxel x_i leads to the prjojection y_j. Adapted from [75].

2.7.2.1 Maximum Likelihood - Expectation Maximization

The Maximum Likelihood - Expectation Maximization (ML-EM) was first discussed by [76] and later introduced to the field of image reconstruction by [77]. This method assumes Poissonian noise on the data and, therefore, is well suited for PET. The probability to measure k given the Poissonian expectation value $\lambda = \sum_i S_{ij} x_i$ is

$$p(k|\lambda) = \frac{e^{-\lambda}\lambda^l}{k!} \tag{2.40}$$

The likelihood function is the multiplication of all probabilities to measure y_i:

$$L(x) = p(\boldsymbol{y}|\boldsymbol{x}) = \prod_i p(y_i|\boldsymbol{x}) = \prod_i \frac{e^{-S_i\boldsymbol{x}}(S_i\boldsymbol{x})^{y_i}}{y_i!} \tag{2.41}$$

This Poissonian model is only true before the rest of the corrections (e.g. scattering, attenuation, random coincidence) are applied. The reconstruction finds the image with the highest probability in order to produce the measured data. This is achieved by finding the activity distribution $\boldsymbol{x}$ that maximizes the likelihood function L. $log(L)$ is maximized in practice because it offers computational advantages over the maximization of L itself. The algorithm used for the maximization of the likelihood function is the expectation maximization algorithm proposed by [76]. It maximizes the logarithm of the likelihood function with respect to an initial guess $x_i^{(0)}$ of the image. Guessing an image at the beginning yields the advantage of having a complete dataset compared to the non-complete data. The algorithm comprises essentially two steps: (1) the calculation of the expectation and (2) the maximization [78]. These two steps can be combined in a single equation:

$$x_i^{(n+1)} = \frac{x_i^{(n)}}{\sum_j S_{ij}} \cdot \sum_j S_{ij} \frac{y_i}{\sum_k A_{kj} x_k^(n)} \tag{2.42}$$

with x_i^{n+1} being the new estimate of the activity in voxel i based on the current estimate $x_i^{(n)}$ of the n^{th} iteration. The reconstructed image of the n^{th} iteration is the reconstructed image of the $n-1^{th}$ iteration multiplied by a correction factor. The overall procedure of the ML-EM can be summarized in six steps:

(1) An initial guess for the activity distribution is made (e.g. filtered backprojection).
(2) A forward projection/simulation of the measured data is performed from the activity distribution/initial guess.
(3) The projection/measurement simulation of the activity distribution is compared to the data and a correction is calculated.
(4) The correction is backprojected into the image domain yielding a correction factor for the initial image.
(5) The current image estimate is multipplied with the correction factor and divided by the weighting term based on the system model.
(6) Steps 2-5 are repeated until the maximum is reached.

If no noise is present and enough statistics are collected, the result of the maximization will lead to the real image. However, the reconstructed image will always be noisy and require a form of smoothing due to the inherent noise of PET. Smoothing can be applied by stopping the reconstruction early or applying standard smoothing operations.

2.7.2.2 System Model

The reconstructed activity distribution should be equal to the real activity distribution if the simulated measurement in step 2 of the ML-EM is equal to the real measurement. This is only the case if the applied system model represents the system sufficiently good. The reconstructed activity can only be a good approximation of the real image if the system matrix is a good approximation of the real detector system. Thus, a good understanding of the detector system, and the underlying physics of PET are necessary to build a reliable reconstruction algorithm. The most important physics effects in PET are: (1) the positron range, (2) photon non-collinearity and (3) random coincidences. Furthermore, including a scattering model from a CT or MRI image can increase the effectiveness of the reconstruction algorithm. The mos improtant detector properties that need to be included in the system model are: (1) gaps in the detector, (2) scattering and absorption in the detector material, (3) dead time, (4) resolution. There are several ways to determine the system model: (1) numerically [79], (2) experimentally with a point-like radioactive source [80] or (3) with dedicated simulations [81].

Chapter 3

The EndoTOFPET-US Project

The EndoTOFPET-US project aims to build a multimodal imaging system including PET and US. The main component is an asymmetric endoscopic time-of-flight PET detector. It consists of two separate parts that detect the two 511 keV photons in coincidence. The following chapters talk about the project goals and challenges, detector design, electronics and reconstruction software.

3.1 Project Goals

There are two main goals of the EndoTOFPET-US project: (1) development of new biomarkers for pancreas and prostate carcinoma and (2) development of a detector that is able to provide intraoperative guidance during prostate and pancreas surgery or biopsy. Pancreas and prostate cancer have been chosen due to their severity and frequency, respectively. Moreover, there are still no biomarkers aimed at pancreas cancer that exhibit a high specificity and good contrast. Intraoperative guidance for prostate cancer biopsy is of particular interest because the prostates position in the human body is not well defined. It depends on the volume of the urinary bladder and bowel movement of the patient. Thus, confirming the prostate's position during biopsy has the potential to increase effectiveness and improve staging of the cancer. The challenges of the project are: (1) to achieve a CTR of 200 ps, (2) to miniaturize the endoscopic PET detector and (3) to develop a fast image reconstruction software that provides real time images.

3.2 Detector Design

The PET detector consists of two parts: (1) an endoscopic head that is composed of a miniaturized PET detector attached to a commercially available ultrasound endoscope and (2) an external PET plate. The idea of this design is to allow the endoscopic head to be close to the organ under study (prostate or pancreas). This leads to background suppression from the surrounding tissue. The endoscopic head can be positioned such that the limited field of view does not include organs that provide a particularly high background (e.g. the bladder in case of prostate imaging). The small detector size allows to use small pixels without increasing the costs of the detector too much. In general, small pixels lead to an improvement in spatial resolution. The external plate is positioned close to the patient in such a way that allows coincidence measurements between the endoscopic head and itself. Both detectors can be freely moved during acquisition. Their position is tracked with a commercial optical tracking system

(Polaris Optical Tracking System from NDI). The arrangement of the detectors in case of the prostate is schematically shown in figure 3.1.

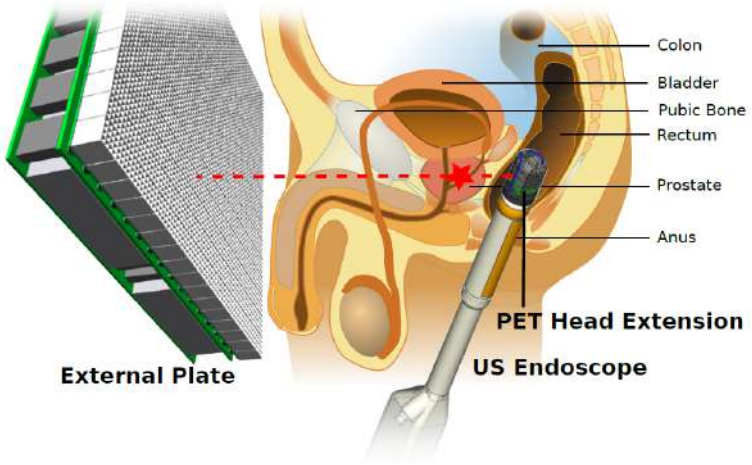

Figure 3.1: Sketch of the EndoTOFPET-US detectors application in the prostate case.

3.2.1 Endoscopic PET Head

Two versions of the endoscopic PET head were foreseen to be build, but were not finished within the timeframe of this thesis: (1) one endoscopic PET head specific for the pancreas and (2) one endoscopic PET head specific for the prostate. The composition of these intended endoscopic PET heads and the development of a prototype will be presented in this section.

The prostate endoscopic PET head shall be mounted on a transrectal US endoscope (EUP_U533 from Hitachi). The size of the endoscopic PET head is restrained by the anatomy of the human body and cannot exceed 23 x 23 x 40 mm^3. The pixel size is chosen to be 0.71 x 0.71 mm^2. Small pixels do not only improve the spatial resolution of the detector, but are also necessary to deal with the high rate of events expected in such close proximity to the prostate. Bigger pixels would lead to pile up in the detector and, thus, reduce sensitivity of the system. Two matrices of 9 x 18 LYSO crystals (Proteus) with a size of 0.71 x 0.71 x 15 mm^3 that are optically coupled to multichannel digital SiPMs (MD-SiPMs) through optically glue are chosen as detector. The endoscopic head also includes a front end printed circuit board (PCB) which is connected via a cable to the data acquisition (DAQ) card. Furthermore, it includes water cooling to dissipate the heat from the application-specific integrated circuit (ASIC). This leads to a controllable measurement environment: (1) low DCR, (2) stable CTR, (3) energy resolution and (4) no harm to the patient due to hot parts. A sketch of the foreseen prostate probe and the external plate is shown in figure 3.2. The pancreas probe has a similar layout, but needs to be even smaller to fit through the esophagus and reach the stomach. Thus, a single matrix of 9 x 18 LYSO crystals with a size of 0.71 x 0.71 x 15 mm^3 is chosen for the pancreas probe. A schematic of the pancreas probe and its employment taken from [82] is shown in figure 3.2. The MD-SiPMs that will be employed in the endoscopic PET heads have been developed within the collaboration [83–85]. They are arranged in 9x18 arrays and have a total size of 7.2 x 14.4 mm^2. A single MD-SiPM consists of 16 x 26 SPADs with 30 x 50 μm^2 pixels. In comparison to analog SiPMs, MD-SiPMs include output digitization on the same die as the pixel. Each SPAD is equipped with a one-bit counter providing the digital number of fired

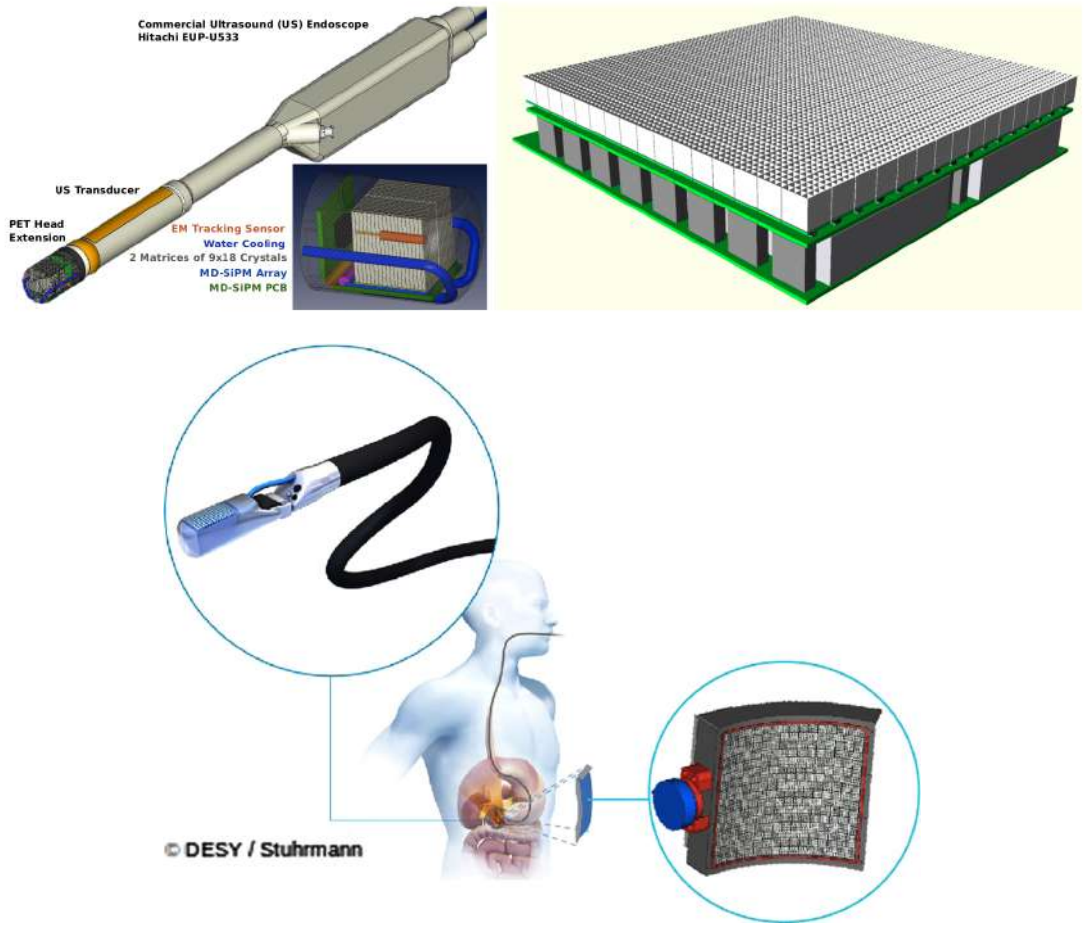

Figure 3.2: (top) Schematic of the prostate probe and the external plate. (bottom) Schematic of the pancreas probe and its employment. Taken from [82].

pixels. This allows to turn off single pixels experiencing high DCR. However, masking pixels reduces the PDE of the device. Nonetheless, single pixels often possess a very large part of the overall DCR. As a result, masking a few pixels can have a major effect on the overall DCR and exceed the negative effect of a minor decrease in PDE. The MD-SiPMS are readout column-wise and include three time to digital converters (TDC) per column. TDCs are directly implemented on the device. Such a design reduces signal propagation time and reduces PDE. Therefore, a tradeoff between fill factor and the amount TDCs is made. The MD-SiPMs developed within the collaboration have a pixel fill factor of 57%. In PET applications using LYSO (lutetium-yttrium oxyorthosilicate) crystals, the hit times of the first five to ten photons usually are the most important to determine the gamma event time, as shown in chapter 2.5. The probability to obtain the hit times of the first five to ten photons is estimated to be relatively high. Figure 3.3 shows the time resolution achieved when using the hit time of the N^{th} photon or the first N photons reaching the MD-SiPM. It can be seen that using multiple triggers improves the time resolution by 50%. The multi trigger approach also reduces the effect of DCR on the time resolution.

Since the prostate and pancreas specific endoscopic PET heads were not finished within the time-frame of this thesis, an endoscopic head prototype was build to show prove of concept. The endoscopic head prototype is made up of an 8×8 LYSO:Ce scintillator array coupled one-to-one to an

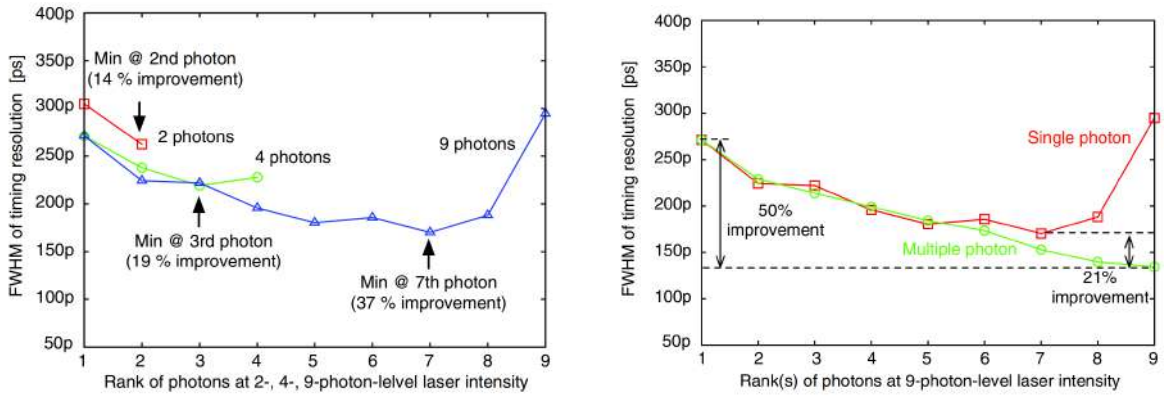

Figure 3.3: (left) Time resolution as a function of photon trigger level (rank of photons) and laser intensity. (right) Time resolution as a function of trigger level for single triggers (red) and multiple triggers (green) at a laser intensity average of nine photons. Taken from [85].

8 × 8 Hammamatsu MPPC (multi-pixel photon counter) array (S13615-1050). Each crystal has a size of 1.13 × 1.13 × 15 mm^3 wrapped by 70 μm reflector foil. Ultimately, the endoscopic head prototype covers an area of 9.6 × 9.6 mm^2. Analog SiPMs are used for the prototype because they allow to use the same readout electronics as for the external plate. The readout of the analog SiPM signal is performed by the STiC (silicon photomultiplier timing chip) ASIC [86], which has been developed within the collaboration and by the University of Heidelberg. A picture of a not fully wrapped endoscopic head prototype module is presented in figure 3.4. The prostate endoscopic PET head is mounted on a transrectal ultrasound

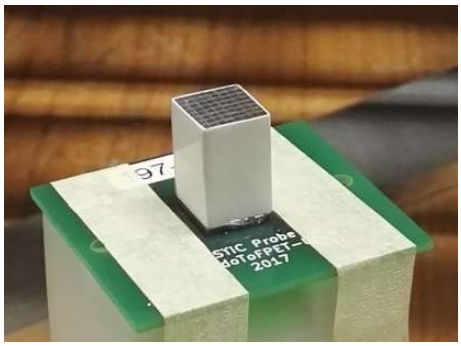

Figure 3.4: Picture of a not fully wrapped endoscopic head module.

endoscope. The proposed model is the EUP_U533 from Hitachi. It is a simultaneous biplane intracavity transducer with a frequency range of 4.5 MHz to 9.0 MHz. This frequency range yields high resolution in the near field and a high enough penetration depth if necessary. The field of view is 200 mm in the transverse plane times 64 mm longitudinal with an angle of view of 200° [87].

3.2.2 External PET Plate

The external plate detects the second photon arising from electron positron annihilation in coincidence with the endoscopic head. The detector plate covers an area of 23 × 23 cm^2 divided into 4096 single channels. It is made up of 256 modules, each consisting of 4 × 4 LYSO:Ce crystal arrays coupled to 4 × 4 Hamamatsu MPPC arrays (S12643-050CN). Each crystal has a size of 3.5 × 3.5 × 15 mm^3 and is

wrapped with 100 μm Vikuiti 3M^{TM} reflector foil. The single MPPCs have an active size of 3x3 mm^2, a pitch of 0.6 mm and 3600 single pixels of 50 x 50 μm size. The MPPC arrays are comprised of discrete SiPMs implicating that they have individual cathodes. This allows for a true differential readout of the SiPMs leading to less electronic crosstalk and, thus, to an overall better time resolution [88]. The SiPMs use through silicon vertical interconnect access technology that decreases the dead space and shortens the electric connection length compared to wire bonds. Furthermore, the external plate houses the analog front-end boards (FEB-As) and digital frontend boards (FEB-Ds). The FEB-As consist of two 64 channel ASICs and eight connectors for the detector modules. Such a design allows for easy replacement of broken modules. The connections within FEB-As (from SiPM output to ASIC input stage) are short in order to reduce electronic time jitter. Overall, 32 FEB-As are housed in the external plate. The FEB-Ds form the interface between the DAQ and the ASICs. They provide connections for: (1) bias voltage of the ASICs, (2) bias voltages of the SiPMs, (3) reference clocks, (4) control bus and (5) output links. In total, four FEB-Ds each holding eight FEB-As each are installed in the external plate. Moreover, the plate houses two water cooling plates, build out of aluminum, designed to dissipate heat from the analog and digital front-end boards.

All SiPM arrays used for the external plate have been characterized in a dedicated test setup [89–91]. Several parameters of the SiPMs such as DCR, breakdown voltage, correlated noise and their respective temperature dependence have been determined. The requirements on the SiPMs were defined as a DCR below 3 MHz per SiPM and a breakdown voltage difference below 500 mV within a single 4 x 4 SiPM array. A picture of the opened external plate is presented in figure 3.5.

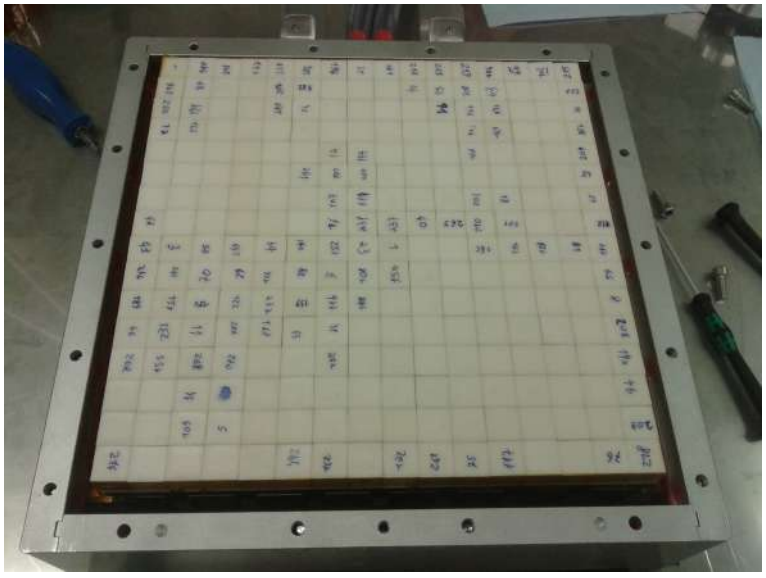

Figure 3.5: View into the open external plate. The individual modules are visible, each under a teflon cap.

3.2.3 Application-Specific Integrated Circuits

The requirements on the ASICs for this project are: (1) excellent time resolution of tens of picoseconds, (2) a linear input stage of 0.5 V and (3) a low power consumption. Two dedicated ASICs have been developed within the collaboration, namely the STiC ASIC and the TOFPET ASIC. Both are suited to

extract energy and time information from SiPM signals. The working principle of these two ASICs is explained in the following sections with a focus on the STiC ASIC because it was exclusively used in this work.

3.2.3.1 STiC

STiC is a mixed-mode 64 channel ASIC build in the 180 nm CMOS (complementary metal-oxide-semiconductor) technology with a size of 5 x 5 mm^2 and a power consumption of 25 mW per channel [86, 92–95]. It has a differential structure that allows differential or single ended connection of the SiPMs. Differential input reduces the influence of common mode noise of the digital part in the chip. Furthermore, STiC provides the option to tune the bias voltage to the SiPMs up to ∼800 mV per channel. STiC employs two thresholds, one for timing and one for energy measurement. The time and energy threshold produce a signal corresponding to the time over threshold (T-trigger and E-trigger). The timing threshold is set low, to a few photo electron level, while the energy threshold is set high, to a photon number equivalent to a few hundred keV. The energy is extracted via the time over threshold (ToT) approach. The two trigger signals are combined in a way that the leading edge of the low threshold and the falling edge of the high threshold get preserved. A schematic of the trigger scheme is presented in figure 3.6. The time of a hit is defined by the leading edge of the T-trigger. Energy is defined as the distance of the rising edge of the T-trigger and the falling edge of the E-Trigger. The timestamps are digitized by a built-in TDC with a bin size of 50 ps and a resolution of 20 ps sigma. A system employing two thresholds leads to a good time resolution (low threshold) and a dark count/noise reduction (high threshold). The digitized data is stored in an on chip first in first out (FIFO) buffer that is read out

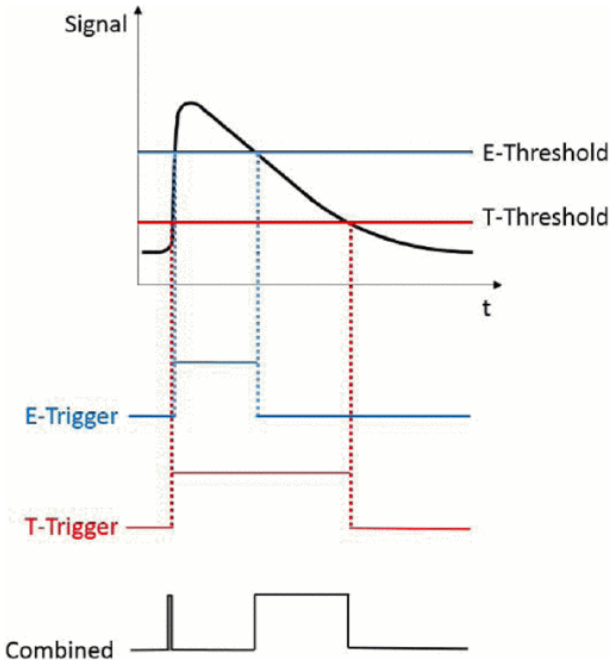

Figure 3.6: Threshold scheme and combination of the two thresholds. A single time threshold (red) and a single energy threshold (blue) are employed. They are combined such that the leading edge of the time trigger and the time over threshold of the energy trigger are preserved. Taken from [93].

every 6.5 μs via a 160 MBit/s LVDS link.

Since ToT is a highly non-linear method for determining energy, it yields poor energy resolution for large signals. As a consequence, a linearized ToT method has been implemented in STiC. If the signal is sufficiently high, it provides the complete bias current to the positive signal input stage of STiC so that no current flows through the input transistor. As a result, the input stage is turned off and the E-Trigger stays active during the discharge. Therefore, the ToT is the time it takes to discharge the SiPM with the constant current I_{bias}. This leads to a virtual integration of the signal on the SiPM capacitance. The linearized ToT response of STiC3 (third version of STiC) and a typical ToT spectrum of a ^{22}Na source acquired with the external plate are presented in figure 3.7. The time jitter of the analog frontend stage

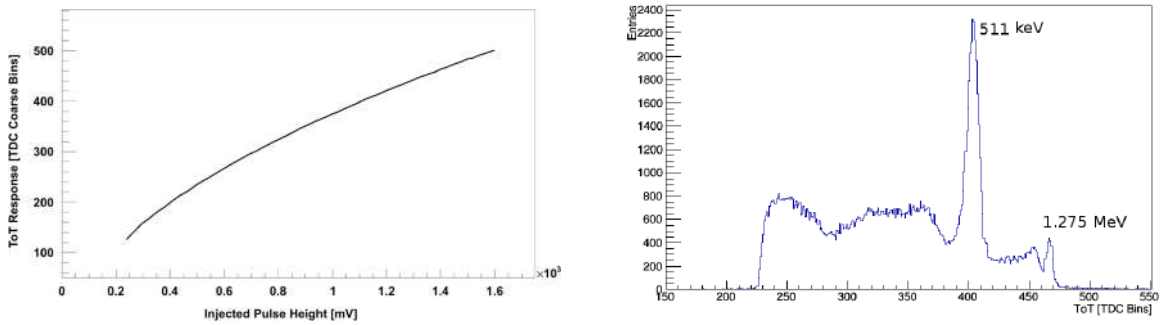

Figure 3.7: (left) Linearized time over threshold (ToT) of the third version of silicon photomultuplier timing chip (STiC3). Taken from [92]. (right) A typical ToT energy spectrum of a ^{22}Na source acquired with the external plate readout by STiC3.

was determined to be 35 ps for the equivalent charge of a single photo electron and only 18 ps for three photo electrons. The time jitter as a function of the input charge is presented in figure 3.8. The single

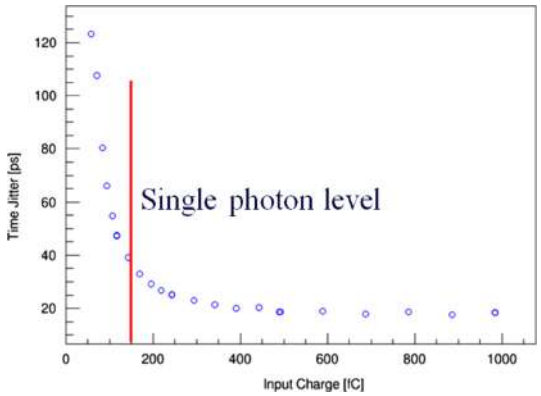

Figure 3.8: Time jitter of the analog front end stage of the silicon photomultiplier timing chip (STiC) as a function of input charge. Taken from [92].

photon time resolution of a Hamamastsu MPPC S13360-1350CS read out by STiC3 was demonstrated to be 158 ± 6.6 ps FWHM. A typical coincidence time spectrum of the external plate in coincidence with the endoscopic head prototype (both read out by STiC3) is presented in figure 3.9. The CTR defined as the FWHM of coincidence time spectrum is 250 ps.

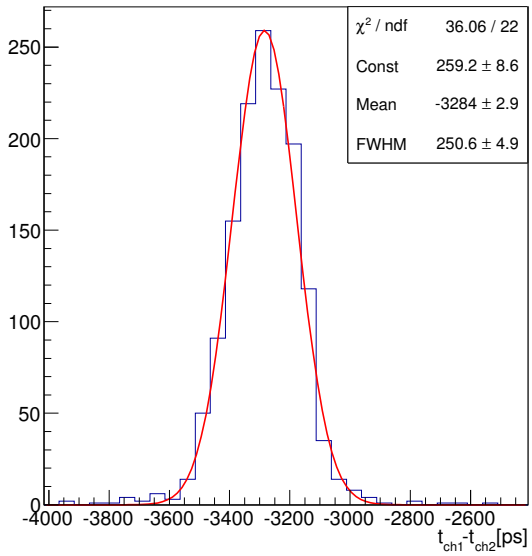

Figure 3.9: Typical coincidence time spectrum of the external plate in coincidence with the endoscopic head prototype. The coincidence time resolution (CTR) is defined as the full width half maximum (FWHM).

3.2.3.2 TOFPET ASIC

The TOFPET ASIC [96,97] is a 64 channel mixed mode ASIC build in the 110 nm CMOS technology. It is optimized to the readout of scintillators coupled to SiPMs. A rate of 600 kHz per channel with a dark count rejection rate of 2 MHz is achieved due to multi event buffering. It features an adjustable input impedance (10-60 Ω) and two separate trans-impedance amplifier branches each optimized for either time or energy measurements. The TOFPET ASIC employs a quad buffered analogue interpolation TDC with a time binning of 20 ps and a charge integration ADC that yields a linear response up to 1500 pC. The timing is determined by a single threshold and a time resolution of below 100 ps is achieved for the first photo-electron. It features a very low power consumption of ∼8 mW per channel.

3.2.4 DAQ and Software Environment

In the EndoTOFPET-US detector, two data streams from the the endoscopic head and the external plate are combined inside the DAQ. Event rates on the order of 40 MHz and 200 kHz are expected from the external plate and endoscopic head, respectively. The close proximity of the detectors to the patient leads to these high rates. An application-specific high-performance DAQ has been developed to control and readout the two detectors [98, 99]. A two-stage approach was chosen for the DAQ, combining field programmable gate array (FPGA) and software. A peripheral component interconnect express (PCIe) card that can be placed directly in the PC of the acquisition workstation is used in order to keep the whole system compact .

The complete schematic of the data processing path is presented in figure 3.10. The two data streams are send to the FPGA in order to merge the data. Afterwards data is preselected to define the coincidence events. The preselection can include an energy cut and a pairing of events in a coarse (12.5 ns) coincidence

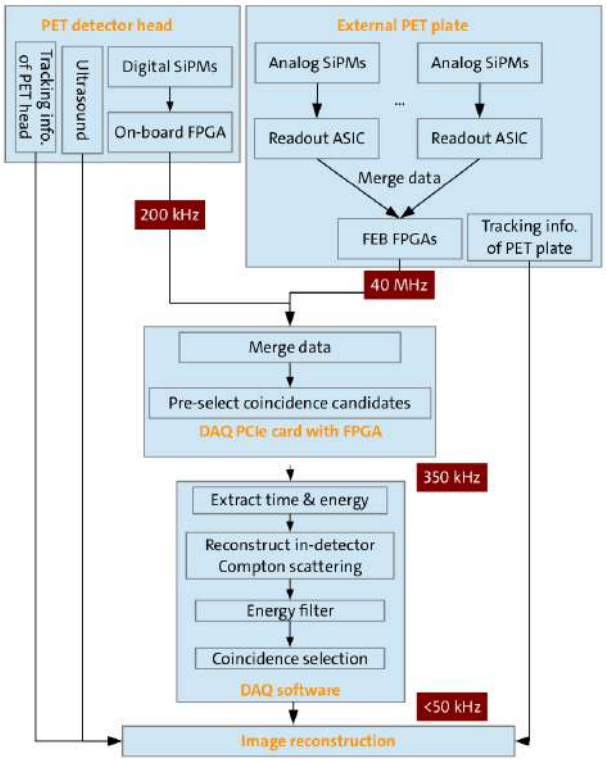

Figure 3.10: Schematic of the data processing path. Taken from [100].

window. The amount of data that needs to be further processed is considerably reduced to about 350 kHz. Later a dedicated analysis software utilizes the exact time and energy information to find coincidence pairs, reducing the amount of data further to below 50 kHz. The identified coincidences are directly send in listmode to the reconstruction software. The PCIe card distributes the 160 MHz clock synchronization signals and the signals that synchronize the position tracking and US system.

3.2.5 Slow Control and Tracking

A simple to use and open source communication framework for multimodal imaging (CAMPCom) has been developed within the project [101]. It controls the communication between the various devices that work simultaneously within the EndoTOFPET-US scanner. It allows for full monitoring of all processes, slow control and quality control, but is efficient, platform independent and easily extendable. It also provides a graphical interface (CAMPVis) for medical doctors to display the acquired images that can be used to display PET and US images.

3.2.5.1 Tracking in the Case of Prostate Imaging

The external plate and the transrectal probe can be moved during data acquisition. While movement of the transrectal probe is limited to rotation around one axis, the external plate can be freely moved around the patient. Knowledge of the exact detector positions is necessary to be able to reconstruct the PET images correctly. Therefore, an optical tracking system (Polaris optical tracking system from NDI) is utilized to monitor the location and rotation of the two detectors. The optical tracking works as follows: (1) Retro-reflective spheres are attached to the handle of the US endoscope and the external

plate. (2) These spheres reflect the infrared light emitted by the illuminator inside the position sensor of the tracking system. (3) The pattern of the reflected light is measured by two CCD (charge-coupled device) cameras with an accuracy of 0.5 mm and 0.5°. (4) The measured reflection can be translated to a position of the two detectors. A direct line of sight between the spheres and the optical tracking sensor is necessary for this kind of tracking. The medical doctor needs to get accustomed to working with the detector, especially during guided surgery.

3.2.5.2 Tracking in the Case of Pancreas Imaging

Tracking of the external plate is performed optically as described above. However, it is not be possible to use optical tracking for the pancreatic probe due to the flexible cable it is attached to. Therefore, electromagnetic tracking is planned for the pancreatic probe. New electromagnetic evaluation methods show promising results (i.e. to reach a tracking accuracy of below 1 mm) to make this approach feasible [102].

3.3 Performance Characterization

A performance characterization of all detector components (LYSO crystals, SiPMs and the ASICs) has been performed at the start of the project. For more information on this see [89, 90, 94, 103].

3.4 EndoTOFPET-US Image Reconstruction

A specialized image reconstruction algorithm has been developed for the EndoTOFPET-US project [104]. It is based on the ML-EM and incorporates the limited FOV and the freehand nature of the detector. Several reconstruction methods have been implemented and can be chosen from depending on the specific need. Standard listmode reconstruction handles the data on an event to event basis including TOF and depth of interaction (DOI) information and is widely used in PET imaging. But listmode reconstruction also discards LORs that do not contain any coincidences. Empty LORs can potentially improve the reconstructed image by restricting the activity distribution. A simplified example of how the empty LORs can contain the activity in a region is shown in figure 3.11. The custom reconstruction framework developed within the collaboration [104] runs on graphics processing units (GPUs) in order to provide realtime images.

3.4.1 Listmode Reconstruction and Ray Tracing

As stated above, listmode reconstruction is an event based approach. The position of the two detector crystals at the time of the coincidence is known for each coincidence from the tracking data. The position of the interaction inside the crystals is either calculated by a Gaussian quadrature in the center of the crystals (ray tracing) or is defined by four sample points in each crystal that form a total of 256 possible LORs (multi ray tracing). Multi ray tracing is more computational expensive, but also leads to smoother results of the reconstruction. The probability of absorbing the 511 keV photon in the crystal depends on the length of the LOR inside the crystal. The emission probability ($p_{emission} = \frac{l_v}{l_{tot}}$) per voxel depends on the length of the LOR through the specific voxel (l_v) divided by the total length of the LOR (l_{tot}).

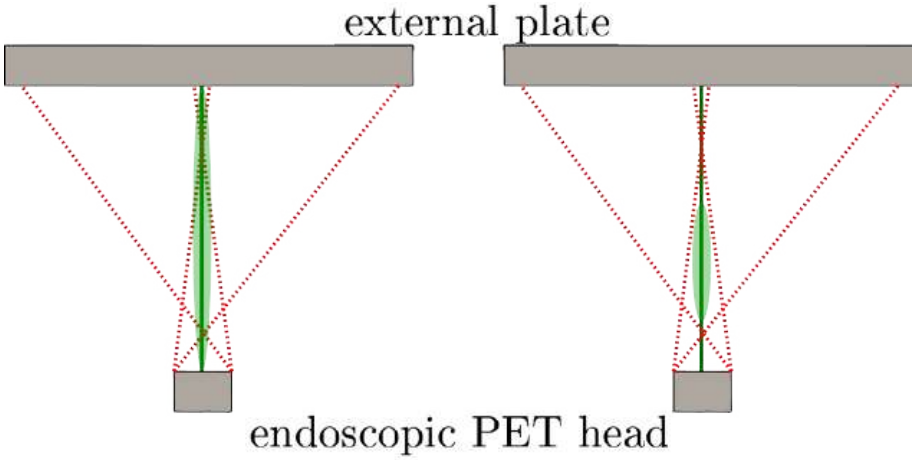

Figure 3.11: Representation of how empty LORs can contain the activity in the reconstruction. The LOR containing coincidences (green) and the LORs not containing coincidences (red) are presented. The green ellipse represents the region that can contain activity before (left) and after (right) the empty LORs information has been utilized.

Attenuation inside the patient/phantom can be implemented on a voxel basis

$$I = I_0 e^{-\sum_i \sigma_i l_{v,i}} \tag{3.1}$$

with $l_{v,i}$ being the length of the LOR in voxel i and σ_i being the attenuation coefficient of voxel i. The detection probability is

$$p_{det} = (1 - e^{-l\sigma_{tot}}) \frac{\sigma_{absorbed}}{\sigma_{tot}}. \tag{3.2}$$

The single elements of the system matrix representing the probability that a coincidence j originates from a voxel i is calculated by

$$A_{ij} = p_{emission} \cdot p_{detection,probe} \cdot p_{detection,plate} \tag{3.3}$$

with $p_{detection,probe}$ and $p_{detection,plate}$ being the probability to detect the 511 keV in the probe and external plate, respectively. TOF can be added to this equation by weighting the emission probability with a Gaussian distribution with the mean at the position defined by the time difference of the two hits and a FWHM defined as the CTR of the system leading to

$$A'_{ij} = A_{ij} \cdot w_{\mathrm{TOF}}. \tag{3.4}$$

with w_{TOF} being the TOF weight. The image is produced by backprojecting the system matrix over the FOV. The system matrix includes contributions from all coincidences.

3.4.2 Histogram Reconstruction

Histogram reconstruction treats the coincidences not individually but grouped depending on detector crystal pairs. The energy and time information of the single coincidences are lost. However, systems with low sensitivity and a limited FOV can gain from using histogram reconstruction. This is because the empty LORs can be used in histogram reconstruction, as sketched in figure 3.11. The calculation of

A_{ij} is analogous to equation 2.42. The ML-EM algorithm, as described in section 2.7.2.1, backprojects scalar values onto the FOV. A vector is backprojected if TOF is included into the algorithm. The vector includes the probability of emission as a function of the voxel, which depends on the detection time of both hits and the CTR. The distribution of coincidences on a single LOR is the sum of individual Gaussians originating from each single coincidence

$$y_{ij} = \sum_{e_j} G_j(i, e, \sigma_t) \tag{3.5}$$

with e_j being all coincidences on the LOR j and

$$G_j(i, e, \sigma) = \frac{1}{\sigma_t \sqrt{2\pi}} e^{-\left(\frac{dt_{ij} - dt_e}{\sqrt{2}\mathrm{CTR}}\right)^2} \tag{3.6}$$

where dt_{ij} is the TOF information of emission in voxel i along LOR j. The measurement y_{ij} and the forward projections y_{ij}^{sim} are vectors that contain the same amount of information. This is achieved by multiplying the line integral with a Gaussian smearing kernel depending on the time resolution of the system $[G(i, k, \mathrm{CTR})]$

$$y_{ij}^{sim} = \sum_k A_{kj} x_k^{(n)} G_j(i, k, \mathrm{CTR}). \tag{3.7}$$

Inserting this equation into the ML-EM algorithm results in

$$X_i^{(n+1)} = x_i^{(n)} \frac{1}{\sum_j A_{ij}} \sum_j A_{ij} \frac{\sum_e G_j(i, e, \sigma_t)}{\sum_k A_{kj} x_k^{(n)} G_j(i, e, \sigma_t)} \tag{3.8}$$

For the first boundary condition $\sigma_t \to \infty \to G_j(l, m, \infty) \equiv 1$, we gain the normal equation for the ML-EM without TOF is obtained. For the second boundary condition $\sigma_t \to 0 \to G_j(l, m, 0) = 1$ if $l = m$ and $G_j(l, m, 0) = 0$ if $l \neq m$, we gain

$$x_i^{(n+1)} = \frac{\sum_j y_{ij}}{\sum_j A_{ij}} \tag{3.9}$$

This equation looses its iterative character because with perfect CTR a simple backprojection already yields the correct image.

3.4.3 Freehand Reconstruction

The EndoTOFPET-US detector foresees to be freely movable during acquisition. This makes it necessary to track the detector positions at all times. The reconstruction software needs to take this into account. Continuous movement of the detector can lead to up to 10^8 possible unique LORs per second and, therefore, to a unreasonable computing time. A solution to this problem is to introduce a fixed grid of virtual detector pixels around the volume of interest (VOI) leading to virtual LORs. The virtual LORs can subsequently be remapped to the real LORs. There is a fixed number of detector position independent LORs available in the system [105]. There are essentially two options to build virtual LORs: (1) by mapping events to two virtual detector planes on each side of the VOI or (2) by mapping events to the surface of a sphere around the VOI. Both approaches are visualized in figure 3.12. Two pieces of information need to be saved: (1) the number of coincidences per virtual LOR and (2) the coincidence time between real and virtual LOR. The freehand nature leads to an inhomogeneous sensitivity that needs to be taken into account during reconstruction. It can be implemented in the reconstruction by

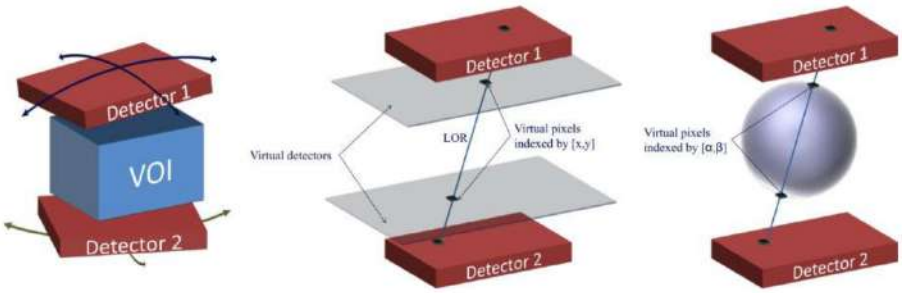

Figure 3.12: (left) Freehand movement of two individual detectors around the volume of interest (VOI). Two different approaches building virtual (line of responses) LORs are demonstrated to minimize the number of possible LORs: (center) implementing virtual detector planes in front of the two detectors or (right) mapping LORs to a point on the surface of a sphere where each point is defined by the Euler angles α and β. Taken from [90].

adding time weights to the rows of the system matrix. For the EndoTOFPET-US project, the sphere based approach was chosen since it is faster and allows for a higher amount of tracking data per time compared to the planar approach.

3.4.4 Implementation on Graphics Processing Units

The reconstruction software is written in C++ using Nvidia CUDA [106] capabilities in order to be able to run on GPUs. This has been done to meet the high computational requirements that come with computing a unique ratio of simulated and measured values for each combination of LOR and voxel. The TOF information of the single events is stored in a list, which is easily and quickly accessible, while the activity $x_i^{(n)}$ is stored in a texture (cached memory space specific to GPUs), which is also very fast to access and increases the speed of the reconstruction immensely. Only TOF and $x_i^{(n)}$ are stored, while everything else is calculated on the fly resulting in no bottle neck in memory management. Consequently, the reconstruction algorithm can run on a single PC.

Chapter 4

X-Ray Fluorescence Imaging

X-ray fluorescence imaging (XFI) is a widely used imaging modality with applications in environmental, forensic and biological studies. By scanning the sample with X-rays and measuring the energies of the resulting fluorescence photons, the material composition of the sample can be determined. Furthermore, there are several methods to determine the spatial distribution of the materials inside the sample (e.g. tomographic scans with focused X-ray beams).

4.1 Fluorescence

Fluorescence describes the process of the absorption of light that results in the emission of light at a material-specific wavelength. It was already observed in the seventeenth century, when the aqueous infusion of a certain kind of wood glowed blueish when shown upon by light. George Gabriel Stokes published a treatise on the subject [107] in 1852 and concluded from his observations that the emitting light must have a longer wavelength than the absorbed light (Stokes shift). Fabian Goppelsröder performed the first analysis utilizing fluorescence in 1867 and coined the term fluorescence analysis [108].

The absorption of the incident light can result in an excitation of an electron in the atom shell or can even cause the electron to escape the atom. In the first case, the relaxation of the electron to its original energy state, including non-radiative relaxations to intermediate energy states, generates the fluorescence light. This process was described by Aleksander Jablonski in 1933 [109] and can be illustrated by a so called Jablonski diagram as presented in figure 4.1. In the second case, the electron escapes the atom and the fluorescence light is generated by an electron from a higher shell that relaxes into the lower, now free, energy state. Hence, the fluorescence photon energies are in the range of electron binding energies in atoms, ranging from 13.6 eV (Hydrogen) up to 115.61 keV for the K $1s$ electron of uranium.

The absorption probability of the incident light is a strong function of photon energy and material type as explained in subsections 2.3.1 and 2.3.2. Which of the photon interactions triggers the energy transfer is irrelevant as long as enough energy is transferred to the electron to overcome the atomic binding energy.

The fluorescence yield is defined as [110]

$$Q = \frac{photons_{em}}{photons_{abs}} \tag{4.1}$$

with $photons_{em}$ being the number of emitted fluorescence photons and $photons_{abs}$ the number of absorbed

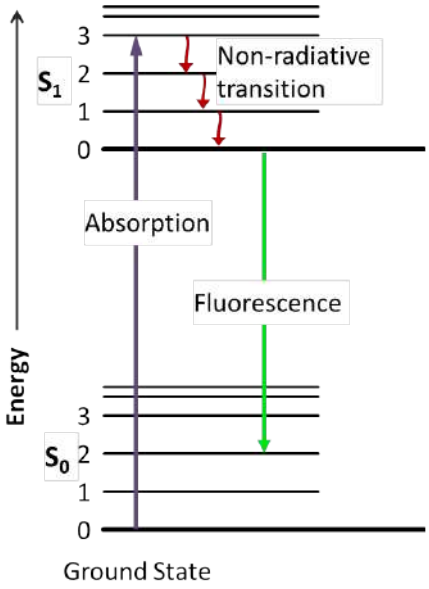

Figure 4.1: Jablonski diagram indicating the energy states traversed by an electron during fluorescence, including vibrational energy states. At first the electron is excited from the ground state (S_0-0 state) to an excited state. Afterwards several non-radiative transitions take place until an optical transition leads to the emission of a fluorescence photon.

photons. It can also be written in terms of radiative and non-radiative decay rate

$$Q = \frac{\Sigma}{\Sigma + k_{nr}} \tag{4.2}$$

with Σ being the radiative decay rate and k_{nr} the non-radiative decay rate. The rate of radiative decay can be approximated as

$$\Sigma \approx 2.88 \cdot 10^{-9} n^2 \frac{\int F(\nu) d\nu}{\int F(\nu) d\frac{\nu}{nu^3}} \int \frac{\epsilon(\nu)}{\nu} d\nu \tag{4.3}$$

with n being the refractive index, $F(\nu)$ the emission spectrum, $\epsilon(\nu)$ the absorption spectrum and ν the frequency.

4.2 Principle of Medical X-Ray Fluorescence Imaging

In case of XFI, the material under study is irradiated by an X-ray source and the resulting radiation is detected. The measured photons are composed of scattered photons from the X-ray beam and fluorescence photons of the illuminated sample as well as scattered fluorescence photons. The resulting spectrum exhibits element specific fluorescence energies allowing to deduce the contents of the material under study. Such an imaging technique can potentially also be used in medical applications, as proposed by [10]. Instead of the naturally occurring elements in the human body, the distribution of a tracer molecule or drug is imaged in case of medical imaging. In case of PET, a tracer is a functionalized, biologically active molecule with an active imaging component attached to it. In contrast to PET, the

attached active imaging component in case of XFI is not a radioactive isotope, but a heavy biocompatible atom or nanocluster of heavy biocompatible atoms For example, heavy metals such as gold can be used. As explained in section 2.6, the tracer can be a metabolic agent or a molecule only binding to specific receptors leading to accumulation in specific tissue types. Furthermore, XFI has the promising potential to investigate the distribution of diagnostic metal complexes or platinum containing anti cancer drugs in-vivo, especially with new ways to produce brilliant high energy focused X-ray beams on the horizon (i.e. laser wakefield accelerated Thomson sources). Heavy atoms are favored as active imaging component in case of human imaging because the fluorescence photon energy is higher than for lighter atoms. A higher energy increases the probability that the photon escapes the body without scattering, which is crucial for efficient fluorescence imaging. The fluorescence photon energy is not as crucial for imaging of smaller animals as for imaging of larger objects. Therefore, lighter atoms can be used.

In case of medical XFI, the origin of the fluorescence photons also needs to be determined. The imaging and reconstruction methods to achieve this are still under investigation. Especially the background from Compton scattered photons constitutes a challenge in this regard. There are huge efforts being made to understand and reduce that background. A software method to do so is proposed in [10]. Most of the proposed methods utilize a collimated X-ray source, with which the region of interest (ROI) is scanned. Scanning only the ROI has the advantage that dose is only applied to a limited area of the patient. This is a big upside compared to PET, in which the radioactive tracer molecule is distributed over and dose is applied to the whole body. Several imaging and reconstruction methods that use a collimated X-ray beam is introduced in chapter 9. A collimated X-ray source can be produced easily by collimating the beam of a commercial X-ray tube. However, conventional X-ray sources such as like X-ray tubes have a broad energy spectrum and a big opening angle, emerging from Bremsstrahlung of electrons in a high Z material. A sketch of a typical energy spectrum of an X-ray source is presented in figure 4.2 The

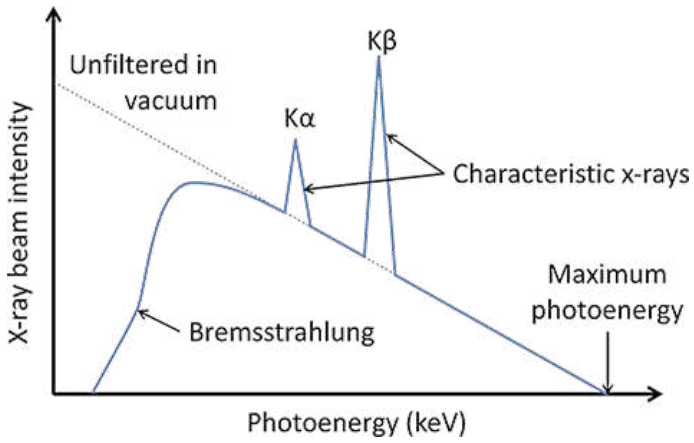

Figure 4.2: Sketch of a typical X-ray spectrum from an X-ray tube. The maximum photoenergy is defined by the acceleration voltage in the tube and the number of photons is defined by the tube current (i.e. the number of accelerated electrons per second). The spectrum without filtering is indicated by the dashed line. The K_α and K_β lines of the stopping material are also indicated. Taken from [111].

broad energy spectrum makes X-ray tubes inefficient for fluorescence stimulation because fluorescence probability is a strong function of incident photon absorption rate. The incident photon absorption rate, in turn, depends on the photon energy and the material, as indicated in figure 2.8. It can be seen that the most efficient absorption resulting in a vacancy occurs slightly above the energy of a bound electron

state. Thus, using an X-ray source with a narrow and adaptable energy spectrum allows to have optimal conversion of incident X-rays to fluorescence photons for varying emitter materials. An X-ray beam can be provided by a laser driven Thomson source, while it can still have a reasonable size when using laser plasma acceleration for the acceleration of the electrons [112, 113]. The fundamental functionality of an X-ray Thomson source is discussed in the following sections.

4.3 Thomson X-Ray Source

A Thomson X-ray source uses inverse Compton/Thomson scattering to transfer energy from relativistic electrons to optical photons. Acceleration of the electrons can be achieved with conventional methods (i.e. radiofrequency cavities) or via laser-wakefield acceleration (LWFA). For the latter, there are designs that use the same high energy laser for the acceleration and inverse Compton scattering. A sketch of a possible setup for a Thomson X-ray source is presented in figure 4.3. LWFA is a cheap and space-saving

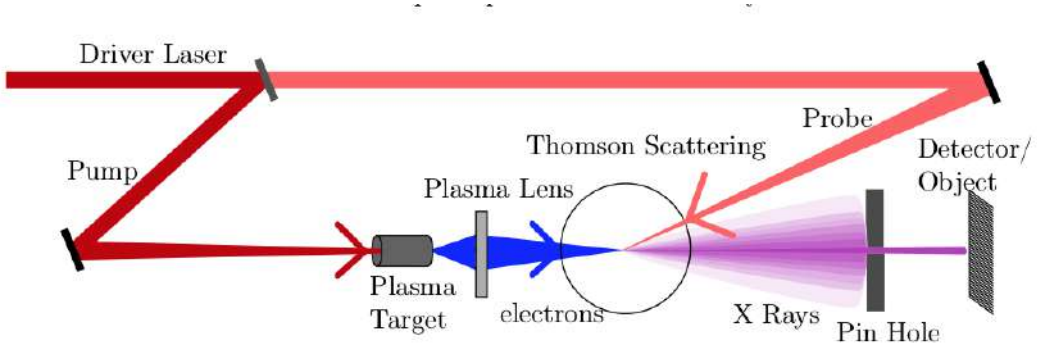

Figure 4.3: A sketch of a laser driven X-ray source combining laser-wakefield acceleration (LWFA) and Thomson scattering. Only a single laser, the driver laser, is used in the design. It is separated into pump and probe via a beam splitter. The pump is used to accelerate electrons in a plasma target. A plasma lens focuses the arising electron beam onto the interaction point with the focused probe laser beam. The emerging X-rays are filtered through a pin hole and then shone upon the measured object. Taken from [114].

alternative compared to conventional accelerator methods and, thus, is investigated and perfected by groups around the world. Typical energy spectrum of a Thomson X-ray source for varying parameters are presented in figure 4.4. An introduction to the theory of LWFA and Thomson scattering are presented in the next sections.

4.3.1 Laser-Wakefield Acceleration and Thomson Scattering

A plasma needs to be present in order to make LWFA work. It is a highly ionized gas, in which ions and electrons can move independently. There are several ways to ionize the gas before utilizing LWFA (e.g. discharge current or high intensity laser pulse). Once the gas is ionized, electrons can be accelerated by means of LWFA. A high intensity laser pulse can displace electrons in the ionized gas by means of the ponderomotive force, which is given by

$$F_p = -\frac{e}{4m_e\omega} \bigtriangledown E^2 \tag{4.4}$$

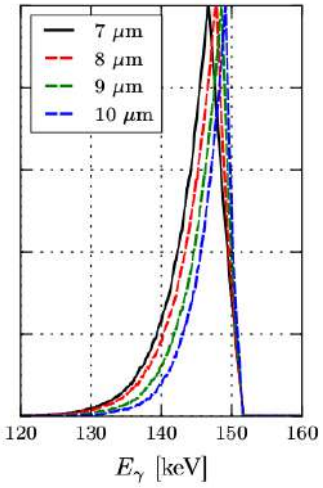

Figure 4.4: Thomson energy spectra within a cone of ±0.5 mrad. The laser duration is constant at $\tau = 4$ ps, while the laser waist is varied from 1 to 10 μm. These spectra are for a laser without chirp, meaning that the instantaneous light frequency does not depend on the time. Adapted from [114].

with m_e being the electron mass, e the electron charge, ω the laser frequency and $\bigtriangledown E^2$ the derivative of the electric field [115]. The ponderomotive force occurs only in non-uniform electric fields as can be deduced from the derivative. If an electron starts oscillation along a Gaussian shaped electric field of a laser pulse, it will be displaced by a stronger field as exposed to after the original displacement. Thus, it will not reach its original position after one full wavelength of the laser, leading to a net displacement unequal to zero. This force is only strong enough, however, to achieve a significant displacement of free electrons provided that a high-power laser with strong electric field variations is used. The force's effect on ions is negligible due to the high mass of ions compared to electrons. While electrons are pushed away from the high field region, ions are unaffected by the laser traversing the ionized gas. This leads to a strongly positively charged region located right behind the laser pulse that moves at the phase velocity of the laser. Electrons can be accelerated by the strong electric fields arising from to the high density of positively charged ions if placed into the accelerating/focusing phase of the wakefield. Electrons are placed in the accelerating phase by either internal injection [116–118] or external injection [119, 120]. Electrons from the plasma are used in internal injection, whereas a pre-accelerated electron bunch is injected into the accelerating phase in external injection. Wakefields on the order of 96 GV/m are achievable over small regions (proportional to the plasma period) in such accelerators leading to a large amount of acceleration over a small distance [121].

The accelerated electrons can be used to generate X-rays by means of Thomson scattering. Thomson scattering can be described in two different ways: (1) as inverse Compton scattering or (2) as undulator radiation. Inverse Compton scattering describes the particle view of the process during which a low energy photon (e.g. visible photon) scatters on a high energy electron. In contrast to Compton scattering, the electron transfers energy to the photon, leading to a hard X-ray beam of photons in the electron movement direction.

Classically, Thomson radiation can be compared to undulator radiation. An undulator is an arrangement of magnets with alternating field direction. If electrons traverse this magnetic field arrangement, they start oscillating and emitting radiation. The radiation characteristics depend on magnetic field

strength, periodicity and electron momentum. The emission wavelength of the n^{th} harmonic is [122]

$$\lambda = \frac{\lambda_u}{2n\gamma^2}(1 + \frac{K^2}{2} + \gamma^2\Theta^2) \tag{4.5}$$

with λ_u being the undulator period, γ the electron Lorentz boost, Θ the emission angle and K the undulator strength. The undulator strength is $K \propto B \cdot \lambda_u$ with B being magnetic field strength. If an electron beam meets a photon beam head on, the electromagnetic field of the photons functions as an undulator in which the electrons starts oscillating and emitting light. The emitted photons energy is

$$E = \frac{2\gamma^2[1 - \beta cos(\alpha)]E_L}{1 + \frac{a_0^2}{2} + \gamma^2\Theta^2} \tag{4.6}$$

with $\beta = \sqrt{1 - 1/\gamma^2}$, $E_L = hc/\lambda_L$ with Planck's constant h and speed of light c, α the collision angle, Θ the emission angle and a_0 the dimensionless laser strength parameter [123]. The laser strength parameter is defined as

$$a_0 = \frac{eE_0\lambda}{2\pi m_e c^2} \tag{4.7}$$

where E_0 is the laser field amplitude, λ the laser wavelength, m_e the electron mass and c the speed of light.

In contrast to conventional X-ray tubes, a laser plasma accelerator makes it possible to achieve a brilliant hard X-ray source. For further specifications and a design study of a laser driven Thomson source see [114].

Chapter 5

Simulation Tools

Simulations are an essential tool for detector development. Underlying anatomy and physiology might not be well known in patient scans. Further factors that might be unknown are: (1) statistical fluctuations, (2) attenuation and scattering in the patient/phantom, (3) artifacts of the detector (spatial resolution, dead time, noise), (4) patient motion, (5) reconstruction artifacts. It may be hard or even impossible to determine the effects on a reconstructed image during an experiment. In contrast, a controlled environment can be set up in simulations so that the influence of each contribution can be studied individually. By means of controlled simulations, an understanding of the detector response as well as the influence of the reconstruction algorithm can be studied. Such an approach allows for a guided optimization of the detector design, image reconstruction method as well as tests and implementation of new clinical imaging procedures [124, 125]. A detailed description of the utilized software tools and their specific application for the EndoTOFPET-US prototype is given in this chapter.

5.1 Geant4

Geant4 (geomatry and tracking) is a software toolkit used to simulate particles passing through matter [126–128]. It includes a considerable amount of utilities dedicated to enable highly individualized complex simulations of physics experiments: (1) to build complex detector geometries, (2) to model detector response, (3) graphics systems, (4) to transport particles through matter (tracking), (5) material specification, (6) to manage events and more. Upon interaction of a particle with the detector volume, a detector response can be modeled that is comparable to a real detector's response. Furthermore, Geant4 allows to specify allowed interactions, their cross sections, and decays of particles depending on simulation demand. The main structure of a Geant4 simulation and the terminology behind it will be explained in the following paragraphs.

The largest unit of simulation in Geant4 is a *Run*. A defined number of events is simulated while keeping the detector geometry, response modeling and setup as well as the physics processes (including cross sections) unchanged. *Events* are objects containing four major types of information and are created by the primary generator. They contain the primary vertex and particles, along with secondary particles and trajectories, and hits generated by the sensitive detector volumes.

There are seven major categories of physics processes defined in Geant4: (1) electromagnetic, (2)hadronic, (3) decay, (4) photolepton-hadron, (5) optical, (6) parametrization and (7) transportation. There is a big variety of *Physics Lists* that can be chosen from. A physics list defines the type of interactions that are

allowed and their respective energy dependent cross sections. A large amount of competing physics list exist for different energy ranges or handling processes with various amounts of precision depending on the need of the simulation. Furthermore, the highly customizable nature of Geant4 allows to design new interactions and physics processes as well as to assign them to any particle with a specific cross section. The precision of physics processes described in the physics list has implications on the simulation time resulting in a decision about a tradeoff between precision and expenditure of time. The interactions in the simulation are defined by two groups: (1) the step length, defined as the 4D (space, time) distance between two interactions and calculated from the interaction cross sections and (2) detailed information of the interaction itself including energy, directionality, position changes and the creation of secondary particles.

A *Step* is invoked every time an interaction takes place or a particle crosses the boarder between two volumes. It includes the 4D information of when and where the interaction took place along with the information of how much energy was deposited and time was spent during the interaction. *Tracks* hold the current information of a given particle (i.e. energy, momentum, position, mass, charge) and initial state (i.e. trackID, primary vertex). It is updated after each invocation of a step. Any single track exists until either the track leaves the boundaries of the simulated volume, the track reaches a kinetic energy of zero or the particle is absorbed. *Logical volumes* manage information on detector elements, which are build from specific solids and materials. They are independent of the physical position of the detector element. Physical volumes can be placed inside the logical volumes. Therefore, a logical volume is a defined hierarchy of volumes with defined relative positions. The single detector elements consist of a specified material that can be described by elements, isotopes and macroscopic properties. *Hits* can be created in the sensitive detector volume. A hit is always created if a step arises within a detector volume and is a snapshot of the physical interaction of the track inside the detector. It can include several pieces of information: (1) time and position of the step, (2) energy deposition, (3) momentum and energy of track. A digitization module can be defined for each detector modeling the detector response to approximate a real detector. This digitization step includes: (1) the simulation of an analogue to digital converter (ADC) and TDC, (2) a readout scheme, (3) generation of raw data, (4) trigger logics and (5) pile up.

5.2 GAMOS

GAMOS (Geant4-based architecture for medicine-oriented simulations) is a Monte Carlo simulation framework based on Geant4 toolkit [129–131]. It includes the main functionality of Geant4 and adds specific applications for several medical imaging modalities such as PET, SPECT and CT. GAMOS is based on the plug-in concept that allows the main program to run without predefined components and allows the user to define components in separate text files and to load these at runtime when needed.

5.2.1 Detector Geometry

The detector geometry is defined by volumes of a specified material. These volumes can be arranged into modules and submodules. By repeating and positioning these modules arbitrary detector geometries can be easily build. The detectors are subsequently placed in the world volume, which is defined in a separate file and filled with air.

5.2.1.1 EndoTOFPET-US prototype

A simplified version of the EndoTOFPET-US prototype as described in chapter 3 was recreated in the GAMOS framework. It only consists of the scintillator crystals excluding the SiPMs, the readout electronics and the support structure. The effects of photodetectors and readout electronics are considered in the detector digitization. The smallest building block of the external PET plate is a 3.5 x 3.5 x 15 mm^3 LYSO crystal. This crystal is arranged in submodules of 4 x 4 with a crystal pitch of 3.6 mm taking into account the Vikuti reflector foil. Modules are organized out of 2 x 2 arrays of submodules with a 0.4 mm gap between the single submodules. These modules are repeatedly placed until they form the full external plate with its 4096 channels arranged in a square of approximately 23 x 23 cm^2. The endoscopic head prototype is recreated in the GAMOS framework as described in section 3.2.1. It consists of 1.13 x 1.13 x 15 mm^3 LYSO crystals that are arranged in a 8 x 8 matrix with a pitch of 1.2 mm taking into account the 0.7 mm thick reflector foil they are wrapped in. A visualization of the two detectors is presented in figure 5.1. It represents a view along the z axis onto the two detectors, as seen from the endoscopic head prototype towards the external plate.

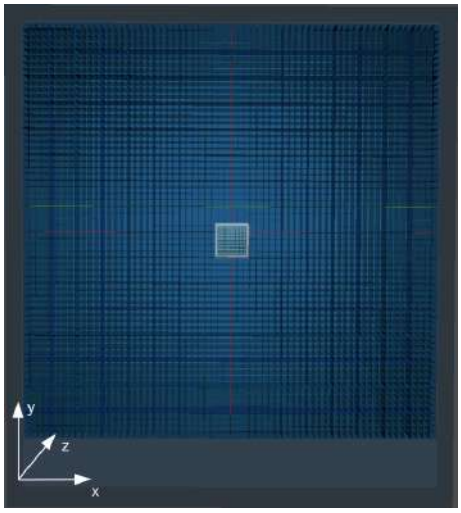

Figure 5.1: Visualization of the EndoTOFPET-US prototype simulation, as seen from the endoscopic head prototype towards the external plate. The scintillator crystals of the endoscopic prototype are light blue and the crystals of the external plate are dark blue.

5.2.1.2 X-Ray Fluorescence Imaging

In the case of XFI, a few detector geometries were set up and tested. All of them take into account that a collimated X-ray beam needs to be scanned over the ROI. If a high brilliance photon source such as a laser driven Thomson source is used, it is easier to move the phantom than the X-ray beam. Thus, two openings will be needed in the detector design, one for the X-ray beam to enter and one for the machinery moving the phantom. A representation of two possible detector design is presented in figure 5.2. The detector setup that was chosen for the studies is a ring detector with a diameter of 20 cm. The pixel size is defined according to the simulation.

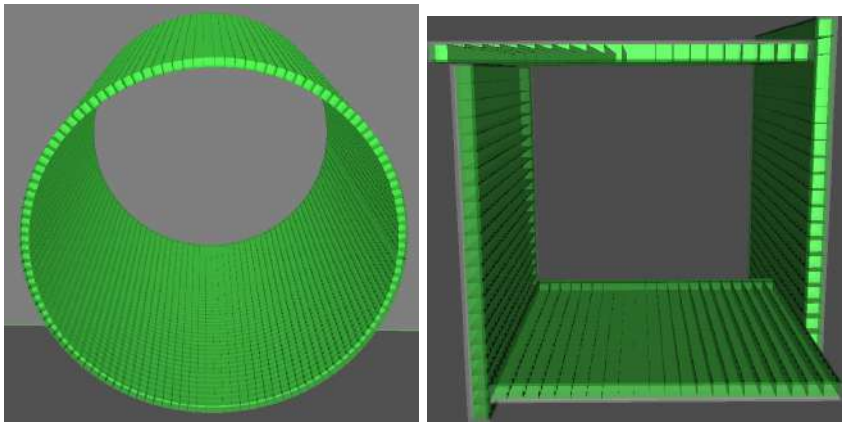

Figure 5.2: Visualization of the simulated detector used for the X-ray fluorescence imaging studies. (left) Ring detector, as often used in PET and (right) a design that involves four overlapping plates.

5.2.2 Volume Movement

Movement and rotation of either the detector or the phantom during a run can be easily implemented. GAMOS allows to displace and/or rotate any volume, either after a certain time has elapsed or after a certain number of events has been processed. The time that passed in the simulation world is checked after each event. Hence, the specified time interval will only be approximated. Four things need to be defined for each movement: (1) a volume, (2) an axis along which to displace/around which to rotate, (3) the displacement/rotation angle and (4) the time interval or number of events after which the movement shall take place. A delay for each movement can be defined either by a time interval or the number of events. The movement commands can be repeated indefinitely whereby arbitrary movements of phantom and detector can be performed.

5.2.3 Simulation Walkthrough

A simulation walkthrough for the two imagin scenarios is presented in the following two sections.

5.2.3.1 EndoTOFPET-US

Back-to-back pairs of 511 keV photons or positron emission and subsequent thermalization and electron-positron-annihilation can be simulated depending on the simulation needs. In case of simulating positron emission, a probability density function modeling the positron energy after emission can be implemented for each isotope. Photon non-collinearity due to residuum momentum of the positron-electron-system is also implemented. In case of simulating back-to-back photon pairs, the positron range and non-collinearity are neglected. This leads to slightly improved images compared to real measurements, but also allows for a faster simulation. Furthermore, for both cases an activity and half life can be specified to imitate the time structure of events in real measurements. Simulating the positron path through the phantom is computationally expensive because of the large amount of interactions that take place. Therefore, it is decided on a case to case basis whether the positron emission is included in the simulation or not. The physics list used is the GmEMPhysics provided in GAMOS. It is the basic electromagnetic physics list and instantiates the most common processes for gammas, electrons, positrons and optical photons. It utilizes models based on Livermore data for low energy gamma and electrons, whereas it uses standard

models for positrons.

If a particle deposits energy in a LYSO crystal (the sensitive detector volume), a hit including the time and the energy is created at the center of volume. The processes following the energy transfer to the scintillator, such as ionization and scintillation do not yield further information but cost a lot of time. Thus, the scintillation process is not simulated. Further processes such as atomic de-excitation, fluorescence and Auger effect can be switched on and off depending on the needs of the simulation study. If multiple energy depositions of a single track occur within one detector volume they are merged to a single hit. Hits are converted to reconstructed hits that take into account the detector digitization. The digitization includes the single time resolution (STR) of the detectors. The STR is always assumed to be the same for the external plate and the endoscopic head. This assumption is valid because the smearing of the events only depends on the overall CTR ($\mathrm{CTR} = \sqrt{\mathrm{STR}_{plate}^2 + \mathrm{STR}_{endo}^2}$) and does not depend on the STRs. The time of each hit is smeared according to the STRs. Furthermore, an energy resolution is applied, smearing the energy of the hit accordingly. The energy resolution is set to 13% at 511 keV. The dead time of the single pixels is set to zero. If two hits occur within 500 ns of each other they will be merged. GAMOS directly identifies coincidences and writes them into an output file. A coincidence time window and an energy window can be defined for the coincidence search. They are defined depending on the simulation's needs. A standard value for the coincidence time window is one nanosecond and a typical energy range is from 300 keV to 600 keV. If more than two hits occur within the coincidence time window, the two closer to an energy of 511 keV are chosen and the third one is discarded. The coincidence output file contains the ID of the two crystals involved, energy of both hits, time of the first event and the time difference of the two events.

5.2.3.2 X-Ray Fluorescence

The same GmEmPhysics list as introduced above was used for the simulation of the X-ray fluorescence detector. An X-ray pencil beam is simulated for the XFI simulations. The origin of the photons can be defined as a position or area in the world volume. Several options for size, divergence, energy spectrum and structure of the beam are available. The beam was defined as a cone with a radius of 0.5 mm and a divergence of 1 mrad. The energy spectrum of a Thomson source is approximated by a Gaussian with a standard deviation of $\sigma = 0.03 * E_\gamma$, where E_γ is the mean photon energy. The X-ray energies used in this work range from 100 keV to 190 keV. The temporal length of the X-ray beam is zero in all simulations. Only very simple phantoms are used because in this work only a proof of concept study is performed. The phantoms is specified in chapter 9. The energy and time resolution of the detector are implemented depending on the detector material and are also specified in chapter 9. The dead time and measurement time of the detectors are set to zero in the simulations. This is done because it is necessary to achieve the highest possible sensitivity of the imaging system in order to be able to reconstruct small tracer densities. These settings are justified with the assumption that the number of photons per X-ray shot can be tuned in such a way that almost no photons are lost due to dead time or measurement time. Throughout the simulations, the detector and X-ray source position are unchanged and all movements necessary for the imaging procedures are performed on the phantom.

Chapter 6

Commissioning of an EndoTOFPET-US Prototype

The commissioning of a prototype was once performed and first data were acquired in a more premature state of the development. The results of this first commissioning and data taking with an EndoTOFPET-US prototype are presented in [89, 90]. A more complete commissioning of the detector, closer to a final version, is planed and performed in this work. Two versions of the external plate exist, one using the STiC ASIC developed by the University of Heidelberg and one using the TOFPET ASIC developed by the University of Lisbon. The external plate using the STiC ASIC is used exclusively in this work. The setup used for the present work includes the external plate connected to a rack, which holds the cooling unit, the power supply unit and the computer communicating to the external plate via a dedicated data acquisition card (FPGA logic). The commissioning of an EndoTOFPET-US prototype is presented in this chapter, including: (1) maintenance and calibration of the external plate, (2) implementation of slow control, (3) realization of improved cooling, (4) CTR optimization of each single detector pixel and (5) assembly of an endoscopic head prototype.

6.1 Maintenance, System Calibration and Slow Control

The assembly of the external plate and a provisional endoscopic probe (consisting of two modules from the external plate) was performed during the first commissioning phase of the detector. The work presented here takes up the work performed in [89, 90].

6.1.1 Maintenance

At first check ups on the system were performed. FEB-Ds were tested in regard to: (1) communication with the PC and (2) power supply to the ASICs and SiPMs. One of the four FEB-Ds needed to be replaced due to communication issues with the PC. Another FEB-D required replacement of one of its low-dropout regulators. ASIC performance was tested in regard to: (1) communication with PC, (2) TDC function and (3) SiPM readout. The communication with the PC was easily tested by configuring the ASICs and checking whether the same configuration can be read back. For verification of TDC function and SiPM readout, automated procedures were implemented that also function as a system calibration. The first system calibration procedure synchronized the ASICs to an external clock provided by the

FEB-Ds. The second system calibration procedure used the radioactive background from the lutetium inside the scintillator crystals to perform a coarse energy calibration. ASICs that cannot be calibrated, which means that they do not lock their phase locked loop (PLL) or produce the energy spectrum of lutetium, were exchanged.

6.1.1.1 Phase Locked Loop Locking

TDCs in the STiC ASIC utilize a digital interpolation method based on the phase locked loop (PLL). They need to be locked a stable reference clock in order to prevent variations in the TDCs caused by power or temperature differences. The timebase unit of the STiC is presented in figure 6.1. Its main component is a voltage controlled oscillator (VCO) divided into 16 delay elements and are called fine counter. The time delay of each of those delay elements can be tuned by a reference voltage that is controlled by the PLL circuit. One coarse counter is equal to 32 fine counters. An automated PLL

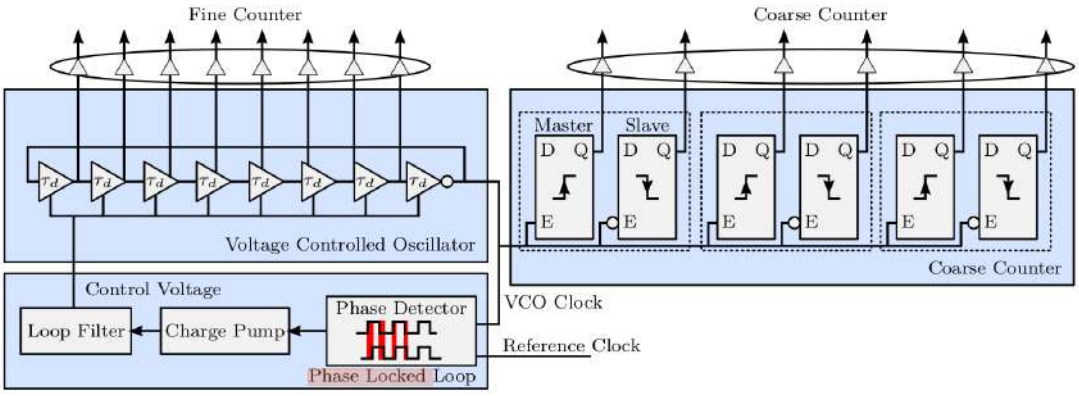

Figure 6.1: A schematic of the STiC timebase unit. It is composed of a fine counter build out off 16 voltage controlled oscillators, a coarse counter and a reference clock input. Taken from [94].

locking software was put in place and performed once for the whole plate. The external clock signal produced by the FEB-Ds is directly fed into the TDCs of each STiC. As mentioned in chapter 3, the energy of the photon absorbed in the scintillator is determined by the time difference between the rising edge of one signal to the rising edge of the next signal (with a coarse counter accuracy of 1.6 ns). Thus, the energy information represents the frequency of an incoming signal. The automated procedure checks the mean energy of one channel per TDC and compares it to the frequency of the reference signal. The PLL is designed to lock at a frequency of 625 MHz resulting in an average fine counter bin size of 50 ps and a coarse counter bin size of 1.6 ns. The reference signal from the FEB-D has a frequency of ∼152 kHz corresponding to a signal in the energy spectrum of $\frac{1}{152.6\ kHZ*1.6\ ns} \approx 4096$ provided that the PLL is locked. The reference voltage is tuned until the PLL is locked and the energy spectrum shows a single peak at 4096. The energy spectrum of a PLL locked channel and the mean of the energy spectrum for each TDC in the whole external plate and the endoscopic head prototype are presented in figure 6.2. After exchanging faulty ASICs, the whole external plate and the ASIC of the endoscopic head module were able to be locked.

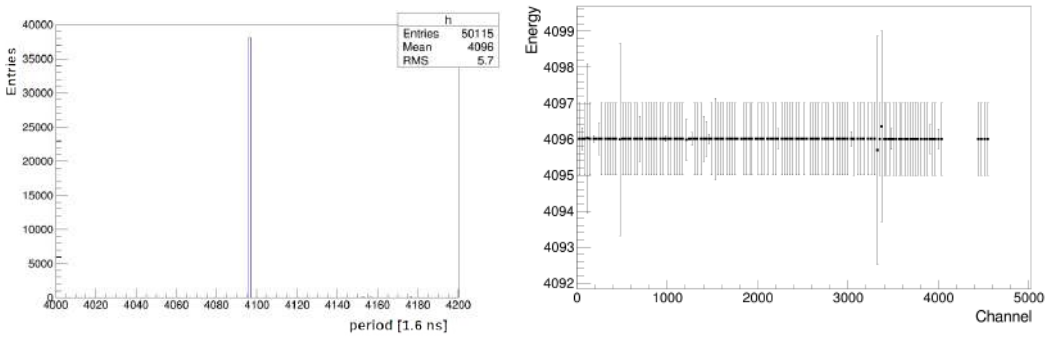

Figure 6.2: (left) Time difference between two events with a frequency of 152 kHz for a phase locked loop (PLL) locked channel represented in coarse counter bins of 1.6 ns. (right) Mean value of the PLL locked single channel spectra (as shown left) of one channel for each time-to-digital converter (TDC) for the whole external plate (everything below 4096 channel) and the endoscopic module.

6.1.1.2 Energy Calibration

A first coarse energy calibration of the plate was performed. This served to find malfunctioning ASICs and to get a feeling for the range of useful energy threshold settings. The radioactive decay of lutetium-176 (^{176}Lu) was utilized for this energy calibration. ^{176}Lu is a naturally occurring radioactive isotope and constitutes about 2.6 % of the lutetium on earth, leading to an activity of a few tens of Bq per crystal in the external plate. It decays mostly via β^- decay with subsequent gamma transmission at an energy of 307 keV and 202 keV, which occur almost simultaneously. The decay diagram of ^{176}Lu is depicted in figure 6.3. The energy threshold of each of the 4096 channels was adjusted during the calibration until the measured rate of events matched the expected rate originating from the ^{176}Lu background. The result of this coarse calibration is presented in figure 6.3. The number of events acquired per channel during a one-minute acquisition are presented in a two dimensional hit map and a histogram. A uniform response to the ^{176}Lu background was achieved over the whole plate.

6.1.2 Slow control

Slow control such as temperature measurements, control of the cooling and the power supply was implemented in the overall software package of the EndoTOFPET-US detector. While the latter two were implemented without any problems, the temperature measurement revealed an issue with the external plate's cooling system and power routing of the FEB-Ds.

6.1.3 Cooling of the External Plate

Each of the FEB-As in the external plate is equipped with a single temperature sensor that is positioned close to the SiPMs. This leads to a total of eight temperature sensors per FEB-D. One ancillary temperature sensor was added to one of the FEB-Ds of the external plate, placed in the position where the highest temperature is reached during operation. The position of highest operational temperature was located with a thermographic camera. The position of the temperature sensors on FEB-D and FEB-A are indicated in figure 6.4 Only three sensors per FEB-D were read out at a time due to lack of power along the connection of the temperature sensors. Two out of eight temperature sensors on the FEB-As and the one temperature sensor on the FEB-D were used. A first temperature measurement during which only one FEB-D is fully powered is presented in figure 6.5. It can be seen that the temperature on the

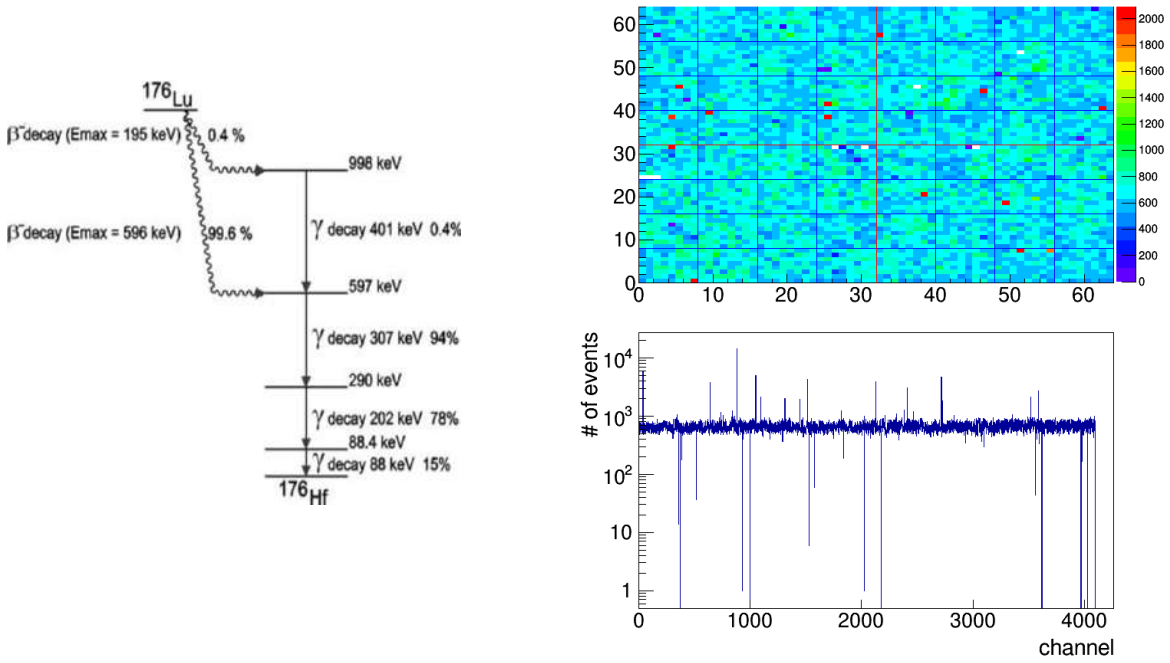

Figure 6.3: (left) Lutetium-176 (^{176}Lu) decay diagram. Taken from [132]. (right) Energy calibration of the external plate using the ^{176}Lu background of the LYSO crystals. (top right) Two dimensional hit map of the external plate indicating the number of events acquired during a one-minute acquisition. (bottom right) Histogram showing the number of events for each channel in the external plate acquired during a one-minute acquisition. Taken from [133].

FEB-D and the FEB-As reaches ∼54 °C and ∼25-27 °C, respectively. Furthermore, it can be seen that FEB-A1 is about two degrees warmer than FEB-A0. This can be explained by the proximity to the main heat source on FEB-D, i.e. FEB-A1 is closer to the heat source than FEB-A0. FEB-As positioned closer to the heat source are likely to reach an even higher temperature during operation as a result. These high temperatures are undesired because they increase the noise of the SiPM and, thus, reduce CTR of the system. Instead, the desired temperature of the SiPMs is 20 °C or lower. The temperature measured at the three different positions are presented in figure 6.6 for two ASICs and all 16 ASICs of a single FEB-D powered. Additionally, it shows the CTR of 16 channel pairs at the stable temperature that is reached with two and 16 ASICs powered. The 16 channels of FEB-A1 exhibit a temperature difference of 6 °C between the two states of operation (two or 16 ASICs powered). The temperature dependence of the breakdown voltage (V_{bd}) of the SiPMs installed in the external plate was determined as approximately 70 mV/°C by [90]. Therefore, increasing the bias voltage by 420 mV should compensate the increase in V_{bd} and lead to the same over voltage (V_{ov}). However, as evident from figure 6.6, the compensation of V_{ov} does not improve the reduced CTR at higher temperatures. This is due to the increased SiPM noise.

A solution to the cooling problem needed to be found in order to reach optimal performance of the EndoTOFPET-US prototype. In addition, ASIC damaging was observed during long temperature tests that might be caused by the high temperatures. The temperature inside the electronic components and the ASICs, however, is unknown. There are two possible reasons for the insufficient cooling: (1) the power consumption of STiC is too high or (2) a cooling vias to the cooling plate in the FEB-D is missing, leading to ineffective cooling through the PCB. Tests during which the external plate's back panel was

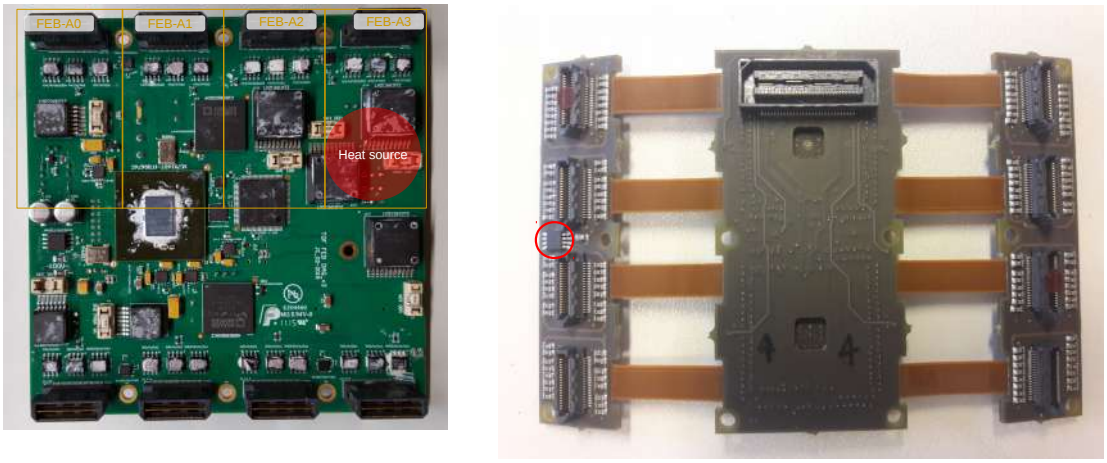

Figure 6.4: (left) A photo of a FEB-D, indicated are the positions of FEB-A0 until FEB-A4 and the location of the not sufficiently cooled heat source. (right) Photo of a FEB-A, indicated is the position of the temperature sensor close to a SiPM connector.

opened to allow additional cooling via air circulation showed no improvement. Hence, it is assumed that the heat travels directly through the electronics. A solution that did not require new FEB-D, ASIC or plate cooling design was found and tested. Components producing the most heat were identified and removed from the FEB-D. They were placed on dedicated PCBs with mechanical cooling structures and connected via cables through holes in the back of the external plate as presented in figure 6.7. Temperature measurements performed with the new cooling solution in place with all 64 ASICs of the external plate powered are presented in figure 6.7. A stable temperature of approximately 23°C is reached in the hottest FEB-A when all 64 ASICs of the external plate are powered. This is still not the desired temperature of 20°C, but close enough to not deteriorate the CTR or damage any electronics. The temperature of the parts that were air cooled outside the plate was measured with a digital infrared thermometer. They reach a maximum temperature of approximately 40°C (compared to the 55°C measured through a PCB).

6.2 Coincidence Time Resolution Optimization

CTR optimization is the final step in the commissioning of the external plate. It has a big influence on feasibility of PET detectors with limited FOV. Therefore, a lot of effort went into achieving the best possible CTR with the EndoTOFPET-US prototype. The influence of tunable parameters on the CTR was investigated and an automated online optimization method based on the Nelder-Mead algorithm was developed. It is necessary to optimize the settings for each of the 4096 channels of the external plate to achieve the best possible system wide CTR. An automated optimization procedure was developed to achieve this within a reasonable time frame. For the optimization only events within an energy cut of 1.5 σ around the 511 keV peak are considered for the coincidence time spectrum. A detailed explanation of the influence of tunable parameters on the CTR, the optimization setup and the developed online optimization is given in this section.

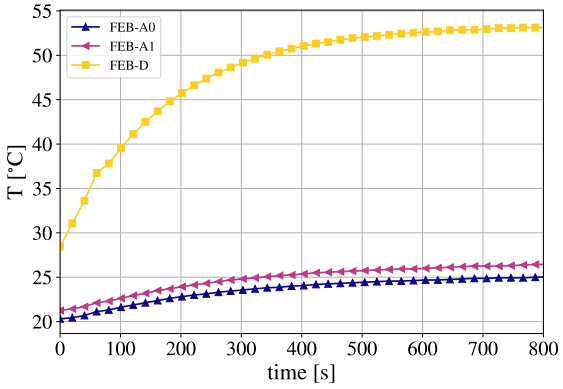

Figure 6.5: (left) Temperature as a function of time measured at the two FEB-As (analogue front-end board) and the FEB-D (digital front-end board). FEB-A0 is the FEB-A farthest away from the heat source on the FEB-D and FEB-A1 is the FEB-A on spot closer to the heat source on the FEB-D. 16 ASICs of the FEB-D are powered.

6.2.1 Tunable Parameter Influence on Coincidence Time Resolution

In preparation for the CTR optimization, the influence of tunable electronic parameters on the CTR was investigated. A dedicated setup was built at the University of Hamburg for this purpose. The small PET detector included two spare modules of the external plate and a so called evaluation kit (provided by University of Heidelberg) containing a STiC, digital processing of the STiC output and communication to a PC via USB. The modules were connected via cables to the evaluation kit, placed facing each other and containing a ^{22}Na between them. The whole setup was placed inside a light tight box. A schematic of the setup is presented in figure 6.8.

STiC has 27 tunable parameters per channel and 24 tunable parameters per TDC that influence: (1) TDC performance, (2) trigger levels, (3) input stage properties and more. These parameters were investigated in regard to their influence on the CTR of the detector system. Three tunable parameters were identified to have an influence on the CTR: (1) time trigger threshold level (t-threshold), (2) input impedance of the chip and (3) the SiPM bias voltage. The influence of SiPM bias voltage and t-threshold level on the CTR were already discussed in section 2.5. SiPM bias voltage shows the expected effect on CTR as presented in figure 6.9. CTR improves with rising bias voltage due to the increased PDE and corresponding reduced time jitter of the n^{th} detected photon. An additional increase of the bias voltage impairs the CTR because of increased noise (dark count rate, optical crosstalk and afterpulse probability) that leads to an increased time jitter of the n^{th} detected photon. T-threshold also shows the expected effect on CTR. A low t-threshold opens the possibility to trigger on noise (SiPM noise, electronic noise from the ASIC) and, thus, leads to low CTR. Increasing the t-threshold above noise level improves CTR. Further increasing the t-threshold can result in triggering on a photon that does not yield the best time resolution and, thus, can impair CTR. This behavior was observed with the miniaturized PET setup, as presented in figure 6.9. The t-threshold in STiC ranges between the single photon level up to approximately five/six photon level. STiC allows to adapt its input impedance. The input impedance of the ASIC needs to be matched to the SiPM impedance in order to achieve optimal coupling to the SiPM, as demonstrated in figure 6.9. It can be seen that an optimal input impedance of the ASIC can be found. Another parameter that is said to have an influence on the CTR is the current mode logic bias (CML). It effects the driver strength between input stage and TDC. In addition, it influences CTR

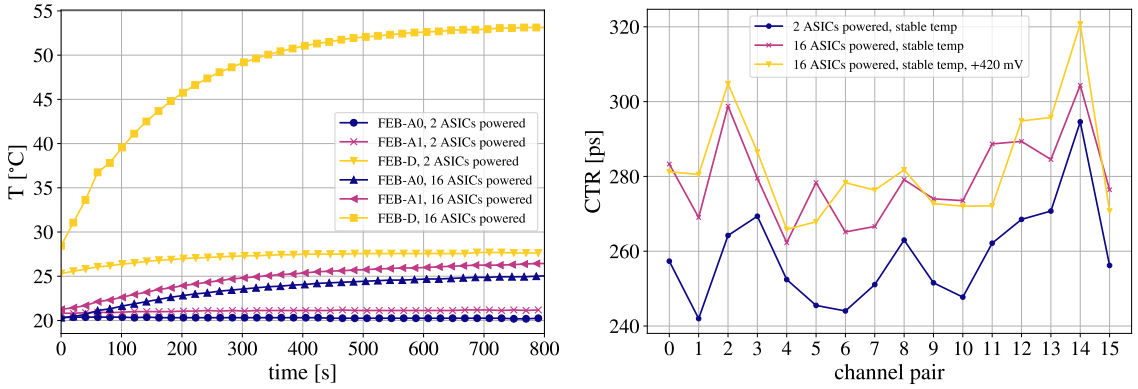

Figure 6.6: (left) Temperature as a function of time measured at the two FEB-As and the FEB-D with only two ASICs and all 16 ASICs of the FEB-D powered. (right) CTR of 16 channel pairs at the stable temperature reached with two ASICs powered and at the stable temperature reached with all 16 ASICs of one FEB-D powered. Additionally, CTR measurement was performed during which the breakdown voltage difference of approximately 420 mV for a temperature difference of 6°C was compensated. This measurement is indicated in the legend with +420 mV.

in condition that the system is not well optimized. An influence of CML on CTR, however, was not observed in the miniaturized PET setup.

6.2.2 Online Coincidence Time Resolution Optimization

Four parameters were considered for the optimization: (1) SiPM bias voltage, (2) t-threshold, (3) input impedance of the ASIC and (4) CML. These four parameters span over a parameter space of over eight million possibilities. The SiPM bias voltage can be regulated over a range of ∼800 mV through an adjustable voltage offset in the STiC input stage (64 DAC values). Figure 6.10 shows the voltage drop as a function of the digital-to-analogue converter (DAC) value for 16 channels. 800 mV was decided to be a big enough range for the SiPM bias voltage because the maximum difference in V_{bd} within a single SiPM array is 500 mV [90]. T-threshold ranges from triggering on the first photoelectron up to a few photoelectrons (64 DAC values) [94]. This varies slightly for each channel and as a function of bias voltage. The CML regulates the driver strength between input stage and TDC and influences the timing of the TDC triggering on the rising edge of the signal. The input impedance of the STiC input stage can be regulated via a DAC (32 DAC values), called DAC_input. In addition to changing the ASIC input impedance, DAC_input also has an influence on the t-threshold step size.

The parameter space can be reduced through experience to a total of approximately one million possible configurations for every single channel. If a 90-second measurement plus 10-second analysis per measurement is considered, a total scan of this parameter space for a single channel would take 142 days. An online CTR optimization was developed in order to increase the speed of the CTR optimization. It is based on the Nelder-Mead algorithm.

6.2.2.1 Nelder-Mead Algorithm

The Nelder-Mead algorithm is a numerical method that finds the minimum or maximum of a function in a multidimensional space [134]. It can be applied on complex functions where derivatives are unknown and, therefore, is highly versatile. It is also known to be quite stable as long as the statistical variations

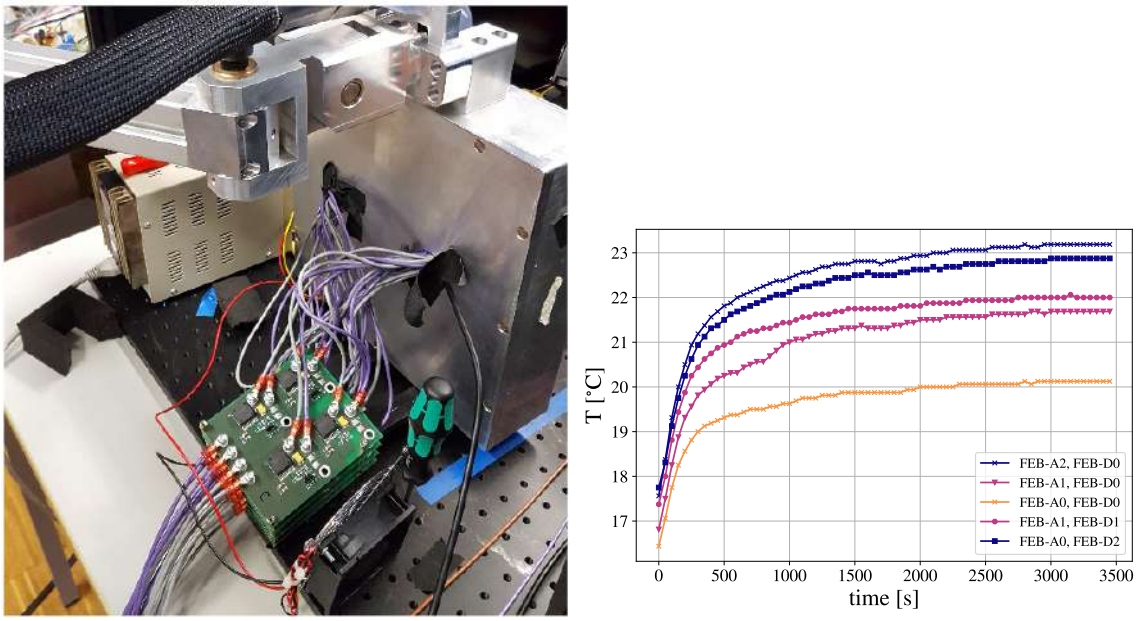

Figure 6.7: (left) The new external plate cooling solution. The hot components are positioned outside on newly designed printed circuit boards (PCBs) and cooled by air. They are connected to the digital front-end boards (FEB-Ds) via cables through a hole in the back of the external plate. (right) Temperature as a function of time for five temperature sensors with all 64 application specific integrated circuits (ASICs) of the external plate powered.

on the measurements are limited. The Nelder-Mead algorithm in the case of a two dimensional parameter space is explained in this section.

First, the starting parameters and step size for each dimension are defined. These define the first measurements of the algorithm. as demonstrated in figure 6.11 for two dimensions. A so called simplex is built out of the first $n+1$ measurements, with n the number of dimensions in the parameter space. The first measurement is defined by the starting parameters. The n next measurements are taken at the starting parameters plus the step size defined for the given parameter. After formation of the simplex, the decision making of the algorithm starts. The decision making process is depicted in figure 6.12.

C_i is defined as the CTR at a specific point P_i in the parameter space. C_H and C_L are defined as the highest and lowest CTR of the simplex, respectively. $\overline{P}$ is the centroid of all points of the simplex, where $i \neq H$. The Nelder-Mead algorithm replaces P_H with a new point P_i until a minimum is found or the algorithm is stopped externally. The three operations used for the replacement are: (1) reflection, (2) expansion and (3) extraction. P_H is reflected initially at the centroid $\overline{P}$, forming the new point

$$P_R = (1+\alpha)\overline{P} - \alpha P_H \tag{6.1}$$

where P_R is the newly found reflection point and α is the reflection coefficient that is defined by the user. If $C_H > C_R > C_L$, then P_R will replace P_H and the algorithm will start again with the newly formed simplex. If $C_R < C_L$, meaning that the reflection is the new minimum, an expansion to P_E will be made

$$P_E = \gamma P_R + (1-\gamma)\overline{P} \tag{6.2}$$

with the expansion coefficient $\gamma > 1$. If $C_E < C_L$, P_E will replace P_H and the process will start from

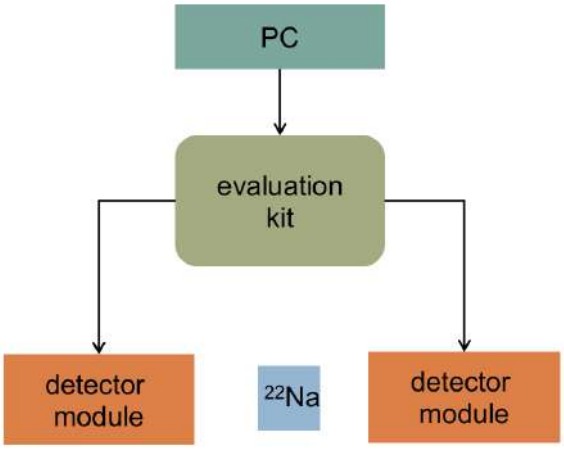

Figure 6.8: A sketch of the small PET setup. The evaluation kit holds a STiC ASIC and the DAQ. Two detector modules from the external plate are connected via a cable to the evaluation kit and a sodium-22 (^{22}Na) source is positioned between the two modules.

the beginning. But if $C_E > C_L$, P_R will replace P_H and the algorithm will start from the beginning. If $C_R > C_i$ for all $i \neq H$ and $C_R < C_H$, then P_H will be replaced by P_R and a contraction will be performed

$$P_C = \beta P_H + (1 - \beta)\overline{P} \tag{6.3}$$

with $0 < \beta < 1$ being the contraction coefficient. P_H will be replaced by P_C and the process will start from the beginning, unless $C_C > min(C_H, C_R)$. If the latter is the case, the whole simplex will shrink such that $P_i = (P_i + P_L)/2$ and the algorithm will start again. This process runs until it is stopped by either defining a maximum number of iterations or a minimum change of the CTR per step.

6.2.2.2 Setup

A schematic of the optimization setup is presented in figure 6.13. A spare module from the TOFPET external plate is used as coincidence detector for the STiC external plate. The spare module is attached to an x-y-moving stage and placed in front of the external plate in a distance of ≈3 cm. A 3D printed holder for the ^{22}Na point-like source is attached to the spare module that holds the radioactive source in a constant distance of 1.5 cm to the external plate and the spare module. The ^{22}Na source is a cylinder with height and radius of 1 mm and is encased in a delrin cylinder. Positioning the spare module directly in front of a module of the external plate leads to a uniform number of coincidences in all opposing channels.

6.2.2.3 Results

The CTR as a function of optimization iteration for a single channel pair is presented in figure 6.14. Four parameters were used for the optimization: (1) SiPM bias voltage, (2) t-threshold, (3) ASIC input impedance and (4) CML. A minimum CTR of ≈263 ps is achieved after 25 iterations. The single module used to detect coincidences with the external plate was optimized beforehand. It was tested whether the optimum configuration of one channel could be used to achieve good CTR within the whole module. In

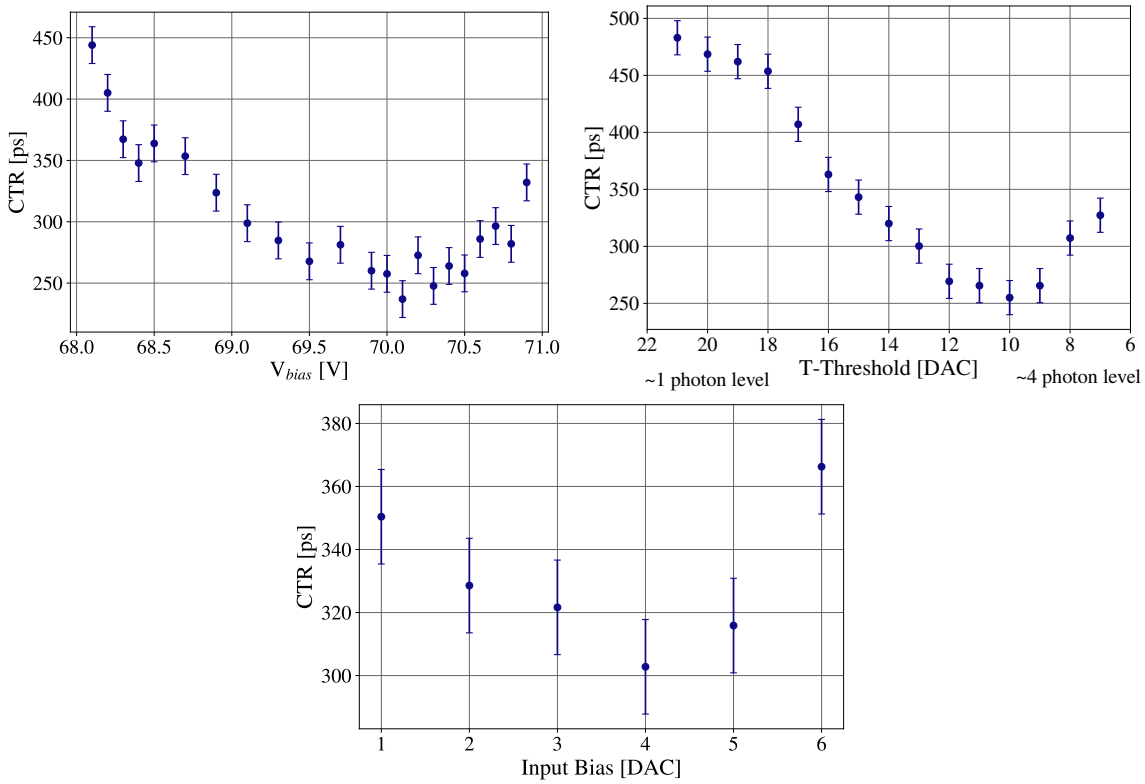

Figure 6.9: CTR as a function of SiPM bias voltage (top left), time threshold level (top right) and STiC input impedance (bottom). T-threshold and input impedance are presented in digital to analog converter (DAC) units. The t-threshold level reaches from approximately the first photon level to approximately the fourth photon level.

the first case, configuration of an optimized channel (one from channel pair 1, called channel 1) was copied to the 15 other channels in the same module and the CTR of each channel was measured. In the second case, the optimization software was used to find the optimum CTR of each channel. The comparison of these two cases is presented in figure 6.15. It can be seen that using the optimal configuration of channel 1 does not yield the best possible CTR with other channels. In case of using the optimum configuration of channel 1, two out of 16 channels do not function at all as a result of high noise and the mean CTR for the 14 channels is 279 ps. In case of using the optimum configuration of each channel as found by the optimization algorithm, all 16 channels work and the mean CTR is 262 ps. Hence, CTR optimization of each single channel is necessary.

By employing the Nelder-Mead algorithm with a maximum of 30 iterations on the four CTR optimization parameters, the optimization time is about 50 minutes per module and ∼3400 hours for the whole plate . The number of parameters can be reduced in order to further reduce the time necessary for the CTR optimization. The CML exhibits no influence on the CTR and the input impedance only influences the CTR in very few cases. The CML and input impedance were set to the mean configuration of the already optimized channels and removed from the optimization without impeding the time resolution. Figure 6.16 shows the CTR after optimization achieved with four and two parameters for ∼320 channels each. In contrast to a maximum of 30 algorithm iterations for the four optimization parameters, a maximum of ten algorithm iterations for the two optimization parameters were performed. It can be seen that

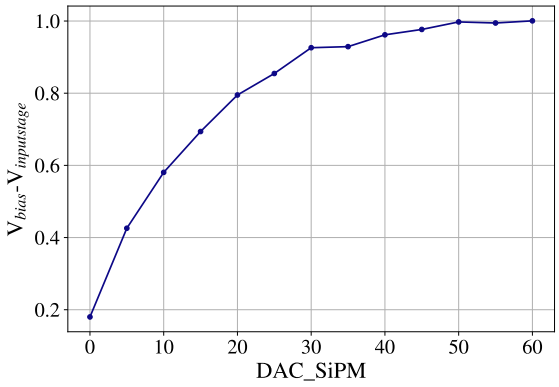

Figure 6.10: Bias voltage drop on the SiPM as a function of the DAC_SiPM value for a typical channel.

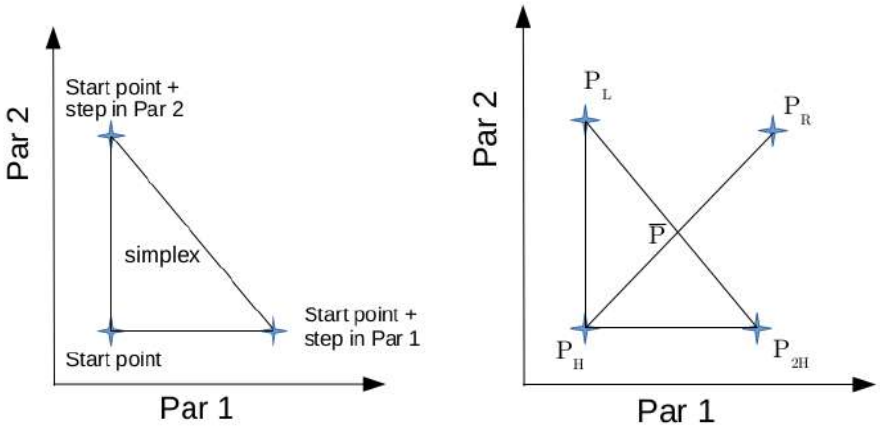

Figure 6.11: (left) First three measurements, performed for a two dimensional Nelder-Mead algorithm, forming the simplex. The first measurement is defined by the starting parameters. The next two measurements are defined by the starting parameters plus the step size for the two parameters. (right) The first step of the Nelder-Mead algorithm. The measurement points are assigned to the lowest (P_L), second highest (P_{2H}) and highest (P_H) function evaluation/measured coincidence time resolution (CTR). A reflection of P_H through the centroid of P_L and P_H is performed.

the overall performance of the CTR optimization is not impeded with two parameters. The optimization result is even slightly better for the sample of channels that is presented in figure 6.16. Therefore, the optimization is reduced to two parameters and ten iterations, which leads to an optimization time of 16 minutes per module and an overall optimization time of ∼71 hours for the whole plate.

The result of the CTR optimization is presented in figure 6.17. It depicts the minimum CTR achieved for each (working) channel of the external plate in coincidence with the spare module of the TOFPET external plate. A mean CTR of 253.7 ps is achieved for 3946 channels.

6.2.3 Energy Cut Influence on Coincidence Time Resolution

The time resolution of a PET detector depends on the number of photons created in the crystal. If one of the 511 keV photons loses energy inside the patient (e.g. by Compton scattering), the number of photons created in the scintillator is reduced. Using a narrow energy cut around the 511 keV peak for coincidence

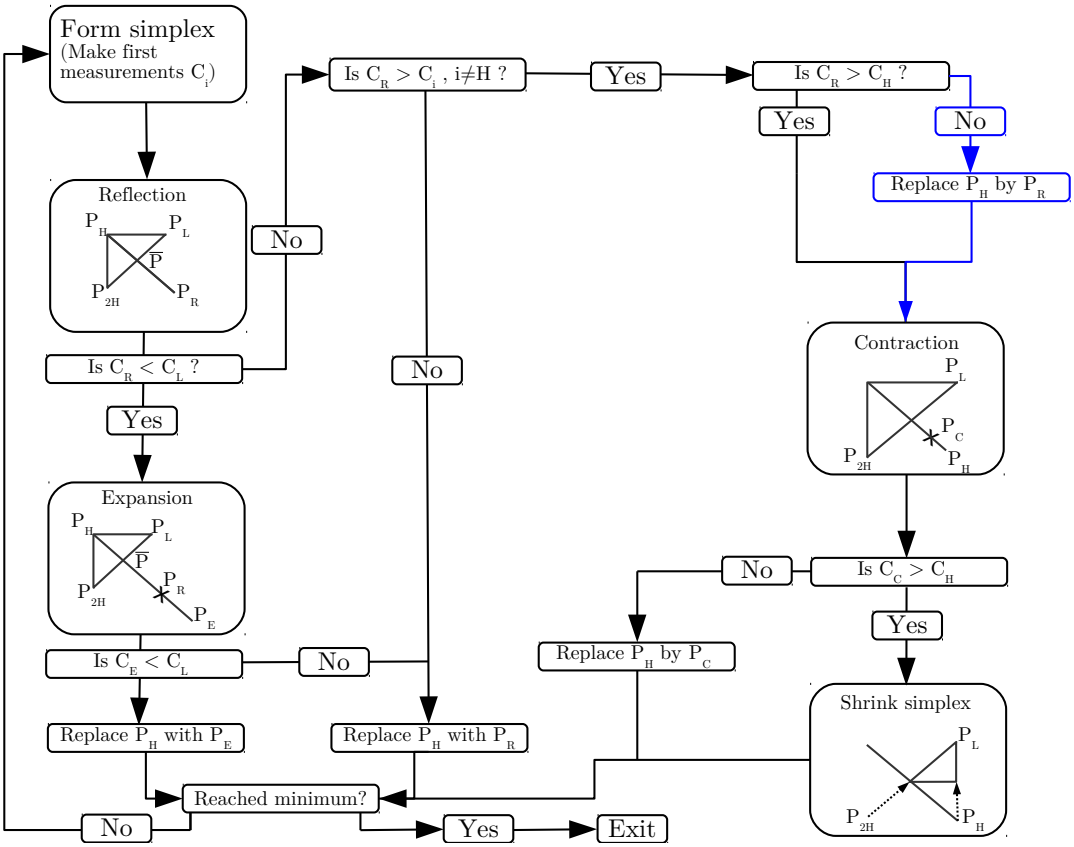

Figure 6.12: Visual representation of the Nelder-Mead-algorithms decision making process. P_L, P_{2H} and P_H are the points with the lowest (C_L), second highest (C_{2H}) and highest (C_H) evaluation of the function that shall be minimized. In this work, P_i is not a function evaluation, but a measurement of the CTR at the given point in the parameter space yielding C_i. The visual representation of the contraction and the shrinking of the simplex are in case of replacing P_H by P_R as indicated by the blue path.

selection leads to an improved CTR, but also to a decreased sensitivity of the detector. A tradeoff has to be made between CTR and sensitivity accordingly. The CTR as a function of the energy cut for coincidence selection was studied. The number of coincidences and the CTR as a function of energy cut are presented in figure 6.18. The energy cut is given in sigma of the 511 keV peak. It can be seen that increasing the energy window leads to an impaired CTR and an improved sensitivity of the detector.

6.2.4 Time Alignment

Time alignment is necessary in order to utilize the time information of the two 511 keV photons. The hit time of each photon is affected by: (1) electronic path length, (2) t-threshold, (3) SiPM bias voltage. Electronic path length adds a fixed delay to the hit time. T-threshold adds another offset and the SiPM bias voltage influences the PDE and, therefore, the signal generation, both of which add an offset to the hit time. The time alignment measures the offset for each channel. This is done by measuring the mean of the coincidence time spectrum for each channel combination, while having the external plate and coincidence module at a fixed distance and a point-like source located at the center between them. Using a point-like source ensures that all coincidences come from the same position. Knowing the length of all possible LORs and the position of the radioactive source along them allows to calculate the expected

Figure 6.13: A sketch of the optimization setup.

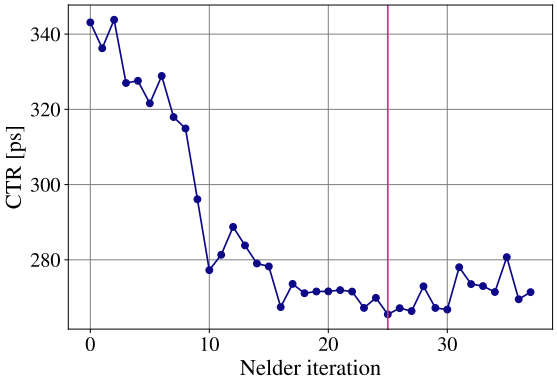

Figure 6.14: Coincidence time resolution (CTR) as a function of optimization iteration for a single channel pair. Four parameters were used for the optimization: (1) silicon photomultiplier (SiPM) bias voltage, (2) t-threshold, (3) ASIC input impedance and (4) current mode logic bias.

mean of the coincidence time spectrum. The difference between the expected mean and the measured mean is the correction value, which is unique for each channel combination. The time alignment was performed by determining the mean of the coincidence time spectrum of each channel combination from the external plate and coincidence module, while the point-like ^{22}Na source was positioned directly in the center between them. The summed coincidence time spectrum for a one-minute acquisition of the whole system before and after applying the time alignment correction is presented in figure 6.19. A system wide CTR of 255 ps FWHM is achieved after applying the time alignment correction.

6.2.5 Endoscopic Head Prototype

The final EndoTOFPET-US endoscopic head module was planned to utilize digital SiPM technology and a crystal size of 0.7 x 0.7 x 15 mm^3. This version of the endoscopic head, however, was not yet functional at the time of this thesis. An endoscopic head prototype was build accordingly. It consists of 64 LYSO crystals with a size of 1.13 x 1.13 x 15 mm^3 wrapped in 70 µm Vikuti reflector foil. The

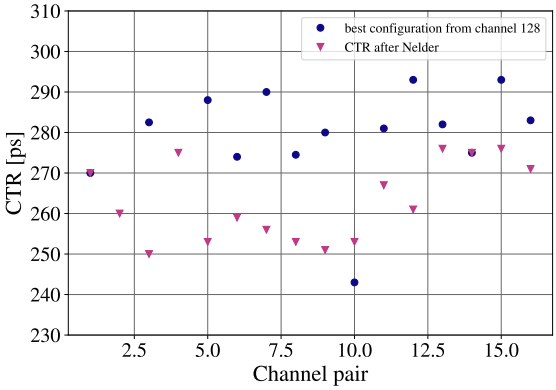

Figure 6.15: Comparison of the coincidence time resolution (CTR) reached with the 16 channels within a single module in case of using the optimum configuration of one channel from the module (blue) and in case of using the optimum configuration of each channel as found by the optimization algorithm (pink).

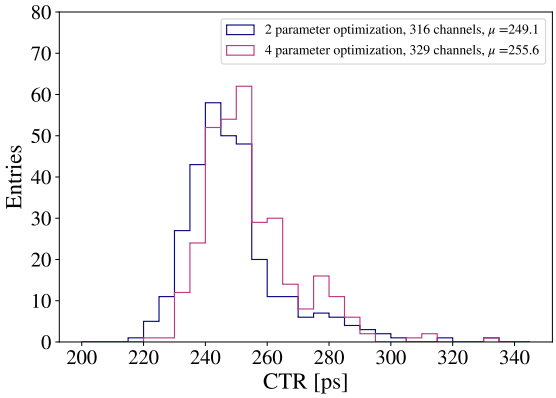

Figure 6.16: Mean coincidence time resolution (CTR) after optimization with four parameters (pink) and with two parameters (blue) for 329 and 316 channels, respectively.

crystals are glued to an 8 x 8 Hamamatsu MPPC array (S13615-1050 LCT) with 50 x 50 µm^2 SPAD size and 1.2 mm pitch. Sixtyfour channels were chosen for the endoscopic head prototype to be able to use a single STiC ASIC for the readout. This leads to an overall small size of the endoscopic head as well as an easy and quick implementation into the existing setup. A PCB was produced by the University of Heidelberg to connect the endoscopic head prototype module directly to a FEB-A. It is a simple fanout which distributes the 64 channel connections to four Samtec connectors on the FEB-A. After assembling the endoscopic head prototype module at CERN (Group of Etiennette Auffray Hillemanns), a first test was conducted measuring the energy spectrum of a ^{22}Na source. The signal from the SiPM was integrated by a modified CAEN educational kit digitizer. A photo of the endoscopic head, the energy spectrum of a ^{22}Na source acquired at CERN and the energy spectrum acquired with the EndoTOFPET-US readout chain are presented in figure 6.20. The difference between integrating the SiPM signal and using ToT in measuring the energy is clearly visible. ToT leads to a compression of the signal. It leads to a worse discrimination between 511 keV peak and the Compton background as well as makes it impossible to identify the 1.2 MeV peak. Nonetheless, the discrimination of the 511 keV peak from background is everything necessary for PET.

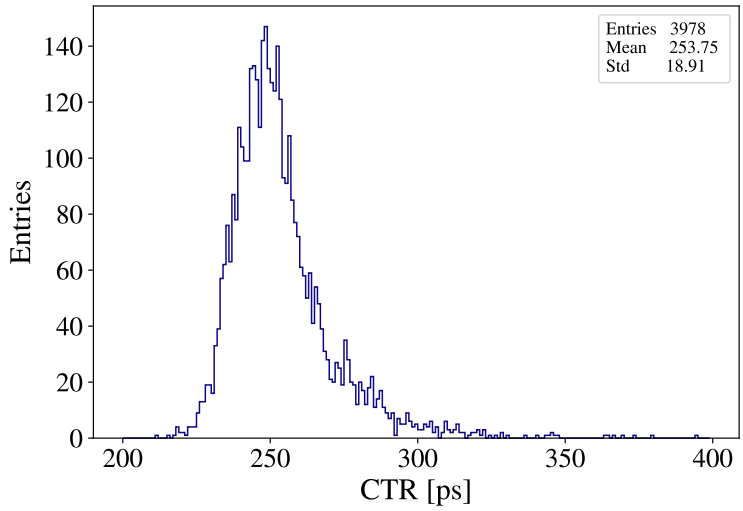

Figure 6.17: Results of the coincidence time resolution (CTR) optimization. Depicted is the minimum CTR achieved with each of the external plate's channels in coincidence with the spare module of the TOFPET external plate.

The CTR optimization of the endoscopic head prototype was performed in coincidence with an optimized module of the external plate utilizing the Nelder-Mead online optimization. The result of this optimization shows no degradation of CTR compared to the module that was used to optimize the CTR of the external plate. An example for a typical coincidence time spectrum is presented in figure 6.21. The mean CTR of the 64 channel endoscopic head prototype in coincidence with a single module from the external plate is 264 ps. In contrast, the mean CTR of the spare module that was used for CTR optimization in coincidence with a single module from the external plate is 265 ps. No degradation of the system CTR occurs by using the 64 channel endoscopic head prototype. However, it could have been naively assumed that the CTR of a new module consisting of new and improved crystals and SiPMs would yield a better time resolution. But the smaller crystals lead to more scattering on the crystal surface that, in turn, cause more photon losses. The worse energy resolution also leads to a degradation of time resolution, as shown in section 6.2.3.

6.3 Conclusion

The final commission of the external plate was performed. The cooling of the external plate was improved leading to a maximum temperature of 23°C inside the plate. A full calibration and CTR optimization of the external plate were performed. An endoscopic head prototype was constructed, it consists of 64 channels of 1.13 x 1.13 x 1.13 mm^3 in 70 µm thick reflector foil wrapped LYSO crystals glued to an 8 x 8 Hamamatsu MPPC array (S13615-1050 LCT) with 50 x 50 $µm^2$ SPAD size and 1.2 mm pitch. A system CTR of 255 ps was achieved after time alignment.

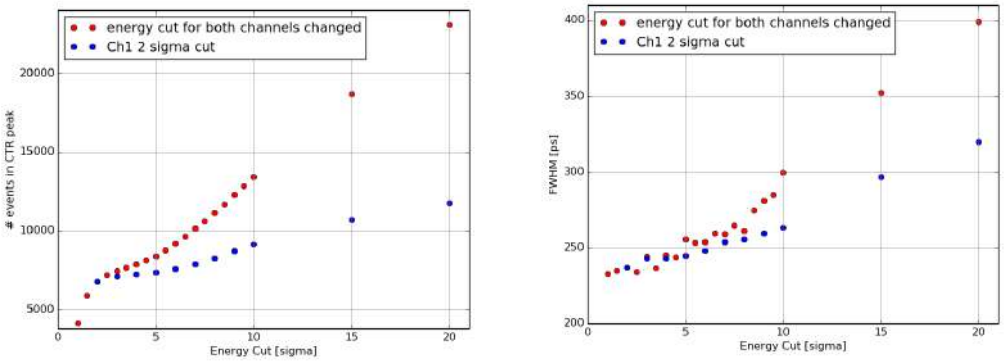

Figure 6.18: (left) Number of coincidences as a function of the applied energy cut. (right) Coincidence time resolution CTR as a function of the applied energy cut.

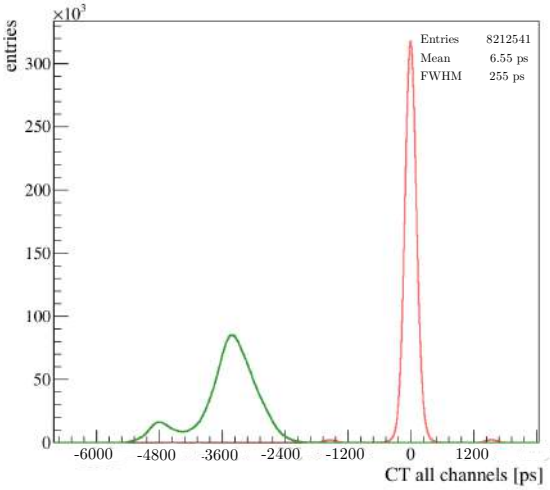

Figure 6.19: Coincidence time resolution (CTR) of all coincidences measured within one-minute acquisition time per matrix before (green) and after (orange) applying the time alignment. The number of entries of both distributions as well as the mean and $\mathrm{CTR}_{\mathrm{FWHM}}$ of the distribution after alignment are specified (Mean = 6.55 ps and $\mathrm{CTR}_{\mathrm{FWHM}}$ = 255 ps)

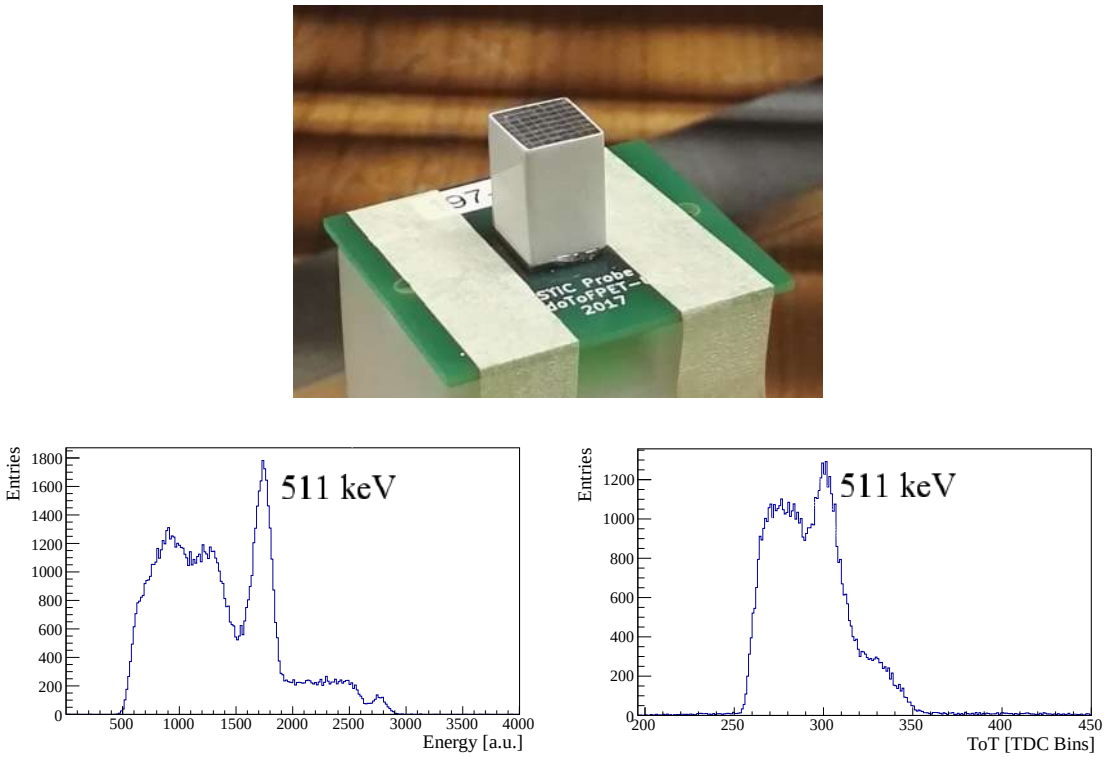

Figure 6.20: (top) Photo of the endoscopic head prototype module after its assembly. (bottom left) ^{22}Na energy spectra for a single channel of the new endoscopic head prototype module acquired at the CERN test stand. Energy is determined by integration of the SiPM current via a modified CAEN educational kit digitizer. Non-linearities originate only from the limited number of cells in the SiPM. The 511 keV peak and the 1.27 MeV peak can be clearly identified. (bottom right) Typical energy spectrum acquired with the endoscopic head prototype module acquired with the EndoTOFPET-US readout chain in units of TDC bins. The influence of the time-over-threshold (ToT) approach for energy determination is clearly visible as the spectrum is highly compressed, the 511 kEv peak is clearly visible and the 1.2 MeV peak is not.

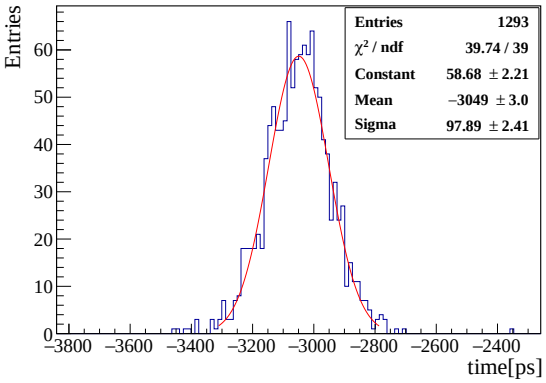

Figure 6.21: A typical coincidence time spectrum. A Gaussian fit is performed to extract the CTR. The CTR is $97.89 * 2.35 = 230$ ps FWHM.

Chapter 7

Data Acquisition and Reconstruction with a Fully Functional EndoTOFPET-US Prototype

After the commissioning, calibration and optimization of the EndoTOFPET-US prototype, first data were acquired at University Heidelberg and subsequently reconstructed using the EndoTOFPET-US reconstruction software.

7.1 Point-like Source Measurements

First data were taken with the fully equipped and calibrated EndoTOFPET-US prototype using a small ^{22}Na cylinder source, with height and diameter of 1 mm. The external plate and the endoscopic head prototype were placed facing each other in a distance of either 20 cm or 30 cm, while the radioactive source was placed in either 1 cm or 2 cm distance to the endoscopic head prototype. These setups were chosen to imitate the application of the EndoTOFEPT-US detector, where the endoscopic head is close to the lesion and the external plate is constrained by the patient's body. A photo of the setup and a schematic are presented in figure 7.1. The ^{22}Na source has an activity of $\sim$150 kBq and the acquisition time is 20 minutes for all configurations. The data were converted after acquisition into a format readable by the EndoTOFPET-US reconstruction software. The data format of choice is listmode containing a unique detector ID for each channel combination of the plate and the endoscopic head module, the real time of the event, coincidence time as well as energy of both hits. Further information that can be added is the depth of interaction, which is not available from the EndoTOFPET-US prototype and, therefore, is set to the center of the crystal.

7.1.1 Point Resolution

The reconstructed activity is presented in figure 7.2. The reconstructed activity is confined to a small area in the transverse view, whereas it is elongated along the z-dimension in the coronal and sagittal view as expected. In addition, a small amount of smearing along the y-dimension is visible in the sagittal view. This smearing stems from a minor misalignment of the external plate and endoscopic head prototype in the y-dimension on the order of $\sim$1 mm. The fact that such a small amount of misalignment is visible

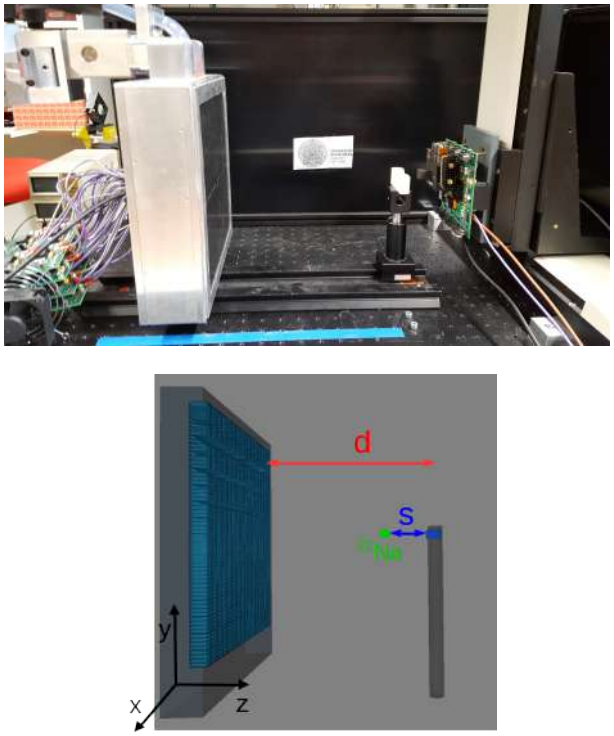

Figure 7.1: (Top) Photo of the measurement setup. The external plate is positioned on the left side of the photo and the endoscopic head prototype is positioned on the right side of the photo. The radioactive source is placed in the white 3D printed holder that is positioned close to the endoscopic head prototype. (bottom) Schematic of the measurement setup. d denotes the distance from the endoscopic head to the external plate, while s denotes the distance from the ^{22}Na source to the endoscopic head.

in the reconstruction emphasizes the necessity of having an excellent tracking of the two detectors. The point resolution of the system can be determined from the reconstructed data of a point-like source. The resolution is defined as the FWHM of the reconstructed activity along the three dimensions. The reconstructed activity is assigned per voxel in the FOV, as mentioned in section 2.7. The activity is assigned to the center of each voxel and a spline interpolation between the voxel activities is performed in each dimension in order to determination of the spatial resolution, as shown in figure 7.2. The FWHM of the spline interpolation is interpreted as the spatial resolution. The same analysis was performed for all four acquisition setups. The results for all setups are presented in table 7.1. No influence of TOF is

d [mm]: / s [mm]:	200	300
10	7.3 1.7	8.9 1.6
20	8.9 1.9	9.1 1.5

Table 7.1: Spatial resolution in z (blue) and in x/y (red) for the different acquisition setups. All numbers quoted in millimeter.

visible in the case of point sources.

The number of noisy channels was higher during the acquisition than during the optimization of the CTR for unknown reasons. Masking noisy channels in the reconstruction has an effect on the point

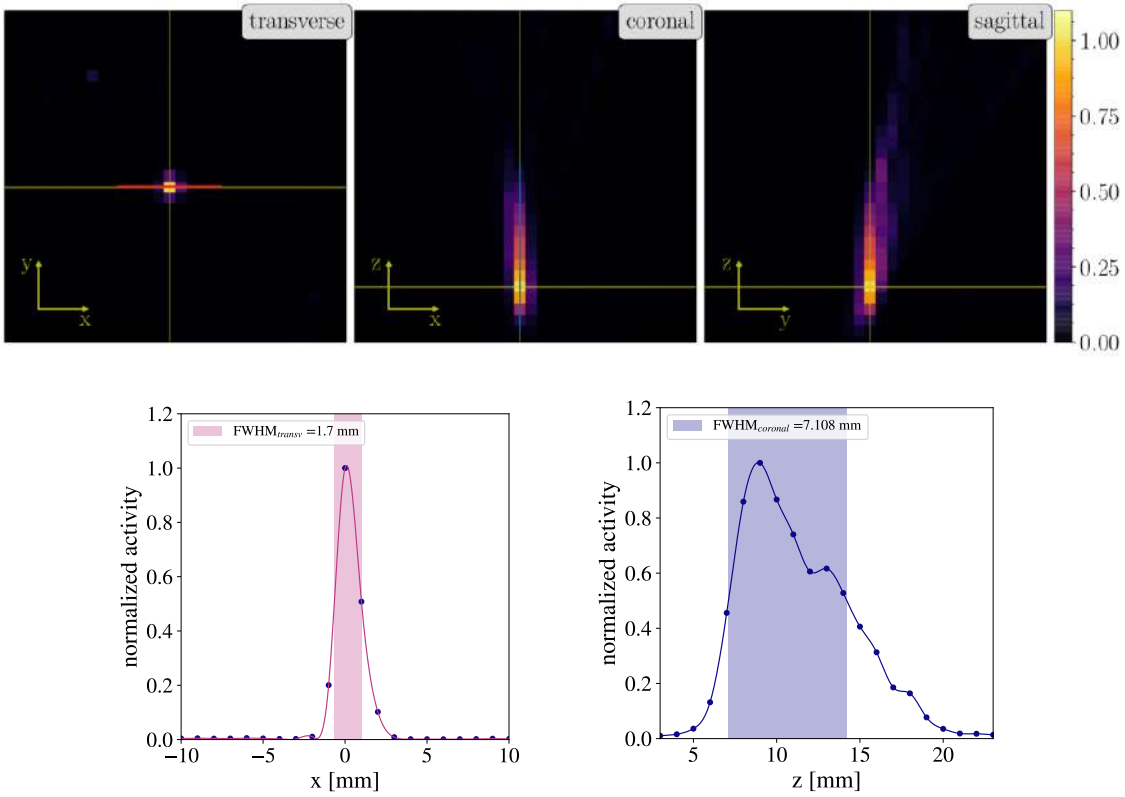

Figure 7.2: Reconstructed radioactivity in the transverse view (top left), coronal view (top center) and sagittal view (top right) with a voxel size of 1 x 1 x 1 mm^3. The transverse view shows the view from the endoscopic head prototype towards the external plate. The endoscopic head prototype is facing up towards the external plate in the coronal and sagittal view. The normalized color scale gives the relative activity in arbitrary units. The line profile through the normalized reconstructed activity in the (bottom left) transverse plane and (bottom right) coronal plane as indicated by red and blue lines. The FWHM of the spline interpolation indicates the spatial resolution in z and x/y, respectively.

resolution of the system as presented in table 7.2 . A total of 69 channels were masked in the reconstruction to reach this result. Further analysis in terms of image quality are not meaningful at this stage since point-like sources do not allow for more analysis.

7.2 Error Estimation of the Reconstructed Activity

Error estimation on the reconstructed activity is difficult to do because the reconstruction does not converge to the real image, but approaches the real image and then moves away from it again. It is only possible in comparison to the real image that has to be known. No quantitative comparison of real and reconstructed image can be performed since the reconstruction algorithm used in this thesis yields only qualitative results. Nevertheless, an error can be estimated as the standard deviation of the reconstructed activity in an image area known to be homogeneous in activity concentration. However, this does not account for the distance that photons had to travel in order to reach the detector (increasing probability of Compton scattering with increasing path length) and for the sensitivity of the detector as a function of photon origin, both of which would naturally lead to inhomogeneity in the reconstructed image. Especially sensitivity of the EndoTOFPET-US detector varies vastly over the FOV. Moreover,

s [mm]: \ d [mm]:	200	300
10	7.0 1.4	9.0 1.5
20	9.0 1.4	9.1 1.3

Table 7.2: Spatial resolution in z (blue) and in x/y (red) for the different acquisition setups. All numbers quoted in millimeter. After excluding noisy 69 channels from the data.

the elongation along the z-axis might lead to a leakage of activity of one homogenous area to another one, which can potentially increase the estimated error immensely. Furthermore, the error estimate can be a strong function of the statistics/number of collected coincidences. The smaller the number of gathered coincidences is, the bigger the error estimate will be. The limitations of such an error estimate are evident and include, in addition to the already mentioned problems, the drawback of not being applicable to small activity distributions that only cover a few voxels. The reason for this limitation being, that the area of homogeneous activity is only one voxel leading to a standard deviation of zero.

A second option is to use the number of coincidences per voxel to estimate an error on the reconstructed activity. Such an approach would mean that errors highly depend on voxel size and might be overestimated for a lot of cases.

A final option for error determination is to redo a certain measurement/simulation several times and determine the standard deviation on certain properties such as signal to noise ratio. However, this approach has its own limitations. For example it would only be able to determine the standard deviation of the maximum signal to noise ratio and not the error in dependence of reconstruction iteration. Overall this is a reasonable approach to get errors not on the reconstructed activity itself but on image quality parameters and will be used in the rest of the thesis.

7.3 Conclusion

First data taking with a completely functional, calibrated and optimized EndoTOFPET-US was performed with a point-like (cylinder with height and diameter of 1 mm) ^{22}Na source. Four different detector setups were realized. The detectors were positioned in a distance of either 20 or 30 cm too each other while the ^{22}Na source was positioned in either 1 or 2 cm distance to the endoscopic head module. The data were reconstructed and the FWHM point resolution for all four setups was extracted. In the x and y-dimension the detector has an excellent point resolution of $\sim$1.4 mm independent of detector position (within the four setups) while in the z-dimension the point resolution is 7-9 mm depending on detector positioning.

Chapter 8

EndoTOFPET-US Simulation Studies

The measurements presented so far are still very simple and cannot show the influence of CTR (coincidence time resolution) on image quality and feasibility of the EndoTOFPET-US concept. Therefore, a simulation of the EndoTOFPET-US prototype has been developed. It allows to investigate the feasibility of the EndoTOFPET-US concept with a variety of measurement scenarios.

A walkthrough of the performed simulations is given in this chapter. It starts with verifying that the simulation fully represents the EndoTOFPET-US prototype by repeating the measurements presented in chapter 7. A phantom utilized for more complex application-oriented simulation scenarios and image quality parameters is introduced. The simulation scenarios and the achieved image quality are presented afterwards. The influence of CTR as well as StB (signal to background ratio) on image quality is investigated. As mentioned in chapter 3, the EndoTOFPET-US detector is not meant for diagnosis of cancer, but as intraoperative guidance tool. A diagnostic PET/CT or PET/MRI image, called prior, is already present when acquiring data with an EndoTOFPET-US detector. Co-registration with a prior PET image is demonstrated by means of two conventional ring PET detector simulations. Finally, a sensitivity study of the EndoTOFPET-US prototype is performed.

8.1 Pointlike Source Simulation

As a first step, the point-like source measurements presented in section 7.1 are replicated in order to verify that the simulation fully represents the EndoTOFPET-US prototype. Therefore, a cylindric ^{22}Na source with height 1 mm, diameter 1 mm and an activity of 150 kBq was simulated with an acquisition time of 20 minutes and at specified distances (s = 10 mm and 20 mm between ^{22}Na source and endoscopic head prototype, d = 200 mm and 300 mm between external plate and endoscopic head prototype). The ^{22}Na source is encased in a delrin cylinder with a diameter of 2 cm and a height of 0.5 cm, as is the source used for the measurements. The positron range is included by specifying a probability function of the positron emission energy of ^{22}Na. Additionally, the dead and noisy channels that were present during the data acquisition are masked in the simulation. A reconstructed image with a voxel size of 1 x 1 x 1 mm^3 is presented in figure 8.1 including the line profile of the reconstructed activity through the ^{22}Na source along the x- and z-axes. The external plate distance to the endoscopic head prototype is d = 300 mm and the source distance to the endoscopic head prototype is s = 10 mm. The line profiles are compared to the line profiles arising from data. It can be seen that simulation and data match and lead to the same point resolution of 1.3 mm FWHM (full width half maximum) along the x-

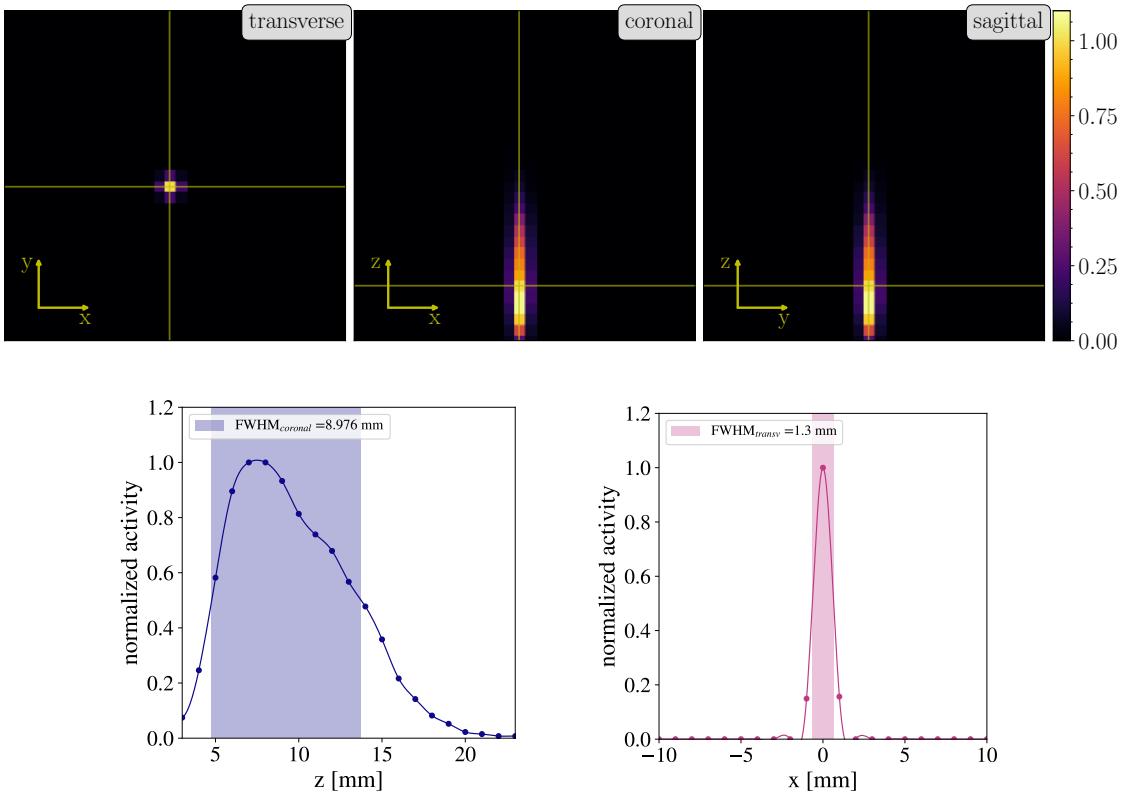

Figure 8.1: Reconstructed radioactivity in the transverse view (top left), coronal view (top center) and sagittal view (top right) with a voxel size of 1 x 1 x 1 mm^3. The transverse view shows the view from the endoscopic head prototype towards the external plate. The endoscopic head prototype is facing up towards the external plate in the coronal and sagittal view. The normalized color scale gives the relative activity in arbitrary units. The line profile through the normalized reconstructed activity in the (bottom left) transverse plane and (bottom right) coronal plane as indicated by red and blue lines. The FWHM of the spline interpolation indicates the spatial resolution in z and x/y, respectively.

and y-axes and 7.3 mm FWHM along the z-axis. Data and simulation are compared for all acquisition scenarios in terms of resolution and summarized in table 8.1. The spatial resolution of the simulation and data match extremely well. Therefore, it is from here presumed that the simulation fully represents the EndoTOFPET-US prototype behavior. TOF has no influence on point source measurements. Its influence on image quality, however, is presented in section 8.2. For all studies presented from here the EndoTOFPET-US prototype is simulated without dead or noisy channels.

8.1.1 Point Resolution and Voxel Size Influence on Resolution

A true point source has been simulated in GAMOS using the back-to-back photon option for this study. The voxel size of the reconstructed image can potentially have a big influence on image resolution. It can not only limit the resolution but also change the number of events per voxel and thereby increase or reduce statistical errors. Hence, the spatial resolution as a function of the voxel size can and should be studied. In order to investigate the effect of voxel size on the reconstructed image, a point source has been simulated at the center of FOV (field of view) at a distance of $s = 20$ mm to the endoscopic head prototype while external plate and endoscopic head prototype are at a distance of $d = 200$ mm apart

d [mm]: / s [mm]:	200		300	
	Meas	Sim	Meas	Sim
10	7.0 1.4	7.0 1.5	9.0 1.5	9.0 1.3
20	9.0 1.4	9.0 1.4	9.1 1.3	9.2 1.3

Table 8.1: Comparison of resolution from measurement (noisy pixel excluded) and simulation with a realistic ^{22}Na cylindric source. All numbers are quoted in millimeter.

from each other. The spatial resolution reached in x and z as a function of voxel size is presented in figure 8.2. The intrinsic resolution in the x- and y-axes is about 1.3 mm. Consequently, the resolution

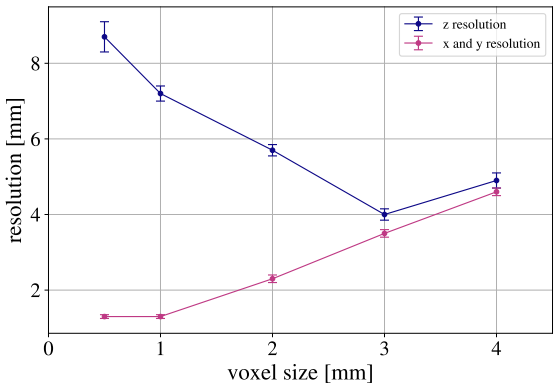

Figure 8.2: Point resolution along the x- and z-axes as a function of voxel size. The point source is positioned in the center of field of view at a distance of $s = 20$ mm from the endoscopic head prototype. The external plate and endoscopic head prototype are $d = 200$ mm apart.

in the x- and y-axes is limited by voxel size provided that voxels are bigger than 1.3 x 1.3 x 1.3 mm^3. The point resolution in the z-axis first improves and then deteriorates with increasing voxel size. The minimum resolution in z is reached for a voxel size of 3 x 3 x 3 mm^3. This knowledge allows to adapt the voxel size to the imaging needs. If x-y-resolution on the order of 1 mm, for example, is necessary, small voxels (1 x 1 x 1 mm^3) need to be used. Otherwise, bigger voxels can be utilized. Imaging procedures where images with varying voxel sizes are overlayed can potentially combine advantages of smaller and bigger voxels. Asymmetric voxels that are elongated in the z-axis can also be applied. However, this utility is not yet implemented in the EndoTOFPET-US reconstruction software and needs to be tested for viability.

8.2 NEMA IEC Body Phantom Set^{TM}

The NEMA IEC Body Phantom Set^{TM} is a phantom that is often used for image quality determination of PET scanners. The phantom is composed of a torso shaped bulk, a cylindric inlay at the center with a diameter of 51 mm and six fillable spheres arranged in a hexagon around the cylinder. The fillable spheres have a diameter of 10, 13, 17, 22, 28 and 37 mm. The cylindric inlay with a diameter of 51 mm at the

center of the phantom allows for application-specific imaging with the EndoTOFPET-US prototype. The endoscopic PET head prototype can be placed inside the emptied cylindric inlay while the external plate can be placed close to the bulk. Hence, the spheres can be positioned between the two detectors resembling a real patient measurement. A photo of the phantom along with a representation of the simulation are presented in figure 8.3. All simulations performed with the NEMA IEC Body Phantom Set^{TM} can be

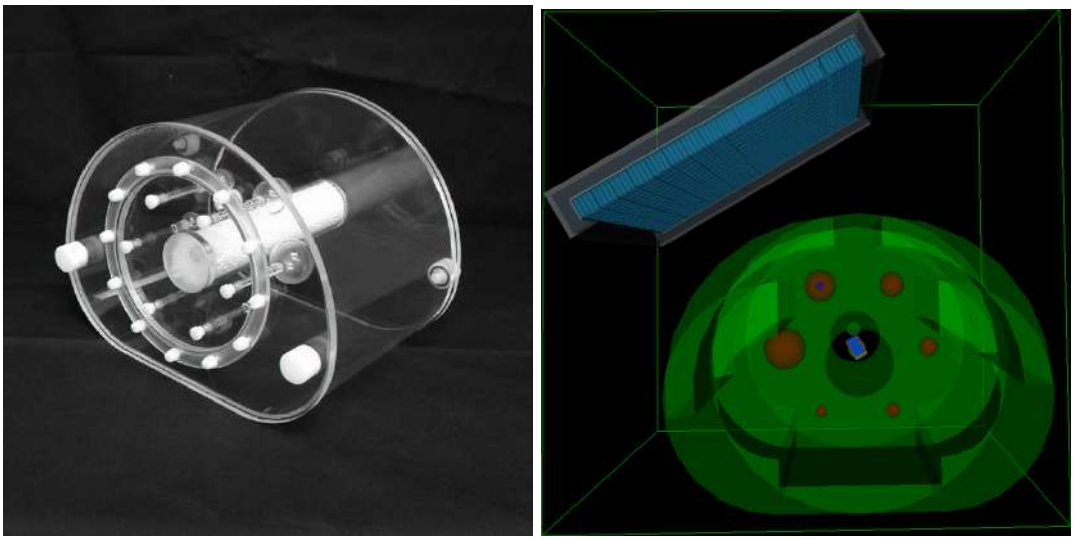

Figure 8.3: A photo of the NEMA IEC Body Phantom Set^{TM} (left) and a representation of the simulation with the NEMA IEC Body Phantom Set^{TM} (right).

replicated in the lab at a later stage without the necessity of modifying the EndoTOFPET-US prototype.

8.3 Image Quality Parameters

Comprehensive image analysis is indispensable to quantify image quality and to compare reconstruction results of different scanners. All image quality parameters used in this thesis are defined in this section.

8.3.1 Qualitative Image Analysis

Qualitative image analysis is based on lesion visibility. There is no real objective measure to define qualitative image quality. It can be defined as the probability that trained personnel identifies a lesion as such without prior knowledge of it existence and the accuracy with which position and size of the lesion is determined.

8.3.2 Quantitative Image Analysis

There are a number of quantitative measures that can be used to determine the quality of a PET image. The most commonly used are signal to noise ratio (SNR), contrast recovery percentage (CRP), background variability (BGV), spatial resolution and contrast recovery coefficient error (CRE) . They can be used to define and compare scanner performance. The image quality parameters used in this thesis are introduced in the following subsections.

8.3.2.1 Signal to Noise Ratio

The signal to noise ratio (SNR) is one of the main characteristics of any imaging technique. In the case of medical imaging, it is usually defined as the difference between the mean activity in the signal region and the mean activity in a defined background region divided by the background standard deviation

$$\mathrm{SNR} = \frac{\mu_{sig} - \mu_{BG}}{\sigma_{BG}} \tag{8.1}$$

with σ_{BG} being the standard deviation of the background activity, μ_{sig} and μ_{BG} being the mean of the signal and background activity, respectively. SNR reaches preferably a high value indicating good signal to background distinction.

8.3.2.2 Contrast Recovery Percentage

Contrast recovery percentage (CRP) is a measure for how good the detector and reconstruction confines an object of known dimension and location. It is defined as

$$\mathrm{CRP} = \frac{A^{sig}_{rec}/A^{BG}_{rec} - 1}{A^{sig}_{sim}/A^{BG}_{sim} - 1} * 100[\%] \tag{8.2}$$

with A^{sig}_{rec} and A^{BG}_{rec} being the mean reconstructed activity in signal and background regions, respectively, and A^{sig}_{sim} and A^{BG}_{sim} the mean simulated activity in signal and background regions, respectively. CRP is 100% in case of a perfect reconstruction and 0% in case that a flat activity distribution is reconstructed.

8.3.2.3 Contrast Recovery Coefficient

The contrast recovery coefficient (CRC) defines how precisely the signal and background regions are separated. It is given by

$$\mathrm{CRC} = 1 - \left(\frac{\sum\limits_{BG\ voxels} x_i}{\sum\limits_{sig\ voxels} x_j} * \frac{N_i}{N_j} \right) - \frac{A^{BG}_{sim}}{A^{sig}_{sim}} \tag{8.3}$$

where the sum over the activity in all background voxels x_i is divided by the sum over the activity in all signal voxels x_j and then normalized to the number of background and signal voxels N_i, N_j and finally the actual signal to background is subtracted. The CRC reaches 1 in case of perfect separation and 0 in case that a uniform activity is reconstructed.

8.3.2.4 Background Variability

The background variability defines the smoothness of a known uniform background region. It is defined by

$$\mathrm{BGV} = \frac{\sigma_{BG}}{\mu_{BG}} \tag{8.4}$$

with σ_{BG} and μ_{BG} being the standard deviation and mean of reconstructed activity in the background region, respectively. BGV is preferably small.

8.3.2.5 Object Size/Spatial Resolution and Object Localization

Spatial resolution or object size is defined as the FWHM (full width half maximum) of a spline interpolation between the reconstructed activity along all three dimensions, as it has already been done

in section 8.1. The FWHM is defined as the first and last intersection of the spline interpolation and $0.5 * activity_{max}$. If the spline interpolation drops below $0.5 * activity_{max}$, three times the first and third intersections are used to determine the FWHM. A depiction of this is presented in figure 8.4. Due to the unique geometry of the EndoTOFPET-US design, the inherent point resolution does not need to be the resolution for extended/larger objects. A bigger object would - considering a geometrical point of view - have a worse resolution in the z-dimension than a smaller object. Additionally, reconstructed object size/spatial resolution, especially in the z-coordinate, highly depends on the number of reconstruction iterations and voxel size. An assessment of resolution needs to be made for each simulation scenario accordingly. The real z-position of the object also needs to be determined since images are elongated along the z-axis. A straightforward way to estimate the actual z-position of the object is to take the central position of the FWHM along the z-axis.

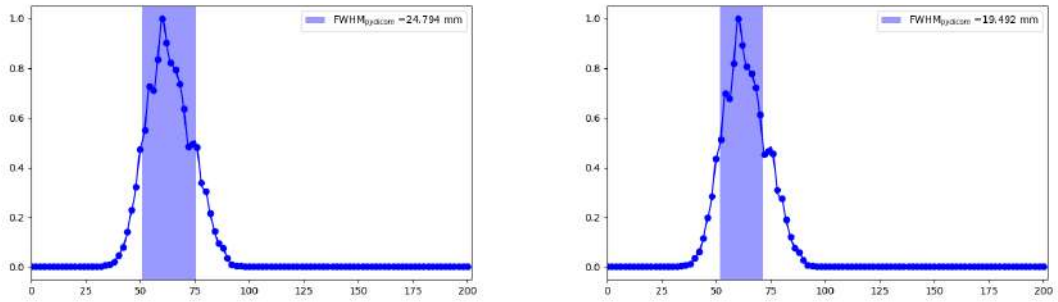

Figure 8.4: Line profile through the normalized reconstructed activity in the transverse plane. (left) The third and (right) the fourth iteration is presented. In the third iteration there are three intersections of the spline interpolation of the data and 0.5. Hence, the third and the first intersections are used to determine the full width half maximum (FWHM).

8.4 Influence of TOF and Detector Movement on EndoTOFPET-US Performance

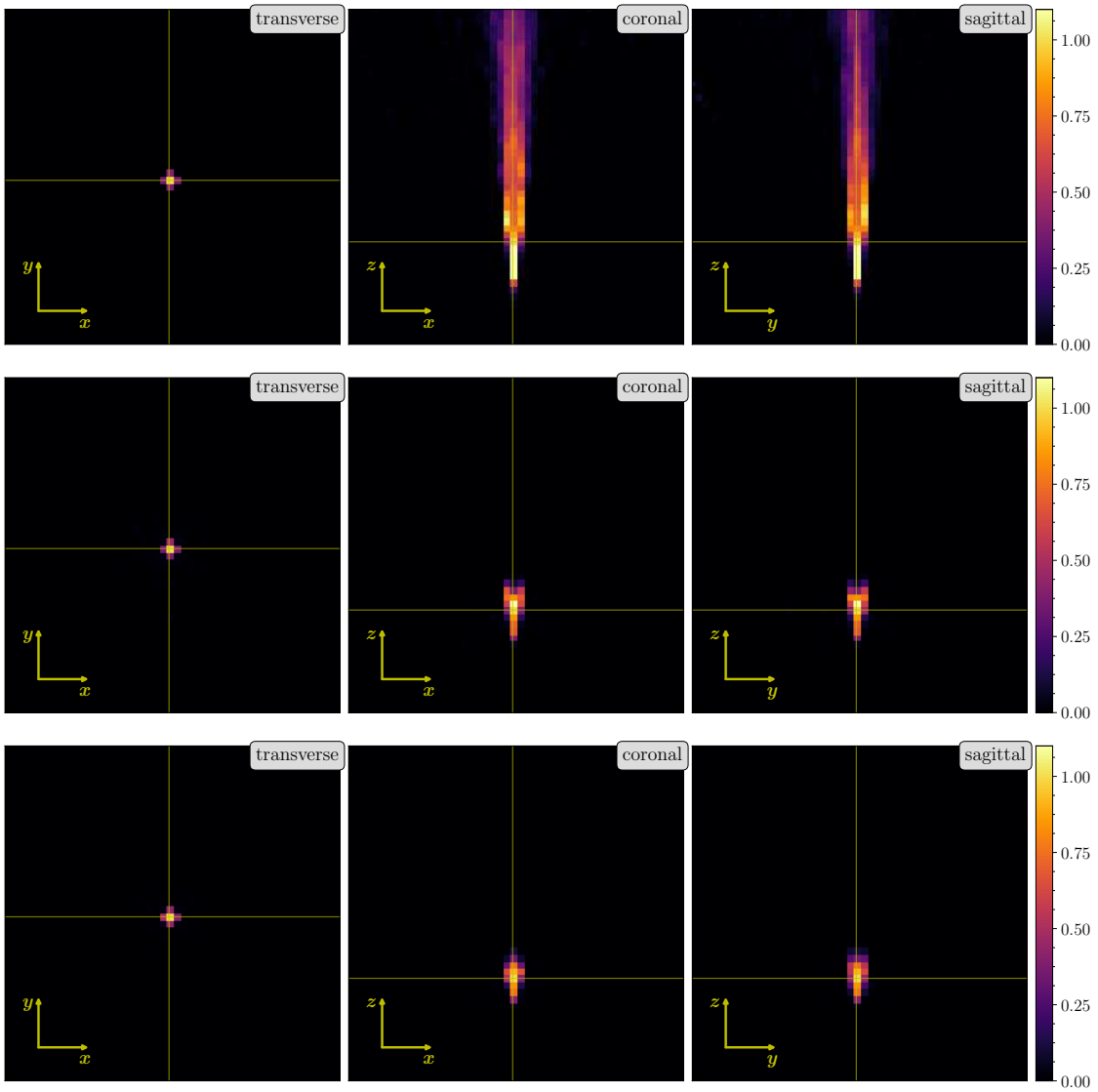

Figure 8.5: Reconstruction of a 10 mm diameter sphere inside the NEMA IEC Body Phantom Set^{TM}. The rest of the phantom is filled with water. A total of ∼80000 coincidences were acquired for each reconstruction. (top) Reconstruction without TOF, (middle) reconstruction with TOF (CTR = 255 ps) and (bottom) reconstruction with TOF (CTR = 255 ps) and a 10° rotation of the two detectors around the sphere are presented. For all images the 15^{th} iteration is presented.

The necessity of TOF for the EndOTOFPET-US detector can be demonstrated with the NEMA IEC Body Phantom Set^{TM}. A simple simulation is performed during which one of the spheres in the phantom is filled with activity while the rest of the phantom is filled with water. The endoscopic head prototype is placed in the center of the 51 mm diameter cylindric inlay. The external plate is positioned in 200 mm distance to the endoscopic head prototype. The activity filled 10 mm/28 mm diameter sphere is positioned in the center of the FOV, the rest of the phantom is filled with water. Reconstructed images of the 10 mm

sphere without TOF, with TOF and with TOF and a 10° rotation of the two detectors around the sphere are presented in figure 8.5. In case of TOF reconstruction, the EndoTOFPET-US CTR of 255 ps is used. In case of reconstruction without TOF, no restrictions of the reconstructed activity along the line of responses (LORs) exist due to the limited angular coverage. Thus, the activity is smeared over the whole FOV making an identification of the source impossible. This holds in particular for objects that have a larger diameter in the transverse plane than the endoscopic head. In case of reconstruction without TOF, only empty LORs can restrict the activity distribution in in the z-axis, as explained in section 3.4. However, there can only be empty LORs restricting the z position of the annihilation if the activity distribution is smaller than the endoscopic head. Ultimately, good CTR is necessary when imaging bigger objects like the prostate. Using TOF information restricts the origin of the 511 keV photons and, hence, confines the reconstructed activity, as visible in figure 8.5. This demonstrates the value of TOF for the EndoTOFPET-US detector. Furthermore, rotation of the external plate and the endoscopic head prototype around the radioactive source can potentially improve reconstructed images. Rotation of the two detectors increases the angular coverage and, thus, image quality. An acquisition including a 10° rotation in both directions of the two detectors around the spheres in both directions is simulated. The overall acquisition time is not changed but divided equally between the three acquisition setups. A reconstructed image including the rotation are presented in figure 8.6. It can be seen that a small rotation of the external plate and endoscopic head prototype can remove imaging artifacts and lead to a more reliable reconstruction. For larger objects the small rotation of 10° does yield any obvious qualitative improvement of image quality. Figure 8.6 shows the reconstructed images of the 28 mm diameter sphere in the NEMA IEC Body Phantom Set^{TM}. It can be seen that the small rotation does not yield any advantage for an object of this size.

8.5 Application-Oriented Simulation

A small modification of the NEMA IEC Body Phantom Set^{TM} allows to perform application oriented measurements/simulations. A small cylinder with 6 mm diameter and 28 mm height is inserted into the 28 mm diameter sphere of the phantom. In this scenario, the cylinder represents the lesion and is filled with activity accordingly. The 28 mm sphere is filled with activity according to the prostate uptake. Furthermore, the biggest sphere in the phantom which is next to the 28 mm sphere and has a diameter of 37 mm is used to represent the bladder. A schematic of the setup and a representation of the simulation are presented in figure 8.7. Such a setup resembles a realistic measurement scenario for the prostate rather closely in case that prostate specific membrane antigen (PSMA) is used as tracer and can be easily reproduced in the lab. PSMA has a high specificity to prostate, prostate lesion and bladder as well as a very low uptake in the rest of the body. First simulation results and image analysis of the specified simulation scenario are presented in the following paragraphs.

Typical patient activities for prostate, prostate lesion and bladder achieved with PSMA are taken from [90]. Bladder activity will be constant throughout all studies presented in this thesis at 10.4 kBq/cm^3 leading to 275.8 kBq in the 37 mm sphere. Prostate lesion activity will also be constant throughout the simulations. It will be at 4.5 kBq/cm^3 leading to an activity of 3.56 kBq in the cylindric lesion. Activity in the prostate is adjusted according to the desired signal to background ratio (StB). The first simulation is performed with the EndoTOFPET-US prototype's CTR of 255 ps and a prostate activity of 0.450 kBq/cm^3, leading to a StB of 10:1. A very long acquisition time of 12.13 hours is simulated, corresponding to a total of $\sim 12^{10}$ events. This yields approximately 32000 coincidences from the lesion.

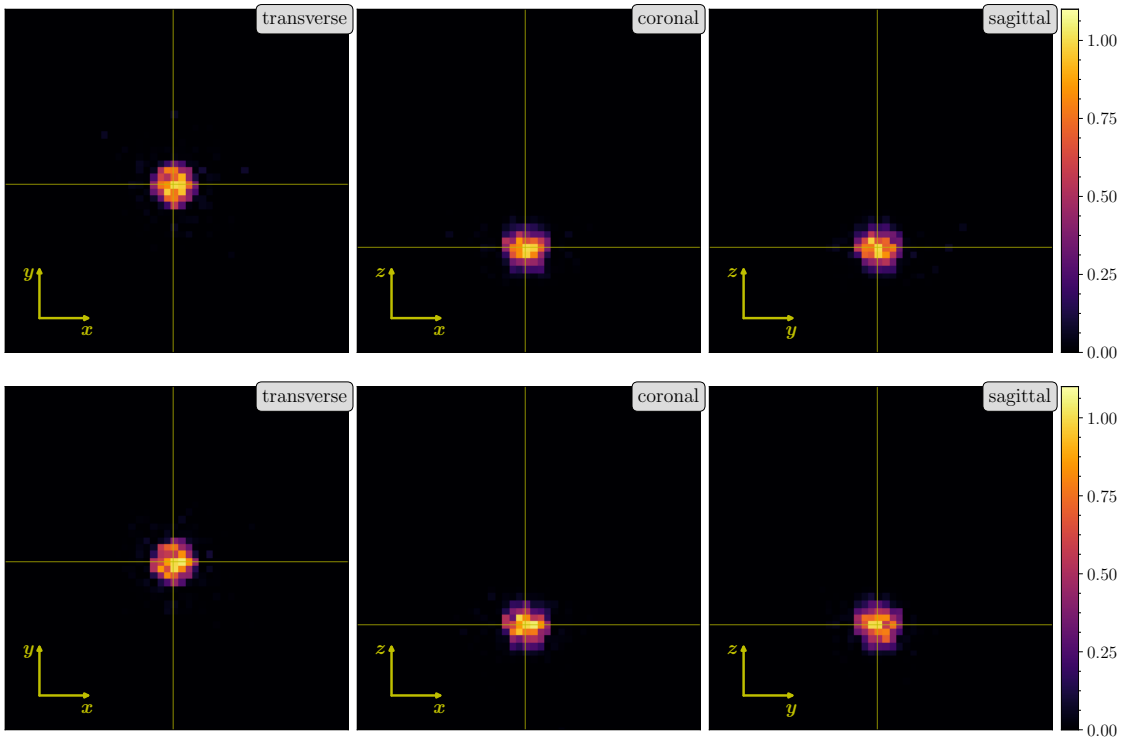

Figure 8.6: Reconstruction of a 28 mm diameter sphere inside the NEMA IEC Body Phantom Set^{TM}. The rest of the phantom is filled with water. A total of ∼54000 coincidences were acquired for each reconstruction. (top) reconstruction with TOF (CTR = 255 ps) and without detector rotation and (bottom) reconstruction with TOF (CTR = 255 ps) and a 10° rotation of the two detectors around the sphere are presented. For both images the 25^{th} iteration is presented.

Such a long acquisition time is chosen in order to ensure that the image quality is not strongly limited by statistics. The active area of the endoscopic head prototype is smaller than that of the original design and the distance from the endoscopic head prototype to the lesion is bigger than in a realistic patient scenario, resulting in a low sensitivity and long acquisition time. A comprehensive study of detector sensitivity is presented in section 8.6. The reconstruction of the simulation is presented in figure 8.8 The hot cylindric lesion can be clearly identified inside the warm sphere. Furthermore, the bladder is not insight the FOV of the EndoTOFPET-US prototype and only visible in the coronal view due to photons scattering into the FOV. It was already shown that the external plate and endoscopic head prototype can be positioned in such a way that the bladder is outside the FOV during patient acquisition [90].

The signal and background regions for image analysis are defined as the ground truth of the cylinder and the 28 mm prostate sphere, respectively. Reconstruction is performed with 4 x 4 x 4 mm^3 voxels and 2 x 2 x 2 mm^3 voxels. For the former, the cylinder is defined as the seven voxels passing through the center of the sphere parallel to the y-axis. For the latter, the cylinder is defined as the central 3 x 3 x 14 voxels in the center of the sphere parallel to the y-axis. Of course these are only approximations of the real cylinder shape which always need to be made when dealing with voxelized volumes.

Another option to define the signal region for the image analysis is to use the spline interpolations between the activity of each voxel and integrate these over the whole volume of the cylinder. This approach, however, is more complicated and yields no advantages for this comparative study.

One hundred reconstruction iterations are performed for both voxel sizes and the image quality pa-

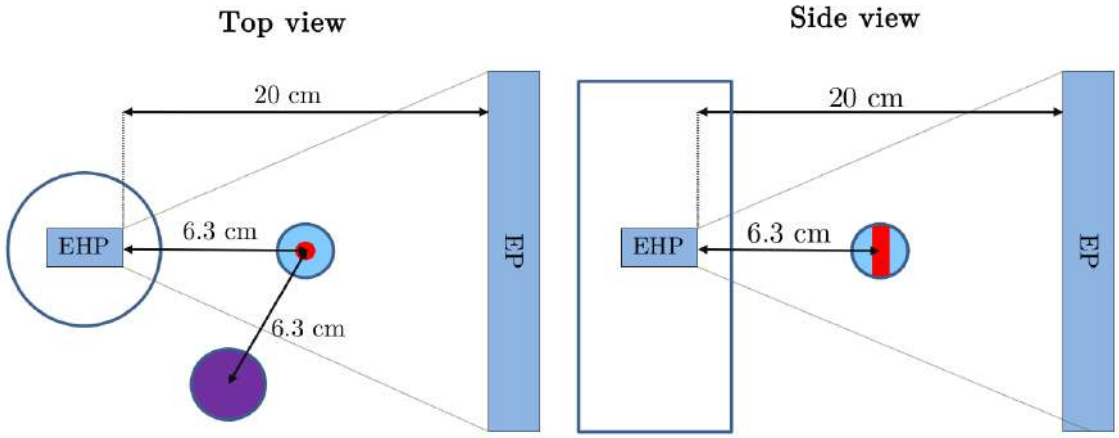

Figure 8.7: Sketch of the simulation setup. A cylinder (red, 6 mm diameter and 28 mm height) is positioned inside the 28 mm diameter sphere (light blue) of the NEMA IEC Body Phantom Set^{TM}. The cylinder is the hot volume inside the warm background of the 28 mm sphere. The 37 mm sphere (purple) represents the bladder. EHP is the endoscopic head prototype and EP is the external plate. The field of view of the EndoTOFPET-US prototype is represented by the dashed lines.

rameters are calculated at each iteration. All image quality parameters as a function of reconstruction iteration are presented in figure 8.9. An understanding of image quality as a function of reconstruction iteration is necessary since the reconstruction has to be stopped at a specific iteration in order to gain the best possible image. Increasing the number of reconstruction iterations above the optimal number of iterations can result in increased noise and enhanced formation of reconstruction artifacts. The image quality parameters for the 4 x 4 x 4 mm^3 and 2 x 2 x 2 mm^3 voxels behave similar. SNR rises steeply before plateauing around 20-30 iterations. It is higher for the bigger voxels by a factor ∼1.4. CRC and CRP show a similar behavior, but reach a plateau later and exhibit a less flat plateau. CRP does not show a plateau for 2 x 2 x 2 mm^3 voxels. BGV improves from the second to approximately tenth iteration and then deteriorates. BGV is worse for smaller voxels.. This is expected because BGV depends on the σ_{BG} which is inversely proportional to number of events per voxel. Z-resolution improves over the whole iteration range for both voxel sizes. It reaches a minimum of ∼14 mm and ∼9 mm for 4 x 4 x 4 mm^3 and 2 x 2 x 2 mm^3 voxels, respectively. Z-position improves during the first few iterations and stays constant during the subsequent iterations. The reconstruction with 2 x 2 x 2 mm^3 voxels leads to some abrupt jumps in z-position and z-resolution. These jumps are related to the determination of FWHM, as explained in section 8.3.2.5. A jump occurs when more than two intersections of the spline interpolation with $0.5 * max(activity)$ exist and one of the outer (first or last) intersections disappears within the following reconstruction iteration. This is demonstrated in figure 8.10. Furthermore, an early onset of pixelization of the reconstructed image is observed in smaller voxels. This behavior is linked to the smaller amount of events per reconstructed voxel and the corresponding bigger statistical uncertainty. The pixelization is demonstrated in figure 8.11, which depicts the 36$^{\text{th}}$ iteration of the reconstruction showing a very inhomogeneous activity distribution and, thus, making lesion recognition difficult. One possible countermeasure to these problems is to apply a simple smoothing to the reconstructed image in the case of smaller voxels. Smoothing can be applied in a vast amount of ways and is often beneficial to image quality when performed correctly. Smoothing in PET reconstruction is common, while the

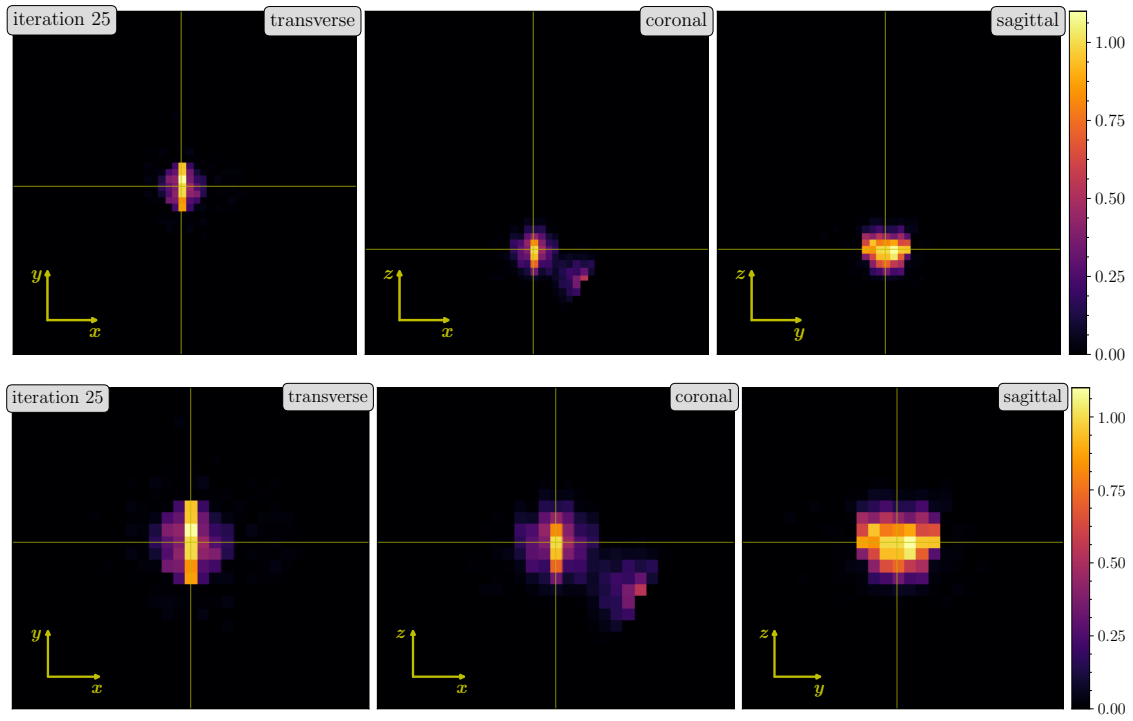

Figure 8.8: Slices of a reconstructed image after 25 iterations in the transverse, coronal and sagittal plane (from left to right). The intersection of the two lines indicate the center of the lesion cylinder in each slice. The activity is normalized to the activity in the center voxel of the cylinder. The voxel size is 4 x 4 x 4 mm^3 and a volume of 51 x 51 x 51 voxels is reconstructed. (top) The whole field of view (FOV) is depicted spanning from the endoscopic head (located at the center of the bottom edge in the transverse and sagittal view) to the external plate (located at the top edge in the transverse and sagittal view). It can be clearly distinguished between the lesion cylinder, the prostate sphere and the bladder scattering into the FOV. (bottom) Zoom of the top image. The voxel activity is for every image normalized to the center voxel of the cylinder (indicated by crossing lines).

most used way of smoothing is to stop the reconstruction early. Several ways of smoothing the data have been tested. The selected smoothing is fairly simple and still specific to the EndoTOFPET-US detector geometry. The smoothing recalculates the activity in each voxel as the mean activity of itself and its eight direct neighbors in the yz-plane. This simple way of smoothing impedes the resolution in z and y. The corresponding impairment in z, however, is of limited concern due to the intrinsically worse resolution. The yz-plane is chosen for smoothing because of the lesion geometry. The prior can be used to determine the best suited smoothing operation in a real imaging scenario. As an alternative to the prior, smoothing in both xz- and yz-planes could be performed and resulting images could be combined or even separately investigated to extract x- and y-positions of the lesion. This would ensure that the excellent spatial resolution in the xy-plane of the EndoTOFPET-US detector can be used. A smoothed and non-smoothed reconstruction are presented in figure 8.11. The qualitative influence of the simple smoothing becomes obvious. While the image with smoothing clearly depicts the cylinder in the transverse view, the image without smoothing does not noticeably display the cylinder. Applying extra smoothing, however, does not improve image quality for 4 x 4 x 4 mm^3 voxels. The influence of smoothing on the image quality parameters is presented in figure 8.12. Smoothing results in an improved SNR due to the smoothing inherent decrease in BGV, a very similar CRP and CRC with a slight decrease

for higher reconstruction iterations compared to non-smoothing. The abrupt jumps in z-position and z-resolution disappeared after smoothing. Z-position is slightly improved for most of the range, whereas z-resolution is understandably slightly deteriorated. From now on all results of the 2 x 2 x 2 mm^3 voxels are presented after applying smoothing.

It can be concluded from the behavior of the image quality parameters that it is beneficial to let the reconstruction software run even further than 100 iterations. Besides quantitative image quality parameters, qualitative image quality also needs to be investigated in order to point out obvious flaws of letting the reconstruction run for too many iterations. In figures 8.13 and 8.14, the coronal, transverse and sagittal view at several reconstruction iterations are presented for a voxel size of 4 x 4 x 4 mm^3 and 2 x 2 x 2 mm^3, respectively. In the case of 4 x 4 x 4 mm^3 voxels, the image converges towards the truth and lesion visibility increases from the first iteration until the 25$^{\text{th}}$ iteration. The subsequent iterations cause a degradation of image quality: (1) the contrast in the lower part of the cylinder reduces and (2) the prostate sphere size in the z-direction shrinks below the actual size of 28 mm. These two conditions are visualized in figure 8.15. It shows the line profile parallel to the x-axis through the cylinder two voxels below center voxel as a function of reconstruction iteration. The activity is normalized to the activity in the center voxel of the cylinder. It can be seen that the activity in the center voxel decreases after 25 iterations and causes a degradation of the contrast to the background. In the case of 2 x 2 x 2 mm^3 voxels the effect is less pronounced. The shrunken prostate sphere size in z can be seen by the eye. It can be quantified by examining the full width tenth maximum (FWTM) and full width twentieth maximum (FWTWM) of the reconstructed activity. The FWTM and FWTWM of the prostate sphere along the z-axis and the x-axis as a function of reconstruction iteration are compared in figure 8.16. It can be seen that the FWTM along the x-axis (FWTM$_x$) is, except for the first iterations, independent of the reconstruction iteration. It represents the real sphere size of 28 mm for 4 x 4 x 4 mm^3 and 2 x 2 x 2 mm^3 voxels. It can be concluded that the FWTM can be used as a reference for the sphere size. The FWTM along the z-axis (FWTM$_z$) is a strong function of the reconstruction iteration. It crosses 28 mm after 25 and 36 iterations for 4 x 4 x 4 mm^3 voxels and 2 x 2 x 2 mm^3 voxels, respectively. This behavior stems from the limited information the EndoTOFPET-US prototype and the reconstruction have along z. The CTR of 255 ps still allows to localize most positron annihilation positions in the center of the sphere with sufficient high probability independent of the real annihilation location. Therefore, the reconstruction seems to lean towards an activity distribution that is rather localized in z. In addition to the shrinking in z, the background becomes more inhomogeneous as shown in figure 8.14. Distortions of the reconstructed activity can occur in the coronal view due to these inhomogeneities. Unknown distortions of the image yield a problem because they cannot be anticipated by the physicians when trying to locate possible lesions. Furthermore, elongation along one dimension is preferred to shrinkage since overestimation of lesion size is less critical than underestimation in most clinical cases.

The obtained results point out that the reconstruction algorithm needs to be stopped before any of the quantitative image quality parameters reaches a maximum. The stopping iteration can be determined as the iteration at which the image prostate size in z matches the real prostate size. Real prostate size can be estimated from the PET image. In the presented simulation scenario, the size of the prostate along the x-axis is unperturbed/unaltered by the lesion and well known. Comparing the real size of the prostate in the x-axis to the full width ith maximum (FWithM) along the x-axis yields the ratio of lesion activity to prostate activity. Once this ratio is known, the size of the prostate along the z-axis can be determined using the FWithM$_z$ along the z-axis. In a real imaging scenario prostate size can be estimated from the prior or the US image. The image reconstruction should be stopped when the FWithM$_z$ reaches a value

Voxel size	SNR	CRP [%]	CRC	BGV [%]	z resolution [mm]	Δ z position [mm]
4x4x4 mm^3	3.6	28.7	0.82	71.8	17.5	-0.5
2x2x2 mm^3	2.5	28.5	0.82	102.9	10.5	0.24
2x2x2 mm^3 smoothed	3.1	27.0	0.81	79.6	14.2	0.09

Table 8.2: Image quality parameters at iteration 25 for 4 x 4 x 4 mm^3 voxels and iteration 36 for 2 x 2 x 2 mm^3 voxels.

smaller than the real prostate size in z. As presented in figure 8.16, the prostate size along the x- and z-axes in the presented scenario can be estimated as the FWTM. Hence, the stopping iteration is the iteration at which the $FWTM_z$ crosses the $FWTM_z$, i.e. iteration 25 and iteration 36 for 4 x 4 x 4 mm^3 voxels and 2 x 2 x 2 mm^3 voxels, respectively. A rough estimate/determination of the prostate size suffices because lesion visibility and image quality do not undergo drastic changes at the interesting iteration range.

The obtained results point out that the reconstruction algorithm needs to be stopped before any of the quantitative image quality parameters reaches a maximum. The stopping iteration can be determined as the iteration at which the image prostate size in z matches the real prostate size. The prostate size can be estimated by the physician from the prior or the US image in a real imaging scenario. The prostate size estimate can be fed into the reconstruction which stops as soon as the prostate size is reached in z.

It can be concluded from the presented image analysis that the EndoTOFPET-US prototype allows to visualize a hot lesion inside a warm background for StB ratio of 10:1. Images show the expected elongation in z-direction while exhibiting good resolution in x- and y-direction. The optimal reconstruction iteration can be defined via the prostate size. It is 25 and 36 for the presented simulation scenario reconstructed with 4 x 4 x 4 mm^3 voxels and 2 x 2 x 2 mm^3 voxels, respectively. At the optimum reconstruction iteration, cylinder size in z is 17.5 mm for 4 x 4 x 4 mm^3 voxels and 14.2 mm for 2 x 2 x 2 mm^3 voxels, whereas the center position estimation is 0.5 mm for 4 x 4 x 4 mm^3 voxels and 0.1 mm for 2 x 2 x 2 mm^3 voxels off the real position. Bladder influence on the reconstructed image is negligible. A smoothing in the yz- or xz-plane is beneficial provided that small voxels ($\leq$ 2 x 2 x 2 mm^3) are used. The image quality parameters at stopping iteration are summarized in table 8.2.

All the reconstructed images presented so far, even though some smoothing is applied, are still voxelized. Voxelized images show the shortcomings of the reconstruction algorithm and detector geometry more clearly and, thus, are better suited for analyzing reconstructed images. In the end, a physician almost exclusively looks at smoothed images. Since smoothing can remove some of the reconstruction artifacts, images with smoothing represent the reconstructed activity better in most cases. Images smoothed with a Gaussian smoothing kernel for 2 x 2 x 2 mm^3 voxels and 4 x 4 x 4 mm^3 voxels at their specific stopping iteration (25 and 36) are presented in figure 8.17.

One way to improve image quality is to utilize the prostate position and size as known from the US image in order to constrain the coincidence time window. Knowing the prostate size and position allows to define a specific coincidence time window, which is only possible due to the prostate specificity of the EndoTOFPET-US detector design and used tracers. Figure 8.18 shows how a coincidence time window can be placed around the prostate. A physician can define a region of interest (ROI) in the US image that

Voxel size timecut	SNR	CRP [%]	CRC	BGV [%]	z resolution [mm]	Δ z position [mm]
4x4x4 mm^3	3.6	28.7	0.82	71.8	17.5	-0.5
4x4x4 mm^3 timecut	3.6	28.7	0.82	71.8	17.3	-0.4
2x2x2 mm^3 smoothed	3.1	27.0	0.81	79.6	14.2	0.09
2x2x2 mm^3 smoothed timecut	3.1	27.8	0.81	80.0	14.1	0.13

Table 8.3: Image quality parameters at the stopping iteration, for 4 x 4 x 4 mm^3 voxels and for smoothed 2 x 2 x 2 mm^3 voxels data. Either the standard 1.5 ns coincidence time window is applied or the prostate specific time window is applied. The voxel activity is for every image normalized to the center voxel of the cylinder (indicated by crossing lines)

is translated to a coincidence time window by the reconstruction software. The coincidence time is defined as CT $= t_{endo} - t_{plate}$, where t_{endo} and t_{plate} are the hit times of the two photons in the endoscopic head and external plate. The maximum and minimum time difference, forming the coincidence time window, can be defined as $t_{max} + \mathrm{CTR}/2$ and $t_{min} - \mathrm{CTR}/2$. The coincidence time window can potentially reduce the influence of Compton scattered photons. The comparison of image quality parameters at stopping iteration with and without applying the coincidence time window are presented in table 8.3. In the presented simulation scenario, almost no changes in image quality are observed when applying an extra coincidence time window as a function of prostate location and size. In the case of a second warm/hot volume located on the same LOR as the organ under study (prostate) or in the case of a worse CTR, a specialized coincidence time window might yield big improvements. Another way to improve image quality, which cannot be tested without modifying the reconstruction software, is to use attenuation correction. The prior yields the attenuation coefficients that can be directly fed into the reconstruction software.

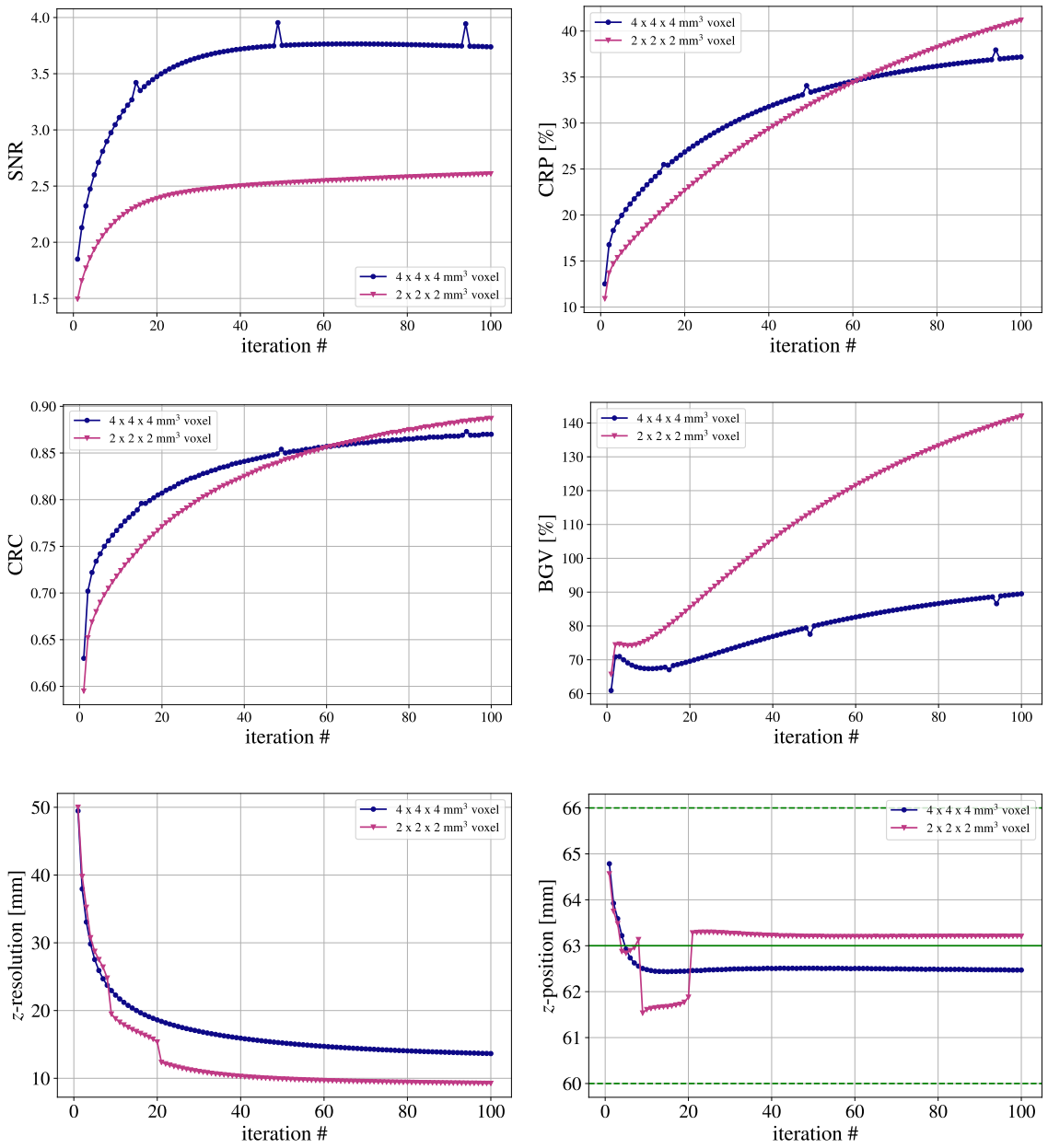

Figure 8.9: Image quality parameters as a function of reconstruction iteration and voxel size: (top left) the signal-to-noise ratio (SNR), (top right) contrast recovery percentage (CRP), (center left) contrast recovery coefficient (CRC), (center right) background variability (BGV), (bottom left) z-resolution and (bottom right) z-position. The green lines indicate the center of the cylinder (solid line) and the edges of the cylinder (dotted lines).

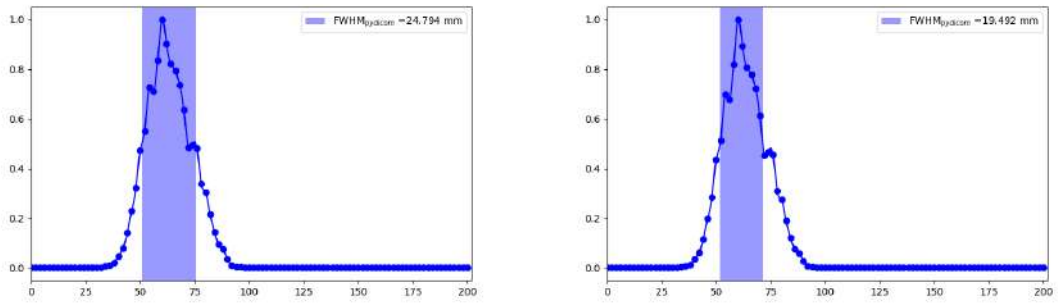

Figure 8.10: The reconstructed activity along the z-axis at the center of the lesion cylinder for iteration 8 (left) and iteration 9 (right) of the reconstruction. The behavior causing the jumps in z-resolution and z-position can be identified as there being three intersections of the spline with $0.5 * max(activity)$ in one iteration and two intersections in the next iteration.

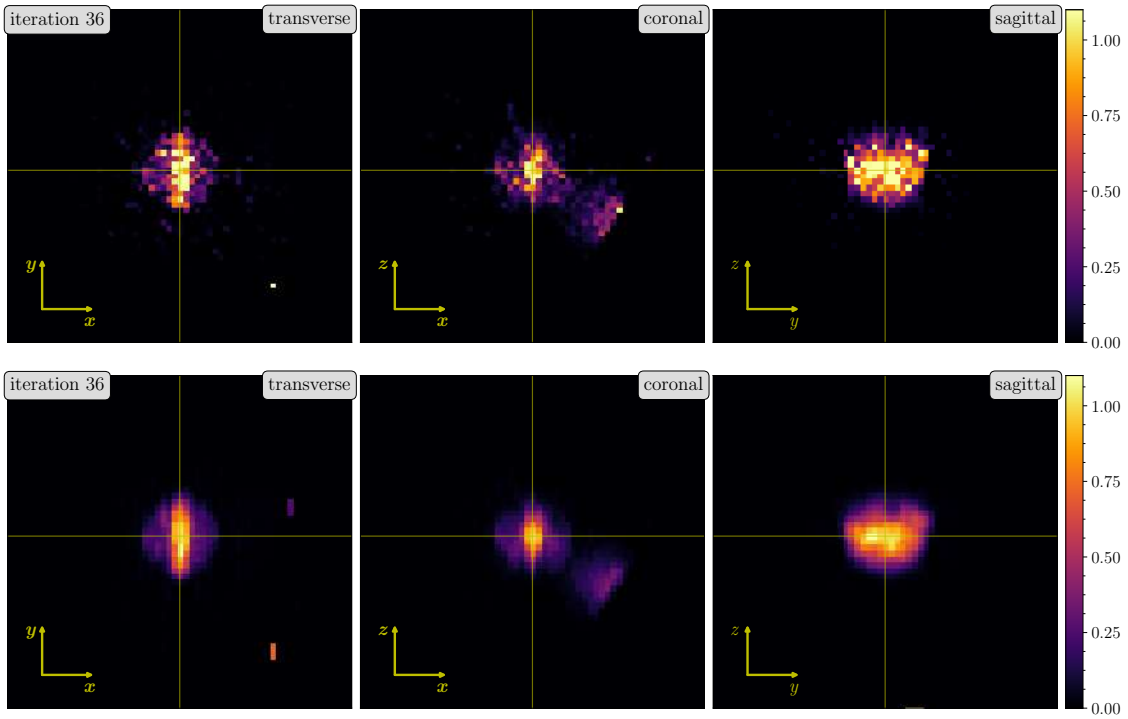

Figure 8.11: (top) Reconstructed image after 36 iterations with 2 x 2 x 2 mm^3 voxels. (bottom) Reconstructed image after 36 iterations with 2 x 2 x 2 mm^3 voxels with applied smoothing. The voxel activity is for every image normalized to the center voxel of the cylinder (indicated by crossing lines).

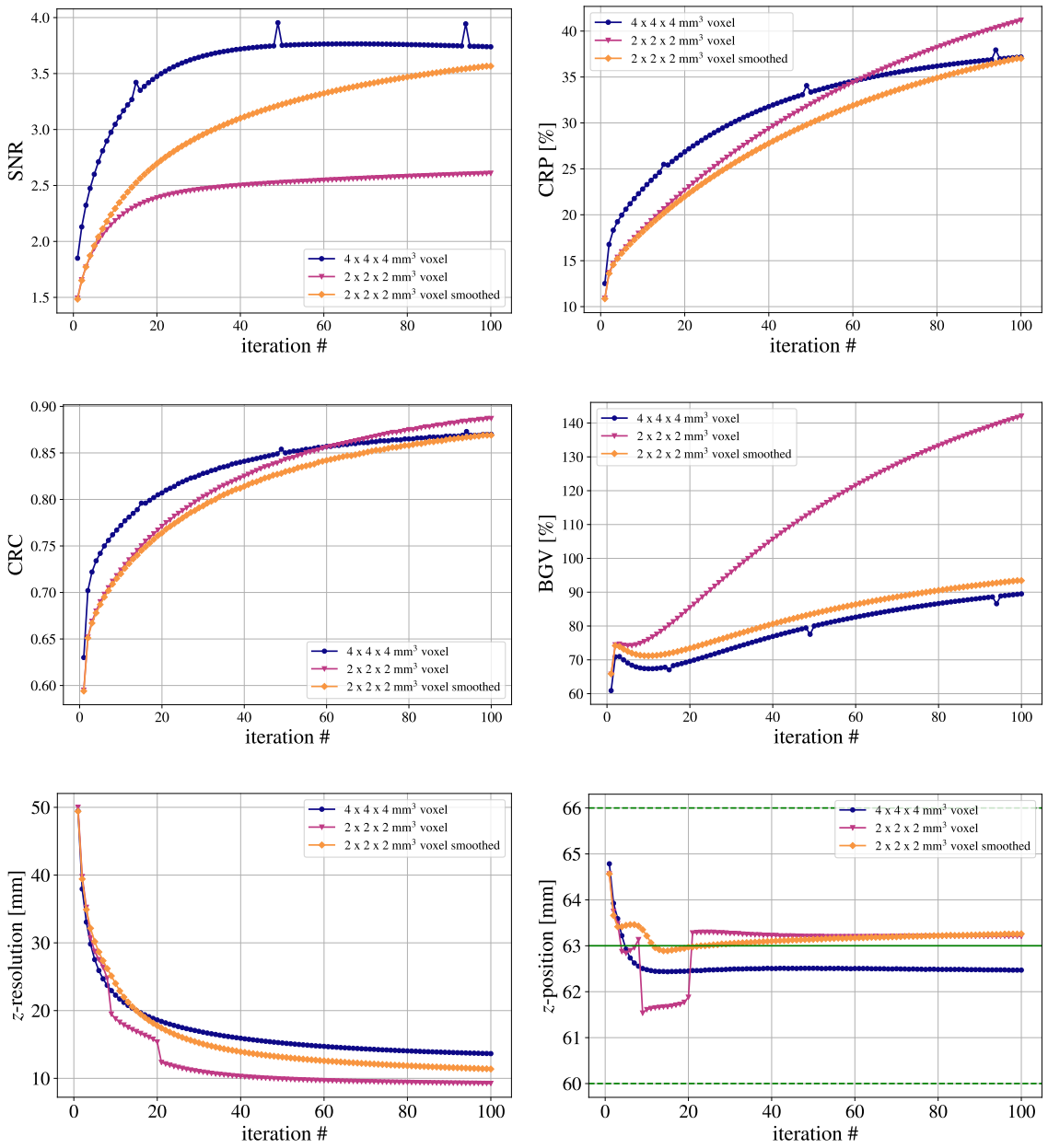

Figure 8.12: Image quality parameters as a function of reconstruction iteration and voxel size: (top left) the signal-to-noise ratio (SNR), (top right) contrast recovery percentage (CRP), (center left) contrast recovery coefficient (CRC), (center right) background variability (BGV), (bottom left) z-resolution and (bottom right) z-position. The green lines indicate the center of the cylinder (solid line) and the edges of the cylinder (dotted lines). results before and after applying smoothing are presented for the 2 x 2 x 2 mm^3 voxels.

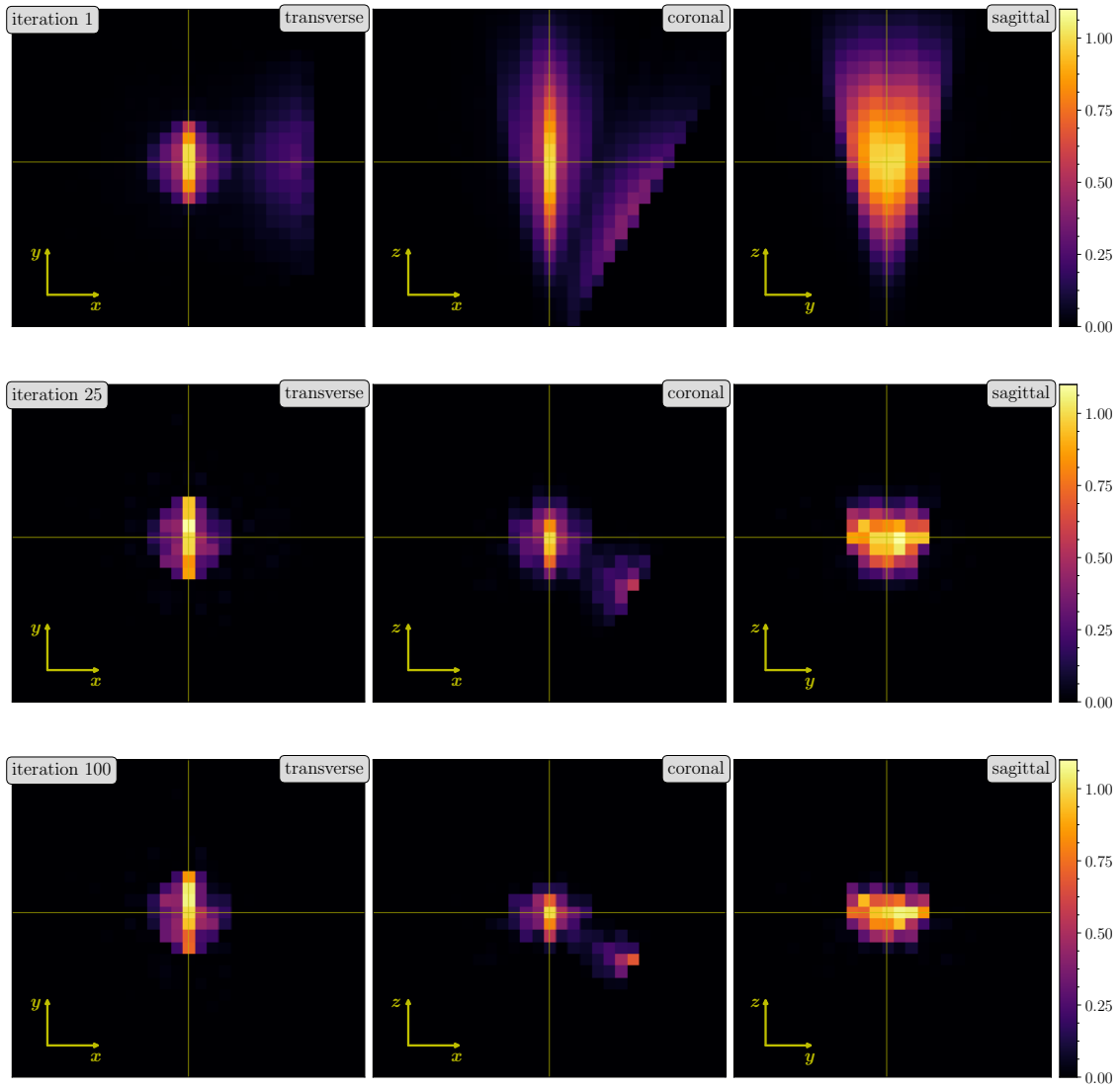

Figure 8.13: Slices of the reconstructed image after 1, 25 and 100 iterations in the transverse, coronal and sagittal view with 4 x 4 x 4 mm^3 voxel size at reconstruction iteration 1, 25 and 100. The voxel activity is for every image normalized to the center voxel of the cylinder (indicated by crossing lines).

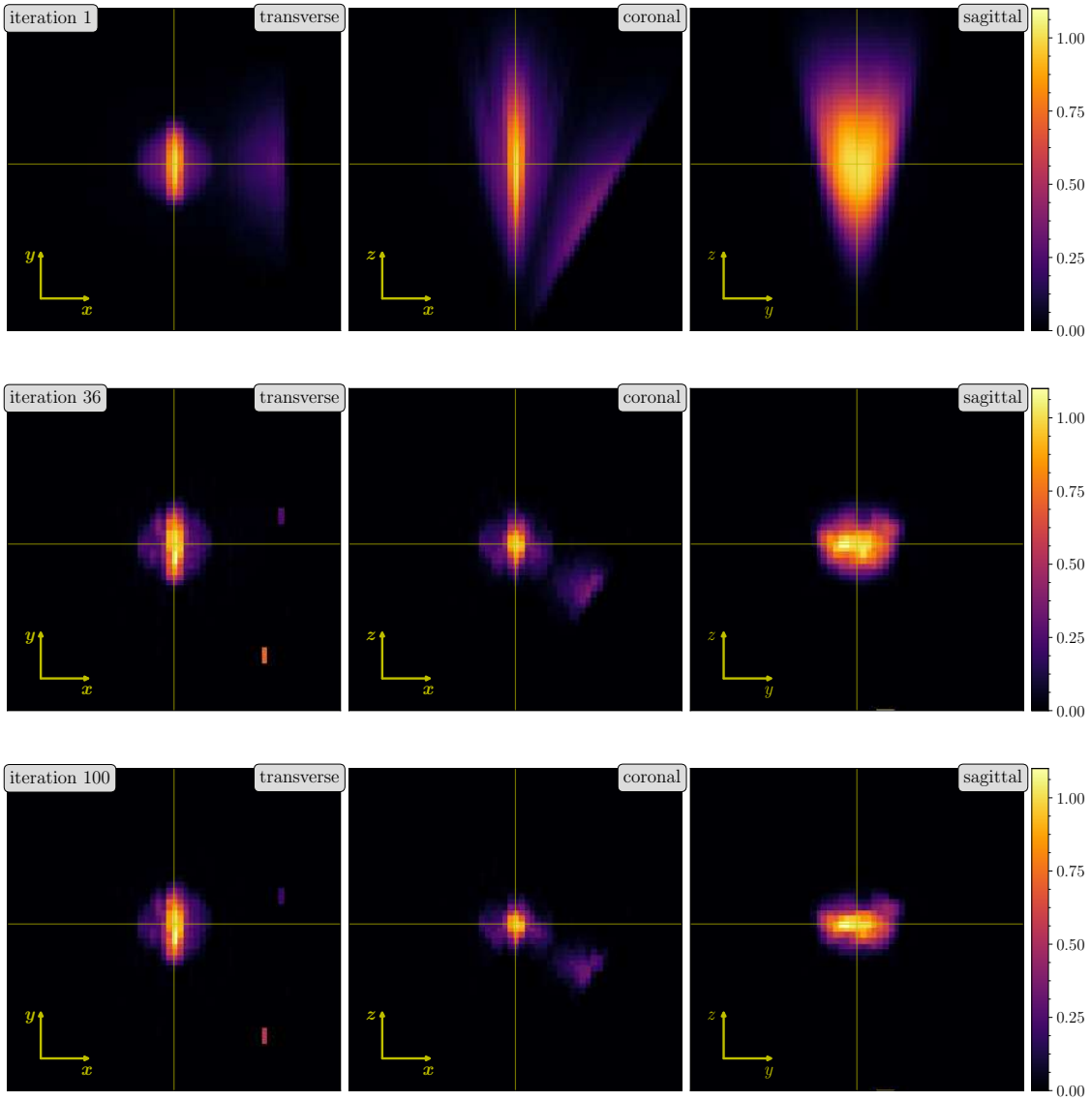

Figure 8.14: Slices of the reconstructed image after 1, 25 and 100 iterations in the transverse, coronal and sagittal view with 2 x 2 x 2 mm^3 voxel size at reconstruction iteration 1, 36 and 100. The voxel activity is for every image normalized to the center voxel of the cylinder (indicated by crossing lines).

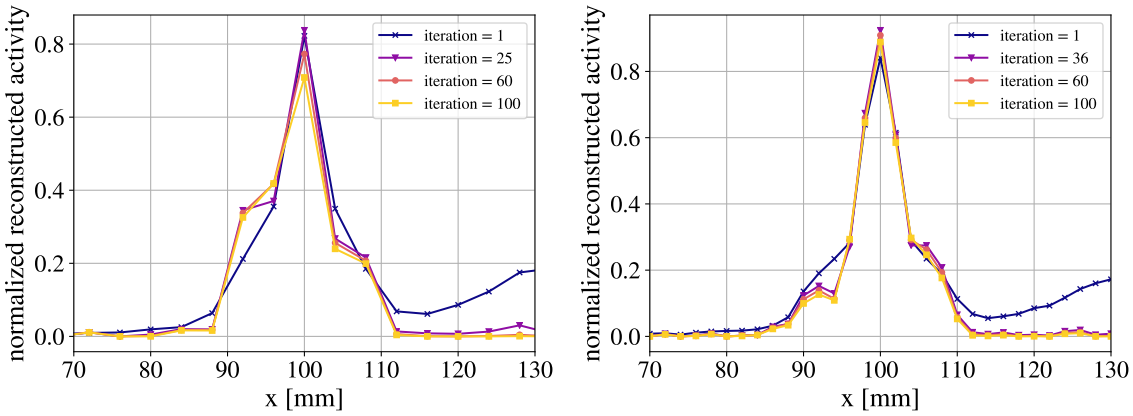

Figure 8.15: (left) Line profile parallel to the x-axis through the cylinder two voxels below center voxel at several reconstruction iterations, in the case of 4 x 4 x 4 mm^3 voxels. The activity is normalized to the activity in the center voxel of the cylinder. (right) Line profile parallel to the z-axis through the cylinder at several reconstruction iterations, in the case of 2 x 2 x 2 mm^3 voxels.

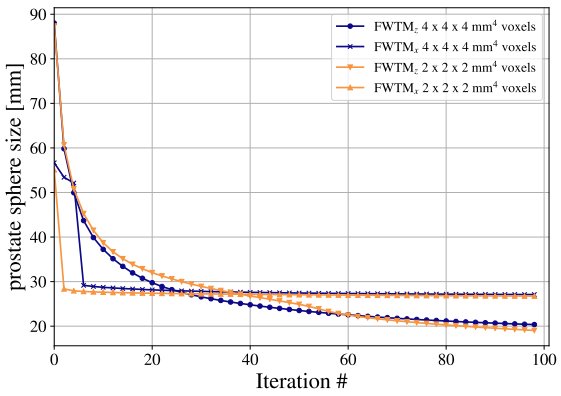

Figure 8.16: Full width tenth maximum of the prostate sphere along the z-axis (FWTM$_z$)) and the x-axis (FWTM$_x$) as a function of reconstruction iteration. They are determined at the center of the sphere in both directions. FWTM is presented for 4 x 4 x 4 mm^3 and 2 x 2 x 2 mm^3 voxels.

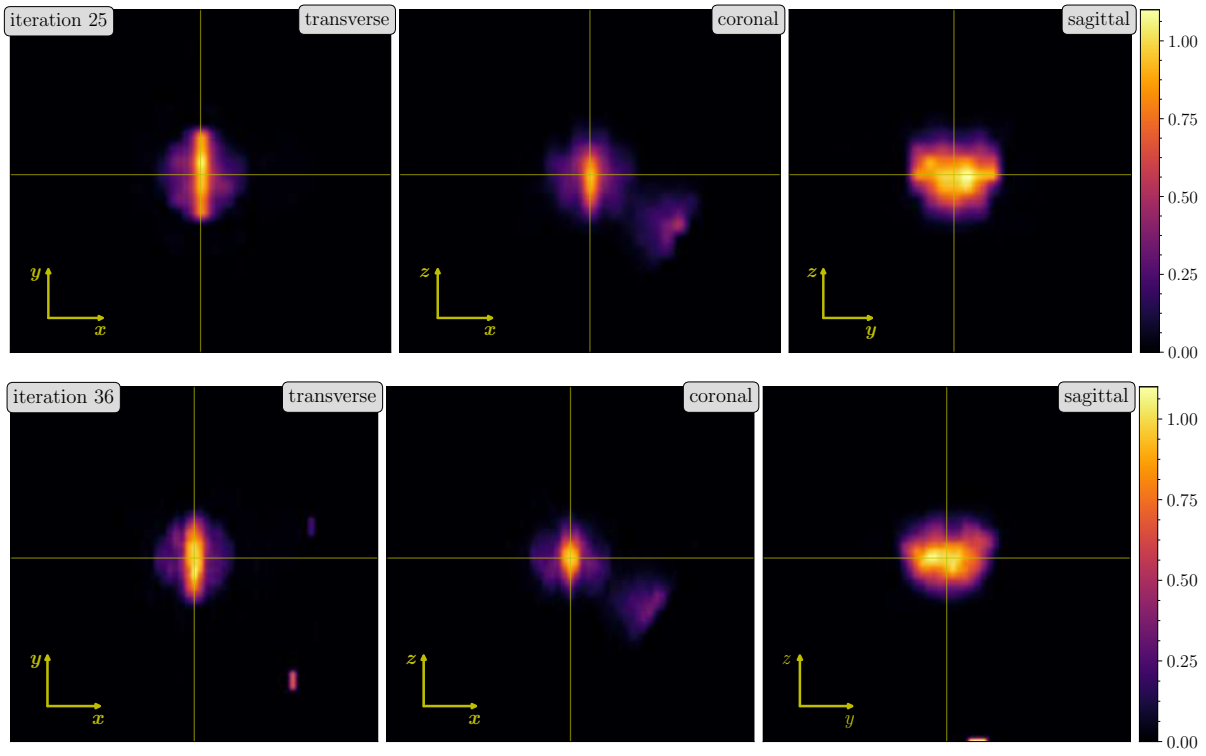

Figure 8.17: Reconstructed images with 4 x 4 x 4 mm^3 voxels (top) and 2 x 2 x 2 mm^3 voxels at their respective stopping iteration, smoothed with Hamming smoothing kernel. The voxel activity is for every image normalized to the center voxel of the cylinder (indicated by crossing lines).

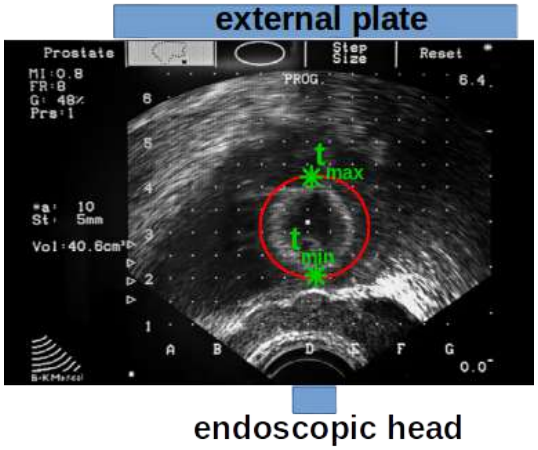

Figure 8.18: Ultrasound image of the prostate including possible region of interest. Adapted from [135].

8.5.1 Comparison between CASToR and EndoTOFPET-US Reconstruction

CASToR (customizable and advanced software for tomographic reconstruction) [136] is a well established and benchmarked open source multiplatform project for 4D emission and transmission tomographic reconstruction. It provides a number of different utilities to develop methods in image reconstruction: (1) specific projectors, (2) optimization algorithms, (3) dynamic data modeling and more. CASToR can be easily adapted to reconstruct data acquired or simulated with the EndoTOFPET-US prototype. Therefore, it can be used to verify the results of the EndoTOFPET-US reconstruction algorithm and to provide a benchmark in regard to image quality. The reconstruction is performed on the data with StB = 10:1 and CTR = 255 ps. CASToR reconstruction is performed using the MLEM (maximum-likelihood estimation-maximization) optimization, the same voxel size as for the EndoTOFPET-US reconstruction and otherwise the default settings (i.e. Siddon projector, no multithreading, no attenuation/scatter corrections, no multiray reconstruction). For the CASToR reconstruction, the stopping condition $\mathrm{FWTM}_Z <$ 28 mm is never fulfilled and image quality parameters do not reach a maximum within the first 100 iterations. Therefore, CASToR reconstruction is manually stopped after visual inspection of all reconstruction iterations. The image achieved with the CASToR reconstruction after 47 iterations and the image achieved with the EndoTOFPET-US reconstruction after 25 iterations are presented in figure 8.19. A qualitative comparison between the two images shows that the CASToR reconstructed image yields more blurring accompanied by a worse lesion-background-distinction than the EndoTOFPET-US reconstructed image. The image quality parameters at the stopping iteration achieved with the CASToR and EndoTOFPET-

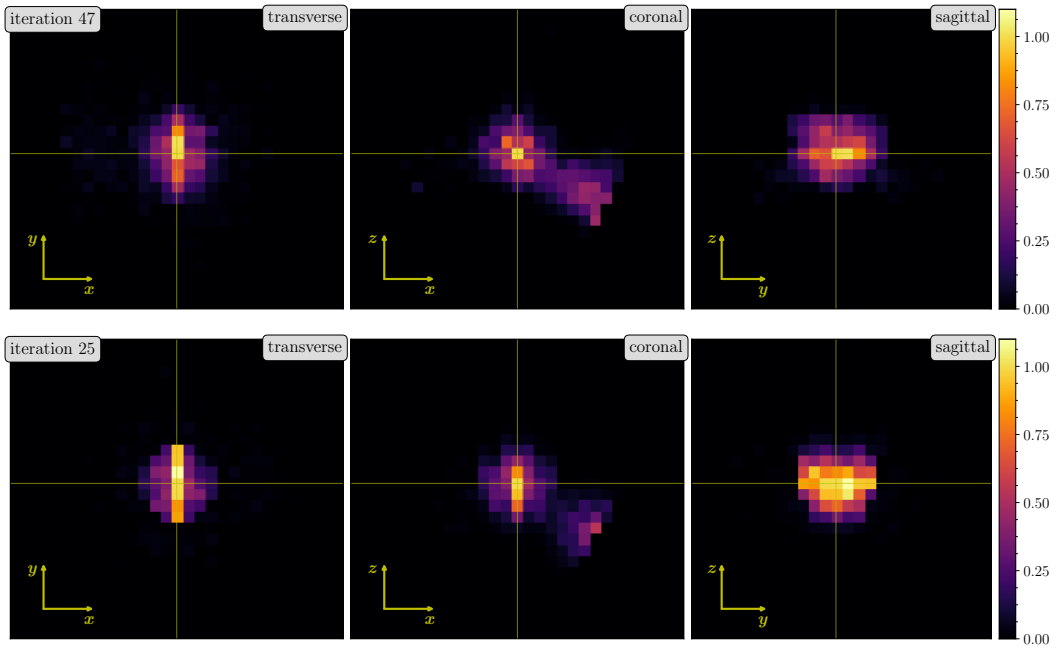

Figure 8.19: (top) Reconstructed image after 47 iterations utilizing the CASToR reconstrcution package with 4 x 4 x 4 mm^3 voxels. (bottom) Reconstructed image after 25 iterations utilizing the EndoTOFPET-US reconstrcution package with 4 x 4 x 4 mm^3 voxels. The voxel activity is for every image normalized to the center voxel of the cylinder (indicated by crossing lines).

US reconstruction software are summarized in table 8.4. Overall, the EndoTOFPET-US reconstruction achieves better results than the CASToR reconstruction. This is expected since the CASToR reconstruc-

Reconstruction	SNR	CRP [%]	CRC	BGV [%]	z-resolution [mm]	Δ z-position [mm]
EndoTOFPET-US	3.61	28.93	0.82	72.18	17.34	-0.52
CASToR	2.66	17.16	0.71	58.1	9.47	0.48

Table 8.4: Image quality parameters for both reconstruction softwares. Presented are contrast recovery percentage (CRP), contrast recovery coefficient (CRC), background variability (BGV), z-resolution and estimated z-position.

tion is not optimized for the EndoTOFPET-US detector. Nonetheless, the comparison is a good and necessary exercise that verifies a correct and proper functioning of the EndoTOFPET-US reconstruction.

8.5.2 Influence of Signal to Background Ratio on Image Quality

So far only simulations with a signal to background ratio (StB) of 10:1 was presented. In real patient measurements, however, the StB in unknown and varies from patient to patient. Patient data from [90] exhibit StB of approximately 3:1. Hence, a variety of StB is simulated to investigate the effects on lesion visibility and image quality. The StB ratios investigated are: 3:1, 5:1, 8:1, 10:1, 20:1 and 30:1. The activity in the bladder and the cylindric lesion are kept constant at 10.4 kBq/cm^3 and 4.5 kBq/cm^3, respectively, during all simulations. Only the background activity in the prostate sphere is changed depending on the StB. All simulations are performed for the same simulated time leading to a fixed number of collected coincidences from the cylinder. Figure 8.21 shows the coronal, transverse and sagittal view for all the investigated StB at their respective stopping iteration. Stopping iteration is determined for each simulation independently and is defined as the iteration at which the prostate sphere size along the z-axis reaches a value below 28 mm. A qualitative difference between low and high StB simulations

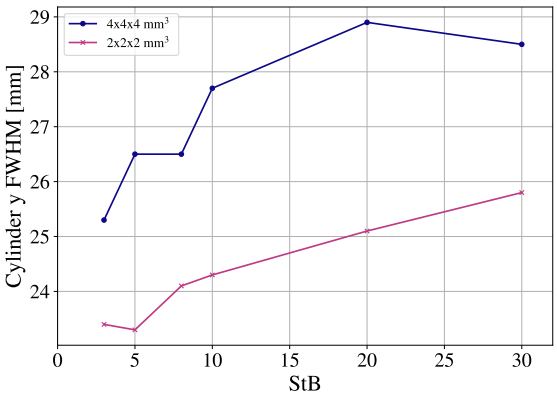

Figure 8.20: Cylinder full width half maximum (FWHM) along the y-axis as a function of signal to background ratio (StB).

can be seen immediately. In case of StB = 3:1, a low contrast between signal and background can be seen. In all other cases, the cylinder can be visually distinguished from the background. The cylinder size along the y-axis can be quantified with the FWHM of a spline interpolation on reconstructed activity. The FWHM of the cylinder along the y-axis as a function of StB is presented in figure 8.20 for both voxel sizes. 2 x 2 x 2 mm^3 voxels show a reduced FWHM for all StBs. This is probably due to the comparatively lower number of coincidences per voxel within the smaller voxels. It can lead to reconstructed activity that is smeared towards the edge of the sphere. Additionally, it can lead to an underestimation of lesion size. The minimum cylinder height is 23.18 mm for the 2 x 2 x 2 mm^3 and 24.9 mm for the 4 x 4 x 4 mm^3 voxels. 4 x 4 x 4 mm^3 voxels show a correct or slightly overestimated FWHM for StB = 10:1 or higher. All image quality parameters at stopping iteration for all StBs and both voxel sizes are summarized in table 8.5. It can be seen that SNR only improves slowly as a function of StB. This can be explained with a deterioration in the standard deviation of the background activity. BGV increases also as a function of StB. CRP and CRC clearly improve with increasing StB. Δ z position and z resolution seem to be independent of StB and are below 1.8 mm and 20.5 mm, respectively. Furthermore, it can be seen that smaller voxels seem to be better suited for low StB imaging as image quality does not disintegrate quite as quickly as for larger voxels.

In case of StB = 3:1, as mentioned above, the cylinder becomes indistinguishable from background

4 x 4 x 4 mm^3 voxels						
StB	SNR	CRP [%]	CRC	BGV [%]	z resolution [mm]	Δ z position [mm]
3:1	2.2	10.31	0.58	42.5	20.5	0.13
5:1	2.9	17.32	0.71	54.1	19.1	0.08
8:1	3.3	23.41	0.78	64.67	16.8	0.57
10:1	3.6	28.93	0.82	72.18	17.3	-0.52
20:1	3.3	35.5	0.86	97.6	18.75	0.7
30:1	3.8	45.3	0.90	108.1	16.7	0.73

2 x 2 x 2 mm^3 voxels smoothed						
StB	SNR	CRP [%]	CRC	BGV [%]	z resolution [mm]	Δ z position [mm]
3:1	2.3	14.6	0.67	57.1	15.6	1.3
5:1	2.6	17.4	0.71	60.0	14.7	0.2
8:1	3.0	23.6	0.78	71.0	13.0	1.8
10:1	3.1	27.0	0.81	79.6	14.2	0.1
20:1	3.3	38.0	0.87	107.4	15.1	1.5
30:1	3.6	47.8	0.91	120.7	12.5	0.6

Table 8.5: Image quality parameters as a function of signal to background ratio (StB) for both reconstruction voxel sizes. Presented are StB, contrast recovery percentage (CRP), contrast recovery coefficient (CRC), background variability (BGV), z-resolution and Δ z-position.

provided that it is not in the center of the FOV. A possible improvement of cylinder visibility at the edge of FOV can be achieved by moving the external plate and endoscopic head prototype. A simple movement scenario was simulated for StB = 3:1. The acquisitions are performed in three steps during which the position of the external plate and the endoscopic head prototype are stationary. Only the y-position of the two detector is changed between acquisitions. The positions of the endoscopic head prototype are $\begin{pmatrix} x \\ y \\ z \end{pmatrix} = \begin{pmatrix} 0 \\ 0 \\ 0 \end{pmatrix}, \begin{pmatrix} 0 \\ 7 \\ 0 \end{pmatrix}$ and $\begin{pmatrix} 0 \\ -7 \\ 0 \end{pmatrix}$, whereas the external plate positions are $\begin{pmatrix} x \\ y \\ z \end{pmatrix} = \begin{pmatrix} 0 \\ 0 \\ 200 \end{pmatrix}, \begin{pmatrix} 0 \\ 7 \\ 200 \end{pmatrix}$ and $\begin{pmatrix} 0 \\ -7 \\ 200 \end{pmatrix}$ (all numbers are in millimeter). The cylinder is at the same position as indicated in figure 8.7 (left). The time spent at each detector position is one third of the original simulation time, leaving the total simulation time unchanged. A comparison between the reconstructed image with and without movement of the detector is presented in figure 8.22. The inclusion of movement along the cylinder improves the cylinder visibility. However, its influence on reconstructed cylinder size in terms of FWHM along the y-axis is negligible. FWHM along the z-axis is slightly reduced (by 1 mm), but FWHM along the y-axis is effectively unchanged when including movement (24.9 mm without and 25.4 mm with movement). FWHM at the cylinder center along the x-axis is increased in the simulation containing detector movement, which is due to decreased statistics in the center of the cylinder compared to a static acquisition. CRC, CRP and SNR are increased by $\sim$1 %, while BGV is reduced by $\sim$1 % compared to static acquisition showing an insignificant improvement. In the case of a single lesion with maximum extension of 28 mm in x or y and location at the center of FOV, it can be concluded that detector movement yields no significant improvement in image quality. However, movement yields a slight improvement in lesion visibility.

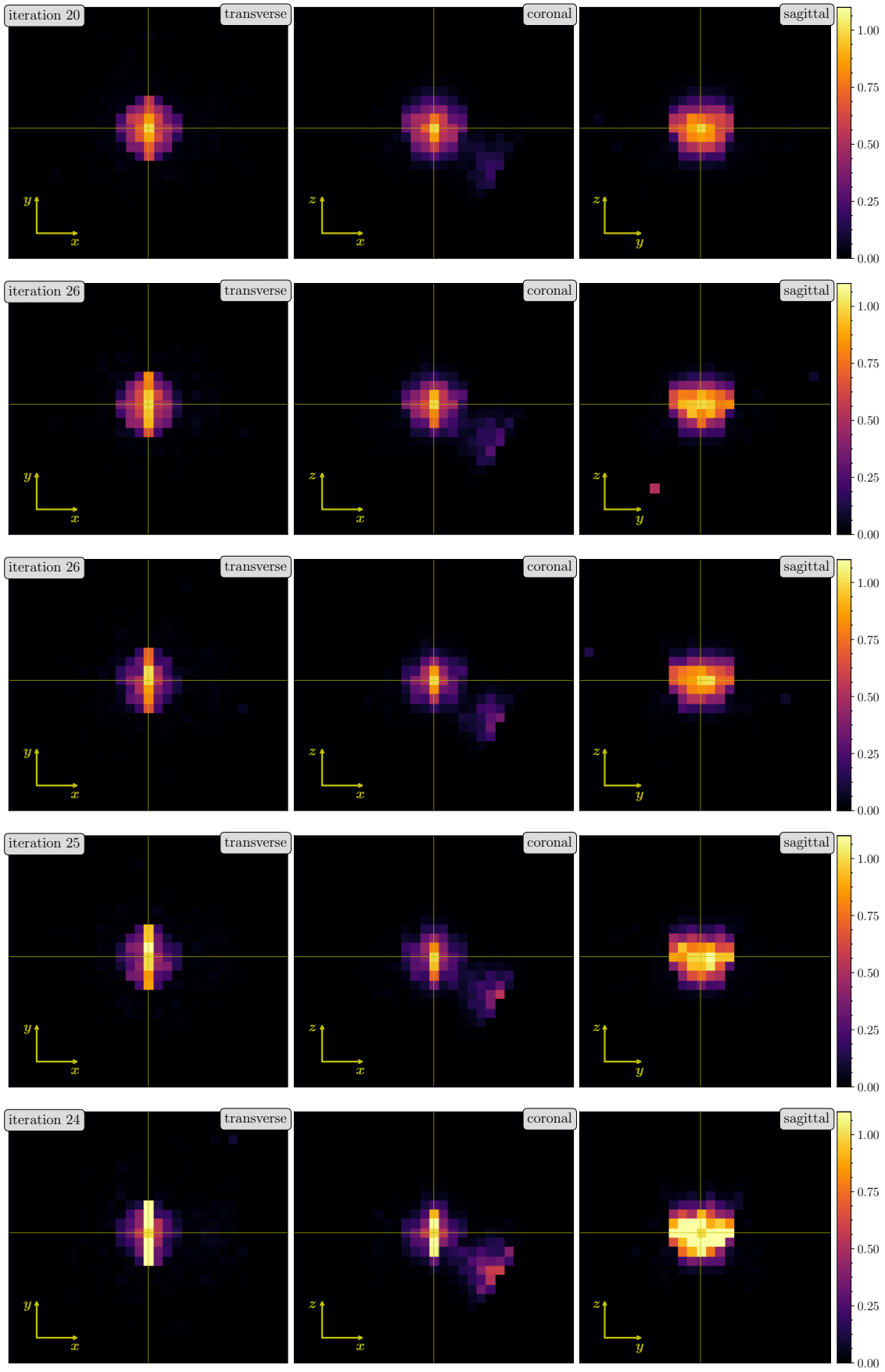

Figure 8.21: The transverse, coronal and sagittal view (left to right) of reconstructed activity for all simulated signal-to-background ratio (StB), from top to bottom: 3:1, 5:1, 8:1, 10:1, 20:1. The stopping iteration is specified in the top left corner of each coronal view. Voxel size is 4x4x4 mm^3. The voxel activity is for every image normalized to the center voxel of the cylinder (indicated by crossing lines).

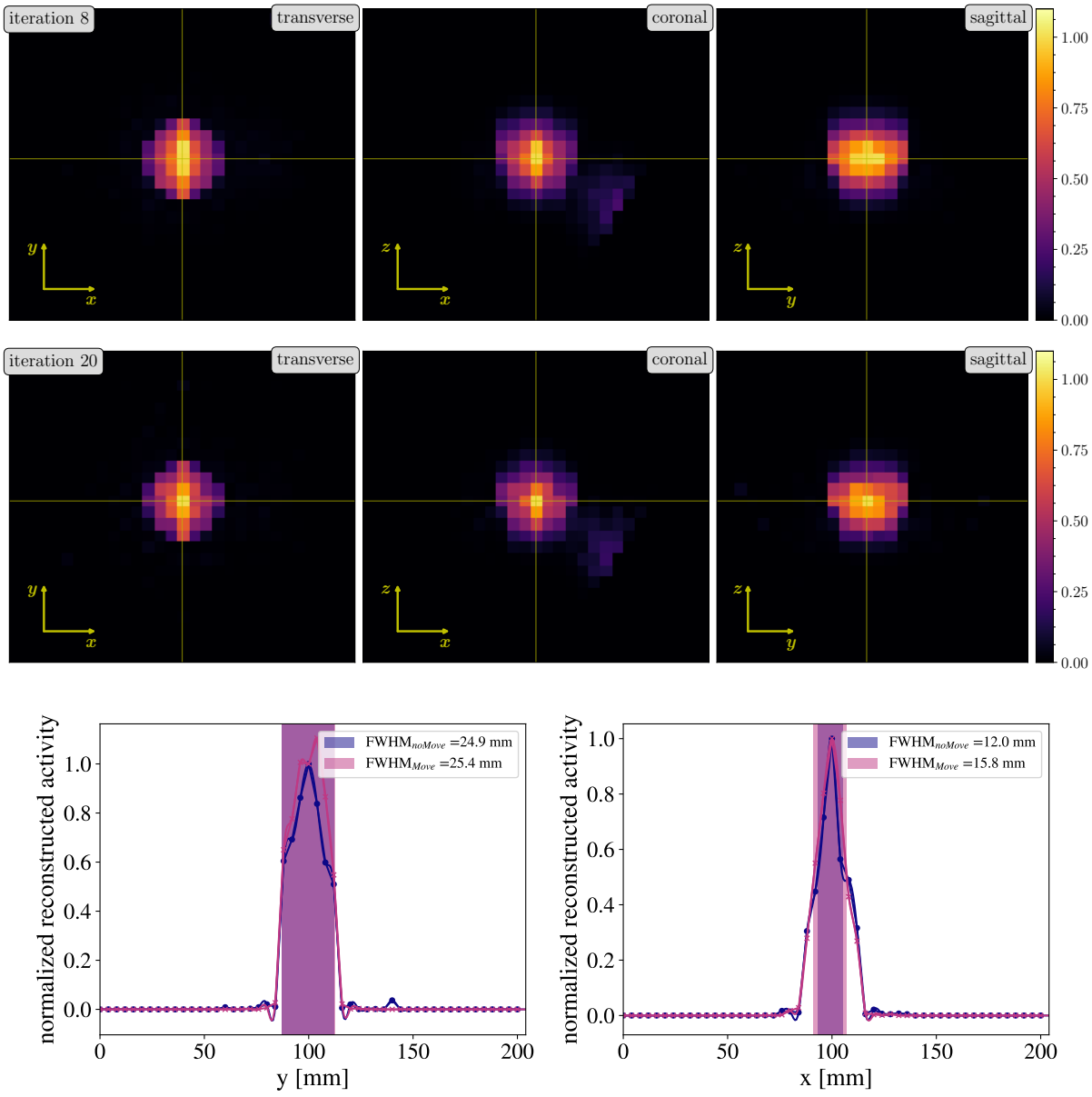

Figure 8.22: Comparison of the reconstructed image achieved with (top) and without (middle) movement of the detectors along the y-axis for StB = 3:1. The voxel size is 4 x 4 x 4 mm^3. The voxel activity is for every image normalized to the center voxel of the cylinder (indicated by crossing lines). The full width half maximum (FWHM) of the cylinder along the y-axis (bottom left) and the x-axis (bottom right) are also presented. The darker purple color stems from the two FWHM overlapping.

8.5.3 Influence of Coincidence Time Resolution on Image Quality

The qualitative influence of TOF on detector feasibility and image quality was already presented in section 8.4. It was demonstrated that TOF capabilities are necessary for the EndoTOFPET-US design because of its low angular coverage and small FOV. The influence of CTR on image quality is presented in this section. Simulations are performed during which only the CTR of the EndoTOFPET-US detector was changed. StB is fixed at 10:1 for all simulations presented in this section. Approximately 32000 coincidences from the cylinder region are acquired for each simulation. Figure 8.23 shows the reconstructed images of the application specific simulation scenario for selected CTR values (10 ps, 100 ps, 255 ps, 500 ps and no TOF) at their respective stopping iteration. It can be seen that improving the CTR has a big influence on image quality. The elongation of the reconstructed activity along the z-axis is inversely proportional to the CTR of the system. A 50 ps CTR already yields an artifact free reconstruction of the simulated activity distribution without elongation along the z-axis. The image quality parameters as a function of CTR at the respective stopping iteration are presented in figure 8.24. SNR, CRP and CRC are inversely proportional to CTR. Unexpectedly, the BGV does not show this proportionality. Overall, the low sensitivity of the EndoTOFPET-US detector always leads to a big BGV in comparison to conventional PET designs. Nonetheless, it was expected to see a more prominent relation between CTR and BGV. It is possible that the varying sensitivity over the background volume limits the achievable BGV. A high BGV, in turn, limits the achievable SNR. Furthermore, it is unexpected that 23 ps CTR yields slightly better results than 10 ps CTR. Although agreeing within the errors, SNR, CRC and CRP show a slightly higher value for 23 ps CTR compared to 10 ps CTR hinting towards a systematic effect. At this point no certain statement can be made as to why the behavior is observed. It can be seen that the image quality parameters change as a function of iteration for 23 ps CTR, while the reconstructed image and the image quality parameters do not show any dependence on reconstruction iteration for 10 ps CTR. Hence, it is possible that the reconstruction artificially enhances the result of the 23 ps simulation by allocating activity to the wrong volume.

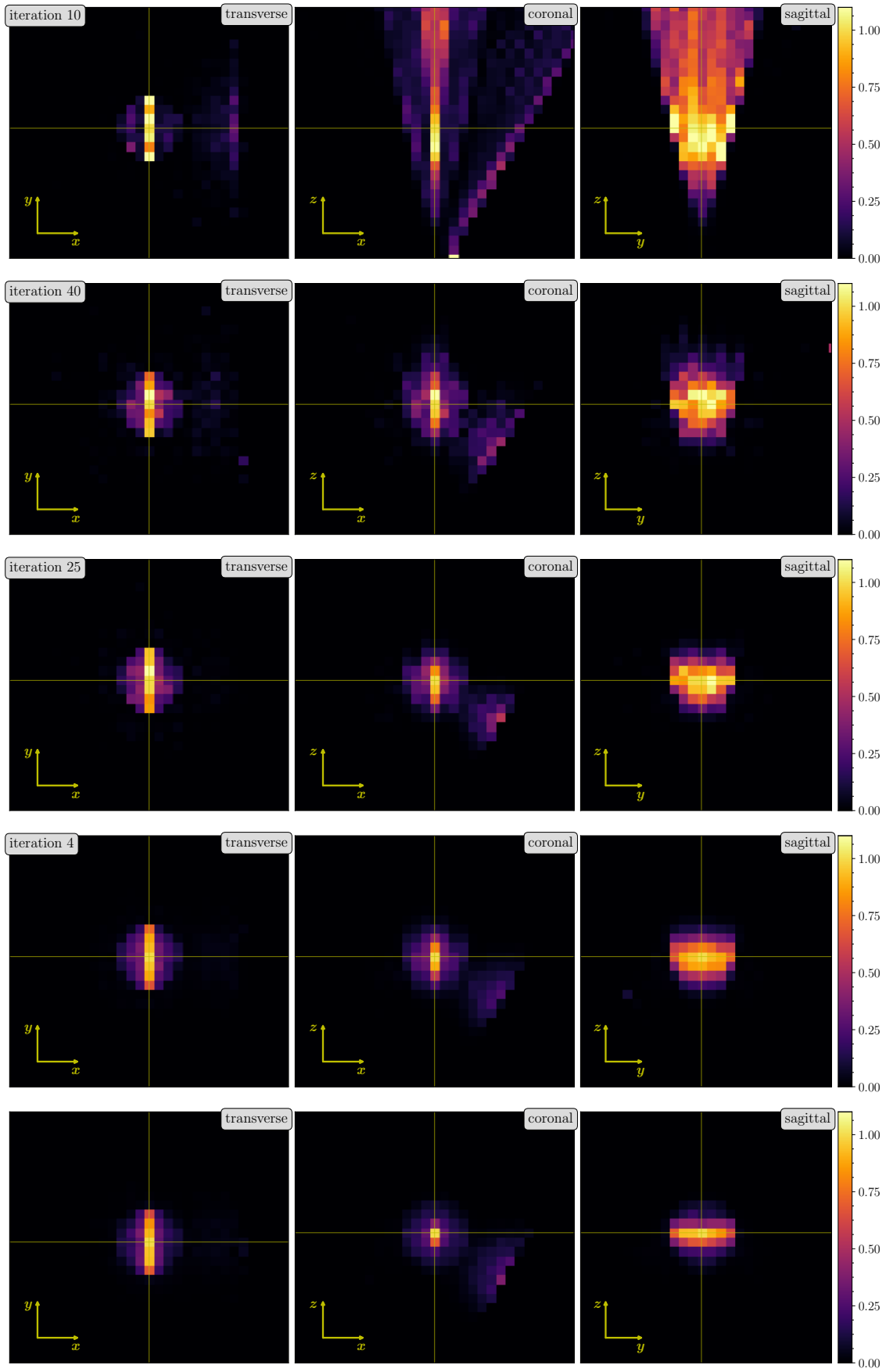

Figure 8.23: Reconstructed images at the respective stopping iteration from top to bottom with no TOF, 500 ps TOF, 255 ps TOF, 100 ps TOF and 10 ps TOF. From left to right the transverse, coronal and sagittal view of the cylinder are presented. The voxels have a size of 4 x 4 x 4 mm^3. The voxel activity is for every image normalized to the center voxel of the cylinder (indicated by crossing lines).

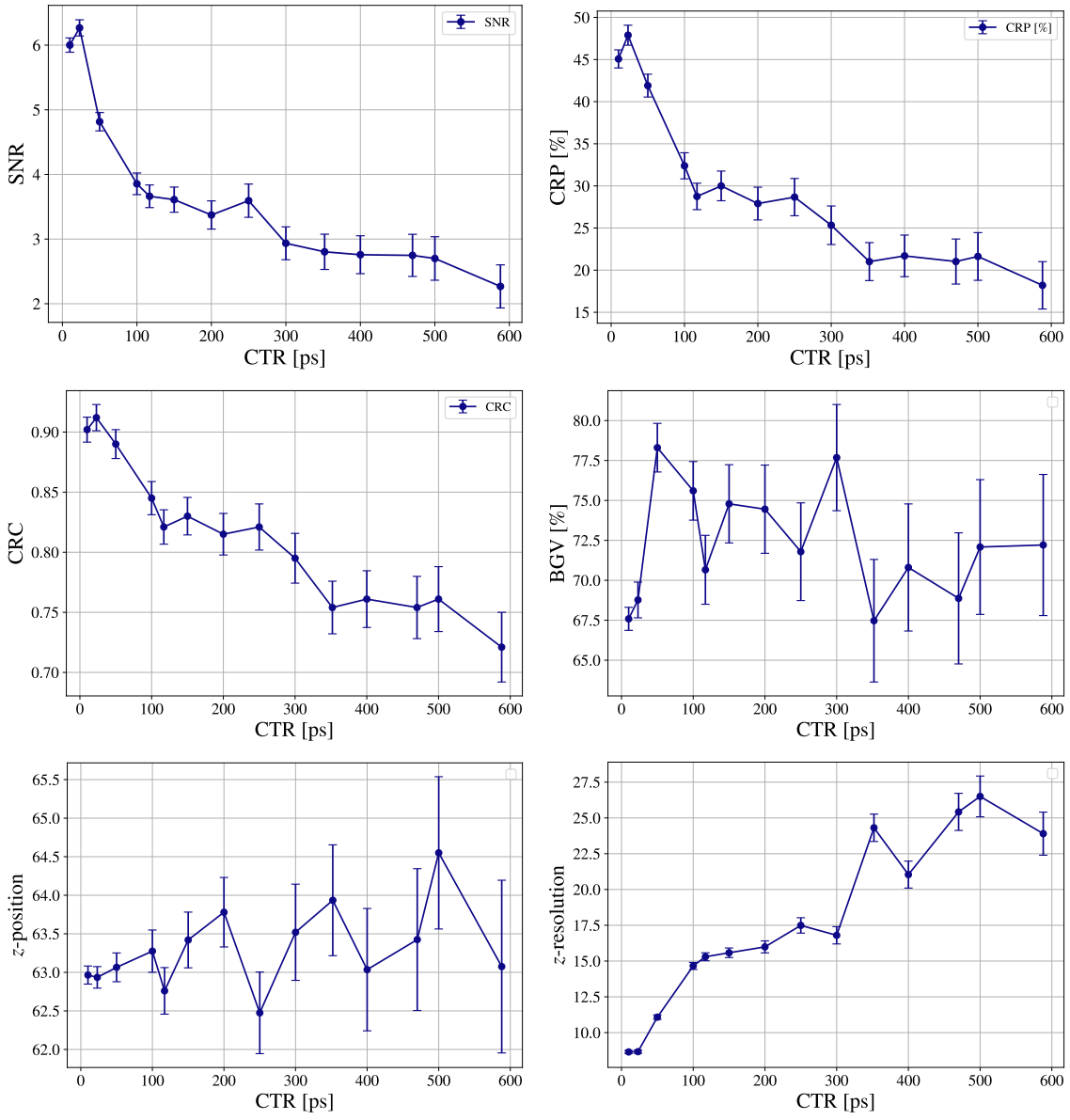

Figure 8.24: (top left) Signal-to-noise ratio (SNR), (top right) contrast recovery percentage (CRP), (center left) contrast recovery coefficient CRC, (center right) background variability (BGV), (bottom left) z resolution and (bottom right) Δ z-position as a function of coincidence time resolution (CTR). The green lines indicate the center of the cylinder (solid line) and the edges of the cylinder (dotted lines).

8.5.4 Conventional PET Scanners and Co-Registration

The EndoTOFPET-US detector's application, as mentioned, is mainly in intraoperative guidance during surgery or biopsy and not in diagnostics. Therefore, a so called prior will be present during the EndoTOFPET-US examination. It will be the diagnostic image that will most likely come from a PET/CT or PET/MRI image. Co-registration to the prior is essential for the EndoTOFPET-US detector in order to use the EndoTOFPET-US detector to its utmost efficiency. Since the PET and CT images or PET and MRI images of the prior are already co-registered, it is only necessary to match the EndoTOFPET-US image to one of these images. Two conventional PET scanners are simulated in order to investigate the imaging result achieved for a prostate specific application and the possibility to co-register the EndoTOFPET-US image to a prior of varying quality. Two scanners are chosen for the co-registration tests: (1) an older scanner with relatively low resolution and small FOV, (2) a state of the art scanner with excellent CTR. The older scanner is modeled after the Siemens CTI ECAT EXACT 922 scanner, whereas the state of the art scanner is modeled after the Digital Siemens Biograph Vision PET/CT system. The simulated detectors are only approximations of the real scanners since specifications such as crystal wrapping thickness, module and submodule pitch are not exactly known. Respective scanner specifications are summarized in table 8.6 [137] [138].

Scanner	Scint.	N_{rings}	N_{mod}	N_{submod}	N_{crys}	P_{axial} [mm]	P_{trans} [mm]	TOF [ps]
EXACT 922	BGO	3	48	1	8 x 8	20	6.39	no TOF
Biograph Vision	LYSO	8	38	4 x 2	5x5	20	3.2	210-215

Table 8.6: Specifications of the two conventional PET scanners simulated in this thesis. Given are the scintillator material (Scint.), number of rings (N_{rings}), number of modules (N_{mod}, number of submodules per module (N_{submod}), number of crystals per submodule (N_{crys}), axial pixel size (P_{axial}), transaxial pixel size (P_{trans}) and the TOF capabilities.

A representation of the simulation for both of the detectors is presented in figure 8.25. Activities for the two spheres and the cylinder are the same as for the EndoTOFPET-US simulation with StB = 10:1 (bladder: 10.4 kBq/cm^3, prostate sphere: 0.45 kBq/cm^3, lesion cylinder: 4.5 kBq/cm^3). The cylinder is placed in the center of the FOV like in the EndoTOFPET-US simulations. The simulation time is set so that the number of acquired coincidences in the cylinder is the same for all three detectors. Approximately 32000 coincidences from the cylinder are acquired for each detector. Furthermore, the same number and size of voxels is used for the reconstruction. The data from the ring detectors is reconstructed using the CASToR reconstruction framework with standard settings (i.e. Siddon projector, no multithreading, no attenuation/scatter corrections and no multi ray reconstruction). The same voxel size of 4 x 4 x 4 mm^3 was chosen for all three detectors to make sure that spill over from the lesion to the background depends only on the resolution of the detectors and not on the voxel size of the reconstruction. For the detector modeled after the Siemens Biograph Vision, CTR is set to 212.5 ps and each detector pixel is assumed to have the same time resolution of ∼150 ps. For the detector modeled after CTI ECAT EXACT 922, no TOF capabilities are included. Stopping iteration for the two ring detectors is defined as the iteration at which the maximum SNR is achieved. Reconstructed images of all three detectors at their respective stopping iteration are presented in figure 8.26 The cylinder can be clearly identified inside the warm prostate sphere in the transverse view of all three images. The tomographic information of the ring detectors

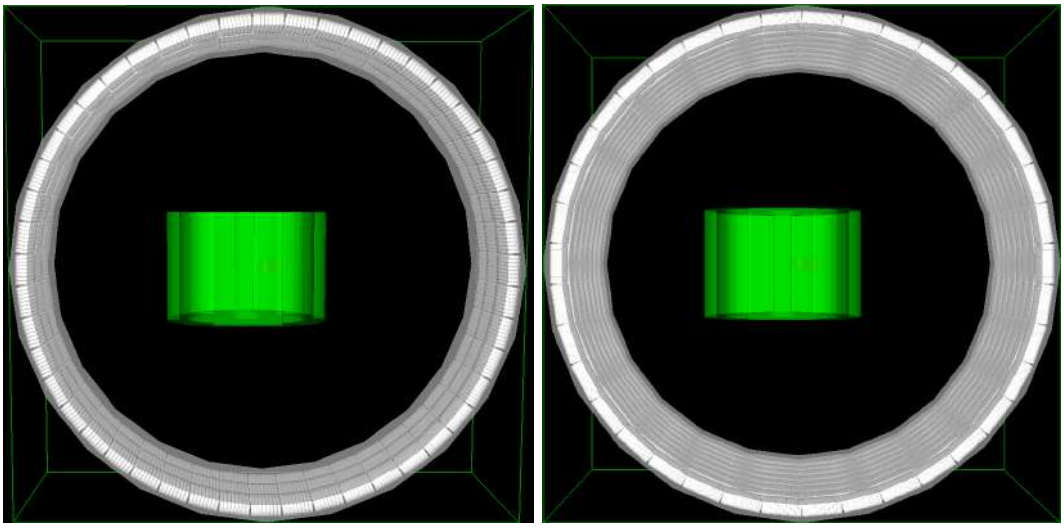

Figure 8.25: Simulation of the two ring detectors: detector modeled after CTI ECAT EXACT 922 (left) and the detector modeled after Siemens Biograph Vision PET/CT (right).

Scanner	StB	SNR	CRP [%]	CRC	BGV	z_{res} [mm]	x_{res} [mm]
EXACT 922	3:1	4.4	19.8	0.74	40.6	10.0	10.4
EXACT 922	10:1	6.5	55.0	0.93	78.0	9.9	9.9
Biograph Vision	3:1	5.5	17.2	0.71	28.3	9.3	9.3
Biograph Vision	10:1	9.7	55.9	0.93	51.8	6.1	6.2

Table 8.7: Image quality parameters for the two simulated ring detectors at the respective stopping iteration. Signal-to-noise ratio (SNR), contrast recovery percentage (CRP), contrast recovery coefficient (CRC), background variability (BGV), resolution along the z-axis (z_{res}) and resolution along the x-axis (x_res) are presented. Signal to background is 3:1 and 10:1.

results in the same spatial resolution in all three dimensions, meaning that no elongation in visible in any dimension. Only scattered photons from the bladder sphere are visible in the EndoTOFPET-US detector due to its limited FOV, whereas the bladder sphere is clearly visible and easily identified in the two ring detectors. For the detector modeled after the CTI ECAT EXACT 922, the FOV does not include the complete bladder sphere and shows a cut in the coronal view at the right and left of the image. The image quality parameters at the stopping iteration are reported in table 8.7 The detector modeled after the Digital Siemens Biograph Vision PET/CT scanner clearly achieves the best results in terms of image quality as expected. At this point it has to be mentioned that the results achieved with the two ring detectors are not representative of what can potentially be achieved with them. The image quality of the two ring detectors can potentially be improved with a highly optimized reconstruction software.

Images achieved with the EndoTOFPET-US prototype show good resemblance of the simulated activity distribution and allow for easy co-registration with the conventional PET scanner images. Co-registration is performed using the python scikit package. This python based software package can compare two similar images and calculate the shift between them. Figure A.1 shows the overlayed trans-

verse views of the EndoTOFPET-US and ring PET scanner images before and after co-registration. In case of the scanner modeled after the Digital Siemens Biograph Vision, the calculated shift in voxels between the two images is $(9, 1)$. It can be seen that the cylinders are correctly aligned after co-registration. Hence, the exact location of the cylinder in z can be derived either from the center of the FWHM of the EndoTOFPET-US image or from the position of the cylinder in the prior. The 37 mm bladder sphere has to be masked in the image of the ring scanner in order to achieve correct co-registration. If the 37 mm sphere is not masked, wrong matching can occur where the prostate sphere of the EndoTOFPET-US image gets matched to the bladder sphere of the ring detector. It is unlikely that this happens in a real imaging scenario because the size difference between the prostate and the bladder in human patients is more pronounced than in the proposed simulation scenario. Co-registration of the EndoTOFPET-US prototype to the detector modeled after the Exact922 works in the same way and is presented in the Appendix.

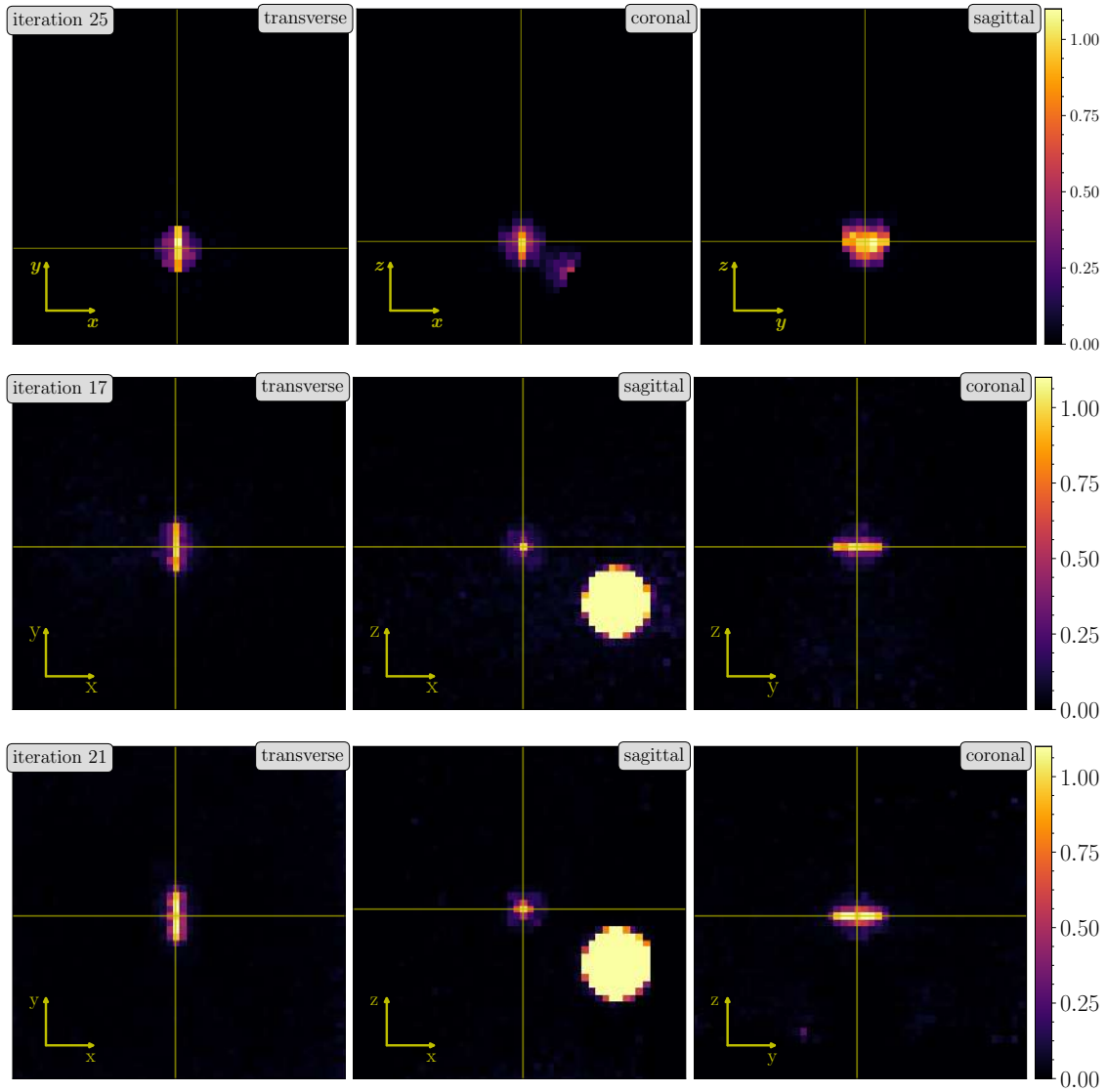

Figure 8.26: Reconstructed images of the same scenario with all three detectors at their respective stopping iteration: (top) EndoTOFPET-US detector, (center) detector modeled after Siemens Biograph Vision PET/CT, (bottom) detector modeled after CTI ECAT EXACT 922. The voxel size is 4 x 4 x 4 mm^3. All images are normalized to the center voxel of the cylindric lesion inlay indicated by the yellow lines. The transverse, coronal and sagittal view are presented from left to right.

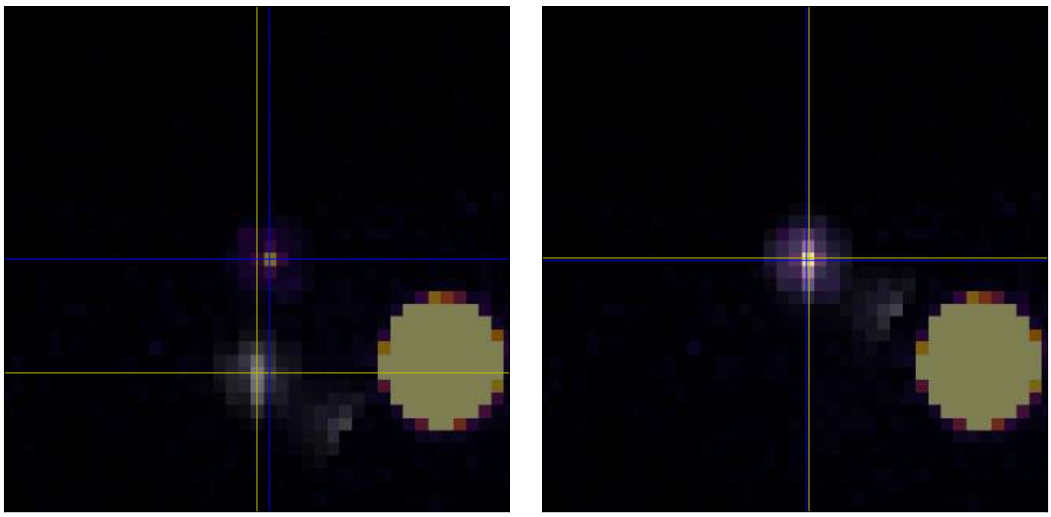

Figure 8.27: Overlayed transverse images of the cylinder center acquired with the EndoTOFPET-US detector and the scanner modeled after the Digital Siemens Biograph Vision before (left) and after (right) co-registration. The EndoTOFPET-US image is visualized with a gray color scheme and the image achieved with the ring detector is visualized with the inferno color scheme. The intersection of the blue lines indicate the center position of the cylinder in the image acquired with the detector modeled after the Siemens Biograph Vision and the intersection of the yellow lines indicate the center of the cylinder in the image EndoTOFPET-US prototype image. The voxel size is 4 x 4 x 4 mm^3 for both images.

8.6 Sensitivity Study

The sensitivity of the detector is of vital importance to the feasibility of the detector concept. All presented simulations performed with the NEMA IEC body phantom so far consider a very long acquisition time of ∼12 hours. This is in part due to the distance between the endoscopic head prototype and the hot volume in the phantom. The prostate length along the z-axis usually is between 37 mm and 41 mm. Since it is reasonable to assume that a prostate lesion is inside the prostate or on its surface, the maximum distance of the lesion to the endoscopic head is ∼45 mm. Therefore, the distance between lesion and endoscopic head will be smaller in most cases than simulated so far. Nevertheless, sensitivity might be reduced due to a smaller field of view (FOV) if the lesion is closer to the endoscopic head. The FOV of the EndoTOFPET-US detector is a strong function of distance to the endoscopic head. It is a quadratic pyramid trunk: one side is the size of the endoscopic head and another side is the size of the external plate. The opening angle α of the FOV for given detector sizes is defined by the distance between the two detectors. In case of $d = 200$ mm between endoscopic head prototype and external plate, the opening angle is $\alpha = 29.51°$. The side length FOV_{side} of the 2D FOV square as a function of the distance to the endosopic head design is presented in figure 8.28 for the prototype and the original endoscopic head design. The biggest difference in FOV size occurs closest to the endoscopic head where it is most significant for imaging. The FOV size in the region of interest (0 to 50 mm) varies from 9.6 x 9.6 mm^2 to ∼66.2 x 66.2 mm^2 for the prototype and from 14.48 x 14.48 mm^2 to ∼69.9 x 69.9 mm^2 for the original design of the endoscopic head. The FOV sizes at $d = 63$ mm are 80.9 x 80.9 mm^2 for the endoscopic head prototype and 84.3 x 84.3 mm^2 for the original design of the endoscopic head. As a first step to investigate

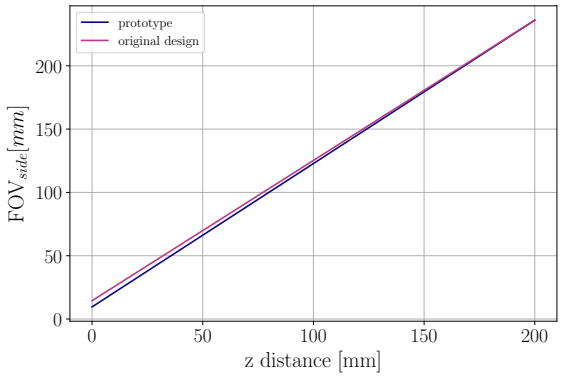

Figure 8.28: Edge size of the 2D field of view (FOV) square as a function of distance to the endoscopic head for the endoscopic head prototype and the original design.

sensitivity, a true point source is simulated in the center of FOV at several distances to the endoscopic head prototype and the original endoscopic head design. The back-to-back photon option in GAMOS is chosen and a total of 10^7 photon pairs are simulated at each position. Energy cuts on coincidences are performed at 100 keV and 700 keV. The number of coincidences acquired with the prototype and original design of the endoscopic head are presented in figure 8.29. It is evident from figure 8.29 that endoscopic-head-lesion-distance is a crucial aspect for the proposed detector design. In case of the prototype, the numbers of coincidences are ∼182000 at $d = 1$ cm and ∼7200 at $d = 7$ cm. In case of the original design, the numbers of coincidences are ∼314000 at $d = 1$ cm and ∼14000 at $d = 7$ cm. Thus, changing the distance of the point source by 6 cm decreases the number of acquired coincidences by a factor of ∼25.3

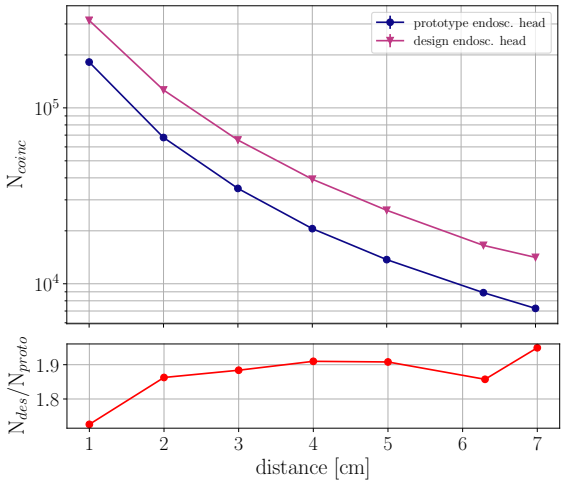

Figure 8.29: (top) Number of detected coincidences as a function of source distance to the endoscopic prototype (blue) and the original endoscopic head design (pink). A true point source at each position and a total of 10^7 events per position are simulated. (bottom) Number of coincidences detected by the original endoscopic head design divided by the number of coincidences detected with the endoscopic head prototype.

for the prototype and ∼22.4 for the original design. This is a significant effect. The original endoscopic head design has on average a factor ∼1.87 higher sensitivity than the endoscopic head prototype over the first 7 cm of the FOV.

Furthermore, a 2D sensitivity map for the endoscopic head prototype is generated. Simulations determining the sensitivity as a function of axial distance to the FOV center are performed for this purpose. Simulations of point sources along several LORs originating from the center of the endoscopic head prototype are performed. The LORs are defined by the angle α_{LOR} between the endoscopic head normal vector and the LOR as indicated in figure 8.30. The number of acquired coincidences for several

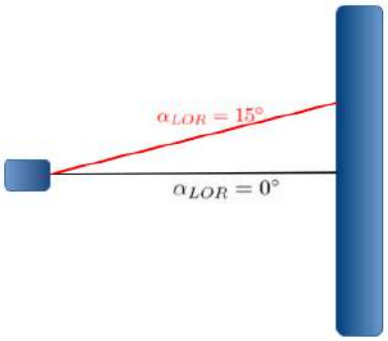

Figure 8.30: Definition of angle α_{LOR}.

α_{LOR} at different distances along the z-axis to the endoscopic head are presented in figure 8.31. α_{LOR} is 9.01°, 17.61°, 25.46° and 32.41° corresponding to a distance of 1 cm, 2 cm, 3 cm and 4 cm to the 0° LOR at $z = 6.3$ cm. A radial distance of 4 cm is close to the maximum FOV half side length that is 4.05 cm at $z = 6.3$. A rough sensitivity heatmap can be estimated from this information by using linear

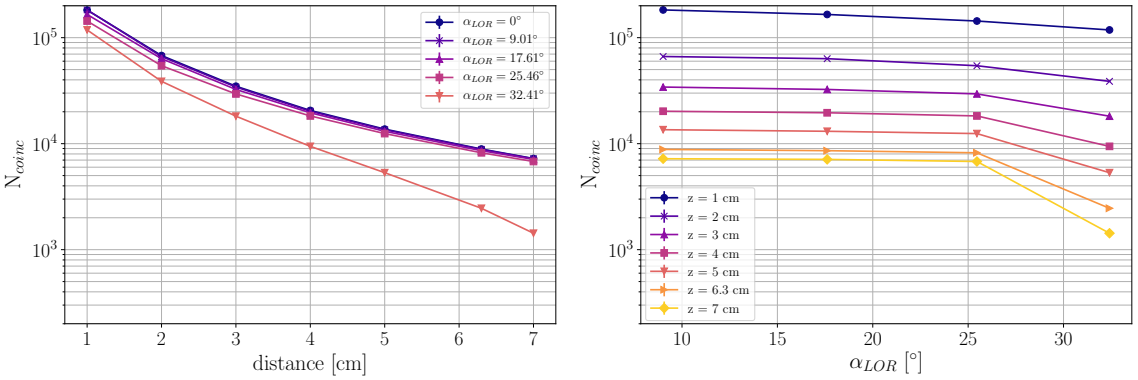

Figure 8.31: (left) Number of acquired coincidences as a function of distance along the z-axis to the endoscopic head at a specific α_{LOR}. (right) Number of coincidences acquired as a function of α_{LOR} at a specific z. True point sources were simulated at the specified positions and a total of 10^7 events per position were simulated.

interpolation of the data. Asymmetric voxels are used to present the sensitivity map. Voxel size is defined by the smallest distance of simulated point sources, being 1 cm in z and 0.16 cm in y. No interpolation of the data is performed along the z-axis, while a linear interpolation of the data is performed along the y-axis as presented in 8.31. A Gaussian smearing is performed on the voxelized interpolated data. The 2D sensitivity map is presented in figure 8.32. The heatmap represents the number of counts per second per simulated kBq. The use of 1 cm voxel size in z leads to a slight underestimation of sensitivity at the beginning and an overestimation at the end of each 1 cm element, which is slightly reduced by the Gaussian smearing. An estimate on data taking time for the presented scenario as a function of cylinder distance to the endoscopic head can be performed, assuming the overall number of coincidences shall stay unchanged. It has to be taken into account that the cylinder from the application-specific simulation is bigger than the FOV side length if it is at a distance of 1 cm to the endoscopic head prototype. Sensitivity is close to constant for the entire cylinder volume in case of $z > 2$ cm. Hence, the acquisition time can be estimated by

$$t^{N}_{acqu}(Z) = \frac{t^{N_{coinc}}_{acqu}(Z = 6.3)}{S(Z)/S(Z = 6.3)} \tag{8.5}$$

with $t^{N_{coinc}}_{acqu}(Z)$ being the time it takes to acquire N coincidences at a distance Z from the endoscopic head and $S(Z)$ the mean sensitivity at a distance Z. In case of $z \leq 2$, an optimal acquisition scenario that reduces the acquisition time to a minimum can be determined. In a real imaging scenario, the optimal acquisition scenario can be determined from the prior. The sensitivity boost and the acquisition time $t^{32000}_{acqu}(Z)$ as a function of cylinder distance are presented in figure 8.33. They are calculated so that the number of acquired coincidences at the edge of the cylinder is unchanged. This leads to an increase of acquired coincidences in the center of the lesion (ratio between center of lesion and edge of lesion is 1.5 for $z = 1$ cm and 18 for $z = 2$ cm). A maximum sensitivity boost of 7 can be achieved over the full cylinder in this specific scenario at $z = 2$ cm, leading to t^{32000}_{acqu} of ∼2 hours. However, this analysis does not take into account reduced Compton scattering probability in direction of the endoscopic head and increased Compton scattering probability in direction of the external plate arising from reduced or increased photon path length. It can be seen that the acquisition time reaches a minimum at $z = 2$ cm. The acquisition times are still large. Therefore, further options to reduce acquisition time are examined.

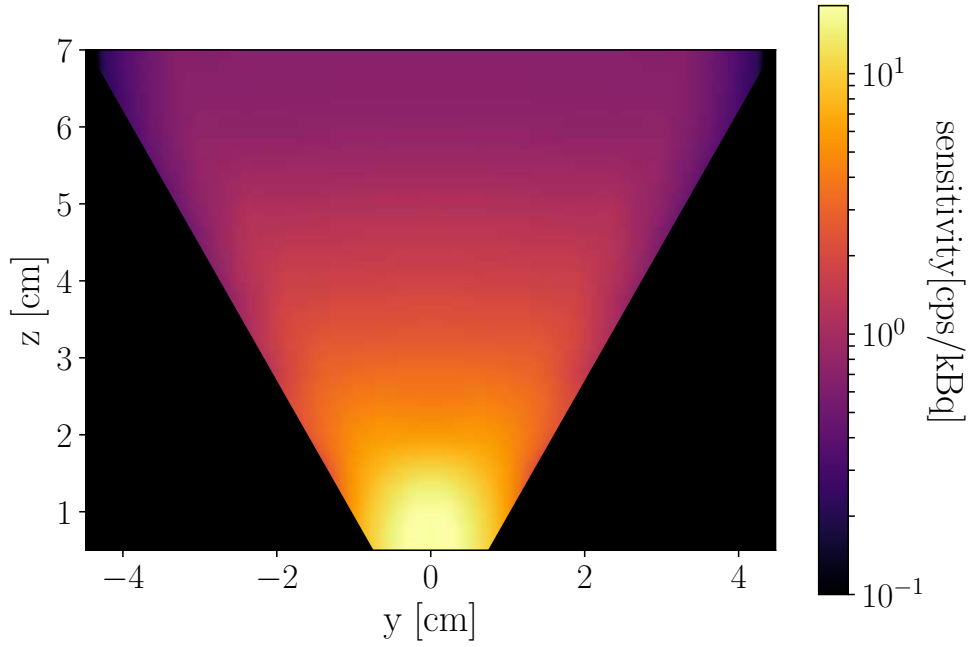

Figure 8.32: The inter- and extrapolated sensitivity map of the EndoTOFPET-US prototype in y and z. The map looks exactly the same in x and z. A Gaussian smoothing is applied to data with 1 x 0.16 cm^2 voxels. The color mapping represents the number of coincidences measured by the EndoTOFPET-US prototype if a point source with 1 kBq activity is positioned at the respective position.

Qualitative and quantitative image parameters as a function of simulation time can indicate if further reductions of acquisition time are possible without sacrificing performance. In figure 8.34, all image quality parameters at the stopping iteration are presented as a function of acquisition time. Maximum acquisition time as specified before is 12.13 hours. The stopping iteration, however, needs to be redefined if the acquisition time is smaller than $1/3 \cdot 12.13 = 4.04$ hours. This is because either the FWTM does not reach 28 mm anymore or the image degrades far before it is reached. The degradation happens due to the low number of coincidences per reconstruction voxel which leads to rather big fluctuations (on the order of $sqrtN_{Vox}/N_{Vox}$) in the first reconstruction iteration. These enhance in further reconstruction iterations and lead to a strong pixelization of the image. Stopping iteration is defined by visual inspection for all reconstructions performed with t_{acqu} <4 hours as a result. The reconstructed images for several acquisition times are presented in figure 8.35. As evident from figures 8.34 and 8.35, image quality is stable for acquisition times of twelve to six hours with an activity typical for prostate lesions. For acquisition times below six hours, a clear drop in image quality is observed. Especially large standard deviations of the reconstruction result occur for lower acquisition times. Hence, the acquisition time can be at least reduced by a factor of two. The acquisition time can be further reduced provided that lower image quality is acceptable or if the image can still be correctly co-registered to the prior. In the second case the prior can be used for correct localization of the lesion. It is possible to perform correct co-registration until an acquisition time of ∼3 hours. Beyond that the co-registration performs the same mis-alignment by exactly one voxel along the z-axis. The co-registered images for an acquisition time of 3 hours and an acquisition time of 72 minutes is presented in figure 8.36

It can be deduced from the two performed studies that an acquisition time of ∼1 - 2.5 hours is necessary

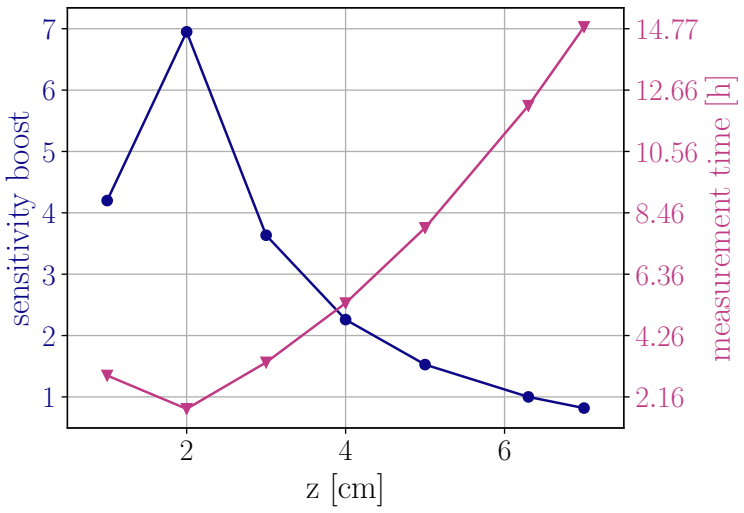

Figure 8.33: Sensitivity boost and respective acquisition time to acquire a constant number of coincidences as a function of lesion distance to the endoscopic head module. Relative errors are just the uncertainties on the number of coincidences acquired quadratically summed and are rather small (not visible behind marker).

to obtain a stable image quality if the distance from endoscopic head prototype to lesion is in the range of 1 cm to 4 cm and a typical activity achieved with PSMA is considered. If correct co-registration to the prior is sufficient, the acquisition time can be further reduced to ∼15-38 minutes. These numbers, however, are only true for the EndoTOFPET-US protoype. If an increase in sensitivity of approximately 1.87 (as presented in figure 8.29) is assumed for the original EndoTOFPET-US design, the acquisition time can be reduced to ∼32 up to ∼80 minutes.

The presented studies, however, do not yield exact knowledge of how long the acquisition time needs to be in a real patient scenario. Several factors play a role in the time it takes to locate and image prostate lesions in a hospital environment: (1) lesion size, (2) lesion position (distance to endoscopic head), (3) patient specific activity uptake, (4) physician experience and more.

There are several options to decrease acquisition time further.
(1) Increasing the crystal length of the crystals in the external plate and the endoscopic head would increase sensitivity. For the external plate, this could be easily done. For the endoscopic head, this would include an adjustment of the design in order to accommodate longer crystals.
(2) Improving CTR of the detector would improve sensitivity so that fewer events would be needed to reconstruct a viable image. A 10 ps CTR, for example, would allow a reduction of acquisition time by a factor of ten without compromising image quality.
(3) Another option to increase sensitivity is to develop new tracers with increased specificity, leading to a higher activity in the lesion and, thus, to a shorter acquisition time. Alternatively, the injected activity could be increased, but would also lead to a non favored, raised patient dose.
(4) A final option to increase sensitivity would be to use Compton compensation. Most of the Compton scattering occurs inside the LYSO crystals, meaning that the first hit still represents the original LOR and can potentially be used for reconstruction. However, it can only be used for reconstruction if the scattered photon is also detected in the detector. Otherwise it is not possible to determine whether or not the Compton scattering took place inside the patient or the detector. Let's assume that one 511 keV

photon is detected in the endoscopic head, while the associated photon undergoes Compton scattering in the external plate. If the Compton scattered photon is detected in a neighboring pixel of the initial compton interaction, the three hits will be in coincidence. The two hits in the external plate will be almost simultaneous, meaning that the hit time of the two hits will be indistinguishable within the time resolution of the detector. Hence, hit time cannot be used to determine which of the two hits in the external plate is the first hit representing the original LOR.

There are three approaches to determine the LOR including two that take into account the condition of two hits in neighboring pixels. (1) The center of the two neighboring pixels can be used as the hit point for the LOR. This approach, however, would degrade resolution of the detector. (2) The multi ray tracing can be extended to utilizing positions in both pixels to determine the most probable LOR considering all other events. This approach would increase computation time of the reconstruction, but needed to be tested in terms of achievable image quality. (3) The hit energy weighting can be used. There might be a relation between hit energy and hit order. It could be decided from this relation which hit is the first and, thus, the one used to form the LOR. A relatively simple simulation scenario, as described below, could uncover if such a relation exists. The simulation scenario includes a point source positioned between a single scintillation crystal that is facing two crystals. The crystals are positioned so that real coincidences can only occur between two of the crystals. Placing the setup inside a vacuum ensures that no scattering occurs outside the crystals. Furthermore, a perfect shield is positioned in front of the non-coincidence crystal to assure that all hits in it originate from scattered hits in the coincidence crystal. If there is a relation between the hit energies in the two crystals that are positioned on the same side, an energy dependent selection on LOR could be made.

It is more likely to have the two hits not in neighboring pixels due to the small pixel size in the endoscopic head module, making it necessary to use the latter option for compensation. The proximity of the endoscopic head to the lesion also leads to a big impact of LOR position on spatial resolution of the image. Therefore, the latter approach for compensation is favorable, even if the two hits occur in neighboring pixels.

8.7 Conclusion

The EndoTOFPET-US prototype was investigated extensively in terms of image quality, lesion visibility, applicability and sensitivity. It was verified that the simulation fully represents the detector by means of reproducing the measurements performed with the prototype. Quantitative image quality parameters for image assessment were introduced. An application-specific simulation scenario utilizing the NEMA IEC Body Phantom Set^{TM} was introduced that can be easily replicated in the lab without modification of the existing EndoTOFPET-US prototype. Lesion visibility and image quality were assessed in terms of signal to background ratio (StB) and coincidence time resolution (CTR) of the prototype. A hot volume inside a warm background can be identified down to StB = 3:1, which is the StB expected in patients with prostate carcinoma. Furthermore, the position of the hot volume can be identified with an accuracy $\leq$1 mm in all three dimensions despite the elongation along the LORs. It was shown that improved CTR leads to enhanced image quality and can reduce acquisition time tremendously. Simulations of two conventional PET scanners were performed. Co-registration of the EndoTOFPET-US image to a prior from these PET scanners was demonstrated successfully. Visibility of a 1 mm lesion down to StB = 3:1 was presented in the presence of a larger lesion. The sensitivity of the EndoTOFPET-US prototype is between 1 cps/Bq and 10 cps/Bq in the distance range interesting for prostate imaging. Several options to

improve sensitivity and/or reduce acquisition time are presented, including: (1) longer scintillator crystals in the external plate, (2) compton compensation, (3) improved CTR, (4) improved tracer specificity, (5) increased tracer injection.

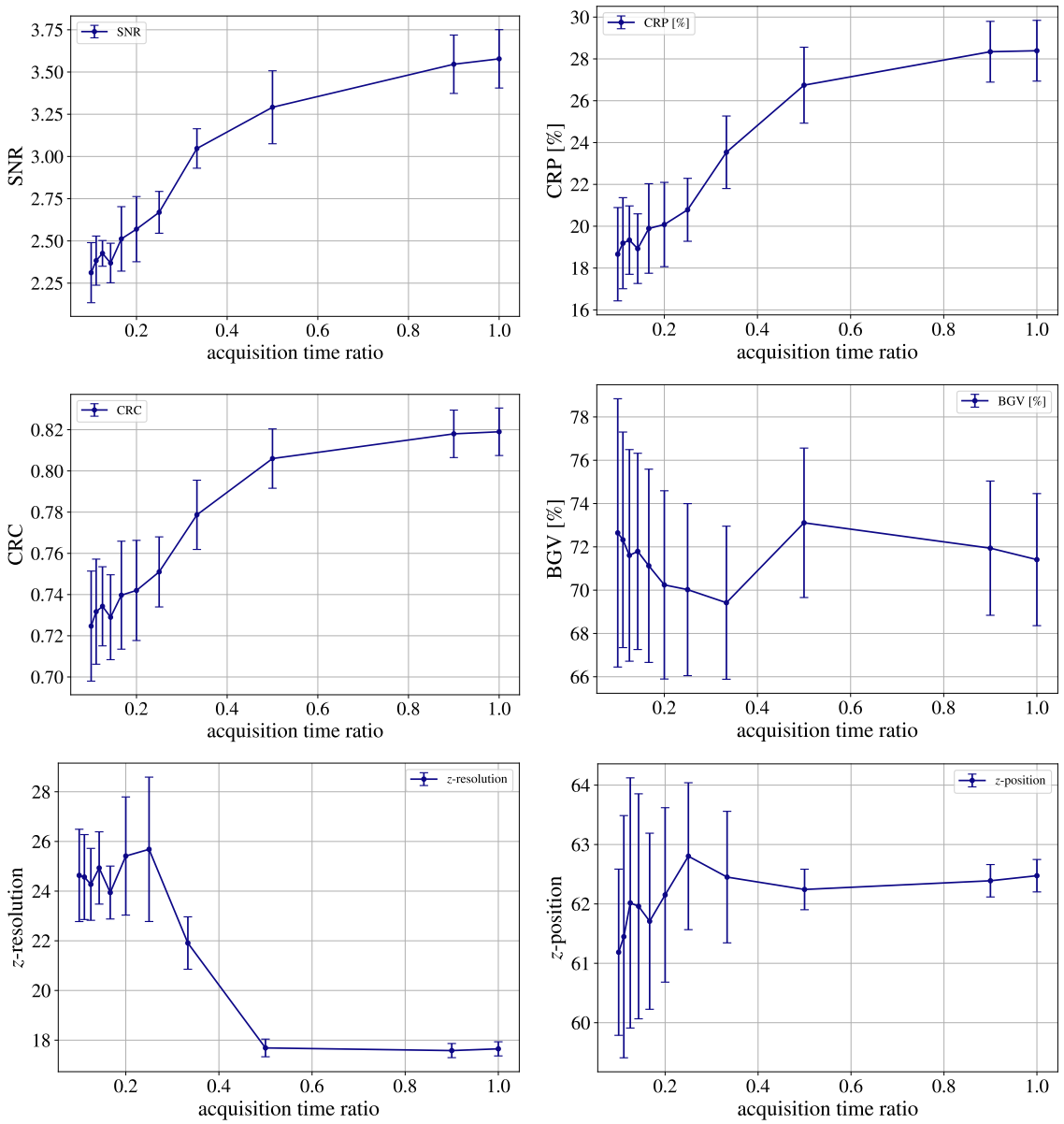

Figure 8.34: (top left) Signal-to-noise ratio (SNR), (top right) contrast recovery percentage (CRP), (center left) contrast recovery coefficient (CRC), (center right) background variability (BGV), (bottom left) z-resolution and (bottom right) z-position. The green lines indicate the center of the cylinder (solid line) and the edges of the cylinder (dotted lines) as a function of acquisition time. The signal to background ratio is 10:1. For acquisition times above four hours, the stopping iteration is defined as the iteration where the full width tenth maximum in z reaches a value below 28 mm for the first time. For acquisition times below four hours, the stopping iteration is the fourth iteration of the reconstruction.

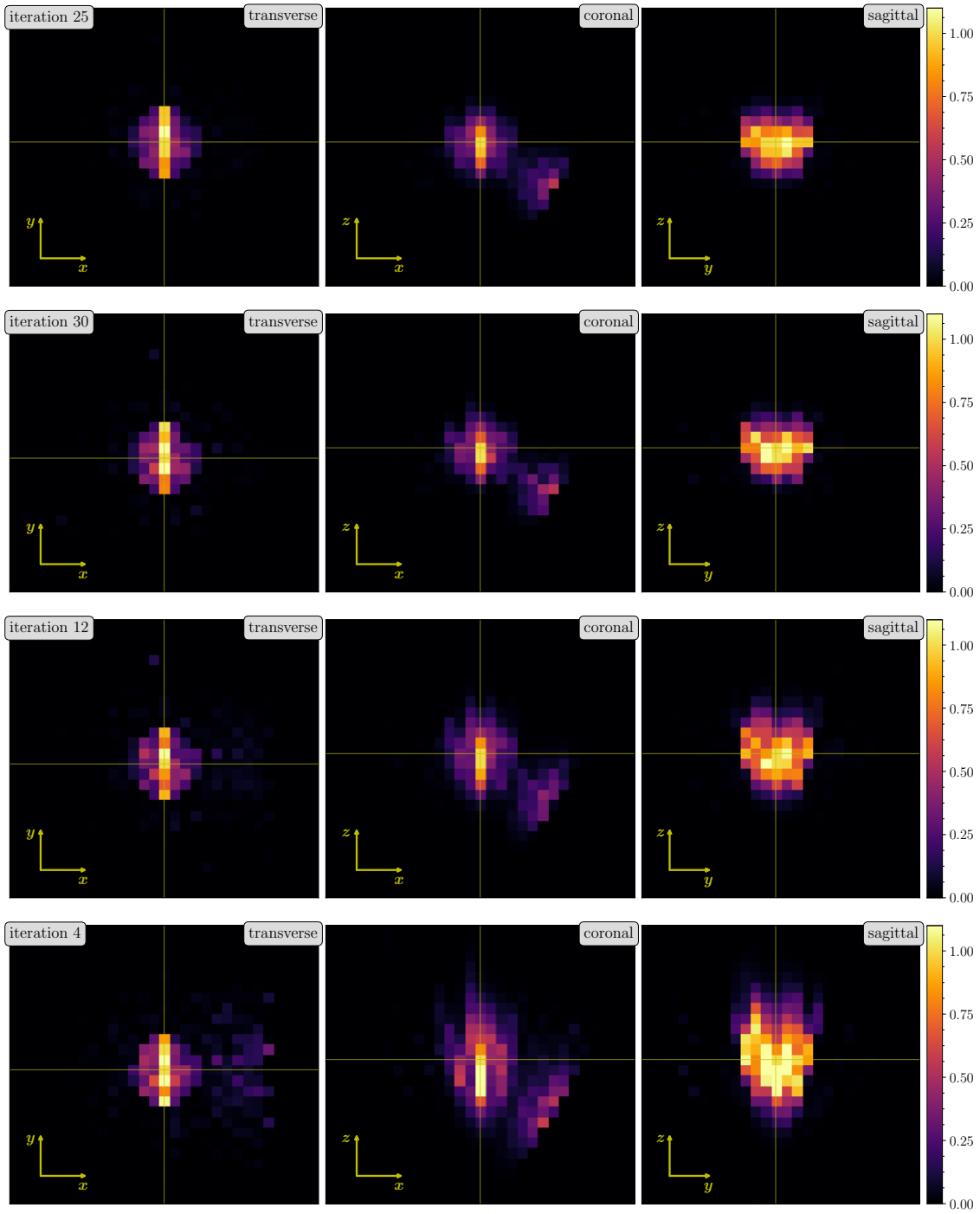

Figure 8.35: Reconstructed images for different acquisition time ratios: 1, 0.5, 0.3 and 0.1 (from top to bottom). Corresponding to an acquisition time of: ∼12, 6, 4 hours and 72 minutes. All images are normalized to the center voxel of the cylindric lesion inlay indicated by the yellow lines. The transverse, coronal and sagittal view are presented from left to right.

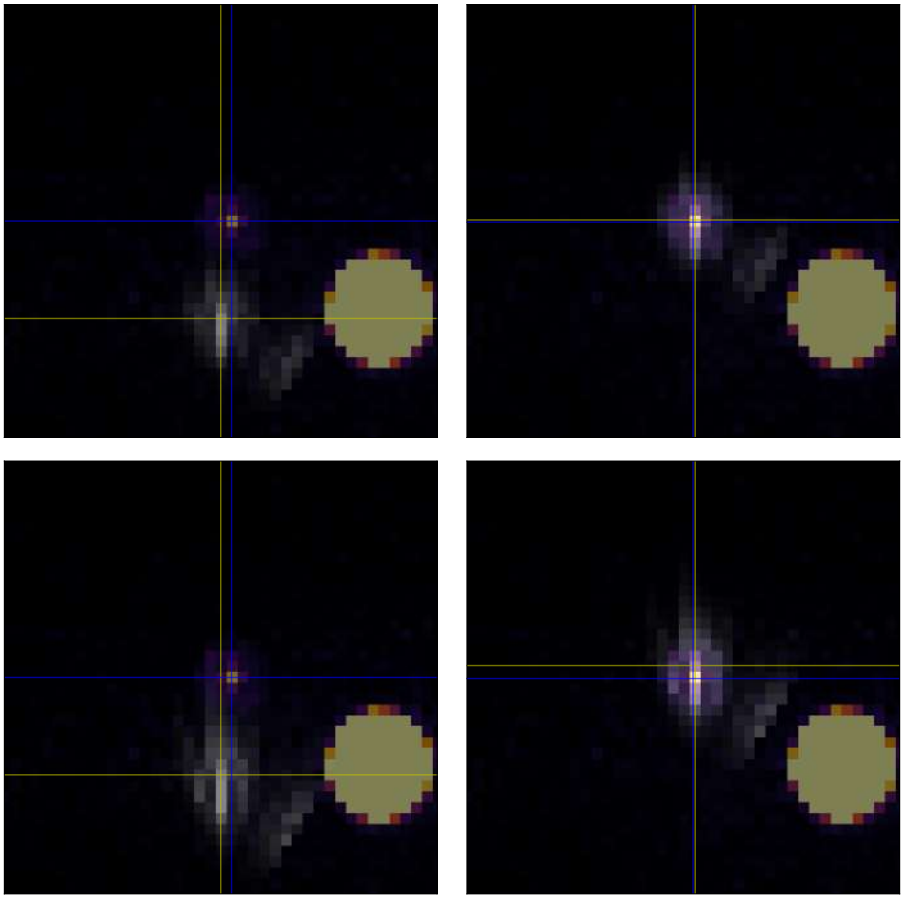

Figure 8.36: Co-registration of the image in the coronal plane acquired with the detector modeled after the Siemens Biograph Vision and the coronal view of the EndoTOFPET-US prototype (top) acquired in 3 hours and (bottom) acquired in 72 minutes. The signal to background ratio is 10:1 for all acquisitions. On the left the images before and on the right the images after co-registration are presented. The intersection of the blue lines indicate the center position of the cylinder in the image acquired with the detector modeled after the Siemens Biograph Vision and the intersection of the yellow lines indicate the center of the cylinder in the image EndoTOFPET-US prototype image. The voxel size is 4 x 4 x 4 mm^3 for both images.

Chapter 9

X-Ray Fluorescence Imaging

In X-ray fluorescence Imaging (XFI), the signal photons have an energy specific to the active imaging component that is used. The only active imaging component used in the presented simulations is gold. Gold has the advantage that it is known to be biocompatible, whereas it is a very heavy atom yielding the possibility to generate high energy fluorescence photons. X-ray energies in the range of 100 keV up to 190 keV are used in this thesis, as mentioned in subsection 5.2.1.2, making the gold $K_{\alpha,1}$ and $K_{\alpha,2}$ lines at 68.8 keV and 66.99 keV the most prominent. The reconstruction of the tracer/drug position in XFI is still subject to investigation since no optimal way has been found so far.

Several possible detection and reconstruction methods for XFI are investigated in this chapter. A proof of concept study is performed for the two methods that seem most promising. The studies presented here are, however, limited to objects that are similar in size to small animals, such as small rodents that are often used in animal studies.

9.1 Reconstruction Methods

Four possible reconstruction methods for the tracer position were thought of in this thesis. They are explained in the following sections. All proposed reconstruction methods consider a pencil X-ray beam for probing the region of interest (ROI). This means that the tracer position is defined by the X-ray beam size in two dimensions. The tracer position only needs to be reconstructed along the X-ray beam direction.

9.1.1 Collimated Detector Reconstruction

A straightforward way for the reconstruction is to use a collimated detector that uses collimation along the X-ray beam's movement of direction. A sketch of this is presented in figure 9.1. By collimating the incoming photons along the X-ray beam movement direction, the photons reaching each detector cell effectively stem from one line segment on the X-ray beam trajectory. The number of fluorescence photons can be determined for each cell and thereof the distribution along the X-ray beam movement direction can be determined. To achieve optimal imaging performance, the background stemming from compton and/or multiple compton interactions has to be well understood and preferably a high energy resolution detector should be used. The achievable spatial resolution of a single collimated detector cell is equivalent to the visible line segment length l. It depends on the collimator length c, collimator

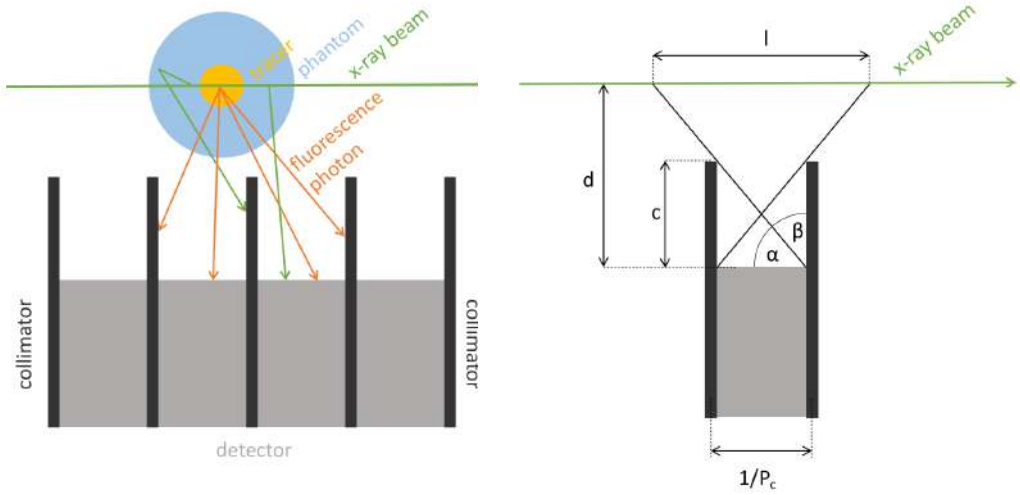

Figure 9.1: Sketch of a collimated detector. The collimator period P_c, collimator height c, detector distance to the X-ray beam d and the line segment visible from a single collimated detector cell l are indicated.

periodicity P_c, collimator material as well as the detector's distance to the X-ray beam d. In the case of a perfect collimator (i.e. collimator stops all impinging photons) it is

$$l = 2\left(d \cdot tan[90° - tan^{-1}(c \cdot P_c)] - \frac{1}{P_c}\right) + \frac{1}{P_c} \tag{9.1}$$

Having an array of cells between which signals can be shared leads to a system point resolution of $l/\sqrt{12}$. Furthermore, the sensitivity of such a system is inversely proportional to the resolution. More complex collimator arrangements can be conceived and were tested by [139].

9.1.2 Fluorescence Photon Flux Reconstruction

The fluorescence light emission is homogeneous as mentioned before. The photons direction is no indicator for the origin of the photon. The flux of a homogeneous point like light source is proportional to $frac1r^2$, where r is the radial distance to the source. Thus, the number of detected photons in a detector volume is proportional to its distance to the fluorescence light emission source. A large surface detector (e.g. ring detector) can potentially resolve the origin of the fluorescence light emission via determining photon density along the detector surface. A simplified sketch of this method is presented in figure 9.2. The sketch shows two small objects containing the fluorescent tracer inside a bigger phantom. The X-ray travels parallel to the detector and through both volumes containing the fluorescent tracer. The number of fluorescence photons as a function of detector position is schematically presented. As in collimator detection, preferably a high energy resolution detector should be used and fundamental understanding of the background is required to achieve optimal reconstruction results.

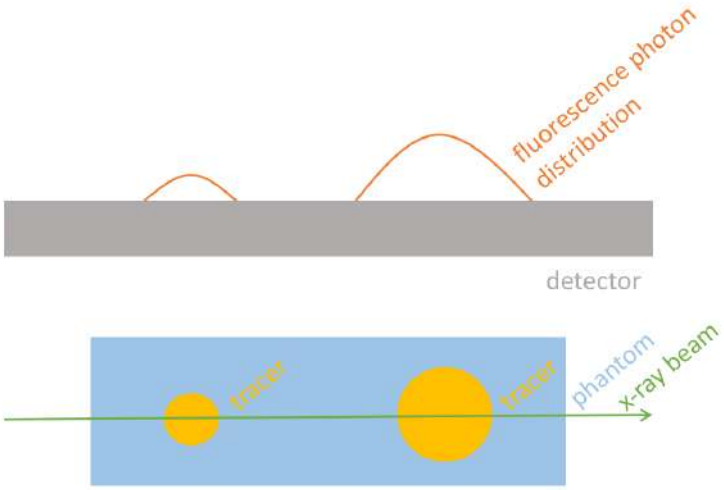

Figure 9.2: Sketch of a detector concept utilizing the fluorescence photon distribution for the reconstruction. A single detector plane is presented in the sketch. However, it is most effective when the biggest possible solid angle is covered by the detector. Two tracer densities along the X-ray beam direction are present inside a larger phantom. The fluorescence photon density as a function of detector position is indicated.

9.1.3 Timing Based Reconstruction

Another possible way to reconstruct the tracer distribution along the X-ray beam is to use the detection time and position of the photons. The detection time of any detected photon depends on the traveled path length. This is indicated in figure **??**. The photons impinging the detector originate either from fluorescence, compton scattering or multiple compton scattering. In the case of fluorescence and single compton scattering, the position (d_1 and d_2) of the interaction is linked to the detection time (t_1 and t_2), whereas the position (d_3) is not linked to the detection time t_3. In the first two cases the position d_i can be calculated correctly by

$$d_i = \frac{(t_i c)^2 - x_i^2 - y_i^2 - z_i^2}{2(t_i c - z_i)} \tag{9.2}$$

where t_i is the detection time and x_i, y_i, z_i are the photon detection coordinates of photon i. It can be seen that the distance d_i is restricted to the phantom size and tracer volume size in the case of compton scattering or fluorescence, respectively. However, multiple compton scattered photons can reach arbitrary $d_i > D$, where D is the distance of X-ray beam origin $\begin{pmatrix} 0 \\ 0 \\ 0 \end{pmatrix}$ to the phantom. Both of the above statements about d_i restrictions assume that scattering outside the phantom is negligible. It is evident that photon detection time of fluorescence photons and single compton scattered photons is indistinguishable. Therefore, choosing the x-ray beam energy in such a way that photons undergoing a single compton interaction have a higher energy than the fluorescence photons makes differentiating Compton and fluorescence photons easy. It allows to simply define an energy window around the fluorescence photon's energy and determine the d distribution of all photons within this energy window. The multiple compton scattered photons form a flat background, whereas the fluorescence photons form a peak at the tracer position. An intrinsic limit to the achievable resolution is the temporal length of the X-ray pulse. However, the temporal length of the X-ray pulse is on the order of ≤ 1 ps and, thus, its influence is negligible. The

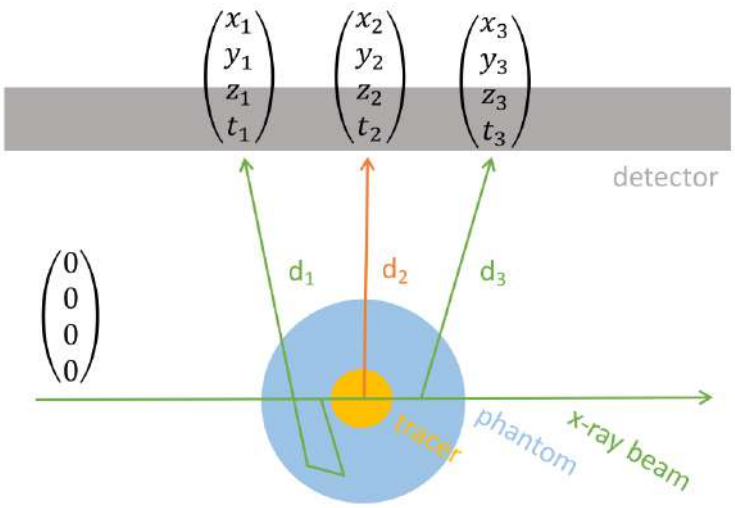

Figure 9.3: Sketch of a detector concept utilizing photon timing for the reconstruction. The beam is initiated at position and time equal to $\begin{pmatrix} x \\ y \\ z \\ t \end{pmatrix} = \begin{pmatrix} 0 \\ 0 \\ 0 \\ 0 \end{pmatrix}$. The photon detection position and time of a X-ray performing multiple compton interactions, a fluorescence photon and a photon undergoing a single compton interaction are indicated by $\begin{pmatrix} x_1 \\ y_1 \\ z_1 \\ t_1 \end{pmatrix}$, $\begin{pmatrix} x_2 \\ y_2 \\ z_2 \\ t_2 \end{pmatrix}$ and $\begin{pmatrix} x_3 \\ y_3 \\ z_3 \\ t_3 \end{pmatrix}$.

spatial resolution σ_{X-ray} along the X-ray beam direction of the proposed system is proportional to the time resolution

$$\sigma_{X-ray} \propto c \cdot \sigma_t \tag{9.3}$$

where c is the speed of light and σ_t is the time resolution of the detector. The spatial resolution orthogonal to the beam direction is approximately equivalent to the beam size.

9.1.4 X-Ray Fluorescence Tomography

The last reconstruction method to be introduced is X-ray fluorescence tomography (XFT). The volume of interest (VOI) is scanned from several directions with the pencil X-ray beam during XFT, similar to computed tomography (CT). In CT, as mentioned in section 2.6, line attenuation coefficients are measured and the attenuation coefficient at each point inside the scanned volume is reconstructed. In XFT, the measured quantity is the number fluorescence photons that are created per X-ray beam and the reconstructed quantity is the tracer density at each point inside the scanned volume. The overall procedure of obtaining these numbers is very similar to CT. (1) The VOI is scanned from multiple angles with a pencil X-ray beam. (2) The number of fluorescence photons per X-ray position is stored in a sinogram. (3) The tracer density is reconstructed via a filtered backprojection (or equivalent reconstruction algorithm). For this kind of reconstruction, the background in the energy range of the fluorescence photons needs to be understood and subtracted from the acquired energy spectrum for each X-ray beam.

The first two reconstruction methods are not further investigated in this thesis. However, a study on fluorescence photon flux reconstruction was performed by [140] and studies including collimators were performed in [139]. Possible detector materials for timing based reconstruction and X-Ray fluorescence tomography are described and first simulation results are presented in the next sections.

9.2 Feasibility Study on Timing Based Reconstruction and X-Ray Fluorescence Tomography

The timing based reconstruction and XFT are tested with a simulation based on GAMOS. Since they are so inherently different in detector requirements, two completely different detection systems need to be used.

9.2.1 Timing Based Reconstruction Simulation

The simulated detector has the ring geometry as described in subsection 5.2.3.2. The detector material is LYSO and the pixel size is 3.5 x 3.5 x 10 mm. Scintillators are chosen because of their excellent time resolution and detection efficiency, which are both necessary for the proposed imaging method. A sketch of the simulation scenario is presented in figure 9.3. The phantom is a cylindrical water phantom (4 cm

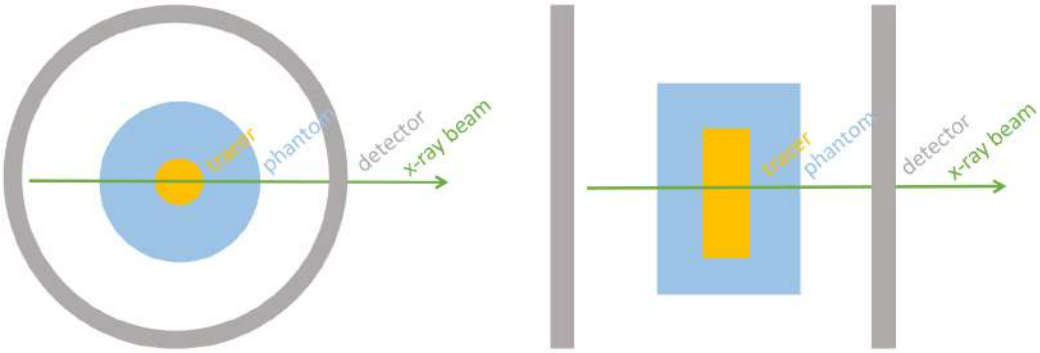

Figure 9.4: Sketch of the simulation setup for the timing based reconstruction.

diameter, 6 cm height), which includes a small cylindrical inlay (8 mm diameter, 3 cm height) containing a gold water mixture. A simulation with the following specifications is performed:

(1) gold concentration of 3 mg/mL in the small cylinder,
(2) 190 keV mean X-ray energy with a standard deviation of 6.5 keV,
(3) a single X-ray beam containing 10^6 photons is shot through the center of the phantom orthogonal to the height of the cylinder,
(4) the beam diameter is 1 mm and the divergence is 1 mrad,
(5) the beam is produced at a distance of 8 cm to the phantom's center,
(6) the phantom is positioned at the center of the detector.

The d-distribution should show an object with a size $d_{\mathrm{FWHM}} = 8$ mm and at a mean position $d_\mu = 8$ cm. As a first feasibility test a perfect time and spatial resolution of the photon detection is simulated. The d-value is calculated for all photons within an energy window ranging from 67 keV to 70 keV. The obtained d-distribution with and without gold present in the phantom are presented in figure 9.4. It can be seen that the background is rather flat while the fluorescence photons show the expected peak. The location and size of the object is obtained by: (1) subtracting the background (obtained via the simulation without gold) from the data, (2) normalizing the resultant spectrum, (3) determining the FWHM of a spline interpolation of the data points, (4) determining the center position of the FWHM.

The FWHM can be interpreted as the reconstructed object size along the X-ray beam direction. The center position of the FWHM can be interpreted as the position of the reconstructed object. The object size is $d_{\text{FWHM}} = 8.0$ mm and the mean position is $d_{\mu} = 8.0$ cm, which represents the phantom perfectly.

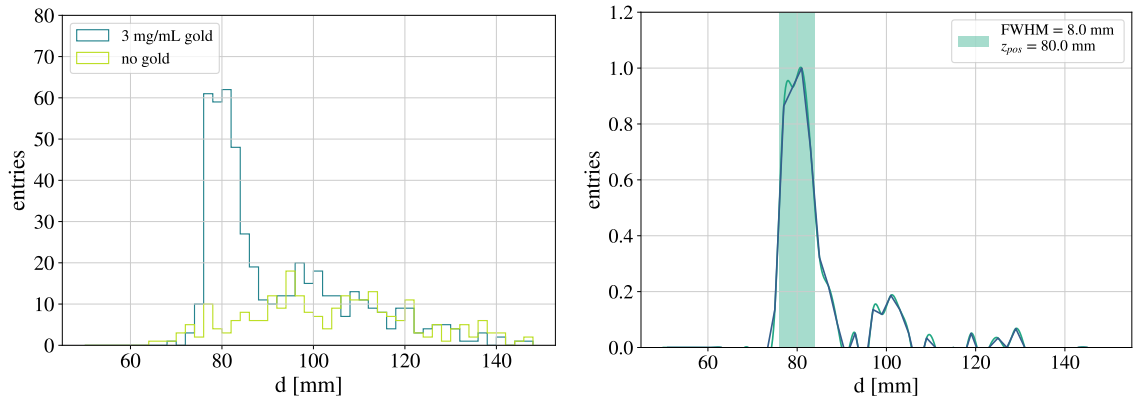

Figure 9.5: (left) The d-distribution in the case of perfect time and spatial resolution of the detector. The simulation is performed without gold and with a gold concentration of 3 mg/mL in the small cylinder. The bin size is 2 mm. (right) The normalized distribution with subtracted background. The full width half maximum (FWHM) of a spline interpolation to the normalized data presents the resolution and the center of the FWHM represents the center position of the cylinder.

First detector effects are included in the next simulations. Including a pixel size of 3.5 x 3.5 mm^2 and interactions occurring in the detector (i.e. detector efficiency, compton scattering inside the detector) into the detection chain without including further detector digitization (i.e. the detector still has perfect time and energy resolution) yields the result as presented in figure 9.5. It can be seen that including

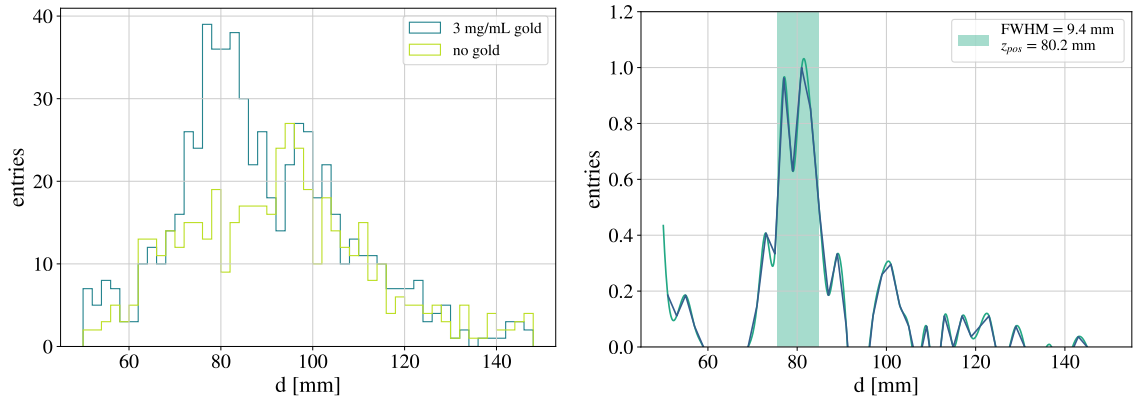

Figure 9.6: (left) The d-distribution in the case of perfect time and energy resolution of the detector as well as inclusion of detector pixel size and efficiency. The simulation is performed without gold and with a gold concentration of 3 mg/mL inside the small cylinder. The bin size is 2 mm. (right) The normalized distribution with subtracted background. The full width half maximum (FWHM) of a spline interpolation to the normalized data presents the resolution and the center of the FWHM represents the center position of the cylinder.

detector efficiency, scattering inside the detector and limited pixel size already reduces the signal strength and degrades the achievable resolution slightly. The object size is $d_{\text{FWHM}} = 9.4$ mm and mean position is

d_μ = 8.2 cm. Finally, a time resolution of 10 ps and an energy resolution of 10% at 70 keV is added to the simulation. The result including detector digitization is presented in figure 9.6. It should be pointed out that in figure 9.6 the bin size was changed to 4 mm (compared to 2 mm bin size in the previous two figures) in order to reach a smoother result. It can be seen that the signal degrades when adding

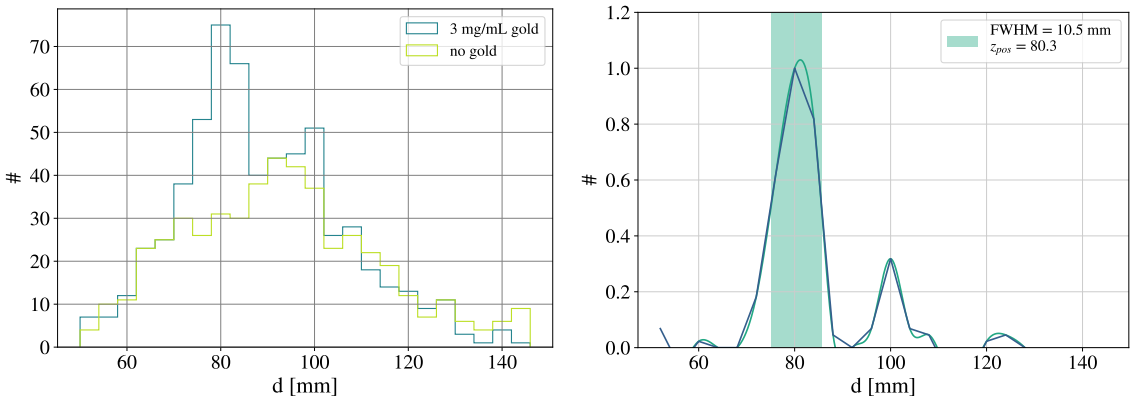

Figure 9.7: (left) The d-distribution in the case of 10 ps time and 10% energy resolution at 70 keV and inclusion of detector pixel size and detector efficiency. The simulation is performed without gold and with a gold concentration of 3 mg/mL inside the small cylinder. The bin size is 4 mm. (right) The normalized distribution with subtracted background. The full width half maximum (FWHM) of a spline interpolation to the normalized data presents the resolution and the center of the FWHM represents the center position of the cylinder.

the detector effects such as: (1) limited efficiency, (2) scattering inside the detector crystal, (3) limited spatial resolution of detection location, (4) limited energy resolution and (5) limited time resolution. The object size is d_{FWHM} = 10.5 mm and the mean position is d_μ = 8.3 cm provided all detector effects are included.

Overall, it is shown that the proposed detection and reconstruction method works. The spatial resolution of the system orthogonal to the X-ray beam is independent of the detectors time and energy resolution. It is in first approximation equivalent to the beam diameter. The resolution along the X-ray beam is in first approximation $\sigma_{X-ray} \approx \sigma_t \cdot c$. Furthermore, the resolution along the X-ray beam direction is a function of detector pixel size. The pixel size influences the ability to localize the detection location of each photon and, thereby, adds to the uncertainty on d. Thus, effectively a time resolution of ∼30 ps is required to achieve a spatial resolution of ∼1 cm along the X-ray beam. 58 ps time was already achieved with LSO:Ce:Ca crystals and SiPMs using 511 keV photons. As explained in section 2.5, however, the achievable time resolution of scintillator is a strong function of scintillation photon number and, thereby, a strong function of incident photon energy. It is unclear if a time resolution below 30 ps can be achieved with ∼70 keV photons in the future and, thus, if the proposed imaging method can be useful for medical imaging. The proposed timing based imaging has the advantage that a single X-ray pulse can potentially give 3D information about the tracer distribution, leading to a small dose application compared to XFT.

9.2.2 X-ray Fluorescence Tomography Simulation

The simulated detector is the ring detector as described in subsection 5.2.3.2. The detector material is cadmium zinc telluride (CdZn:Te) and the single pixels are 0.1 x 0.1 x 0.5 cm^3. A large pixels thickness

is chosen to have optimal detection efficiency (pixelated 5 mm thick CdZn:Te were already presented in [141]) CdZn:Te is a high Z semiconductor that exhibits excellent energy resolution (e.g. commercial CdZn:Te detectors with an energy resolution of ∼550 eV FWHM at 88 keV [142] are available) and detection efficiency for photons below 70 keV (above 90% for 1 mm thickness). Energy resolution and detection efficiency are the most important detector parameters in case of XFT.

Only a single simple phantom is investigated. It consists of a water sphere with 2.5 cm diameter and a cylinder with 1 mm diameter and 3 mm height at its center. The cylinder is filled with a water gold mixture. A first simulation is performed with the following specifications:

(1) gold concentration of 5 mg/mL in the cylinder,
(2) 150 keV mean X-ray energy with a standard deviation of 5 keV,
(3) the phantom is scanned from 21 angles between 0° and 180° in 9° steps,
(4) the phantom is scanned in the plane parallel to the cylinder height,
(5) eleven X-ray shots per angle are performed and the X-ray beam is displaced by 1 mm after each shot,
(6) each X-ray shot includes 10^6 photons,
(7) the beam diameter is 1 mm and the divergence is 1 mrad,
(8) the X-ray beam length is 0 s,
(9) detector energy resolution is 550 eV FWHM.

The reconstruction procedure is as follows: (1) The detected photons are sorted by their energy in 1 keV bins. (2) Two separate binnings are performed: one ranging from 63.3 to 73.3 keV and one ranging from 61.50 to 71.50 keV. These binnings ensure that the $K_{\alpha,1}$ (68.8 keV) line is at the center of a bin in the first case and the $K_{\alpha,2}$ (67 keV) line is at the center of a bin in the second case. The bins containing the $K_{\alpha,1}$ and $K_{\alpha,2}$ lines are called signal bins. (3) The number of background photons inside the signal bins is estimated as

$$N_{BG}^{sig} = (N_{Ph}^{sig+1} + N_{Ph}^{sig-1})/2 \tag{9.4}$$

with N_{Ph}^{sig+1} being the number of photons in the bin above and N_{Ph}^{sig-1} being the number of photons in the bin below the signal bin. This simple interpolation has proven to yield good results. In case of the specified simulation scenario the mean number of background photons in the $K_{\alpha,2}$ bin is 653±18 and the estimated background is 651±24. Using more complex ways such as fitting the background has proven to yield no improvements compared to the simple interpolation since the estimation error is anyhow dominated by statistical fluctuations. (4) The number of fluorescence photons is determined via

$$N_{fluor} = N^{K_{\alpha,1}} - N_{BG}^{K_{\alpha,1}} + N^{K_{\alpha,2}} - N_{BG}^{K_{\alpha,2}} \tag{9.5}$$

with $N^{K_{\alpha,1}}$ and $N^{K_{\alpha,2}}$ being the number of photons in the $K_{\alpha,1}$ and $K_{\alpha,2}$ bins, and $N_{BG}^{K_{\alpha,1}}$ and $N_{BG}^{K_{\alpha,2}}$ being the number of background photons the $K_{\alpha,1}$ and $K_{\alpha,2}$ bins. (5) A sinogram is filled with the number of fluorescence photons acquired at each X-ray beam position (21 angles x 10 positons per angle). (6) The sinogram is fed into a filtered backprojection reconstruction that utilizes the python package *skimage.transform*.

The result of the filtered backprojection along with activity line profiles through the cylinder are presented in figure 9.7. The SNR is calcluated as

$$\text{SNR} = \frac{\mu_{sig} - \mu_{BG}}{\sigma_{BG}} \tag{9.6}$$

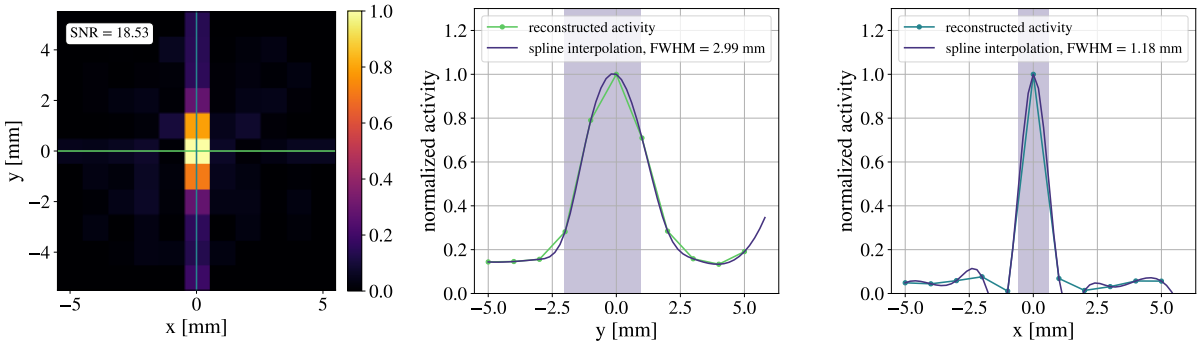

Figure 9.8: (left) Heatmap of the normalized reconstructed gold concentration of the simulation scenario with 1 mm voxel size. The reconstruction is performed with a filtered backprojection algorithm based on the *skimage.transform* python package. (center) Line profile through the cylinder parallel to the y-axis as indicated in the heatmap. A spline interpolation of the data points is added and the full width half maximum (FWHM) is determined. (right) Line profile through the cylinder parallel to the x-axis as indicated in the heatmap. A spline interpolation of the data points is added and the full width half maximum (FWHM) is determined.

with μ_{sig} being the mean signal, μ_{BG} the mean background and σ_{BG} the standard deviation of the background. The signal region is defined as the voxels forming the ground truth of the cylinder, whereas the background is defined as four randomly chosen volumes inside the reconstructed area that have the same size and form as the cylinder. The size of the reconstructed cylinder is defined as the FWHM of a spline interpolation of the data as presented in figure 9.7. It can be seen that the reconstruction yields a SNR of 18.5 and a cylinder size of ∼3 mm along the y-axis and ∼1.2 mm along the x-axis. The SNR can be further improved by using the SART (simultaneous algebraic reconstruction technique) iterative reconstruction method [143]. It is a reconstruction method that can yield better results than the simple backprojection in case of limited data. The second iteration of the SART reconstruction yields the best possible SNR and is presented in figure 9.8. A SNR of 35.5 and a cylinder size of 2.8 mm along the y-axis

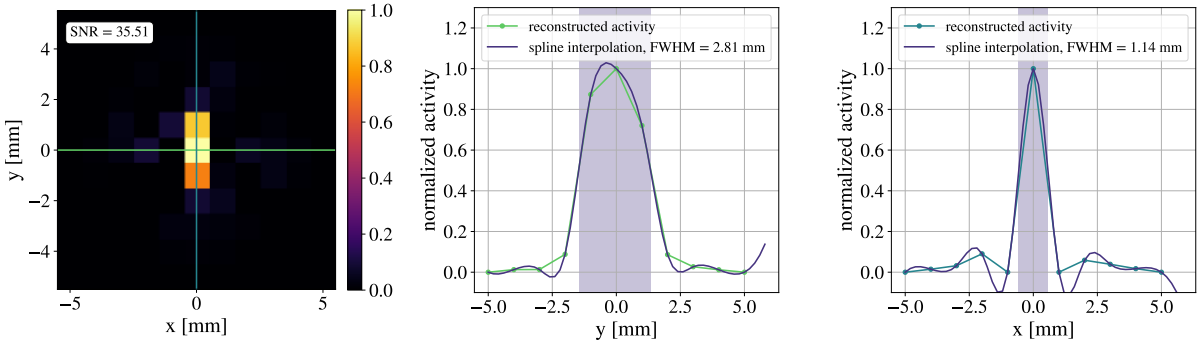

Figure 9.9: (left) Heatmap of the normalized reconstructed gold concentration of the simulation scenario with 1 mm voxel size. The reconstruction is performed with the SART algorithm. (center) Line profile through the cylinder parallel to the y-axis as indicated in the heatmap. A spline interpolation of the data points is added and the full width half maximum (FWHM) is determined. (right) Line profile through the cylinder parallel to the x-axis as indicated in the heatmap. A spline interpolation of the data points is added and the full width half maximum (FWHM) is determined.

and 1.1 mm along the x-axis is achieved with SART.

The SNR is investigated as a function of bin size (explained in imaging procedure step 2) and X-ray beam energy. The X-ray beam energy is varied in 10 keV steps from 110 keV up to 150 keV and bin size is varied in 100 eV steps from 300 eV up to 1200 eV. The best possibe SNR is achieved with 300 eV bins and an X-ray energy of 150 keV. A possible explanation is the following: The statistical fluctuations of the background photons in the signal bins is $\sqrt{N_{BG}^{sig}}$. A small bin size results in a smaller number of background photons in the signal bins. Furthermore, the number of background photons that have the fluorescence energy is inversly proportional to X-ray beam energy. A 150 keV photon statistically undergoes more interactios until it reaches an energy of 70 keV than a 100 keV photon. Hence, the probability for a 150 keV photon to reach 70 keV is smaller than it is for a 100 keV photon. Thus, small bin size and high X-ray beam energy results in the smallest amount of background photons in the signal bins and, thus, in the smallest actual statistical fluctuations of background. The reconstructed image obtained with a bin size of 300 eV, an incident X-ray beam energy of 150 keV and three iterations of the SART reconstruction along with the line profiles through the cylinder are presented in figure 9.9. It can

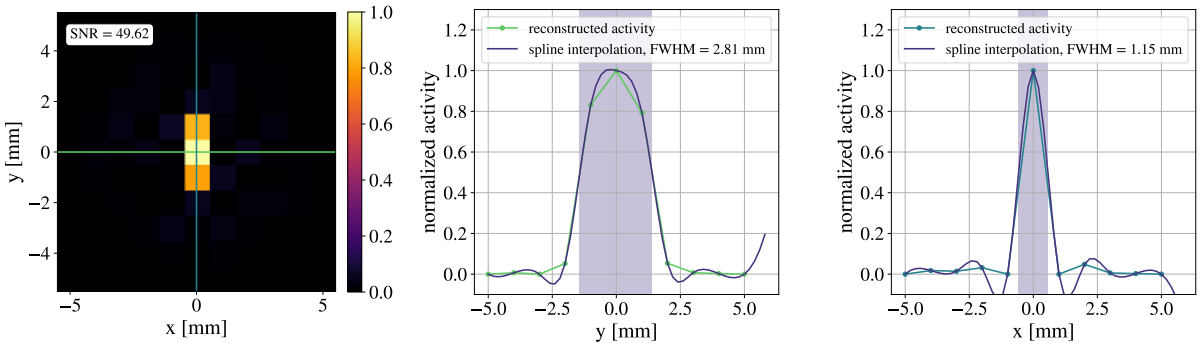

Figure 9.10: (left) Heatmap of the normailzed reconstructed gold concentration of the simulation scenario with 1 mm voxel size. The reconstruction is performed with the SART algorithm and the third iteration is presented. (center) Line profile through the cylinder parallel to the y-axis as indicated in the heatmap. A spline interpolation of the data points is added and the full width half maximum (FWHM) is determined. (right) Line profile through the cylinder parallel to the x-axis as indicated in the heatmap. A spline interpolation of the data points is added and the full width half maximum (FWHM) is determined.

be seen that an excellent SNR of ∼50 and a cylinder size of 2.8 mm along the y-axis and 1.2 mm along the x-axis is achieved.

Finally, the gold concentration in the sphere is reduced to 500 µg/mL. The reconstruced images of two simulations performed with a gold concentration of 500 µg/mL along with the line profiles through the cylinder are presented in figure 9.10. The simulations are performed with 10^6 and $3{\cdot}10^6$ photons per X-ray shot. It can be seen that the background is increased in case of 10^6 photons per X-ray shot and a SNR of 5.82 is achieved. The cylinder size is 2.42 mm along the y-axis and 1.2 mm along the x-axis. Increasing the number of X-ray photons per shot to $3{\cdot}10^6$ yields an improved SNR of 18.7. The cylinder size along the y-axis is only 1.8 mm, whereas th cylinder size along the x-axis is unchanged.

9.3 Conclusion

Four possible detection and reconstruction methods for a pencil beam X-ray fluorescence imaging application are proposed. The reconstruction methods include: (1) collimated detectors, (2) fluorescence photon distribution in a large area detector, (3) detection time and position and (4) XFT. The last

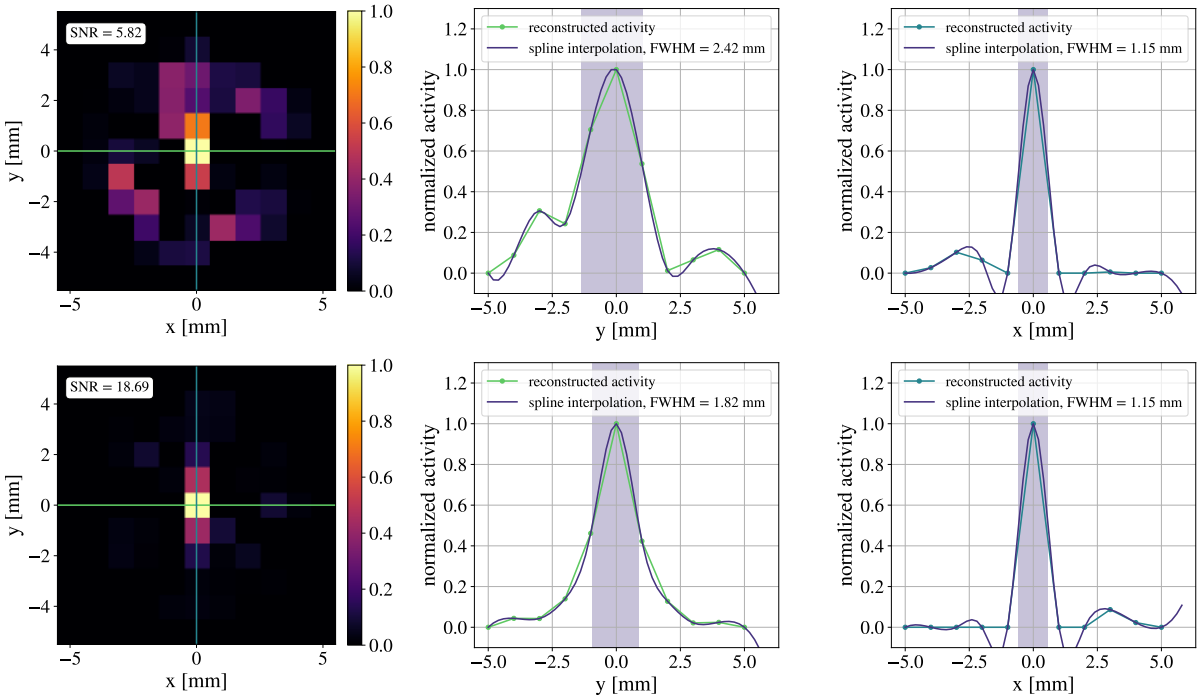

Figure 9.11: (from left to right) Heatmap with 1 mm voxel size and line profile through cylinder along the y-axis and x-axis. A spline interpolation of the data points is added and the full width half maximum (FWHM) is determined. A gold concentration of 500 µg/mL is used. (top) The reconstruction result achieved with 10^6 photons per X-ray shot. (bottom) The reconstruction result achieved with $3{\cdot}10^6$ photons per X-ray shot.

two were tested in terms of general feasibility by means of a simulation. It was shown that using the the photon detection time and position to calculate a the fluorescence photon's origin is possible. This reconstruction method requires outstanding detector properties (i.e. time resolution of 30 ps in order to achieve ∼1 cm spatial resolution along the X-ray beam direction). But it also allows to reconstruct the 3D gold concentration with a single shot resulting in a smaller patient dose compared to XFT. The XFT simulations showed promising results. A water cylinder with 1 mm diameter and 3 mm height containing a gold concentration of 500 µg/mL inside a 5 cm diameter water sphere was succesfully reconstructed with SNR = 18.7. However, the cylinder height was underestimated (1.8 mm). XFT has the advantage that spatial resolution in all three dimension depends solely on X-ray beam diameter and that detector technologies to build an XFT detector already exist.

Chapter 10

Conclusion and Outlook

The work presented in this thesis deals with two functional medical imaging methods, i.e. positron emission tomography (PET) and X-ray fluorescence imaging (XFI).

The first part of this thesis deals with a novel asymmetric multimodal imaging device combining ultrasound (US) and time-of-flight PET (TOFPET) within the EndoTOFPET-US (Endoscopic Time-of-Flight Positron Emission Tomography) project. The detector concept foresees an external plate containing a total of 4096 channels that acquires data in coincidence with an endoscopic PET detector (endoscopic head) that is mounted on top of a commercial US endoscope. The areas of application lie within the development of new tracers for pancreas and prostate carcinoma as well as intraoperative guidance during surgery/biopsy and diagnostics of pancreas and prostate carcinoma. The project aims to achieve a coincidence time resolution (CTR) of 200 ps and a spatial resolution of $\sim$1 mm.

A commissionining and CTR optimization of the already built external plate was performed in cooperation with Dr. Yonathan Munwes for this thesis. The commissioning starts with maintenance phase. Broken and malfunctioning components were identified and exchanged, whereas the main focus was on the STiC (silicon photomultiplier timing chip) ASICs (application-specific integrated circuits). Automated procedures to perform phase locked loop locking (PLL locking) and a preliminary energy calibration were developed. They serve a twofold purpose: (1) calibrating the detector for the subsequent CTR optimization and (2) locating broken and malfunctioning ASICs. Hereafter, slow control was implemented and temperature readout in the external plate was established. A total of 32 analog front-end boards (FEB-As) and four digital front-end boards (FEB-Ds) are in the external plate. Each FEB-D holds eight FEB-As and each FEB-A holds two ASICs and a single temperature sensor that is in close proximity to SiPM connector. It was observed that the temperature of the SiPMs exceeds 27°C and the temperature at the backside of the external plate hotspot exceeds 55°C. The high temperature leads to a degradation of CTR and might be damaging ASICs. A cooling solution was put in place as a result. It removes the hottest components from the FEB-Ds and relocates them outside the plate where they are cooled via air circulation. This ensures that the SiPM temperature does not exceed 23°C.

The pixel size of the endoscopic head is decisive for the system resolution. Thus, the original design intends a pixel size 0.7 x 0.7 x 15 mm^3. An endoscopic head prototype was developed that contains 8 x 8 pixels with a pixel size of 1.2 x 1.2 x 15 mm^3.

CTR has a big influence on image quality and feasibility of the EndoTOFPET-US design. The influence of tunable ASIC parameters on CTR was investigated with the help of a small PET setup. A

CTR optimization setup was set up and an automated online CTR optimization based on the Nelder-Mead algorithm was developed. It is used to optimize each of the 4096 channels of the external plate and the 64 channels of the endoscopic head prototype. Including time alignment, an overall system CTR of 255 ps is achieved.

A first data acquisition with the fully calibrated and optimized EndoTOFPET-US prototype was performed. A point-like sodium-22 (^{22}Na) encased in a delrin casing was used for the acquisition. The point resolution of the prototype was determined to ∼1.4 mm in the plane parallel to the detector surfaces and ∼7.0-9.0 mm orthogonal to the detector surfaces.

Thereafter, a simulation of the EndoTOFPET-US prototype was developed. The previous data acquisition was reproduced in the simulation verifying that the simulation represents the detector fully. The simulation was used to develop application-specific measurement scenarios that show the achievable quantitative and qualitative image quality and can be reproduced in the lab at a later stage. The NEMA IEC Body Phantom Set^{TM} is used in these simulations. It allows to perform prostate and pancreas application-specific measurements with minimal modifications. It is presented that TOF is a necessity when dealing with a detector that yields limited field of view (FOV) and angular coverage like the EndoTOFPET-US design. Qualitative and quantitative image quality as a function of CTR were investigated. The EndoTOFPET-US detector greatly benefits from an improved CTR until the point where no imaging artifacts due to the limited angular coverage are visible anymore (CTR $\leq$ 25 ps).

Studies investigating the image quality as a function of signal-to-background ratio (StB) were performed. It is shown that the EndoTOFPET-US prototype can visualize a hot volume inside a warm background down to a StB = 3:1. A StB = 3:1 is what can be expected for prostate lesions in the case that prostate-specific membrane antigen (PSMA) is used as tracer. Additionally two conventional ring PET detector geometries modeled after existing PET scanners were simulated and co-registration of the EndoTOFPET-US image to a conventional PET scanner image is presented. Furthermore, the results achieved with the EndoTOFPET-US image reconstruction were compared to the well known and benchmarked CASToR (customizable and advanced software for tomographic reconstruction) reconstruction. The EndoTOFPET-US reconstruction yields overall better results.

Finally, the simulation was used to perform a comprehensive sensitivity study of the EndoTOFPET-US prototype. The original EndoTOFPET-US design requires acquisition times of ∼32-80 minutes for usual lesion positions and lesion tracer uptake achieved with PSMA in the case of CTR = 255 ps. Several options of how to improve the sensitivity are provided. For example, a CTR = 10 ps would allow an acquisition time of ∼3-8 minutes without image degradation compared to a 30-80 minute acquisition.

The next step in the EndoTOFPET-US project should be to replicate the application specific simulations in the lab and verify their results. The measurements should preferably be performed with and without the optical tracking system to check its influence on image quality. For the reference without optical tracking a mechanical scaffold can fix the external plate's, endoscopic head's and phantom's positions with respect to each other. This would ensure perfect positioning as it was achieved in the simulation. After that a handheld version of the endoscopic head prototype should be designed and put into the hands of medical doctors. The input of the medical community can bring great insight into possible improvements that can be made and the usefulness of the EndoTOFPET-US detector.

The second part of this thesis deals with X-ray fluorescence imaging (XFI). XFI is well known imaging method for environmental and biological studies that is gaining more interest in the field of functional medical imaging. It can be used to locate metallic compounds in-vivo, which provides a number of

applications in medical imaging (e.g. functionalized tracer, anti cancer drug and diagnostic metal complex localization). Imaging and reconstruction method for XFI are still subject to investigation. Four possible methods are proposed in this thesis: (1) collimated detector reconstruction, (2) fluorescence photon flux reconstruction, (3) timing based reconstruction and (4) X-ray fluorescence tomography (XFT). The latter two options were tested in regard to feasibility by means of a GAMOS based simulation.

The timing based reconstruction overall is feasible but requires remarkable detector properties (i.e. time resolution $\leq$30 ps at a photon energy $\sim$70 keV in case of gold). A 8 mm diameter water cylinder containing a gold concentration of 3 mg/mL can be visualized inside a 4 cm diameter water cylinder if the detector exhibits 10% energy resolution at 70 keV and a time resolution of 10 ps.

XFT shows promising results. A small water cylinder with 1 mm diameter and 3 mm height containing a gold concentration of 500 µg/mL can be visualized inside a 5 cm diameter water sphere. The cylinder diameter is correctly reconstructed with a size of 1.2 mm, whereas the cylinder height is underestimated with a size of 1.8 mm. The detector requirements necessary to achieve this are already fulfilled by modern single channel cadmium zinc telluride (CdZn:Te) detectors. Further studies on feasibility need to be performed. More complex phantoms need to be investigated. More sophisticated background estimations will most likely be necessary for bigger phantoms, especially because background can change depending on X-ray beam position. A prior CT image could be used in order to perform accurate background estimation By means of the prior, background could be simulated for each x-ray beam position. This is rather time-consuming but would also yield a good background estimation. Furthermore, the minimum dose required to resolve a certain tracer concentration should be studied as a function of phantom size.

Nomenclature

ADC	Analogue-to-digital converter
APD	Avalanche photo diode
ASIC	Application-specific integrated circuit
BGO	Bismuth germanate
BGV	Background variability
CASToR	Customizable and advanced software for tomographic reconstruction
CCD	Charge-coupled device
CML	Current mode logic
CN	Correlated noise
CRC	Contrast recovery coefficient
CRP	Contrast recovery percentage
CST	Central slice theorem
CT	Computer tomography
CTR	Coicidence time resultion
d-SiPM	digital silicon photomultipliers
DAC	Digital-to-analogue converter
DAQ	Data aquisition
DCR	Dark count rate
DIO	Depth of interaction
ENF	Excess noise factor
ET	Emission tomography
FBP	Filtered backprojection
FEB-A	Analogue front-end board
FEB-D	Digital front-end board
FF	Fill factor
FIFO	First in first out
FOV	Field of view
FPGA	Field programmable gate array
FWHM	Full width half maximum
FWTM	Full width tenth maximum
FWTWM	Full width twentieth maximum
G-APD	Avalanche photo diode operated in Geiger mode
GAMOS	Geant4-based architecture of medicine-oriented simulations
Geant4	Geomatry tracking
GPU	Graphics processing unit

LOR ..... Line of response
LWFA ..... Laser-wakefield acceleration
LY ..... Light yield
LYSO ..... Lutetium-yttrium oxyorthosilicate
MD-SiPM .... Multichannel digital silicon photomultiplier
ML-EM ..... Maximum likelihood - expectation maximization
MPPC ..... Multi-pixel photon counter
MRI ..... Magnetic resonance imaging
oP ..... ortho-positronium
PCB ..... Printed circuit board
PCIe ..... Peripheral component interconnect express
PDE ..... Photon detection effeciency
PLL ..... Phase locked loop
PMT ..... Photomultiplier tubes
pP ..... para-positronium
PSMA ..... Prostate-specific membrane antigen
QE ..... Quantum efficiency
ROI ..... Region of interest
SART ..... Simultaneous algebraic reconstruction technique
SiPM ..... Silicon photomultiplier
SNR ..... Signal-to-noise ratio
SPAD ..... Single photon avalanche diodes
SPECT ..... Single photon emission computed tomography
StB ..... Signal-to-background ratio
STiC ..... Silicon photomultiplier timing chip
TDC ..... Time-to-digital converter
TOF ..... Time-of-flight
ToT ..... Time over threshold
TT ..... Transmission tomography
US ..... Ultrasound
UV ..... Ultraviolet
VCO ..... Voltage controlled oscillator
VOI ..... Volume of interest
XFI ..... X-ray fluorenscence imaging
XFT ..... X-ray fluorenscence tomography

Appendix A

Appendix

A.1 Conventional PET Scanners and Co-Registration

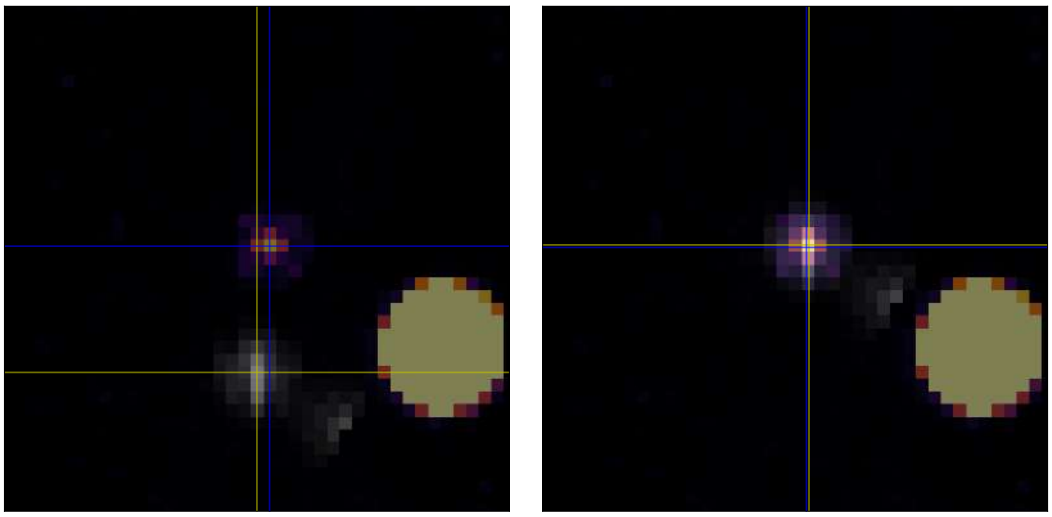

Figure A.1: Overlayed transverse images of the cylinder center acquired with the EndoTOFPET-US detector and the scanner modeled after the CTI ECAT EXACT 922 before (left) and after (right) co-registration. The EndoTOFPET-US image is visualized with a gray color scheme and the image achieved with the ring detector is visualized with the inferno color scheme. The intersection of the blue lines indicate the center position of the cylinder in the image acquired with the detector modeled after the Siemens Biograph Vision and the intersection of the yellow lines indicate the center of the cylinder in the image EndoTOFPET-US prototype image. The voxel size is 4 x 4 x 4 mm^3 for both images.

A.2 Application-Oriented Simulation

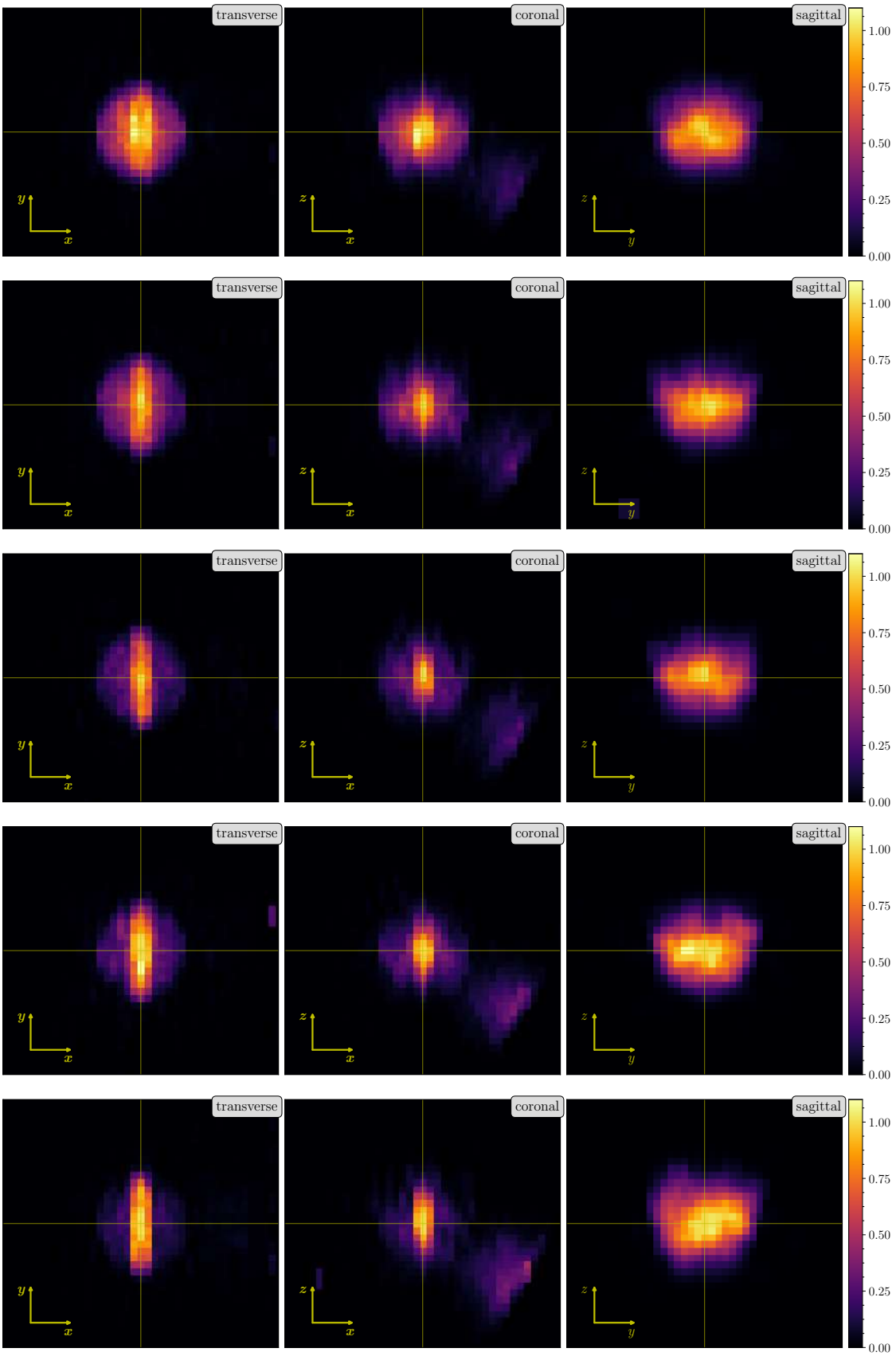

Figure A.2: Reconstructed images of all simulated signal to background ratios (StB), starting top with the lowest (3:1) and finishing on the bottom with the highest (30:1). Stopping iteration as well as the StB are mentioned in the top left corner of each image. Voxel size is 2 x 2 x 2 mm^3 and smoothing is applied. The voxel activity is for every image normalized to the center voxel of the cylinder (indicated by crossing lines).

Bibliography

[1] G. Hevesy, "The absorption and translocation of lead by plants: a contribution to the application of the method of radioactive indicators in the investigation of the change of substance in plants," *Biochemical Journal*, vol. 17, no. 4-5, p. 439, 1923.

[2] B. Selverstone, W. H. Sweet, and C. V. Robinson, "The clinical use of radioactive phosphorus in the surgery of brain tumors," *Annals of Surgery*, vol. 130, no. 4, p. 643, 1949.

[3] R. R. Raylman and R. L. Wahl, "A fiber-optically coupled positron-sensitive surgical probe," *Journal of Nuclear Medicine: Official Publication*, vol. 35, no. 5, pp. 909–913, 1994.

[4] F. Bogalhas, Y. Charon, M. A. Duval, F. Lefebvre, S. Palfi, L. Pinot, R. Siebert, and L. Ménard, "Development of a positron probe for localization and excision of brain tumours during surgery," *Physics in Medicine & Biology*, vol. 54, no. 14, p. 4439, 2009.

[5] EndoTOFPET-US Proposal, "Novel multimodal endoscopic probes for simultaneous PET/ultrasound imaging for image-guided interventions," *European Union 7th*, vol. 186, pp. 2007–2013.

[6] M. Zvolskỳ and EndoTOFPET-US Collaboration, "EndoTOFPET-US - A miniaturised calorimeter for endoscopic time-of-flight positron emission tomography," in *Journal of Physics: Conference Series*, vol. 587, 2015.

[7] M. Zvolský and EndoTOFPET-US Collaboration, "EndoTOFPET-US - A miniaturised calorimeter for endoscopic time-of-flight positron emission tomography," in *2013 CHEF Conference Record*, CHEF, 2013.

[8] B. Frisch and EndoTOFPET-US Collaboration, "Combining endoscopic ultrasound with time-of-flight PET: The EndoTOFPET-US project," *Nuclear Instruments and Methods in Physics Research Section A: Accelerators, Spectrometers, Detectors and Associated Equipment*, vol. 732, pp. 577–580, 2013.

[9] E. Garutti, "EndoTOFPET-US - A novel multimodal tool for endoscopy and positron emission tomography," in *2012 IEEE Nuclear Science Symposium and Medical Imaging Conference Record (NSS/MIC)*, pp. 2096–2101, IEEE, 2012.

[10] F. Grüner, F. Blumendorf, O. Schmutzler, T. Staufer, M. Bradbury, U. Wiesner, T. Rosentreter, G. Loers, D. Lutz, B. Richter, *et al.*, "Localising functionalised gold-nanoparticles in murine spinal cords by X-ray fluorescence imaging and background-reduction through spatial filtering for human-sized objects," *Scientific Reports*, vol. 8, no. 1, pp. 1–12, 2018.

[11] W. Pauli, "Wissenschaftlicher Briefwechsel mit Bohr, Einstein, Heisenberg u.a. Band II: 1930-1939 / Scientific Correspondence with Bohr, Einstein, Heisenberg a.o. Volume II: 1930-1939." 2008.

[12] E. Fermi, "An attempt of a theory of beta radiation. 1.," *Z. Phys.*, vol. 88, pp. 161–177, 1934.

[13] C. D. Anderson, "The positive electron," *Physical Review*, vol. 43, no. 6, pp. 491–494, 1933.

[14] L. W. Alvarez, "Nuclear K electron capture," *Physical Review*, vol. 52, no. 2, p. 134, 1937.

[15] L. Meitner, "Über die Entstehung der β-Strahl-Spektren radioaktiver Substanzen," *Zeitschrift für Physik*, vol. 9, no. 1, pp. 131–144, 1922.

[16] M. D. Harpen, "Positronium: Review of symmetry, conserved quantities and decay for the radiological physicist," 2004.

[17] O. E. Mogensen and F. M. Jacobsen, "Positronium yields in liquids determined by lifetime and angular correlation measurements," *Chemical Physics*, vol. 73, no. 1-2, pp. 223–234, 1982.

[18] H. Alva-Sánchez, C. Quintana-Bautista, A. Martínez-Dávalos, M. A. Ávila-Rodríguez, and M. Rodríguez-Villafuerte, "Positron range in tissue-equivalent materials: Experimental microPET studies," *Physics in Medicine & Biology*, vol. 61, no. 17, p. 6307, 2016.

[19] S. DeBenedetti, C. E. Cowan, W. R. Konneker, and H. Primakoff, "On the angular distribution of two-photon annihilation radiation," *Physical Review*, vol. 77, no. 2, pp. 205–212, 1950.

[20] K. Shibuya, E. Yoshida, F. Nishikido, T. Suzuki, T. Tsuda, N. Inadama, T. Yamaya, and H. Murayama, "Annihilation photon acollinearity in PET: Volunteer and phantom FDG studies," *Physics in Medicine & Biology*, vol. 52, no. 17, p. 5249, 2007.

[21] K. Bethge, G. Walter, and B. Wiedmann, *Kernphysik: Eine Einführung*, vol. 3. Springer, 2007.

[22] P. Marmier and E. Sheldon, *Physics of nuclei and particles*, vol. 2. Academic Press, 2013.

[23] S. I. Eidelman and B. A. Shwartz, "Interactions of particles and radiation with matter," in *Handbook of Particle Detection and Imaging* (C. Grupen and I. Buvat, eds.), vol. 2, pp. 3–23, Berlin Heidelberg: Springer, 2012.

[24] J. T. Bushberg, J. A. Seibert, E. M. Leidholdt, and J. M. Boone, *The essential physics of medical imaging*, vol. 3. Lippincott Williams & Wilkins, 2011.

[25] R. D. Evans and A. Noyau, "The atomic nucleus," vol. 582, 1955.

[26] O. Klein and Y. Nishina, "Über die Streuung von Strahlung durch freie Elektronen nach der neuen relativistischen Quantendynamik von Dirac," *Zeitschrift für Physik*, vol. 52, no. 11-12, pp. 853–868, 1929.

[27] S. M. Blinder, "Klein-Nishina formula for Compton effect." http://demonstrations.wolfram.com/KleinNishinaFormulaForComptonEffect/, 2009.

[28] G. Bizarri, "Scintillation mechanisms of inorganic materials: From crystal characteristics to scintillation properties," *Journal of Crystal Growth*, vol. 312, no. 8, pp. 1213–1215, 2010.

[29] S. Gundacker, R. M. Turtos, E. Auffray, and P. Lecoq, "Precise rise and decay time measurements of inorganic scintillators by means of X-ray and 511 keV excitation," *Nuclear Instruments and Methods in Physics Research, Section A: Accelerators, Spectrometers, Detectors and Associated Equipment*, vol. 891, pp. 42–52, 2018.

[30] A. Lempicki, A. J. Wojtowicz, and E. Berman, "Fundamental limits of scintillator performance," *Nuclear Instruments and Methods in Physics Research Section A: Accelerators, Spectrometers, Detectors and Associated Equipment*, vol. 333, no. 2-3, pp. 304–311, 1993.

[31] P. Lecoq, "Development of new scintillators for medical applications," *Nuclear Instruments and Methods in Physics Research, Section A: Accelerators, Spectrometers, Detectors and Associated Equipment*, vol. 809, pp. 130–139, 2016.

[32] W. W. Moses, G. A. Bizarri, R. T. Williams, S. A. Payne, A. N. Vasil'Ev, J. Singh, Q. Li, J. Q. Grim, and W. S. Choong, "The origins of scintillator non-proportionality," *IEEE Transactions on Nuclear Science*, vol. 59, no. 5, pp. 2038–2044, 2012.

[33] S. A. Payne, N. J. Cherepy, G. Hull, J. D. Valentine, W. W. Moses, and W. S. Choong, "Nonproportionality of scintillator detectors: Theory and experiment," *IEEE Transactions on Nuclear Science*, vol. 56, no. 4, pp. 2506–2512, 2009.

[34] S. A. Payne, "Nonproportionality of scintillator detectors. IV. Resolution contribution from delta-rays," *IEEE Transactions on Nuclear Science*, vol. 62, no. 1, pp. 372–380, 2015.

[35] M. Moszyński, A. Syntfeld-Każuch, L. Swiderski, M. Grodzicka, J. Iwanowska, P. Sibczyński, and T. Szczęśniak, "Energy resolution of scintillation detectors," *Nuclear Instruments and Methods in Physics Research Section A: Accelerators, Spectrometers, Detectors and Associated Equipment*, vol. 805, pp. 25–35, 2016.

[36] M. Moszyński, A. Nassalski, A. Syntfeld-Każuch, L. Świderski, and T. Szczçśniak, "Energy resolution of scintillation detectors - New observations," *IEEE Transactions on Nuclear Science*, vol. 55, no. 3, pp. 1062–1068, 2008.

[37] N. Otte, "The silicon photomultiplier - A new device for high energy physics, astroparticle physics, industrial and medical applications," tech. rep., 2006.

[38] S. Dolinsky, G. Fu, and A. Ivan, "Timing resolution performance comparison for fast and standard outputs of SensL SiPM," in *2013 IEEE Nuclear Science Symposium and Medical Imaging Conference (2013 NSS/MIC)*, pp. 1–6, IEEE, 2013.

[39] S. S. Piatek, "Physics and operation of an MPPC," *Hamamatsu Corporation and New Jersey Institute of Technology*, 2014.

[40] O. Marinov, M. J. Deen, and J. A. Jimenez Tejada, "Theory of microplasma fluctuations and noise in silicon diode in avalanche breakdown," *Journal of Applied Physics*, vol. 101, no. 6, p. 064515, 2007.

[41] M. Mazzillo, G. Condorelli, D. Sanfilippo, G. Valvo, B. Carbone, G. Fallica, S. Billotta, M. Belluso, G. Bonanno, L. Cosentino, *et al.*, "Silicon photomultiplier technology at STMicroelectronics," *IEEE Transactions on Nuclear Science*, vol. 56, no. 4, pp. 2434–2442, 2009.

[42] C. R. Crowell and S. M. Sze, "Temperature dependence of avalanche multiplication in semiconductors," *Applied Physics Letters*, vol. 9, no. 6, pp. 242–244, 1966.

[43] E. Roncali and S. R. Cherry, "Application of silicon photomultipliers to positron emission tomography," *Annals of Biomedical Engineering*, vol. 39, no. 4, pp. 1358–1377, 2011.

[44] O. Christensen, "Quantum efficiency of the internal photoelectric effect in silicon and germanium," *Journal of Applied Physics*, vol. 47, no. 2, pp. 689–695, 1976.

[45] M. A. Ward and A. Vacheret, "Impact of after-pulse, pixel crosstalk and recovery time in multi-pixel photon counter™ response," *Nuclear Instruments and Methods in Physics Research Section A: Accelerators, Spectrometers, Detectors and Associated Equipment*, vol. 610, no. 1, pp. 370–373, 2009.

[46] A. S. Grove, *Physics and technology of semiconductor devices*. Wiley, 1967.

[47] A. L. Lacaita, F. Zappa, S. Bigliardi, and M. Manfredi, "On the bremsstrahlung origin of hot-carrier-induced photons in silicon devices," *IEEE Transactions on Electron Devices*, vol. 40, no. 3, pp. 577–582, 1993.

[48] P. Finocchiaro, A. Pappalardo, L. Cosentino, M. Belluso, S. Billotta, G. Bonanno, B. Carbone, G. Condorelli, S. Di Mauro, G. Fallica, *et al.*, "Characterization of a novel 100-channel silicon photomultiplier — Part II: Charge and time," *IEEE Transactions on Electron Devices*, vol. 55, no. 10, pp. 2765–2773, 2008.

[49] A. G. Stewart, V. Saveliev, S. J. Bellis, D. J. Herbert, P. J. Hughes, and J. C. Jackson, "Performance of 1-mm^2 silicon photomultiplier," *IEEE Journal of Quantum Electronics*, vol. 44, no. 2, pp. 157–164, 2008.

[50] S. Gundacker, E. Auffray, N. Di Vara, B. Frisch, H. Hillemanns, P. Jarron, B. Lang, T. Meyer, S. Mosquera-Vazquez, E. Vauthey, *et al.*, "SiPM time resolution: From single photon to saturation," *Nuclear Instruments and Methods in Physics Research, Section A: Accelerators, Spectrometers, Detectors and Associated Equipment*, vol. 718, pp. 569–572, 2013.

[51] F. Powolny, *Characterization of time resolved photodetector systems for positron emission tomography*. PhD thesis, Université de Neuchâtel, 2009.

[52] E. Auffray, B. Frisch, F. Geraci, A. Ghezzi, S. Gundacker, H. Hillemanns, P. Jarron, T. Meyer, M. Paganoni, K. Pauwels, *et al.*, "A comprehensive systematic study of coincidence time resolution and light yield using scintillators of different size, wrapping and doping," in *2011 IEEE Nuclear Science Symposium and Medical Imaging Conference Record (NSS/MIC)*, pp. 64–71, IEEE, 2011.

[53] S. Gundacker, A. Knapitsch, E. Auffray, P. Jarron, T. Meyer, and P. Lecoq, "Time resolution deterioration with increasing crystal length in a TOF-PET system," *Nuclear Instruments and Methods in Physics Research, Section A: Accelerators, Spectrometers, Detectors and Associated Equipment*, vol. 737, pp. 92–100, 2014.

[54] P. Lecoq, M. Korzhik, and A. Vasiliev, "Can transient phenomena help improving time resolution in scintillators?," *IEEE Transactions on Nuclear Science*, vol. 61, no. 1, pp. 229–234, 2014.

[55] R. M. Turtos, S. Gundacker, A. Polovitsyn, S. Christodoulou, M. Salomoni, E. Auffray, I. Moreels, P. Lecoq, and J. Q. Grim, "Ultrafast emission from colloidal nanocrystals under pulsed X-ray excitation," *Journal of Instrumentation*, vol. 11, no. 10, 2016.

[56] S. Korpar, R. Dolenec, P. Križan, R. Pestotnik, and A. Stanovnik, "Study of TOF PET using Cherenkov light," vol. 654, pp. 532–538, 2011.

[57] S. Seifert, H. Dam, and D. Schaart, "The lower bound on the timing resolution of scintillation detectors," *Physics in Medicine & Biology*, vol. 57, no. 7, p. 1797, 2012.

[58] S. Gundacker, R. M. Turtos, E. Auffray, M. Paganoni, and P. Lecoq, "High-frequency SiPM readout advances measured coincidence time resolution limits in TOF-PET," *Physics in Medicine & Biology*, vol. 64, 2019.

[59] P. Kaatsch, C. Spix, A. Katalinic, S. Hentschel, S. Luttmann, C. Stegmaier, S. Caspritz, M. Christ, A. Ernst, J. Folkerts, *et al.*, "Krebs in Deutschland 2011/2012," 2015.

[60] S. N. Reske, N. M. Blumstein, B. Neumaier, H.-W. Gottfried, F. Finsterbusch, D. Kocot, P. Möller, G. Glatting, and S. Perner, "Imaging prostate cancer with 11C-choline PET/CT," *Journal of Nuclear Medicine*, vol. 47, no. 8, pp. 1249–1254, 2006.

[61] K. Kitajima, R. C. Murphy, M. A. Nathan, and K. Sugimura, "Update on positron emission tomography for imaging of prostate cancer," *International Journal of Urology*, vol. 21, no. 1, pp. 12–23, 2014.

[62] T. Heußer, P. Mann, C. M. Rank, M. Schäfer, A. Dimitrakopoulou-Strauss, H. P. Schlemmer, B. A. Hadaschik, K. Kopka, P. Bachert, M. Kachelrieß, *et al.*, "Investigation of the halo-artifact in 68Ga-PSMA-11-PET/MRI," *PLoS One*, vol. 12, no. 8, 2017.

[63] A. Afshar-Oromieh, A. Malcher, M. Eder, M. Eisenhut, H. G. Linhart, B. A. Hadaschik, T. Holland-Letz, F. Giesel, C. Kratochwil, S. Haufe, *et al.*, "PET imaging with a [68 Ga] gallium-labelled PSMA ligand for the diagnosis of prostate cancer: Biodistribution in humans and first evaluation of tumour lesions," *European Journal of Nuclear Medicine and Molecular Imaging*, vol. 40, no. 4, pp. 486–495, 2013.

[64] T. Maurer, M. Eiber, and B. J. Krause, "Molekulare multimodale Hybridbildgebung des Prostata- und Blasenkarzinoms," *Der Urologe*, vol. 53, no. 4, pp. 469–483, 2014.

[65] H. Jadvar and J. A. Parker, *Clinical PET and PET/CT*. Springer, 2005.

[66] M. A. Blake, O. A. Catalano, D. V. Sahani, A. R. Guimaraes, and P. A. Bonaffini, "State-of-the-art PET/CT of the pancreas: Current role and emerging indications," *Radiographics*, vol. 32, no. 4, pp. 1133–1158, 2012.

[67] S. Sahbai, P. Rieping, C. Pfannenberg, C. la Fougére, and M. Reimold, "Pancreatic ductal adenocarcinoma with high radiotracer uptake in 68Ga-prostate-specific membrane antigen PET/CT," *Clinical Nuclear Medicine*, vol. 42, no. 9, pp. 717–718, 2017.

[68] M. Dahlbom, "PET imaging: Basics and new trends," *Handbook of Particle Detection and Imaging*, pp. 935–971, 2012.

[69] G. Delso, S. Fürst, B. Jakoby, R. Ladebeck, C. Ganter, S. G. Nekolla, M. Schwaiger, and S. I. Ziegler, "Performance measurements of the Siemens mMR integrated whole-body PET/MR scanner," *Journal of Nuclear Medicine*, vol. 52, no. 12, pp. 1914–1922, 2011.

[70] C. S. Levin, S. H. Maramraju, M. M. Khalighi, T. W. Deller, G. Delso, and F. Jansen, "Design features and mutual compatibility studies of the time-of-flight PET capable GE SIGNA PET/MR system," *IEEE Transactions on Medical Imaging*, vol. 35, no. 8, pp. 1907–1914, 2016.

[71] H. W. Kwon, A. K. Becker, J. M. Goo, and G. J. Cheon, "FDG whole-body PET/MRI in oncology: A systematic review," *Nuclear Medicine and Molecular Imaging*, vol. 51, no. 1, pp. 22–31, 2017.

[72] A. Mehranian, F. Kotasidis, and H. Zaidi, "Accelerated time-of-flight (TOF) PET image reconstruction using TOF bin subsetization and TOF weighting matrix pre-computation," *Physics in Medicine & Biology*, vol. 61, no. 3, p. 1309, 2016.

[73] J. van Sluis, J. de Jong, J. Schaar, W. Noordzij, P. van Snick, R. Dierckx, R. Borra, A. Willemsen, and R. Boellaard, "Performance characteristics of the digital Biograph Vision PET/CT system," *Journal of Nuclear Medicine*, vol. 60, no. 7, pp. 1031–1036, 2019.

[74] M. Conti, "Focus on time-of-flight PET: The benefits of improved time resolution," *European Journal of Nuclear Medicine and Molecular Imaging*, vol. 38, no. 6, pp. 1147–1157, 2011.

[75] A. Alessio and P. Kinahan, "PET image reconstruction," *Nuclear Medicine*, vol. 1, pp. 1–22, 2006.

[76] A. P. Dempster, N. M. Laird, and D. B. Rubin, "Maximum likelihood from incomplete data via the EM algorithm," *Journal of the Royal Statistical Society: Series B (Methodological)*, vol. 39, no. 1, pp. 1–22, 1977.

[77] L. A. Shepp and Y. Vardi, "Maximum likelihood reconstruction for emission tomography," *IEEE Transactions on Medical Imaging*, vol. 1, no. 2, pp. 113–122, 1982.

[78] C. Comtat, "Image reconstruction," in *Handbook of Particle Detection and Imaging* (C. Grupen and I. Buvat, eds.), pp. 973–1006, Berlin Heidelberg: Springer, 2012.

[79] V. V. Selivanov, Y. Picard, J. Cadorette, S. Rodrigue, and R. Lecomte, "Detector response models for statistical iterative image reconstruction in high resolution PET," *IEEE Transactions on Nuclear Science*, vol. 47, no. 3, pp. 1168–1175, 2000.

[80] V. Y. Panin, F. Kehren, C. Michel, and M. Casey, "Fully 3-d PET reconstruction with system matrix derived from point source measurements," *IEEE Transactions on Medical Imaging*, vol. 25, no. 7, pp. 907–921, 2006.

[81] M. Rafecas, B. Mosler, M. Dietz, M. Pogl, A. Stamatakis, D. P. McElroy, and S. I. Ziegler, "Use of a Monte Carlo-based probability matrix for 3-d iterative reconstruction of MADPET-II data," *IEEE Transactions on Nuclear Science*, vol. 51, no. 5, pp. 2597–2605, 2004.

[82] B. Frisch and EndoTOFPET-US Collaboration, "Combining endoscopic ultrasound with time-of-flight PET: The EndoTOFPET-US project," *Nuclear Instruments and Methods in Physics Research Section A: Accelerators, Spectrometers, Detectors and Associated Equipment*, vol. 732, pp. 577–580, 2013.

[83] S. Mandai and E. Charbon, "Multi-channel digital SiPMs: Concept, analysis and implementation," in *2012 IEEE Nuclear Science Symposium and Medical Imaging Conference Record (NSS/MIC)*, pp. 1840–1844, IEEE, 2012.

[84] S. Mandai, V. Jain, and E. Charbon, "A 780×800 m^2 multichannel digital silicon photomultiplier with column-parallel time-to-digital converter and basic characterization," *IEEE Transactions on Nuclear Science*, vol. 61, no. 1, pp. 44–52, 2014.

[85] S. Mandai, E. Venialgo, and E. Charbon, "Timing optimization utilizing order statistics and multichannel digital silicon photomultipliers," *Optics Letters*, vol. 39, no. 3, pp. 552–554, 2014.

[86] W. Shen, K. Briggl, H. Chen, P. Fischer, A. Gil, T. Harion, M. Ritzert, and H. C. Schultz-Coulon, "STiC - A mixed mode chip for SiPM ToF applications," in *2012 IEEE Nuclear Science Symposium and Medical Imaging Conference Record (NSS/MIC)*, pp. 877–881, IEEE, 2012.

[87] Amptek Inc., "Hitachi medical systems Europe." http://www.hitachi-medical-systems.eu/products/ultrasound/transducers/endocavity.html, 2017.

[88] K. Doroud, E. Auffray, P. Jarron, T. Meyer, and P. Lecoq, "Differential-readout: The technique to optimise timing in a monolithic MPPC array," *Nuclear Instruments and Methods in Physics Research, Section A: Accelerators, Spectrometers, Detectors and Associated Equipment*, vol. 717, pp. 5–10, 2013.

[89] D. Cortinovis, *Characterization studies and prototyping for a novel positron emission tomography detector*. PhD thesis, University of Hamburg, 2016.

[90] M. Zvolský, *Simulation, image reconstruction and SiPM characterisation for a novel endoscopic positron emission tomography detector*. PhD thesis, University of Hamburg, 2017.

[91] E. Auffray, F. B. M. B. Hadj, D. Cortinovis, K. Doroud, E. Garutti, P. Lecoq, Z. Liu, R. Martinez, M. Paganoni, M. Pizzichemi, *et al.*, "Characterization studies of silicon photomultipliers and crystals matrices for a novel time of flight PET detector," *Journal of Instrumentation*, vol. 10, no. 06, 2015.

[92] V. Stankova, W. Shen, K. Briggl, H. Chen, P. Fischer, A. Gil, T. Harion, V. Kiworra, Y. Munwes, M. Ritzert, *et al.*, "STIC3 - Silicon photomultiplier timing chip with picosecond resolution," *Nuclear Instruments and Methods in Physics Research Section A: Accelerators, Spectrometers, Detectors and Associated Equipment*, vol. 787, pp. 284–287, 2015.

[93] Y. Munwes, K. Briggl, H. Chen, T. Harion, H. C. Schultz-Coulon, W. Shen, and V. Stankova, "Single photon time resolution with silicon photomultipliers using the STiC readout chip," in *2015 IEEE Nuclear Science Symposium and Medical Imaging Conference (NSS/MIC)*, pp. 1–4, IEEE, 2015.

[94] T. Harion, *The STiC ASIC high precision timing with silicon photomultipliers*. PhD thesis, 2015.

[95] T. Harion, K. Briggl, H. Chen, P. Fischer, A. Gil, V. Kiworra, M. Ritzert, H.-C. Schultz-Coulon, W. Shen, and V. Stankova, "STiC - a mixed mode silicon photomultiplier readout ASIC for time-of-flight applications," *Journal of Instrumentation*, vol. 9, no. 02, p. C02003, 2014.

[96] M. D. Rolo, R. Bugalho, F. Goncalves, G. Mazza, A. Rivetti, J. C. Silva, R. Silva, and J. Varela, "TOFPET ASIC for PET applications," *Journal of Instrumentation*, vol. 8, no. 02, p. C02050, 2013.

[97] A. Di Francesco, R. Bugalho, L. Oliveira, A. Rivetti, M. Rolo, J. C. Silva, and J. Varela, "TOFPET 2: A high-performance circuit for PET time-of-flight," *Nuclear Instruments and Methods in Physics Research Section A: Accelerators, Spectrometers, Detectors and Associated Equipment*, vol. 824, pp. 194–195, 2016.

[98] R. Bugalho, C. Gaston, M. D. Rolo, J. C. Silva, R. Silva, and J. Varela, "EndoTOFPET-US data acquisition system," *Journal of Instrumentation*, vol. 8, no. 02, p. C02049, 2013.

[99] C. Zorraquino, R. Bugalho, M. Rolo, J. C. Silva, V. Vecklans, R. Silva, C. Ortigão, J. A. Neves, S. Tavernier, P. Guerra, *et al.*, "Asymmetric data acquisition system for an endoscopic PET-US detector," *IEEE Transactions on Nuclear Science*, vol. 63, no. 1, pp. 213–221, 2016.

[100] C. Xu, *Study of the silicon photomultipliers and their applications in positron emission tomography.* PhD thesis, University of Hamburg, 2014.

[101] A. Schoch, B. Fuerst, F. Achilles, S. Demirci, and N. Navab, "A lightweight and portable communication framework for multimodal image-guided therapy," in *The Sixth International Workshop on Systems and Architectures for Computer Assisted Interventions (SACAI)*, 2013.

[102] D. Kügler, H. Krumb, J. Bredemann, I. Stenin, J. Kristin, T. Klenzner, J. Schipper, R. Schmitt, G. Sakas, and A. Mukhopadhyay, "High-precision evaluation of electromagnetic tracking," *International Journal of Computer Assisted Radiology and Surgery*, vol. 14, no. 7, pp. 1127–1135, 2019.

[103] E. Auffray, F. B. M. B. Hadj, D. Cortinovis, K. Doroud, E. Garutti, P. Lecoq, Z. Liu, R. Martinez, M. Paganoni, M. Pizzichemi, *et al.*, "Characterization studies of silicon photomultipliers and crystals matrices for a novel time of flight PET detector," *Journal of Instrumentation*, vol. 10, no. 06, p. P06009, 2015.

[104] A. Cserkaszky, T. Wendler, and S. Wiesner, "GPU accelerated realtime reconstruction of freehand SPECT examinations," in *2012 WMIC*, 2012.

[105] A. Cserkaszky, B. Frisch, M. Zvolský, and G. Cucciati, "Reconstruction of freehand PET examinations," in *2013 WMIC*, 2013.

[106] J. Nickolls, I. Buck, and M. Garland, "Scalable parallel programming," in *2008 IEEE Hot Chips 20 Symposium (HCS)*, pp. 40–53, IEEE, 2008.

[107] G. G. Stokes, "XXX. On the change of refrangibility of light," *Philosophical Transactions of the Royal Society of London*, no. 142, pp. 463–562, 1852.

[108] F. Goppelsröder, "Ueber eine fluoreszierende Substanz aus dem Kubaholze," *Annalen der Physik*, vol. 207, no. 7, pp. 464–471, 1867.

[109] A. Jablonski, "Efficiency of anti-stokes fluorescence in dyes," *Nature*, vol. 131, no. 3319, pp. 839–840, 1933.

[110] J. R. Lakowicz, *Principles of fluorescence spectroscopy.* Springer, 2013.

[111] https://www.radiologycafe.com/radiology-trainees/frcr-physics-notes/production-of-x-rays, Aug 2019.

[112] K. Achterhold, M. Bech, S. Schleede, G. Potdevin, R. Ruth, R. Loewen, and F. Pfeiffer, "Monochromatic computed tomography with a compact laser-driven X-ray source," *Scientific Reports*, vol. 3, p. 1313, 2013.

[113] N. D. Powers, I. Ghebregziabher, G. Golovin, C. Liu, S. Chen, S. Banerjee, J. Zhang, and D. P. Umstadter, "Quasi-monoenergetic and tunable X-rays from a laser-driven Compton light source," *Nature Photonics*, vol. 8, no. 1, p. 28, 2014.

[114] T. Brümmer, *Design study of a laser-driven X-ray source for medical fluorescence imaging*. PhD thesis, University of Hamburg, 2018.

[115] E. Esarey, C. B. Schroeder, and W. P. Leemans, "Physics of laser-driven plasma-based electron accelerators," *Reviews of Modern Physics*, vol. 81, no. 3, p. 1229, 2009.

[116] S. Bulanov, N. Naumova, F. Pegoraro, and J. Sakai, "Particle injection into the wave acceleration phase due to nonlinear wake wave breaking," *Physical Review E*, vol. 58, no. 5, p. R5257, 1998.

[117] J. Faure, C. Rechatin, A. Norlin, A. Lifschitz, Y. Glinec, and V. Malka, "Controlled injection and acceleration of electrons in plasma wakefields by colliding laser pulses," *Nature*, vol. 444, no. 7120, pp. 737–739, 2006.

[118] V. Malka, J. Faure, C. Rechatin, A. Ben-Ismaïl, J. K. Lim, X. Davoine, and E. Lefebvre, "Laser-driven accelerators by colliding pulses injection: A review of simulation and experimental results," *Physics of Plasmas*, vol. 16, no. 5, p. 056703, 2009.

[119] B. Zeitler, I. Dornmair, T. Gehrke, M. Titberidze, A. R. Maier, B. Hidding, K. Flöttmann, and F. Grüner, "Merging conventional and laser wakefield accelerators," in *Laser Acceleration of Electrons, Protons, and Ions II; and Medical Applications of Laser-Generated Beams of Particles II; and Harnessing Relativistic Plasma Waves III*, vol. 8779, p. 877904, International Society for Optics and Photonics, 2013.

[120] http://regae.desy.de., Feb 2019.

[121] E. Esarey, S. K. Ride, and P. Sprangle, "Nonlinear Thomson scattering of intense laser pulses from beams and plasmas," *Physical Review E*, vol. 48, no. 4, p. 3003, 1993.

[122] J. A. Clarke, *The science and technology of undulators and wigglers*, vol. 4. Oxford University Press on Demand, 2004.

[123] S. K. Ride, E. Esarey, and M. Baine, "Thomson scattering of intense lasers from electron beams at arbitrary interaction angles," *Physical Review E*, vol. 52, no. 5, p. 5425, 1995.

[124] J. E. Gillam and M. Rafecas, "Monte-Carlo simulations and image reconstruction for novel imaging scenarios in emission tomography," *Nuclear Instruments and Methods in Physics Research Section A: Accelerators, Spectrometers, Detectors and Associated Equipment*, vol. 809, pp. 76–88, 2016.

[125] R. L. Harrison, "Simulation of medical imaging systems: Emission and transmission tomography," *Handbook of Particle Detection and Imaging*, pp. 1095–1124, 2012.

[126] S. Agostinelli, J. Allison, K. Amako, J. Apostolakis, H. Araujo, P. Arce, M. Asai, D. Axen, S. Banerjee, G. Barrand, *et al.*, "Geant4 — A simulation toolkit," *Nuclear Instruments and Methods in Physics Research Section A: Accelerators, Spectrometers, Detectors and Associated Equipment*, vol. 506, no. 3, pp. 250–303, 2003.

[127] J. Allison, K. Amako, J. Apostolakis, H. Araujo, P. A. Dubois, M. Asai, G. Barrand, R. Capra, S. Chauvie, R. Chytracek, *et al.*, "Geant4 developments and applications," *IEEE Transactions on Nuclear Science*, vol. 53, no. 1, pp. 270–278, 2006.

[128] Geant4 Collaboration, "Geant4 user's guide for application developers," http://geant4.web.cern.ch/geant4/UserDocumentation/UsersGuides/ForApplicationDeveloper/html/index.html.

[129] The GAMOS Collaboration, "Gamos 5.2.0 user's guide," tech. rep., 2018.

[130] M. Canadas, P. Arce, and P. R. Mendes, "Validation of a small-animal PET simulation using GAMOS: A GEANT4-based framework," *Physics in Medicine & Biology*, vol. 56, no. 1, p. 273, 2010.

[131] P. Arce, J. I. Lagares, L. Harkness, D. Pérez-Astudillo, M. Cañadas, P. Rato, M. de Prado, Y. Abreu, G. de Lorenzo, M. Kolstein, *et al.*, "Gamos: A framework to do Geant4 simulations in different physics fields with an user-friendly interface," *Nuclear Instruments and Methods in Physics Research Section A: Accelerators, Spectrometers, Detectors and Associated Equipment*, vol. 735, pp. 304–313, 2014.

[132] T. Kaltsas, L. Caldeira, J. Scheins, L. Tellmann, E. R. Kops, N. J. Shah, and C. Lerche, "Reconstruction of attenuation maps for a PET/MR scanner based on the LSO background activity," in *2015 IEEE Nuclear Science Symposium and Medical Imaging Conference (NSS/MIC)*, pp. 1–4, IEEE, 2015.

[133] O. Brandt and Y. Munwes, "Commissioning and first image reconstruction with a new time-of-flight PET prototype," in *2018 IEEE Nuclear Science Symposium and Medical Imaging Conference Proceedings (NSS/MIC)*, pp. 1–5, IEEE, 2018.

[134] J. A. Nelder and R. Mead, "A simplex method for function minimization," *The Computer Journal*, vol. 7, no. 4, pp. 308–313, 1965.

[135] J. E. Thompson and P. D. Stricker, "Diagnostic accuracy of multi-parametric MRI and transrectal ultrasound-guided biopsy in prostate cancer," *The Lancet*, vol. 389, no. 10071, pp. 767–768, 2017.

[136] T. Merlin, S. Stute, D. Benoit, J. Bert, T. Carlier, C. Comtat, M. Filipovic, F. Lamare, and D. Visvikis, "CASToR: A generic data organization and processing code framework for multi-modal and multi-dimensional tomographic reconstruction," *Physics in Medicine & Biology*, vol. 63, no. 18, p. 185005, 2018.

[137] S. Vallabhajosula, *Molecular imaging: Radiopharmaceuticals for PET and SPECT*. Springer, 2009.

[138] J. J. van Sluis, J. de Jong, J. Schaar, W. Noordzij, P. van Snick, R. Dierckx, R. Borra, A. Willemsen, and R. Boellaard, "Performance characteristics of the digital Biograph Vision PET/CT system," *Journal of Nuclear Medicine*, vol. 60, no. 7, pp. 1031–1036, 2019.

[139] F. Blumendorf, *Background reduction for XFI with human-sized phantoms.* PhD thesis, University of Hamburg, 2020.

[140] C. Körnig, "Spatial reconstruction of small objects for medical X-ray fluorescence imaging using multiple detectors," Master's thesis, University of Hamburg, 2019.

[141] P. Seller, S. Bell, R. J. Cernik, C. Christodoulou, C. K. Egan, J. A. Gaskin, S. Jacques, S. Pani, B. D. Ramsey, C. Reid, *et al.*, "Pixellated Cd (Zn) Te high-energy X-ray instrument," *Journal of Instrumentation*, vol. 6, no. 12, p. C12009, 2011.

[142] Amptek Inc., "Xr-100cdte x-ray & gamma ray detector." http://www.amptek.com/products/cdte-x-ray-and-gamma-ray-detectors/xr-100cdte-x-ray-and-gamma-ray-detector#Applications.htlm, May 2019.

[143] A. H. Andersen and A. C. Kak, "Simultaneous algebraic reconstruction technique (SART): A superior implementation of the ART algorithm," *Ultrasonic Imaging*, vol. 6, no. 1, pp. 81–94, 1984.

Acknowledgement

I would like to dedicate the last words of this work to the many people who helped and accompanied me on my long journey to my doctorate.

First of all, I would like to express my deepest gratitude to Prof. Erika Garutti for supervising me. You passed on knowledge, gave me the space to develop and test my own ideas and also stood by me at all times with advice, compassion and encouragement when things didn't work as planned. Thanks for always keeping an open door for me and making my time in your group highly enjoyable and something I will always look back at fondly. I also would like to thank Dr. Ties Behnke for taking over the co-supervision of this thesis, always questioning ideas and the the work critically, counselling and giving advice at any time.

I would like to thank Dr. Yonathan Munwes with whom I shared a lot of long days over broken electronics - without lacking fun and laughter. I am thankful for my "office mates" who made even the worst days a little more tolerable and even enjoyable: Milan, Sara, Tobias, Bastian, Mateo, Jack and everybody else I shared an office with over the past few years. I would like to thank Milan in particular who always had an open ear, gave good advice or had at least some funny comment at hand and has become a good friend throughout our years in the office.

I would like to give thanks to everybody from the EndoTOFPET family for making this work possible.

Finally, I would like to thank my great love, Anika, for her unwavering patience, never ending support and of course impeccable grammar.

This research project has received funding from the European Union 7th Framework Program (FP7/2007-2013) under Grant Agreement No.256984(EndoTOFPETUS) and is supported by a Marie Curie Early Initial Training Network Program (PITN-GA-2011-289355-PicoSEC-MCNet).

Eidesstattliche Versicherung/ Declaration of oath

Hiermit versichere ich an Eides statt, die vorliegende Dissertationsschrift selbst verfasst und keine anderen als die angegebenen Hilfsmittel und Quellen benutzt zu haben.

Die eingereichte schriftliche Fassung entspricht der auf dem elektronischen Speichermedium.

Die Dissertation wurde in der vorgelegten oder einer ähnlichen Form nicht schon einamal in einem früheren Promotionsverfahren angenommen oder als ungenügend beurteilt.

Hamburg, den 17.10.2019